Conjugated polyelectrolytes and lipid membranes: from exciton transport to membrane dynamics

By

Christina Faye Calver

A thesis submitted to McGill University in partial fulfillment of the requirements for the degree of Doctor of Philosophy

Department of Chemistry, McGill University

Montréal, Québec, Canada

April 2017

I dedicate this thesis

To: my mom, Sandra Calver, whose dedication, work ethic, and kind heart are an inspiration to me. Reflecting on all that you have accomplished while raising four daughters on your own has been a motivation for me to gather my strength and persevere through tough times.

Abstract

Conjugated polymer (CP) materials and their water-soluble counterparts, conjugated polyelectrolytes (CPEs), are currently used in a variety of applications including photovoltaics, light emitting diodes, and chemical/biological sensors. Fundamental studies on the synthesis of ever more complex architectures and on their resulting optoelectronic properties have paved the way to the broad range of innovative applications associated with these materials. A key discovery was the realization that the optical properties of CP/CPE materials, in particular energy migration along the polymer backbone, may be modulated by the polymer morphology and degree of intra/interchain association. CP and CPEs are thus highly sensitive to the nature of the solvating environment. For CPEs, this also includes the ionic strength and the presence of surfactants.

This thesis explores the self-assembly of lipid membranes with CPEs as a means of tuning CPE optical properties, and exploits CPE/lipid membrane interactions as a platform to develop applications centering on the study of membrane biophysics and the advancement of biomimetic light harvesting materials. This thesis additionally describes fundamental studies toward improving CPE photostability, providing protocols to prepare anti-fading cocktails that are required for emerging single particle/molecule bioanalytical and biophysical studies requiring CPE excitation at high duty cycles.

Working with poly(phenylene vinylene) CPE adsorbed onto silicon dioxide nanoparticles, we initially show how the emission enhancement that accompanies a membrane-induced conformational change of a CPE is exploited as a novel means of detecting the dynamics of membrane rearrangement, a topic that has hitherto been difficult to study experimentally despite its importance in cell biology. While in this study the manipulation of energy transfer in a CPE was used as a tool to study membrane biophysics, the ability of the membrane to organize CPEs is an interesting topic in its own right. Along this line, in a second study lipid membranes are evaluated for their ability to direct the self-assembly of CPEs with the goal of achieving efficient energy migration through the membrane to develop a biomimetic light harvesting antenna. Here we show that CPEs can be successfully embedded within the membrane of oppositely charged liposomes at a high density (< 1 nm separation) without self-quenching. Light harvested by the polymers is transferred via through-space mechanisms to a lipophilic energy acceptor, where homotransfer between polymers is shown to play role in funneling energy to the acceptor in a manner analogous to the chlorophyll antenna molecules present in the naturally occurring light

harvesting antennas of green plants. Alongside highlighting opportunities for CPE/lipid interaction and constructs toward the development of applications, in a third and fourth study, different solution additives are evaluated toward the goal of improving the photostability of CPEs under microscopy imaging conditions in order to meet these demands. By using an enzymatic oxygen scavenging system and/or adding small molecule triplet quenchers, the number of photons collected from PPE-CO_2 increases by up to *ca.* 15-fold in aqueous solution and by up to 20-40-fold in lipid membranes.

Overall, the work presented in this thesis highlights the breadth of opportunities available toward developing new single molecule assays and materials based on CPE/lipid interactions.

Résumé

Les polymères conjugués (PC) et leurs homologues solubles dans l'eau les polyélectrolytes conjugués (PEC), sont actuellement utilisés dans plusieurs applications, notamment dans les cellules photovoltaïques, les diodes électroluminescentes ainsi que dans les capteurs chimiques/biologiques. Des études fondamentales sur la synthèse d'architectures de plus en plus complexes et sur les propriétés optoélectroniques des PC / PEC ont contribué à une vaste gamme d'applications innovantes associées à ces matériaux. Une découverte clé a été la réalisation que les propriétés optiques des PEC, en particulier la migration d'énergie le long du squelette du polymère, peuvent être modulées par la morphologie du polymère et son degré d'association intra- et interchaînes. Les PC et les PEC sont donc très sensibles à la nature de l'environnement de solvatation, et pour les PEC en particulier, à la force ionique, et à la présence d'agents de surface.

Cette thèse explore l'auto-assemblage des membranes lipidiques avec les PEC comme un moyen pour régler leurs propriétés optiques, et exploite les interactions PEC / membrane lipidique comme une plateforme pour développer des applications focalisées sur l'étude de la biophysique des membranes et sur l'avancement des matériaux biomimétiques. Cette thèse décrit en outre des études fondamentales visant à améliorer la photostabilité des PEC, et fournie des protocoles nécessaires pour les études bioanalytiques et biophysiques émergentes à l'échelle de la particule / molécule unique nécessitant l'excitation des PEC à des cycles élevés.

En travaillant avec du poly(phénylène vinylène) PEC adsorbé sur des nanoparticules de dioxyde de silicium, nous démontrons tout d'abord comment l'augmentation d'émission qui accompagne un changement de conformation du PEC induit par la membrane est exploitée comme un nouveau moyen de détecter la dynamique du réarrangement de la membrane, un sujet qui a déjà été difficile à étudier expérimentalement malgré son importance dans le domaine de la biologie cellulaire. Alors que dans cette étude la manipulation du transfert d'énergie dans un PEC a été utilisé comme un outil pour élucider la biophysique de la membrane, la capacité de la membrane d'organiser les PEC est un sujet intéressant en soi. De même, dans une deuxième étude les membranes lipidiques sont évaluées pour leur capacité à diriger l'auto-assemblage des PEC dans le but d'obtenir une migration d'énergie efficace à travers la membrane afin de développer une antenne biomimétique photosynthétique. Dans ce projet, nous démontrons que les PEC peuvent être intégrés avec succès dans la membrane de liposomes à charge opposée avec une densité assez élevée (<1 nm de séparation) sans auto-extinction. La lumière récoltée par les polymères est

transférée à travers des mécanismes d'espace à un accepteur d'énergie lipophile, durant lesquels l'homo-transfert entre les polymères joue un rôle dans l'acheminement d'énergie vers l'accepteur d'une manière analogue aux molécules d'antenne de chlorophylle présentes dans les antennes photosynthétiques naturelles des plantes vertes. Parallèlement à la mise en évidence de nombreuses opportunités pour ces interactions de PEC/lipide pouvant assister au développement de nombreuses applications, dans une troisième et quatrième étude, différents additifs sont évalués dans le but d'améliorer la photostabilité des PEC dans des conditions utilisées en imagerie microscopique pour répondre à ces demandes. En utilisant un système enzymatique de piégeage d'oxygène et / ou en ajoutant des désactivateurs d'état triplet, le nombre de photons collectés à partir de PPE-CO_2 augmente d'environ 15 fois en solution aqueuse et jusqu'à 20 à 40 fois dans les membranes lipidiques.

Dans l'ensemble, le travail présenté dans cette thèse souligne la pléthore des opportunités disponibles vers le développement de nouveaux tests à l'échelle de la molécule unique et matériaux basés sur les interactions CPE/lipides.

Acknowledgements

Firstly, I would like to acknowledge my supervisor, Prof. Gonzalo Cosa, for guiding the projects presented in this thesis and working with me to develop my skills as a scientist: from designing effective experiments to honing my presentation and writing style to elegantly communicate the results. Gonzalo brings enthusiasm, energy, and optimism to his work, which results in a constant outpouring of new ideas and an urgency to always move forward. I am grateful that I had the opportunity to work with such a dynamic person over the past six years, and I am sure the group will continue to go in many interesting directions under his leadership in the future.

I feel it is also important to recognize the contributions of many of the staff at McGill: J.P. in the machine shop, Rick and Weihua in the electronics shop, Petr from CSACS, Chantal for administrative support/advice, Robert for helping me with my failing hard drives, everyone who has worked in chem stores and the departmental office, as well as Line, Kaustuv, and Kelly at the McGill facility for electron microscopy research. The research conducted in this thesis could not have been successfully completed without your help. I would also like to thank our collaborator Prof. Kirk S. Schanze for providing the PPE-CO_2 polymers and feedback on several manuscripts.

It is also natural for me to acknowledge my family for supporting me as I moved across the country to pursue my studies. First, thank you to my mom, whose idea it was for me to attend McGill. She said that she heard that Montreal was "so awesome" and on this point, she was correct. Also, a big man hug to my three younger sisters: Tamarra, Ronelle, and Teri, who have all made multiple trips here to visit me. I am sure that Osheaga, cheap beer, and poutine had nothing to do with their decision to holiday in Montreal… I would also like to thank my old buddy Alycia. This thesis has now supplanted the *Shining Force: Behind the Battles* as the longest thing that I've had a hand in writing, but only barely ;). He *was* half-horse, afterall. Also a shout-out to Martino, who took the crazy decision to start dating me at the moment that I started writing my thesis… Thank you for all of your support and understanding during my transformation into a self-absorbed lush who has not been sighted in real pants for months. To more road/camping/ski trips and trivia night victories in our future.

I believe that the most valuable aspect of my time at McGill has been making so many new friends. In no particular order: Amani, for being my first wife and co-conspirator (The Plan is

working…), Viktorija for “Viki Christina Barcelona” and other adventures (mishaps), Rob for necessitating the “Parental Advisory” label, Lana for being my ski wife and BDP bathroom confidant, Mayra for being the nicest Mexican I know, Ricky for his super sweet, personalized valentines, Mei for enabling my cheezies habit and our unspoken races up the mountain, Siqi for always having good ideas for new things to try and for our cat dates, Ryan for being the poorly compensated Corridor Counsellor, Justin for always going first into the Witch’s Twine, my coach Robert, Elisa, Ali, and Hannah for being my track buddies, Casey for being my youngest and most liquor-hard wife, Chris for dealing with okCupid perverts for me with such great style, Hsiao-Wei for keeping the young men in line, Felipe for providing the soundtrack (but we all understand if you never want to play “La Bamba” again), Yasser for bringing the chain and teaching us all not to “FRET” about it, Bri for understanding what it’s like to walk up the stairs of Pulp and Paper after leg day, Pierre for the Burnside basement chat (you tried your best), Andres for cooooooffffeeeeeeeee, Sol for maaaaattteeeeeeee, Katerina for deflating that inflatable toy on the bus returning from Tremblant, Lee for his “old soul” music taste, Mathieu for ensuring that I wasn’t the worst behaved one, Mr. Rebelo for bringing me my own personal giant Portuguese breads, Xavier for laughing at (with?) me, Jack for being a laaaaaaaad, Jesse for asking me to semi-formal and making me feel young again; I wish I said yes, Vanja for always sliding me the unfinished wine in her glass across the kitchen table and for living with me, Danielle for visiting the third floor, often with cupcakes in hand, Kevin for making me coffee (you are still the best new student; keep it up), Aya for being a bad influence (you know what you did), Julia and Semanti for bringing the best dishes to the Christmas potluck, and everyone else who I may have forgotten… I sincerely doubt that I will have the opportunity to be a member of a clubhouse like this again I already miss it dearly. Pulp and paper is truly the breeding ground for kindred spirits. Corridor4Life.

Lastly, I want to thank Luka, who has taught me the pleasures of a life filled with affection, naps in the sunshine, and kibble.

“Journeys end in lovers meeting”

William Shakespeare, Twelfth Night

Table of Contents

List of Figures

List of Tables

List of Abbreviations

$^3O_2$	Ground state oxygen
$^1O_2$	Singlet oxygen
ε	Molar absorptivity ($M^{-1}cm^{-1}$)
κ^2	Dipole orientation factor
λ	Wavelength
θ_c	Critical angle
Φ_D	Fluorescence quantum yield of donor
Φ_f	Fluorescence quantum yield
τ	Lifetime (s^{-1})
A	Pre-exponential factor
AA	Ascorbic acid
AFM	Atomic force microscopy
BME	β-mercaptoethanol
CMC	Critical micelle concentration
CO_2^-	Carboxylate anion
COT	Cyclooctatetraene
CP	Conjugated polymer
CPE	Conjugated polyelectrolyte
Cryo-TEM	Cryogenic transmission electron microscopy
CW	Continuous wave
Cy3	Cyanine3
Cy5	Cyanine5
DiD	1,1′-dioctadecyl-3,3,3′,3′-tetramethylindodicarbocyanine perchlorate

DiI	(3H-indolium, 2-[3-(1,3-dihydro-3,3-dimethyl-1-octadecyl-2H-indol-2-ylidene)-1-propenyl]-3,3-dimethyl-1-octadecyl-perchlorate
DLS	Dynamic light scattering
DOPA	1,2-dioleoyl-sn-glycero-3-phosphate
DOPC	1,2-dioleoyl-sn-glycero-3-phosphocholine
DOTAP	1,2-dioleoyl-sn-glycero-3-phosphocholine
DPPC	1,2-dipalmitoyl-sn-glycero-3-phosphocholine
DTAB	dodecyltrimethylammonium bromide
E. coli.	Escherichia coli
EMCCD	Electron-multiplied charge-coupled device
FCS	Fluorescence correlation spectroscopy
FRET	Förster resonance energy transfer
FSS	Site-selective fluorescence spectroscopy
GODCAT	Glucose oxidase/catalase
GOX	Glucose oxidase
HCl	Hydrochloric acid
HEPES	(4-(2-hydroxyethyl)-1-piperazineethanesulfonic acid
HOMO	Highest occupied molecular orbital
I	Fluorescence intensity
IC	Internal conversion
ISC	Intersystem crossing
J	Overlap integral
k	Rate constant
K_{SV}	Stern-Volmer constant
LUMO	Lowest unoccupied molecular orbital

MEH-PPV	Poly[2-methoxy-5-(2-ethylhexyloxy)-1,4-phenylenevinylene]
MPS-PPV	Poly[5-methoxy-2-(3-sulfopropoxy)-1,4-phenylenevinylene]
MV^{2+}	Methyl viologen
n	Refractive index
N_2	Nitrogen
N_A	Avogadro's number
NA	Numerical aperture
NaCl	Sodium chloride
NaOH	Sodium hydroxide
nm	Nanometer
NP	Nanoparticle
O_2	Oxygen
OLED	Organic light emitting diode
P3HT	Poly(3-hexylthiophene
PANI	Polyaniline
PC	Phosphatidylcholine
PCBM	Phenyl-C_{61}-butryic acid methyl ester
PFS	Perfect focus system
PMMA	Poly(methyl methacrylate)
PPE	Poly(phenylene ethynylene)
PPV	Poly(phenylene vinylene)
PPy	Polypyrrole
PPyV	Poly(*p*-pyridylene vinylene)
PRU	Polymer repeat unit
PSF	Point spread function

R_0	Förster radius
ROS	Reactive oxygen species
ROX	Reduction/oxidation
S_n	n^{th} singlet state
SANS	Small angle neutron scattering
SAXS	Small angle X-ray scattering
SDS	Sodium dodecyl phosphate
SiO_2	Silicon dioxide
SLB	Supported lipid bilayer
SM	Single molecule
SMF	Single molecule fluorescence
SMS	Single molecule spectroscopy
SO_3^-	Sulfonate anion
SVA	Solvent vapour annealing
T_n	n^{th} triplet state
TEM	Transmission electron microscopy
TIRF	Total internal reflection fluorescence
TIRFM	Total internal reflection fluorescence microscopy
TOC	α-tocopherol
TQ	Trolox quinone
TX	Trolox
UV	Ultraviolet
UV-Vis	Ultraviolet-Visible
VR	Vibrational relaxation

Author Contributions

Chapter 2

Reproduced with permission from: "Exploiting conjugated polyelectrolyte photophysics toward monitoring real-time lipid membrane-surface interaction dynamics at the single-particle level", **Christina F. Calver**, Hsiao-Wei Liu, & Gonzalo Cosa, *Langmuir*, **2015**, *31*, 11842–11850.

Author Contributions: **Christina F. Calver** performed experiments, analyzed data, and co-wrote the paper. **Dr. Hsiao-Wei Liu** collected initial data and provided feedback on the manuscript. **Prof. G. Cosa** designed the project, guided the interpretation of data, co-wrote the paper, and designed the journal cover.

Chapter 3

Reproduced with permission from: "Biomimetic light harvesting antenna based on the self-assembly of conjugated polyelectrolytes embedded within lipid membranes", **Christina F. Calver**, Kirk S. Schanze, & Gonzalo Cosa, *ACS Nano*, **2016**, *10*, 10598-10605.

Author contributions: **Christina F. Calver** performed experiments, analyzed data, and co-wrote the paper. **Prof. Kirk S. Schanze** provided the PPE-CO_2-7 polymer and provided feedback on the manuscript. **Prof. G. Cosa** designed the project, guided the interpretation of data, and co-wrote the paper.

Chapter 4

Author contributions: **Christina F. Calver** performed experiments, analyzed data, and co-wrote the manuscript. **Briony A. Lago** collected and analyzed initial data. **Prof. Kirk S. Schanze** provided the PPE-CO_2-49 polymer and provided feedback on the manuscript Prof**. G. Cosa** designed the project, guided the interpretation of data, and co-wrote the manuscript. (*Manuscript submitted to J. Phys. Chem. B, March 2017*)

Chapter 5

Author contributions: **Christina F. Calver** performed experiments, analyzed data, and co-wrote the manuscript. **Briony A. Lago** collected and analyzed initial data. **Prof. Kirk S. Schanze** provided the polymer. **Prof. G. Cosa** designed the project, guided the interpretation of data, and co-wrote the manuscript. (*Manuscript in preparation*)

Chapter 1: Introduction

Following the development of the petroleum industry as a source of feedstock and the continual advancement of organic chemistry techniques, the 20th century has seen an abundance of new manmade, carbon-based materials. In particular, it is difficult to understate the impact of synthetic polymers on modern life, where these materials are ubiquitous in both industrial and household settings. The widespread use of synthetic polymers is due to several factors, including their relatively inexpensive product costs, facile solution processing, and the wide variety of structural/physical properties available. Although many familiar synthetic polymers have saturated backbones with sp^3 hybridized carbon atoms (*e.g.*, polyvinyl chloride, polystyrene), in the 1960s researchers began experimenting more with polymers having unsaturated (*i.e.*, conjugated) backbones, such as poly(phenylene vinylene) (PPV),[1] polypyrrole (PPy),[2-4] and polyaniline (PANI),[5] whose synthesis was reported as early as 1862.[6]

To date, a wide variety of different conjugated polymers (CPs) have been reported in the literature and a significant number of them are commercially available. CPs are typically grouped based on the chemical structure of the polymer backbone, with several of the commonly encountered structures illustrated in Figure 1.1. Here, the addition of side chains (denoted by -R) is generally necessary to improve the solubility and processability of CP materials. In that regard, and of relevance to the work in this thesis, we may cite a special class of CPs called conjugated polyelectrolytes (CPEs), which feature side chains that contain pendant ionic groups. CPEs with a given backbone structure share many of the same photophysical properties with their non-ionic counterparts, but the presence of the charged side chains renders them soluble in water and polar organic solvents such as methanol. Not surprisingly, the water solubility of CPEs combined with their photophysical properties has made them particularly attractive materials for biological applications.

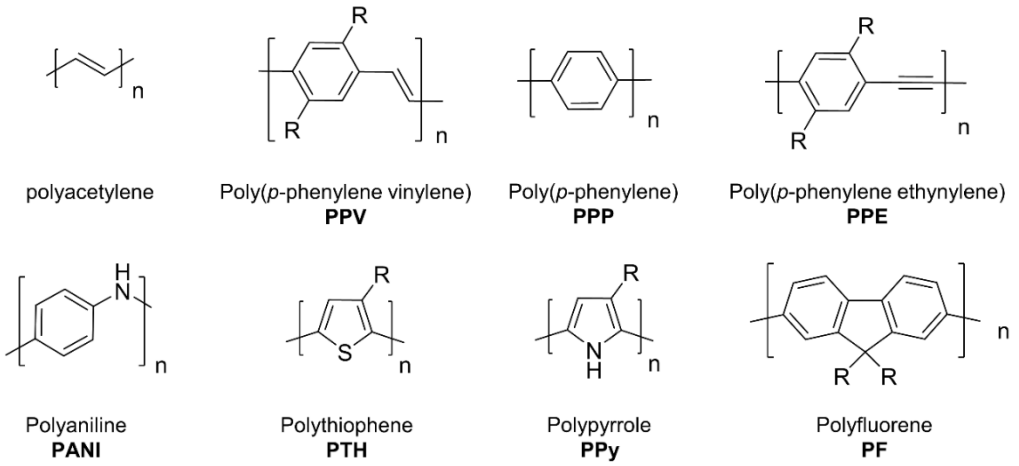

Figure 1.1. Chemical structures of several commonly encountered CP classes.

Interest in conjugated polymers grew dramatically under the promise of realizing plastic electronics using "synthetic metals"[7] after Chiang *et al*. reported in 1977 that the electrical conductivity of polyacetylene could be varied by controlling the type and amount of dopants.[8] Following this seminal work, interest in CPs has intensified due to their unique combination of desirable photophysical and material properties. A measure of the impact of this work is the awarding of the 2000 Nobel Prize in Chemistry to Alan MacDiarmid, Alan J. Heeger, and Hideki Shirakawa for the discovery and development of conductive polymers.

CPs have been investigated in a range of applications that exploit their photophysical and energy transporting properties. These include photovoltaic based applications where light absorbed by the CPs ultimately results in charge separation and the production of electric current.[9-30] By the same token, injecting a charge may result in charge recombination and the emission of light *via* fluorescence, a phenomenon which has been exploited in the production of organic light emitting diodes (OLEDs).[31-36] The modulation of CP fluorescence intensity in the presence of different molecules (*i.e.*, analytes) has been used in turn as the basis for the development of ultrasensitive chemical and biological sensors.[37-56] Critically, the conformation and aggregation/packing behaviour of CPs determines not only their physical properties, but also their photophysical behaviour.[57-66]

CPs oftentimes contain many hundreds of light absorbing units (chromophores) which may communicate with each other *via* energy transfer processes.[67-68] As a result, the photophysical properties of CPs are intimately related to the efficiency of energy transfer. The latter is in turn dictated to a great extent by the CP structure: from the conformation of individual polymer chains in solution to the morphology (*e.g.*, polymer packing) of CP materials in the solid state.[58, 60, 64, 69-72] From a materials point of view, the added complexity provides a greater parameter space to tailor the desired photophysical behaviour, but also introduces additional and undesired opportunities for defects. Understanding the relationship between conformation and energy transfer in CPs is thus of paramount importance to the rational design of new materials/applications as well as to the targeted improvement of existing ones.

This thesis focuses on the development of applications that exploit the photophysical properties of two different CPEs, one bearing a poly(phenylene vinylene) backbone and sulfonate side chains, poly[5-methoxy-2-(3-sulfopropoxy)-1,4-phenylenevinylene] (MPS-PPV) and another bearing a poly(phenylene ethynylene) backbone and carboxylate sidechains, (PPE-CO_2) (Figure 1.2). Chapter 1 begins by reviewing the photophysical and energy transfer processes operating in conjugated polymers and highlights key studies demonstrating the relationship between polymer conformation and energy transfer. A special emphasis is placed on single molecule spectroscopy (SMS), a family of fluorescence microscopy techniques that has been instrumental in unraveling the complex photophysics of CPs. These techniques have allowed researchers to observe the emission from one polymer chain at a time, thus revealing heterogeneity and dynamics that are otherwise masked in ensemble spectroscopy experiments. Strategies to manipulate polymer conformation and film morphology to achieve control over the energy transporting and photophysical properties of the materials are reviewed for both CPs and their water-soluble counterparts, CPEs. Of particular interest in this thesis are self-assembled complexes of CPEs and lipid membranes. In these structures, the lipids impart both structural and photophysical changes in the CPEs. The experiments reported in Chapters 2-5 of this thesis build upon existing knowledge of the structure and photophysics of lipid/CPE complexes to develop applications in other fields, including the study of membrane biophysics, the design of biomimetic light harvesting systems, and the optimization of SMS imaging conditions toward studies aimed at optimizing photostability to in turn enable further applications in the future.

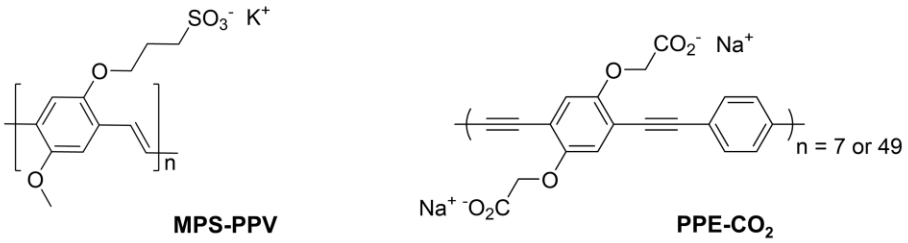

Figure 1.2. Chemical structures of the CPEs under study in this thesis. MPS-PPV is shown on the left and PPE-CO_2 is shown on the right.

1.1 Photophysical concepts

1.1.1 Excited States

When describing the photophysics of CPs, it is useful to review the basic principles of the electronic structure of organic molecules.[73-74] A key principle is that electrons occupy states based on both their electronic and vibrational energy, filling lower energy states before higher ones (the aufbau principle). The lowest energy configuration of the electrons in the molecule is referred to as the ground state. Electrons can be promoted to higher energy levels (excited states) *via* absorption of electromagnetic energy. The amount of energy required depends on the difference in energy between the ground state and the excited state. For vibrational transitions, energy within the infrared region of the electromagnetic spectrum (see Figure 1.3), is sufficient to cause a transition. To promote electrons to higher electronic states, however, higher energy within the UV/visible region of the electromagnetic spectrum is required (see Figure 1.3).

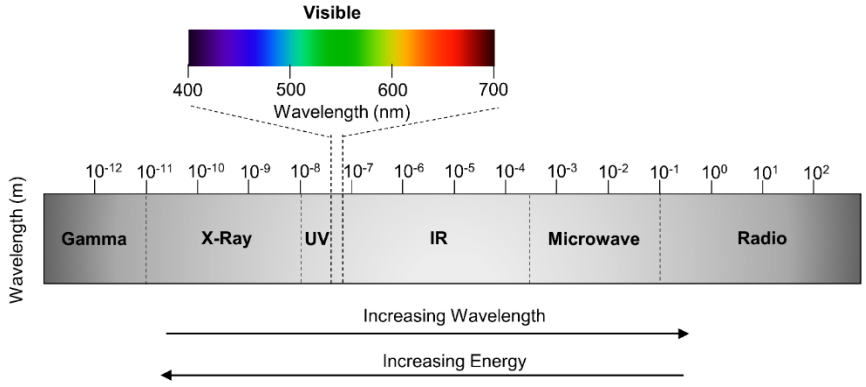

Figure 1.3. Electromagnetic spectrum highlighting the visible light region responsible for electronic transitions in CPs.

The electronic structure of CPs governs the light absorbing and emitting processes essential to their application in solar cells, OLEDS, sensors, and more. Within the literature, a lively debate has ensued over the nature of the electronic structure of CPs.[75] Initially, the electronic structure of CPs including poly(acetylene), poly(*p*-phenylene), poly(phenylyene vinylene), poly(thiophene), and poly(pyrrole) was widely considered to be best described by a 1 dimensional semiconductor band structure.[76-81] In this model, electronic transitions take place from the valence band to the conduction band when the light excitation energy, ħυ, is greater than or equal to the energy of the band gap, *E*g. Luminescence is generated by the recombination of the weakly bound electron/hole pair and is independent of the excitation energy. In the early 1990s, authors Rauscher and Bässler began to challenge the validity of the band model based on the results of site-selective fluorescence spectroscopy (FSS) experiments.[82-84] These studies and others[75] supported the conclusion that the electronic structure of CPs is better described by strongly coupled electron-hole pairs (*i.e.*, Frenkel excitons) that are localized on segments of the polymer chain, making them more similar to small, conjugated organic molecules such as anthracene rather than to inorganic semiconductors like silicon. Within this paradigm, the complex photophysics of CPs then mainly arise due to the migration of excitons throughout the chain, a topic that will be discussed in more detail in section 1.4 (*vide infra)*.

1.1.2 Jablonski diagram

Photon absorption and the promotion of an electron to a higher energy electronic state is an extremely fast process, occurring on the femtosecond timescale (10^{-15} s). The excited state may then dissipate this energy through several different pathways, both radiative (*e.g.*, by emitting a photon) and non-radiative (*e.g.* by emitting heat). The different accessible excited states and the possible transitions between them may be displayed in a Jablonski diagram (Figure 1.4).[73]

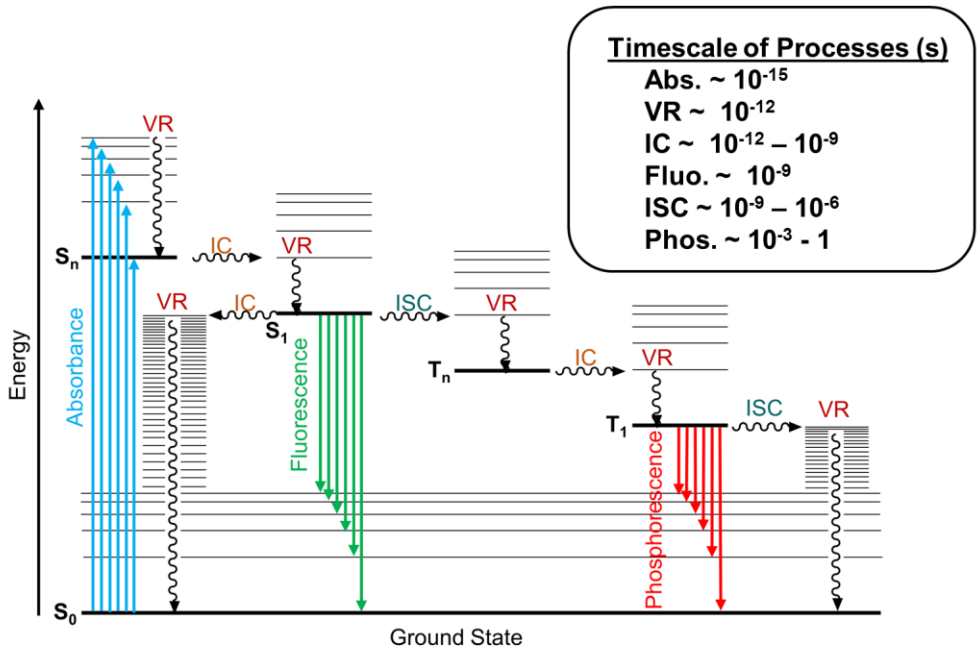

Figure 1.4. Jablonski diagram illustrating the various energy states of a typical organic molecule and the key photophysical processes that can occur from each state. Bold horizontal lines represent electronic states (S for singlet and T for triplet) and thin horizontal lines represent vibrational states. Radiative and non-radiative transitions are represented by straight and by squiggly arrows, respectively. VR, IC, and ISC are abbreviations for vibrational relaxation, internal conversion, and intersystem crossing, respectively.

Selection rules state that electronic transitions must conserve spin multiplicity.[85] Since the ground state of most organic molecules is a singlet state, absorption of a photon of the appropriate energy leads to a transition from S_0 to S_n.[74] According to the Franck-Condon principle, the probability that a particular vibronic transition occurs (*e.g.*, from the fundamental vibronic state in S_0 to any vibronic state in S_n) is proportional to the square of the overlap between the vibrational wavefunctions of the initial and the final electronic states.[74] The excited vibrational states are short lived, however, and decay within picoseconds to the lowest vibrational level of S_n in a process called vibrational relaxation (VR). From here, internal conversion (IC) to S_{n-1} typically occurs within picoseconds, apart from S_1 to S_0, which is typically several orders of magnitude slower because of the relatively large energy gap between these states. Relaxation to the ground state then typically occurs from the lowest energy vibrational level of S_1, Here, the loss of energy through VR results in the photons emitted from S_1 to S_0 being of equal or lower energy than the

photons absorbed from S_0 to S_1, giving rise to a shift between absorption and emission bands known as the Stokes shift.[73]

Relaxation from the first excited singlet state to the ground state occurs through several competing photophysical processes within the singlet manifold. A non-radiative decay may occur *via* IC from S_1 to S_0 followed by VR to the vibrational ground state of S_0. The efficiency of the non-radiative pathway is improved with increasing overlap between the vibrational wavefunctions of S_1 and S_0. The radiative transition between S_1 and S_0 (*i.e.*, fluorescence) is controlled by the same Franck-Condon factors that apply to absorption, meaning that these factors determine the preferred vibrational levels of S_0 where relaxation takes place to, and ultimately the shape of the emission band.

A spin forbidden intersystem crossing (ISC) from S_1 to an excited triplet state, T_n, followed by triplet relaxation to ground state may also occur. Since the transition from T_1 to S_0 is formally spin-forbidden, the rate of relaxation from T_1 to the ground state is several orders of magnitude slower than it is from the S_1 state. Consequently, the molecule is more vulnerable to photochemical reactions from the relatively long-lived triplet excited state, a topic discussed in more detail in section 1.15 (*vide infra)* and in Chapters 4 and 5 of this thesis.

1.1.3 Definition of quantum yield and excited state lifetime

To determine the probability that a photophysical process occurs, knowledge of the rates for all possible deactivation processes from the excited state is required. For many applications using CPs, bright emission is desirable, so the probability that a photon will be emitted upon electronic excitation is an important parameter to establish. This probability, called the fluorescence quantum yield (Φ_f), depends on how large the first order radiative rate constant, k_r, is compared to the first order (or pseudo first order) rate constants of all other competing deactivation pathways, k_{nr}. k_{nr} represents the sum of the rate constants of all other deactivation processes besides fluorescence, and typically includes k_{IC}, k_{ISC}, $k_q[Q]$, and k_{rxn}, which are the rate constants of internal conversion, intersystem crossing, quenching in the presence of quencher [Q], and intramolecular reaction from the excited state, respectively (Equation 1.1). The fluorescence quantum yield is then defined as the ratio of k_r over the sum of all deactivation pathways, k_d

(Equation 1.2). The quantum yield of any photophysical process can be calculated in the same manner, by replacing k_r with the rate constant of the process of interest.

$$k_{nr} = k_{IC} + k_{ISC} + k_q + k_{rxn} \quad (1.1)$$

$$\Phi_f = \frac{k_r}{k_r + k_{nr}} = \frac{k_r}{k_d} \quad (1.2)$$

The fluorescence lifetime, the average time that the molecule spends in the first excited singlet state before decaying to the ground state, is another important parameter defining the photophysical behaviour of CPs, particularly as it concerns energy transfer and fluorescence quenching. The radiative decay is a stochastic process, and as such the decay of an ensemble of molecules from S_1 to S_0 is described by the exponential function Equation 1.3 where N is the population of excited molecules at time t, N_0 is the initial population of excited molecules, and k_d is the radiative decay constant. The fluorescence lifetime, also referred to as the excited state lifetime is defined as the reciprocal of k_d (Equation 1.4). The radiative rate constant can be calculated by determining the emission quantum yield and the excited state lifetime experimentally and then rearranging Equation 1.2.

$$N(t) = N_0 e^{-k_d t} \quad (1.3)$$

$$\tau = \frac{1}{k_d} \quad (1.4)$$

1.1.4 Quenching of excited states

As mentioned in the previous section, the fluorescence quantum yield and the fluorescence lifetime are two important parameters that define the photophysical behaviour of organic fluorophores, including CPs. These parameters are sensitive to the environment, posing challenges to applications that require a reliable photon output, such as OLEDs, but also creating opportunities in fields where a large dynamic range is desired, such as chemical sensing. The radiative decay rate constant is intrinsic to the fluorophore, and remains constant, regardless of environmental conditions, whereas the decay rate constants associated to the multiple non-radiative decay pathways are sensitive to changing experimental conditions, such as temperature, solvent, and most importantly the presence of quenchers, among others.[73]

Fluorescence quenching is a frequently encountered process that increases k_{nr} and correspondingly decreases Φ_f(Equation 1.2). Broadly speaking, a fluorescence quencher provides an alternative pathway to dissipate the energy of the excited singlet state. Quenching mechanisms can be categorized into two classes, physical and chemical. Energy transfer (*via* electron exchange or Förster resonance energy transfer (FRET))[86] and intersystem crossing catalyzed by heavy atoms[87] are examples of physical quenching mechanisms, whereas photoinduced electron transfer[88] is an example of a chemical quenching mechanism.

A distinction is made between dynamic quenching, where the excited state is deactivated by collision with the quencher in a bimolecular process with a rate constant k_q (Equation 1.5), and static quenching, where the fluorescent molecule and the quencher form a ground state complex with an equilibrium association constant K_A (Equation 1.6). For both static and dynamic quenching, there is a linear relationship between the quencher concentration and the emission intensity quenching. This relationship is described by the Stern-Volmer equation, where I is the intensity at a given quencher concentration, $[Q]$, I_0 is the intensity in the absence of quencher, and K_{SV} is the Stern-Volmer quenching constant, equal to the product of $k_q \tau_0$, where τ_0 is the excited state lifetime in the absence of the quencher in the case of dynamic quenching and to K_{eq} in the case of static quenching (Equation 1.7). In the case of purely dynamic quenching, the fluorescence lifetime is reduced by the same factor as the intensity at a given concentration, *i.e.*, τ_0/τ is equal to I_0/I.

$$F^* + Q \xrightarrow{k_q} F + Q \tag{1.5}$$

$$F + Q \rightleftharpoons [FQ] \tag{1.6}$$

$$\frac{I_0}{I} = 1 + K_{SV}[Q] \tag{1.7}$$

Stern-Volmer plots are a useful tool to analyze experimental quenching data.[73] For example, static quenching of conjugated polyanions, the key material class under study in this thesis, is well-known to occur *via* binding of positively charged electron acceptors to the negatively charged polymer acting as an electron donor.[48, 89] Ngo *et al.* in the Cosa group conducted a quenching study to prove the encapsulation of the polyanion poly[5-methoxy-2-(3-sulfopropoxy)-1,4-phenylenevinylene] (MPS-PPV) in liposomes.[90] Addition of the divalent cation methyl

viologen (MV^{2+}) to MPS-PPV free in solution resulted in efficient fluorescence quenching *via* photoinduced electron transfer (Figure 1.5A), where a linear Stern-Volmer plot was obtained. The Stern-Volmer plot for quenching due to addition of MV^{2+} to liposomes containing MPS-PPV showed a markedly different behaviour, however, displaying less efficient quenching that plateaus at an I_0/I value of *ca*. 10, representing an unquenchable fraction of *ca*. 10% (Figure 1.5A). Since MV^{2+} is a highly charged molecule and cannot pass through the lipid membrane,[91] the presence of an unquenchable fraction provided strong evidence for the encapsulation of MPS-PPV inside the liposome.[90]

In another study, Tan *et al.* investigated the quenching of a polyanion with a poly(phenylene) ethynylene backbone by energy transfer to positively charged cyanine dyes in solution.[92] Quenching by the monovalent cation HMIDC produced a linear Stern Volmer plot in contrast to quenching by the trivalent cation Cy^{3+}, which produced a Stern Volmer plot with a strong positive deviation at high quencher concentrations (Figure 1.5B).[92] The positive deviation was attributed to polymer bridging facilitated by the trivalent cation, which resulted in more PRUs being contained within the quenching radius of the cyanine.[92] It should be noted that positive deviations are also observed for systems where both static and dynamic quenching mechanisms are operating,[73] but this explanation was ruled out in this case because $k_{\text{diffusion}}\tau_0$, was orders of magnitude smaller than the approximate K_{SV} value.[92] In the case where K_{SV} is on the order of $k_{\text{diffion}}\tau_0$, static and dynamic quenching can be differentiated by examining the Stern-Volmer plot of τ_0/τ. In the case of purely static quenching, no shortening of the fluorescence lifetime will be observed, since the formation of a ground state complex precludes detection of the excited state (Figure 1.5C), whereas for purely dynamic quenching values of τ will drop with increasing concentration of quencher and the K_{SV} obtained from the plot of τ_0/τ will be identical to that obtained from the plot of I_0/I (Figure 1.5D). Note also that the K_{SV} value for static quenching is typically much larger than it is for dynamic quenching, where the maximum efficiency is constrained by the diffusion limited rate constant ($1x10^{10}$ $s^{-1}M^{-1}$) and the fluorescence lifetime (typically $1x10^{-9}$ s) to a value of *ca.* 10 M^{-1}.

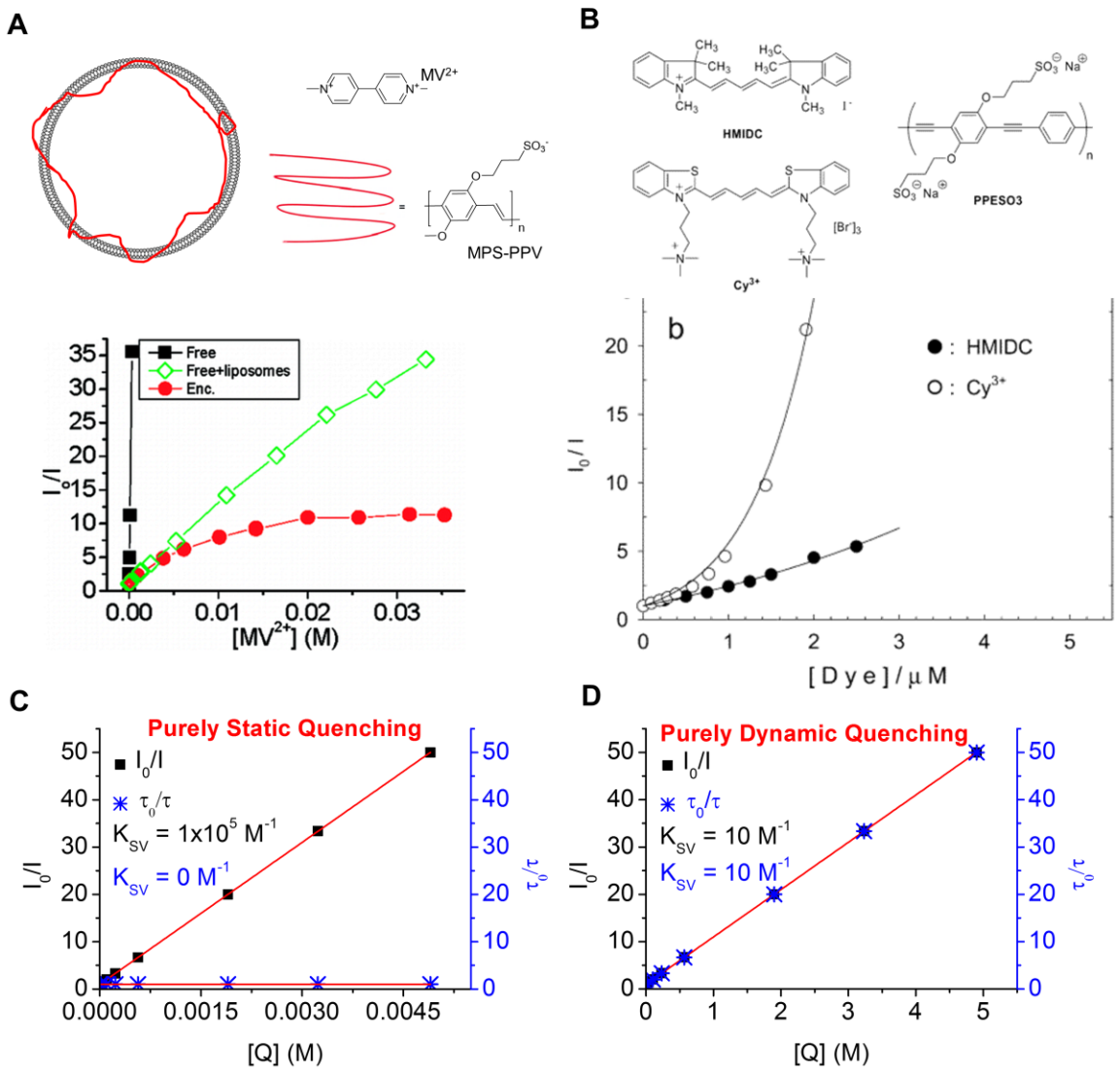

Figure 1.5. Fluorescence quenching as a method to study CPE complexes. (A) Stern-Volmer plots obtained from a quenching study of the polyanion MPS-PPV encapsulated within DOPC liposomes quenched by the positively charged electron acceptor MV^{2+}. Free MPS-PPV was efficiently quenched (black squares) whereas MPS-PPV in liposomes was less efficiently quenched and contained an unquenchable fraction (red circles). Adapted with permission from reference [90] (Copyright, 2008, The American Chemical Society). (B) Stern-Volmer plots obtained from a quenching study of the polyanion PPE-SO_3 quenched by positively charged cyanine energy acceptors in solution. Quenching by the monovalent cation HMIDC resulted in a linear Stern-Volmer plot (solid circles) whereas quenching by the trivalent cation Cy^{3+} resulted in a Stern-Volmer plot with a strong positive deviation at increasing quencher concentration (open circles). Adapted with permission from reference [92] (Copyright, 2004, The American Chemical Society). (C) and (D) Stern-Volmer plots illustrating the difference between fluorescence intensity and lifetime quenching in the case of a purely dynamic and purely static quenching mechanisms, respectively. Note that a much larger quencher concentration is required to achieve dynamic *versus* static quenching.

1.1.5 Photobleaching

Photobleaching refers to processes that deactivate fluorescence permanently; often these involve covalent modifications to the chemical structure of the fluorophore.[73] While both photobleaching and quenching (see above) deactivate emission, the major distinction between them is that in the latter case the excited deactivation is not permanent, (*i.e.*, fluorescence may be restored upon removing the quencher.)[73] Photobleaching of CPs poses a problem for practical applications that demand long-term stability,[93] as well as for scientists who are attempting to unravel the complex photophysics of these materials using fluorescence microscopy techniques, particularly those that require single molecule detection.[94] The excited triplet state of the chromophore is typically involved as a intermediate in the photobleaching of CPs and other organic molecules.[95-96]

Two reasons account for a dominant prevalence of photobleaching arising from the triplet excited state. Because of its relatively long lifetime, molecules in the triplet state are vulnerable to encountering reactive species in the environment, particularly molecular oxygen. In addition, molecular oxygen is a ground state triplet ($^3O_2$) and is unable to undergo reaction with molecules in the singlet ground state (*e.g.*, addition to double bonds is a spin forbidden process). However, sensitization of singlet oxygen ($^1O_2$) *via* energy transfer from the excited triplet state of the fluorophore to the ground state of oxygen is a spin allowed process that yields a highly reactive electrophile capable of undergoing addition reaction with unsaturated molecules (see Equation 1.8 for $^1O_2$ sensitization scheme).[74] Singlet oxygen readily adds to the electron-rich double bonds of fluorophores, breaking the conjugated pi system and changing the electronic structure of the molecule. Singlet oxygen may also lead to the production of other reactive oxygen species such as peroxides or superoxides that can similarly lead to damage. For this reason, one reported strategy to mitigate photobleaching in CPs consists of removing oxygen using enzymatic oxygen scavengers in solution[97-98] or to seal devices under inert atmosphere in the solid state.[99] Another commonly used approach is to add triplet quenchers to reduce the lifetime of the triplet excited state and thus reduce the amount of triplet sensitized singlet oxygen.[94-96, 100-101]

$$T_1^* + {}^3O_2 \xrightarrow{ET} S_0 + {}^1O_2 \qquad (1.8)$$

Experimentally, photobleaching of fluorophores is observed as a decrease in the emission intensity over time under conditions of light illumination. On a molecule-by-molecule basis, the survival time is governed by the quantum yield of photobleaching (*i.e.*, the probability that reactions take place upon excitation). Figure 1.6A shows the fluorescence intensity over time for a single molecule of the fluorophore Cy3 collected in 50 ms intervals during a total internal reflection fluorescence microscopy (TIRFM) experiment.[102] Here, the fluorescence signal shows fluctuations mostly due to noise. Also observed are extended periods with no emission due to transitions to longer lived dark states (*e.g.*, radical anions). The formation of dark states is sometimes called "reversible photobleaching" because photons collection may be reinitialized once the fluorophore is rescued from the intermediate state and the ground state is restored. Because photobleaching is an inherently stochastic process, the ensemble histogram of survival time for hundreds of molecules in the experiment can be fit to a monoexponential function (Figure 1.6B).[102] For large macromolecules such as CPs, exponential photobleaching may be observed in the case that the chromophores along the chain act independently, *i.e.,* the system may be viewed as a collection of hundreds of chromophores that photobleach independently giving rise in a single molecule to an exponential decay, much like would be observed in bulk studies (Figure 1.6C).[70] Importantly, efficient energy transfer within the polymer will cause the chromophores to behave in a concerted manner such that the intensity *versus* time trajectory will resemble that of a single molecule, with stepwise blinking and photobleaching (Figure 1.6D).[70] For this reason, photobleaching studies have become an important method of examining the extent of energy transfer within CP materials, a topic that will be discussed in more detail in section 1.4.2 (*vide infra)*.

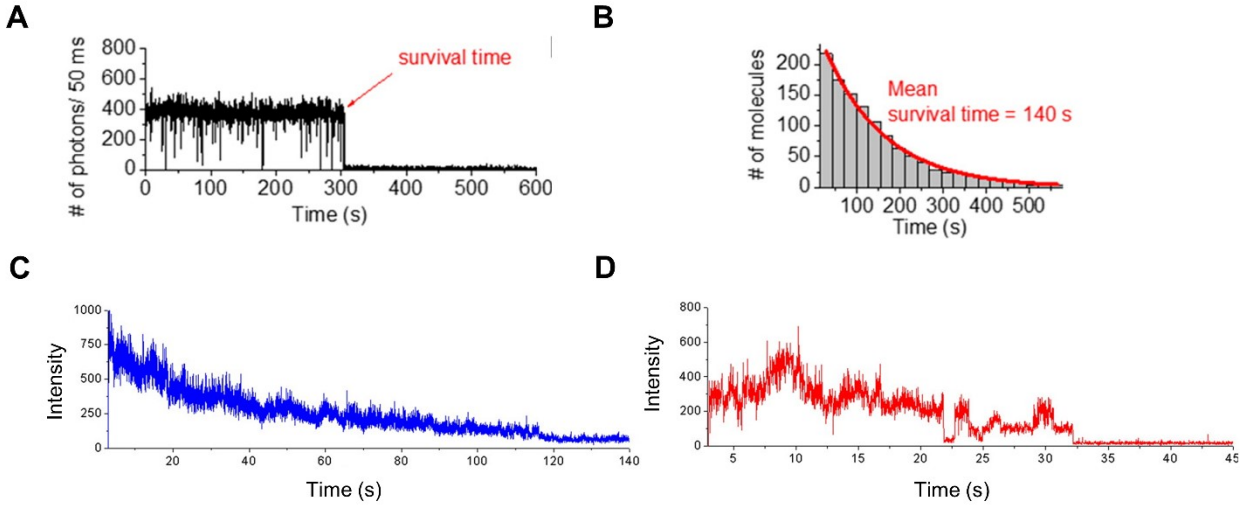

Figure 1.6. (A) Fluorescence intensity *versus* time trajectory of a single molecule in a TIRFM experiment. The molecule photobleaches irreversibly after *ca.* 300 s. (B) Histogram of survival times extracted from a collection of SM trajectories such as the one shown in (A). The number of molecules surviving is an exponential function of time. Adapted with permission from reference [102] (Copyright, 2016, The American Chemical Society). (C) Intensity *versus* time trajectory for a single CPE encapsulated within a liposome that exhibits exponential photobleaching due to large number of independent chromophores contained within the long polymer chain. (D) Intensity *versus* time trajectory for a single CPE that exhibits discrete photobleaching steps due to the concerted behavior of the chromophores along the polymer chain communicating *via* energy transfer. Adapted with permission from reference [70].

1.2 Experimental methodologies to study CP photophysics

Section 1.1 provided an overview of the key photophysical concepts required to understand the behavior of CP materials at a fundamental level. In this section, the spectroscopic techniques used to study the photophysical behavior of CPs will be discussed in more detail, with emphasis placed on the methods used throughout this thesis.

1.2.1 Ensemble versus single molecule techniques

Most familiar spectroscopic techniques are performed in bulk or ensemble, on samples that contain many billions of molecules. The results obtained from such experiments necessarily reflect the average properties/behavior of the ensemble. Single molecule spectroscopy (SMS),[103-105] on the other hand, probes individual molecules and thus allows for observations of the moments of the distribution, not just the average, as well as the visualization of behaviors that represent a

deviation from the average. Overall, the average result for an SMS experiment performed on a large enough number of individual molecules will match the result from an ensemble experiment, but the individual measurements may reveal heterogeneities that are otherwise masked in ensemble experiments.[106-108] An additional advantage to performing experiments at the single molecule level is that the dynamics of asynchronous processes may be resolved (*e.g.*, binding events).[109-111] The main disadvantage of SMS techniques is that more sophisticated instrumentation is required due to the challenge of detecting the emission from single molecules. In addition, a more intensive/lengthy data analysis is also typically required. Ensemble and SMS experiments are complimentary to each other. As such, the conclusions of this thesis are supported heavily by the analysis of both ensemble and SMS data.

1.2.2 Total internal reflection fluorescence microscopy

The SMS technique used in this thesis is total internal reflection fluorescence microscopy (TIRFM). TIRFM was first developed by Prof. Daniel Axelrod at the University of Michigan in the early 1980s. The technique relies on the physical principle of total internal reflection, which occurs when light propagating through a medium of a higher refractive index, n_1, reaches the boundary of a medium with a lower refractive index, n_2, at an angle greater or equal to the critical angle, θ_c (Figure 1.7). The critical angle is related to the ratio of the refractive indices by Snell's law (Equation 1.9). In TIRFM, the sample is typically in air or aqueous media (n_2 = 1 or 1.33, respectively) and is immobilized on a glass or quartz coverslip (n_1 = 1.52), thus satisfying the condition $n_1 > n_2$ required for TIRF. When the excitation light is totally internally reflected, an evanescent field is formed at the boundary between the media and it penetrates the media of lower refractive index The intensity, I_z, of the evanescent field decays from the initial intensity, I_0, exponentially from the surface (displacement, z, = zero) where the penetration depth depends on the wavelength of the excitation light, λ, n_2, and the angle between the incident light and the plane normal to the boundary, θ_1 (equations 1.10 and 1.11). Figure 1.8A shows illustrates that the penetration depth of the evanescent field reaches a maximum at the critical angle and then decays rapidly within the lower refractive index medium. Also noteworthy is that the rate of decay is more pronounced with distance at shorter compared to longer wavelengths (Figure 1.8B).

The main advantage of TIRFM is that due to the evanescent field, the molecules of interest on the surface are excited preferentially, effectively decreasing the background from fluorescent molecules out of the focal plane in solution. This is particularly important for SMS imaging, where a high signal to background ratio is paramount for detecting the emission of single emitters.

$$\theta_c = \sin^{-1}\left(\frac{n_1}{n_2}\right) \tag{1.9}$$

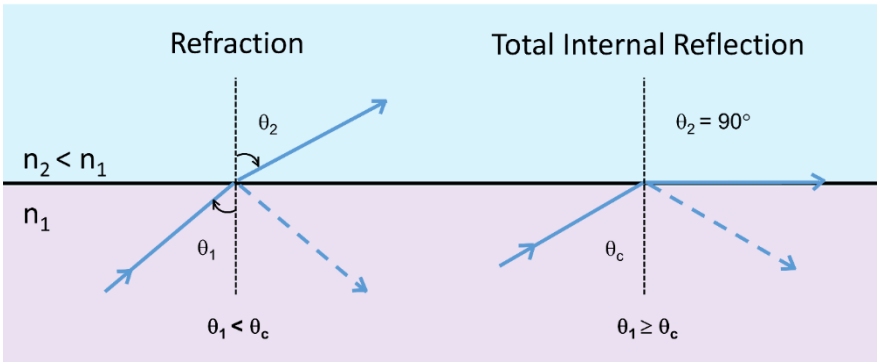

Figure 1.7. Diagram illustrating the refraction, reflection, and total internal reflection of electromagnetic radiation at the boundary of two media with different refractive indices, where n_1 is greater than n_2.

$$I_z = I_0 e^{\left(-\frac{z}{d}\right)} \tag{1.10}$$

$$d = \frac{\lambda}{4\pi\sqrt{n_1^2 \sin^2\theta_1 - n_2^2}} \tag{1.11}$$

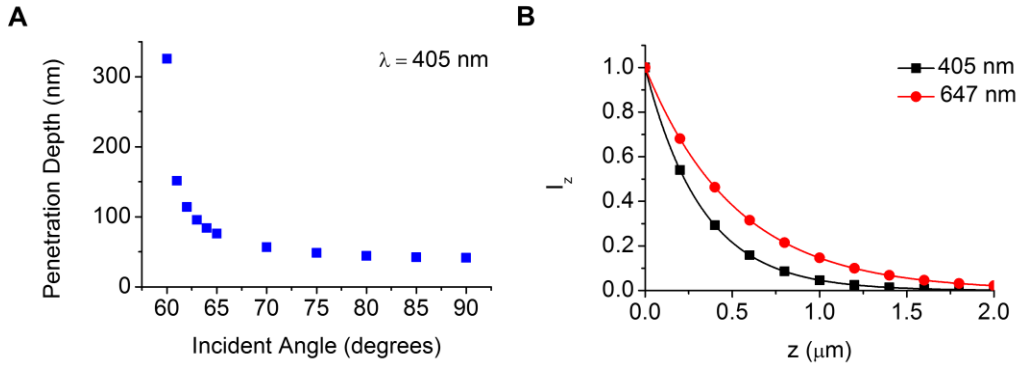

Figure 1.8. Dependence of evanescent field penetration depth on the incident angle and the wavelength of light. (A) Penetration depth of the evanescent field as a function of the incident angle for 405 nm light at the glass/water interface. Under these conditions, the critical angle is 60°. (B) Intensity of the evanescent field recorded at the critical angle as a function of distance from the glass/water interface plotted for 405 nm (black squares) and 647 nm (red circles) light.

The incident angle of the excitation light in TIRF microscopy can be achieved by either a prism or a high numerical aperture (NA) objective, where control is exerted by the angle/position of incidence of the beam, respectively in each optical element. In this thesis, objective-based TIRF is used because of its superior convenience and safety. Continuous wave (CW) lasers are used in our SM TIRFM setups yielding both high power and stability. The laser beam is reflected by a dichroic beam splitter where it enters the objective. By altering the position of the excitation beam on the back focal plane of the objective, the incident angle can be adjusted to the critical angle to achieve TIRF. An area of the sample is then excited by the resulting evanescent wave and the emission is collected through the objective with an efficiency that is determined by its NA. The light exiting the infinity-corrected objective is refocused by a tube lens at the back focal plane onto the detector chip of an electron multiplied charge coupled device (EMCCD) in the one-colour microscope. Figure 1.9 shows a schematic of the microscopes used in this thesis. The basic one-channel TIRF setup (Figure 1.9A) can be modified into a two-channel setup (Figure 1.9B) by installing additional optics in the emission path before the detector.

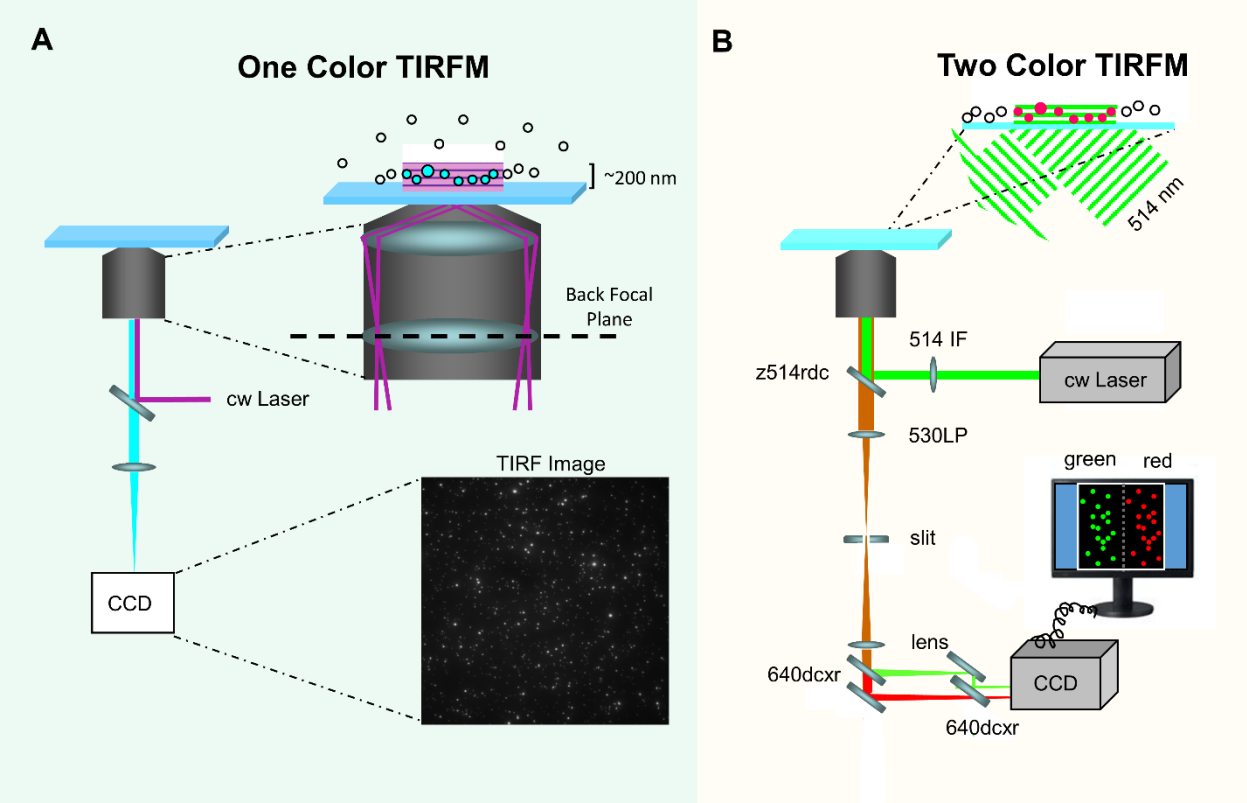

Figure 1.9. Anatomy of the TIRFM setups used in this thesis. (A) Diagram showing the key optics in a one-color channel TIRFM setup. The laser beam was passed through a multiband cleanup filter (ZET405/488/561/647x, Chroma Technology) and coupled into the microscope objective ((CFI SR Apo TIRF 100× Oil Immersion Objective Lens, numerical aperture (NA) 1.49) using a multiband beam splitter (ZT405/488r/561/640rpc, Chroma Technology) Images were recorded onto a 512x512 pixel region of a back-illuminated electron-multiplying charge-coupled device (EMCCD) camera (iXon X3 DU-897-CS0-#BV, Andor Technology). (B) Diagram showing how the one-color setup is modified to split the emission into two different colored channels. Here, the laser beam was filtered by a 514 interference filter (Chroma) and directed to the oil immersion objective (Olympus PLAN APO 60×, NA = 1.45) by a dichroic beamsplitter (z514rdc, Chroma). The emission is cropped vertically to create an image that fills half of the 512x512 pixel area of the CCD camera chip using an adjustable slit. The beam is then split using a 640 nm beamsplitter (640 dcrx, Chroma): wavelengths higher than 640 nm are transmitted whereas wavelengths lower than 640 are reflected. The two emission channels are then reflected 90° by mirrors and are merged by an additional 640 nm beamsplitter onto the EMCCD camera (Cascade 512B EMCCD camera, Roper Scientific, Inc.). Fine tuning of the mirrors separates the path of the two channels slightly such that they do not overlap. Since the EMCCD camera has been moved out of the image plane to make room for the additional optics, a converging relay lens with a focal length of 150 mm is placed in the emission path. The lens was placed 225 mm from the image plane and 450 mm from the camera. These values were chosen by using the ideal lens equation to achieve an additional magnification of 2x.

The raw data in a TIRFM experiment are the images acquired by the EMCCD camera. Multiple images may be sequentially acquired at intervals as short as *ca*. 20 ms for a 512x512 pixel region using our setup. In many cases, the TIRFM movies are further analyzed using automated Matlab routines based on the code originally published by the Ha group[112] that locate the molecules and extract their background subtracted fluorescence intensity vs time trajectories. Close inspection of the images reveals that the emission from a single molecule is spread over more than one pixel, even though the 120-fold magnified (60x objective and 2x relay lens) dimensions of the molecule itself are much smaller than the pixel size of *ca*. 16 µm x16 µm in our setup (Figure 1.10). This is due to the fact that the diffraction of light limits the spatial resolution of optical microscopy to be equal to approximately the wavelength of light divided by two (Equation 1.12).[113] The distribution of the emission intensity over the pixels (*i.e.*, the point spread function (PSF)), is well-approximated by a Gaussian function and mainly arises due to the profile of the laser excitation.[114] Aberrations that distort the profile of the laser beam will also cause a corresponding distortion in the TIRFM image.

$$d = \frac{\lambda}{2NA} \tag{1.12}$$

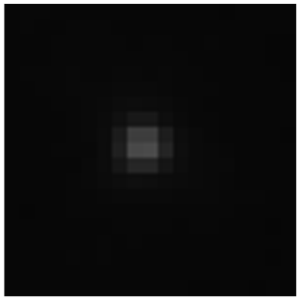

Figure 1.10. (A) Zoomed in portion of a TIRFM image to show the pixilation of a single fluorescent nanoparticle (Ultra Rainbow, Spherotech). The sample was excited with a 405 nm laser at a power of 0.1 mW.

1.3 Energy transfer

As alluded to in the previous sections on quenching and photobleaching, one mechanism by which molecules in an excited electronic state dissipate energy is by transferring it to a molecule characterized by having a lower energy S_0-S_1 energy band. Energy transfer is a prevalent

mechanism of interaction between closely lying chains within single large conjugated polymer molecules coiled within themselves,[64, 115-116] but also between CP molecules in films.[60, 117-118]

There are two main mechanisms of non-radiative energy transfer: electron exchange -also known as Dexter energy transfer- and coulombic dipole-dipole energy transfer also known as -Förster resonance energy transfer (FRET).[73] In the Dexter mechanism, an electron is transferred from the lowest unoccupied molecular orbital (LUMO) of the excited donor to the LUMO of the acceptor while a second electron is transferred from the highest occupied molecular orbital (HOMO) of the acceptor to that of the donor, leaving the acceptor in the excited state and the donor in the ground state. Dexter energy transfer may be viewed as simultaneous $2e^-$ transfer and requires orbital overlap. As a result, it is a short-range mechanism with the transfer efficiency decaying exponentially as a function of donor-acceptor distance. For this reason, Dexter energy transfer is frequently encountered as a collisional quenching mechanism. In contrast, FRET involves the coupling of the excited donor and the ground state acceptor *via* coulombic dipole-dipole interactions, which result in a decay in transfer efficiency that is a function of the inverse sixth power of the donor-acceptor distance. Like Dexter transfer, the final state following FRET is a ground state donor and excited state acceptor. Both energy transfer mechanisms are present in CP materials, but FRET tends to dominate because it operates over a longer range.

1.3.1 Förster resonance energy transfer theory

The theory of non-radiative energy transfer *via* dipole-dipole coupling was developed by German scientist Theodor Förster in the 1940s.[119-120] Förster approximated the donor and the acceptor molecules as weakly coupled point dipoles and applied classical electrodynamics to derive an equation relating the rate of energy transfer to five parameters: the overlap between the donor emission and acceptor absorption spectra (J), the relative orientation of the dipoles (κ^2), the refractive index of the medium (n), the donor-acceptor separation distance (R), and the radiative rate constant of the donor, effectively integrated as the ratio between the decay rate constant and the fluorescence quantum yield of the donor (Φ_D).[121] The efficiency of energy transfer (E) may be written as the ratio of the donor-acceptor distance, R, to the parameter R_0, -defined as the donor-acceptor distance where the efficiency of energy transfer if 50%- to the inverse sixth power (Equations 1.13 and 1.14). Experimentally, the FRET efficiency is also often determined by

computing the ratio of the donor intensity or lifetime (I or τ) in the presence of the acceptor versus the donor intensity or lifetime in the absence of the acceptor (I_0 or τ_0) as per Equation 1.15

$$R_0^6 = \frac{9 \ln 10 \kappa^2 \Phi_D J}{128 \pi^5 N_A n^4} \tag{1.13}$$

$$E = \frac{1}{1+\left(\frac{R}{R_0}\right)^6} \tag{1.14}$$

$$E = 1 - \frac{I}{I_0} = 1 - \frac{\tau}{\tau_0} \tag{1.15}$$

One of the biggest strengths of FRET theory is that the energy transfer efficiency may be calculated using constants and easily obtained experimental data. The overlap integral can be computed as per Equation 1.16 upon obtaining the donor emission spectrum (f_D, in units of cm^{-1} and normalized to an area of 1) and the acceptor absorption spectrum (ε_A, in units of molar absorptivity ($M^{-1}cm^{-1}$) per cm) experimentally. The dipole orientation factor has a range of possible values between 0 and 4 and is defined by Equation 1.17, where $\hat{R}_{DA}$ is the normalized displacement between the donor and the acceptor dipoles and $\hat{\mu}_D$ and $\hat{\mu}_A$ are the normalized donor and acceptor dipole moments, respectively. Many authors assume that κ^2 is 2/3, the value for dipoles that are isotropically oriented within the excited state lifetime. This assumption is dubious in many cases, particularly for large, slowly tumbling molecules (*e.g.*, proteins) or anisotropic environments (*e.g.*, lipid membranes), and can be a significant source of error in comparing theoretical estimations of FRET efficiency to experimental ones.

$$J = \int f_D(\lambda) \varepsilon_A(\lambda) \lambda^4 d\lambda \tag{1.16}$$

$$\kappa = \hat{\mu}_A \cdot \hat{\mu}_D - 3\left(\hat{\mu}_D \cdot \hat{R}_{DA}\right)\left(\hat{\mu}_A \cdot \hat{R}_{DA}\right) \tag{1.17}$$

Typical donor/acceptor pairs used in FRET studies have R_0 values of *ca*. 5 nm. This, combined with the $1/R^6$ dependence on the donor/acceptor distance, means large changes in FRET efficiency are observed for relatively small changes in R (Figure 1.11). Fluorescence techniques based on FRET have been developed to take advantage of this sensitivity to measure distances on the nanometer scale and have become widely used in the chemical[122-124] and biological sciences.[112, 125-127]

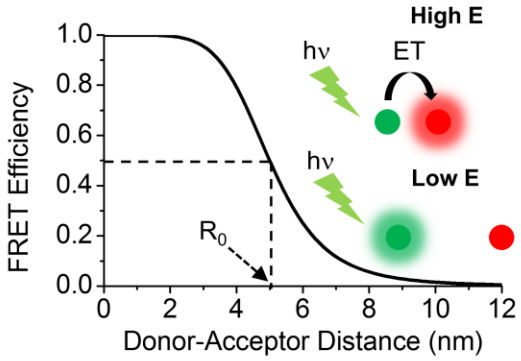

Figure 1.11. Relationship between FRET efficiency and donor-acceptor distance. Graph illustrating the FRET efficiency *versus* R for a donor/acceptor pair with an R_0 value of 5 nm.

1.3.2 Considerations required for multichromophoric systems

Förster's theory of resonance energy transfer was developed for a single donor/acceptor pair where both units are considered located at relatively large distances enabling approximating them both as point dipoles. These assumptions do not necessarily hold true for multichromophoric systems at close distance.[128] In this thesis, the multichromophoric systems under consideration include lipid membranes containing donor or acceptor dyes and conjugated polymers (behaving as acceptors or donors, respectively), where the polymer chain itself contains multiple chromophores, and where the deposition of the polymers into thin films can also result in energy transfer between different polymer chains. In the following section, the attempts by various authors to extend the theory to describe energy transfer to multiple acceptors and between CPs will be briefly outlined.

1.3.2.1 Energy transfer to multiple acceptors in 2 or 3 dimensions

It was Förster himself who first extended his theory to treat the energy transfer from a donor to multiple acceptors in 3 dimensions (*i.e.*, in solution) in 1949.[119] He assumed a homogeneous solution of donors and acceptors as well as the absence of donor/acceptor diffusion and homotransfer between donors. In this case, the problem is considered in terms the number of acceptors within the volume of a sphere ($1/C_0$) of radius equal to the Förster radius, R_0 (Equation 1.18). The time-dependant intensity decay of the donor in the presence of the acceptor, $I_{DA}(t)$, is given by Equation 1.19, where I_D^0 and τ_D are the intensity and the lifetime of the donor in the absence of acceptors, respectively.

$$C_0 = \left(\frac{4}{3}\pi R_0^3\right)^{-1} \tag{1.18}$$

$$I_{\mathrm{DA}}(t) = I_D^0 \exp\left[-\frac{t}{\tau_D} - \frac{\sqrt{\pi}C}{C_0}\sqrt{\frac{t}{\tau_{\mathrm{D}}}}\right] \tag{1.19}$$

It was not until 1964 that Tweet *et al*. developed a similar solution for energy transfer occurring in 2 dimensions, using it to describe energy transfer between chlorophyll *a* and copper pheophytin *a* in monomolecular films in the dilute limit.[129] In 2 dimensions, C_0 is defined by the area of a circle with a radius of $2\pi R_0^2$, rather than by the volume of a sphere. In the 1970s and early 1980s researchers interested in studying processes occurring within lipid membranes using FRET developed the theory further.[130-134] In 1978, Fung and Stryer published plots of I/I_0 and energy transfer efficiency versus acceptor surface density generated *via* numerical integration. The authors recovered values of R_0 that agreed well with experimental values for lipid vesicles containing fluorescently labeled donor and acceptor phospholipids.[130] A year later, Estep and Thompson verified the work of Tweet *et al.* experimentally, and also extended it to show that the theory for a 2 dimensional, infinite plane was also applicable to small unilamellar vesicles and large multilamellar vesicles of egg phosphatidyl choline.[131] Around the same time, Wolber and Hudson derived an analytic solution to the same problem, and also for the case of donor/acceptor binding and the case that there is an excluded volume around the donor that the acceptor cannot access (*e.g.*, the donor is buried inside a protein).[132] They also provided a numerical approximation to their solution that is accurate within 1% for dilute samples where the concentration of acceptors per R_0^2 (a measure of the density) is between 0 and 0.5 (Equation 1.20). At higher acceptor densities, the values of the fitting parameters for various values of the acceptor concentration, *C*, are published in the original paper and have also been reproduced elsewhere.[132, 135] Figure 1.12A shows the relative quantum yield versus acceptor density curves calculated by Wolber and Hudson, and Figure 1.12B shows unpublished experimental data for dilute conjugated polyelectrolyte donors and DiI acceptors embedded within the membrane of DOTAP liposomes, showing that the experimental data follows the general trend predicted by the theory. Dewey and Hammes later provided analytic solutions for energy transfer in other geometries, including parallel infinite planes (*e.g.*, the two layers of the bilayer), the surface of a sphere, the surface of concentric spheres, and the surface of two separated spheres.[133] Snyder and Freire tackled the problem of energy transfer in heterogeneous membranes directly using Monte Carlo calculations to simulate the

mixing process.[134] In addition, they confirmed the previously published analytic solutions under the condition that the excluded volume is small relative to R_0.

$$\frac{I}{I_0} = \Phi_{rel} \approx A_1 e^{-k_1 C} + A_2 e^{-k_2 C} \tag{1.20}$$

In general, the theory for energy transfer in 2 and 3 dimensions is now well-established and has been verified experimentally. [125, 136] The equations work best for systems with small molecule chromophores that are relatively dilute.

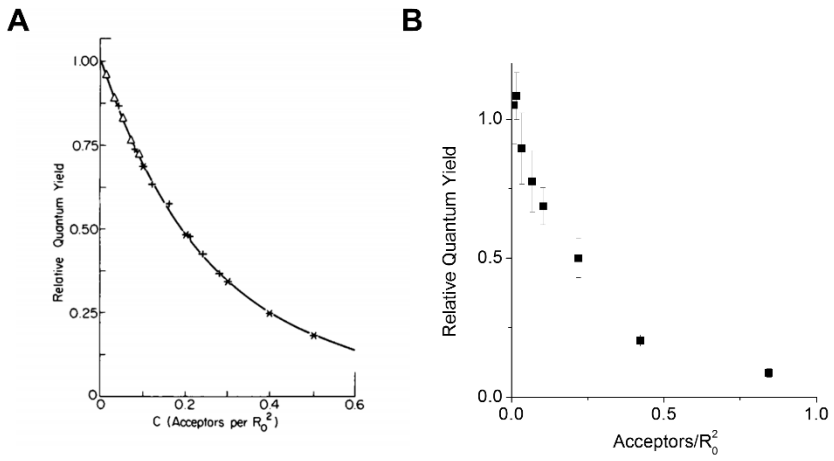

Figure 1.12. FRET in two dimensions. (A) Relative quantum yield versus acceptor surface density for the quenching of randomly distributed donors by randomly distributed acceptors as determined by computer simulations where the donor density is 0.1 donors/R_0^2 (▲) or 0.5 donors/R_0^2 (+), as well as the data points obtained from the numerical approximation equation 1.20 (*). Adapted with permission from reference [132] (Copyright, 1979, Elsevier). (B) Relative quantum yield versus acceptor surface density for experimental data collected using steady state fluorescence spectroscopy. The donor is 0.001 PRU:lipid PPE-CO_2-7 and the acceptor is DiI ranging from 0.008–0.85 DiI/R_0^2. The donor and acceptors are present in the membrane of 200 nm diameter DOTAP liposomes.

1.3.2.2 Failure of the ideal dipole approximation

One of the key assumptions of the FRET theory whose applicability is subject to question is the approximation of the donor and acceptor electronic states as point dipoles.[128, 137] In general, the working assumption is that treating molecules as point dipoles is only appropriate when the donor-acceptor distance is larger than the size of the molecules themselves. Muñoz-Losa *et al*. quantified the donor-acceptor distance where errors due to the ideal dipole approximation became

significant for several commonly employed donor-acceptor pairs, including the cyanine dye pair Cy3-Cy5, most frequently used in SM studies. The authors calculated the rate of energy transfer by applying quantum mechanical methods to calculate the transition density of the donor and the acceptor using the full Coulombic interaction potential over a range of 196 different relative orientations. The authors then compared this to the result found by using the dipole-dipole coupling approximation used in FRET theory.[138] They found significant deviations between the rates of energy transfer using the two methods at donor-acceptor distances less than 2 nm for isotropically averaged orientations ($\kappa^2 = 2/3$) and at distances > 5 nm for certain orientations.[138] The lower error in the isotropically oriented case was attributed to the averaging out of positive and negative deviations over the different orientations. Systems where the donors and acceptors are anisotropically oriented are thus expected to suffer from increased error due to the failure of the ideal dipole approximation compounded by error in the estimation of κ^2.[138]

Several properties of CP materials suggest that they may require a more complex consideration of the interaction potential and knowledge of the orientation effects. Large macromolecules such as CPs do not necessarily undergo isotropic rotation during their excited state lifetime, rendering the commonly held assumption that $\kappa^2 = 2/3$ invalid. In addition, the first excited singlet state of most CPs is delocalized over several PRUs (> 2 nm), which invalidates the ideal dipole approximation that holds that the size of the molecules is much smaller than the distance separating them. This is particularly true for polymers in condensed phases where chains are packed within close proximity.

Several authors have explored the applicability of Förster's theory of resonance energy transfer to conjugated polymers specifically.[118, 139-140] Wong *et al*. studied the energy transfer from a six PRU polyfluorene segment to a tetraphenylporphyrin acceptor using semiempirical quantum chemical methods.[139] Their treatment of the Coulombic interaction potential accounted for the extended transition dipole moment density spread along the donor and acceptor molecules and was compared to a traditional Förster treatment of the molecules as point dipoles. While they found that the Förster rate of energy transfer was recovered at large separations (*ca*. 10 nm), significant deviations were observed at shorter donor-acceptor distances. In particular, the rate produced by the more accurate quantum mechanical calculations showed a short-range distance dependence that was much less sensitive to distance, decaying with an R^{-2} rather than an R^{-6} dependence.[139]

Overall, the authors concluded that the Förster expression would be inappropriate for condensed-phase systems where the donors and acceptors are closely packed, such as in a thin film. This conclusion was also shared by Wiesenhofer *et al*., who studied energy transfer between a pristine ladder-type poly(para-phenylene) and a second polymer chain with a ketonic defect trap site.[140] Like Wong *et al*., they compared the efficiency of energy transfer obtained from a quantum mechanical treatment of the interaction potential versus that obtained from traditional Förster theory. When considering two limiting cases of orientation found between polymers packed in films, head-to-head and co-facial, they found that Förster theory lead to a strong overestimation in the former case and a strong underestimation in the latter.[140] The use of quantum calculations to more accurately treat the transition density of the molecules was also necessary to properly describe the important experimental result of Beljonne *et al*., who used ultrafast spectroscopy to show that the rate of interchain energy transfer between polyindenofluorenes packed in a film is *ca*. 1 order of magnitude faster than intrachain energy transfer along an isolated chain in solution.[118]

In conclusion, care must be taken in applying Förster theory to energy transfer between CPs, since several key assumptions implicit in the theory have been shown to fail for various CP systems. Modifications to the theory to more accurately treat these cases have been achieved, but since these require complex quantum mechanical calculations they are not as easily accessible to the average experimentalist as traditional FRET theory.

1.4 Relationship between conformation, film morphology, and energy transfer efficiency

The importance of energy transfer in CP materials was quickly realized by experimentalists studying CP films using time resolved spectroscopy and site selective fluorescence techniques.[141-145] For example, Hayes *et al*. observed an extremely rapid rise in the emission from unoriented films of MEH-PPV and PPV that was attributed to exciton formation, followed by vibronic relaxation occurring on the femtosecond timescale.[143] Interestingly, a redshift in the emission was observed over time, which was interpreted as exciton migration from less conjugated/higher energy sites to more conjugated/lower energy sites.[143]

To understand the nature of the energy transfer, it is helpful to take a closer look at how excitons are localized at different sites on the polymer. Although CPs may appear as 1D molecules on paper, in reality they are subject to conformational disorder. Twists and kinks in the polymer chain lead to a break in the pi conjugation and lead to the separation of the polymer chain into a series of conformational subunits with a distribution of conjugation lengths. (See Figure 1.13). Typical conjugation lengths for the PPV and PPE polymers investigated in this thesis are 10-17 PRUs[146] and 5 PRUs,[92] respectively. Excitons are initially localized on one conformational subunit following excitation, but may further delocalize along the chain or migrate to other chromophore subunits *via* resonance energy transfer.

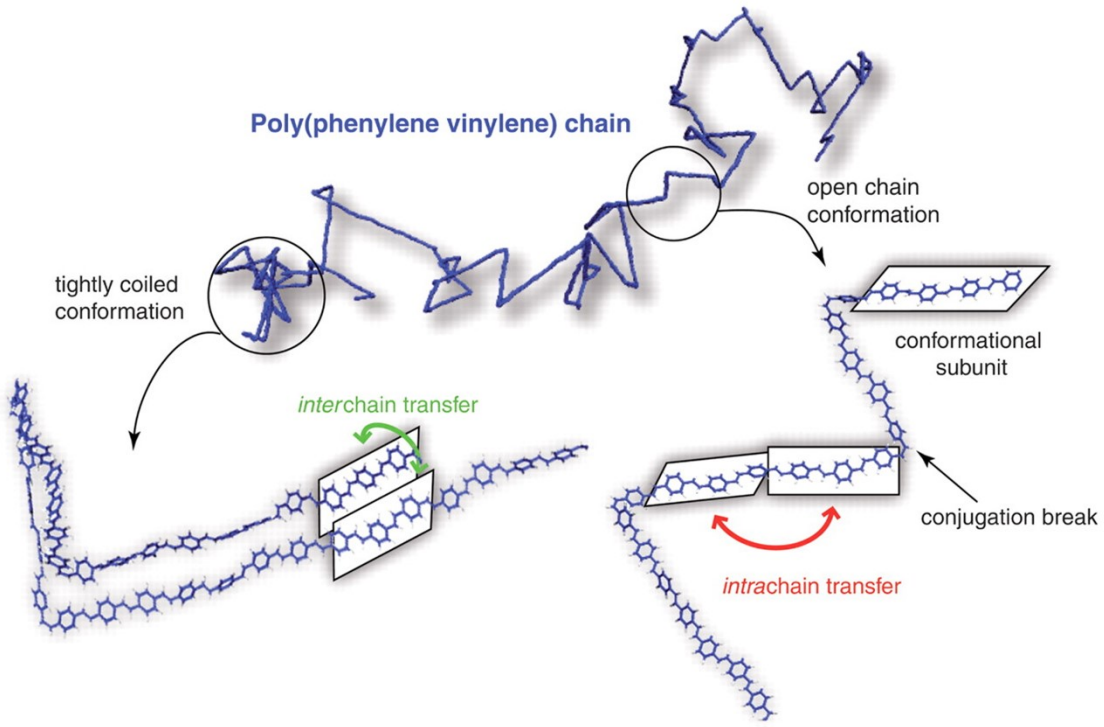

Figure 1.13. Conformation and energy transfer in CPs. Cartoon of a poly(phenylene vinylene) macromolecule illustrating the concepts of conformational subunits, conjugation breaks, and regions of intrachain and interchain energy transfer, corresponding to regions with extended and tightly coiled conformations, respectively. Adapted with permission from reference [147] (Copyright, 2009, American Association for the Advancement of Science).

1.4.1 Intrachain versus interchain energy transfer

When discussing energy transfer processes within CPs, a distinction is made between intrachain and interchain energy transfer.[60, 118, 147] Intrachain transfer occurs between adjacent segments of the polymer chain and tends to dominate in isolated chains with highly rigid, or

extended conformations.[147] Interchain transfer, however, occurs between different chains or between distant segments of the same chain that are brought within close proximity due to conformational flexibility of the macromolecule. This type of energy transfer tends to dominate when the polymer adopts a tightly coiled, or collapsed conformation.[147] Although the existence of energy transfer in CPs was well-established through the 1980s and 1990s, it was difficult to distinguish between intrachain and interchain transfer and to determine how much either pathway contributes towards the observed energy migration in the material. In 2000 and 2001, Schwartz *et al*. reported an elegant strategy to probe intrachain energy transfer by encapsulating single chains of MEH-PPV inside oriented channels within nanoporous silica.[148-149] These extended, oriented chains where only intrachain transfer was possible were then compared to randomly oriented films of MEH-PPV deposited outside of the channel, where both interchain and intrachain energy transfer were possible. Ultrafast emission anisotropy measurements showed that excitons generated in the film outside of the channels migrated to the polymer segments contained within the pores, resulting in an increase in the anisotropy due to emission occurring primarily from the oriented chains. Overall, interchain energy transfer was found to occur more rapidly than intrachain energy transfer. Beljonne *et al*. reached the same conclusion in their study comparing the rates of intra and intermolecular energy transfer in polyindenefluorenes using quantum mechanical calculations.[118, 150] The disparity between the rates was explained by the relatively weak electronic coupling elements between chromophores arranged head-to-tail, as they would be for chromophore subunits undergoing intramolecular energy transfer *versus* other orientations, such as co-facial, that could be considered in the case of intermolecular energy transfer (see also Figure 1.13).

1.4.2 Single molecule spectroscopy studies demonstrating energy migration

Although the presence of energy migration in CPs was well-documented and its importance to the functioning of CPs in devices was clear, developing a complete understanding of the energy transporting properties has been a longstanding challenge for the scientific community. A large part of the difficulty is that CP materials are inherently heterogeneous, both at the level of individual chains (distributions in chain length, conformation[64, 151-152], and chemical defects[153-154]) and at the level of films in devices (morphology[117] and the formation of interchain species[154-155]) (Figure 1.14).

SMS studies have been instrumental in deconstructing the complex photophysical properties of CP materials in bulk into behavior at the level of single polymer chains.[72, 156] In this section, several landmark SMS studies that demonstrated the relationship between chain conformation and energy transporting properties will be reviewed, followed by a summary of the most recent progress in the field.

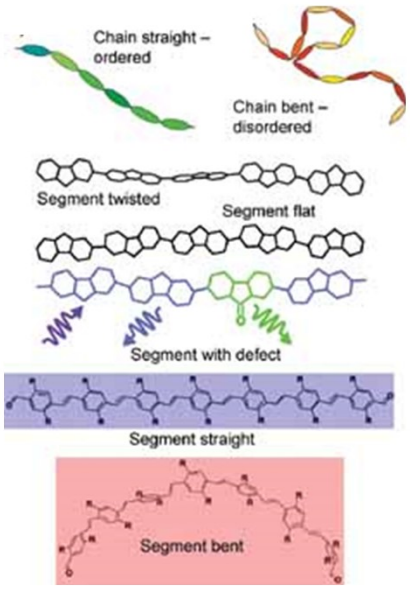

Figure 1.14. Heterogeneity within conjugated polymers. Possible modes include twisting and bending of the polymer chain as well as the presence of chemical defects. Adapted with permission from reference [156] (Copyright, 2010, John Wiley and Sons).

In 1997, the first SMS study on single conjugated polymers was published by Vanden Bout *et al*. in the journal *Science*.[116] A dilute solution of a copolymer with a poly(*p*-phenylene vinylene) (PPV) and a poly(*p*-pyridylene vinylene) (PPyV) backbone (Figure 1.15A) was spincast onto a polystyrene surface and imaged using scanning confocal microscopy (Figure 1.15B). Remarkably, the intensity *versus* time trajectories acquired for individual polymer chains showed discrete on-off transitions and single step photobleaching (Figure 1.15C and Figure 1.15D). This result was remarkable because it implied that the entire polymer chain was acting as a single molecule despite containing many individual chromophore subunits. With an average molecular weight of *ca*. 2000, this corresponds to *ca.* 80 phenyl-vinyl units per polymer. The dark states were interpreted as either reversible or irreversible photobleaching of one of the chromophores, followed by rapid

(*i.e.*, faster than the radiative decay rate) energy migration from all other excited states to the trap site.

One of the important implications of this study was that a few chemical defects could quench the emission of an entire polymer chain, an observation that was later exploited to develop ultrasensitive chemical and biological sensors.[39, 157-158] In addition, the work showed that the energy migration occurring in PPV thin films was also occurring to some extent at the level of an individual chain.

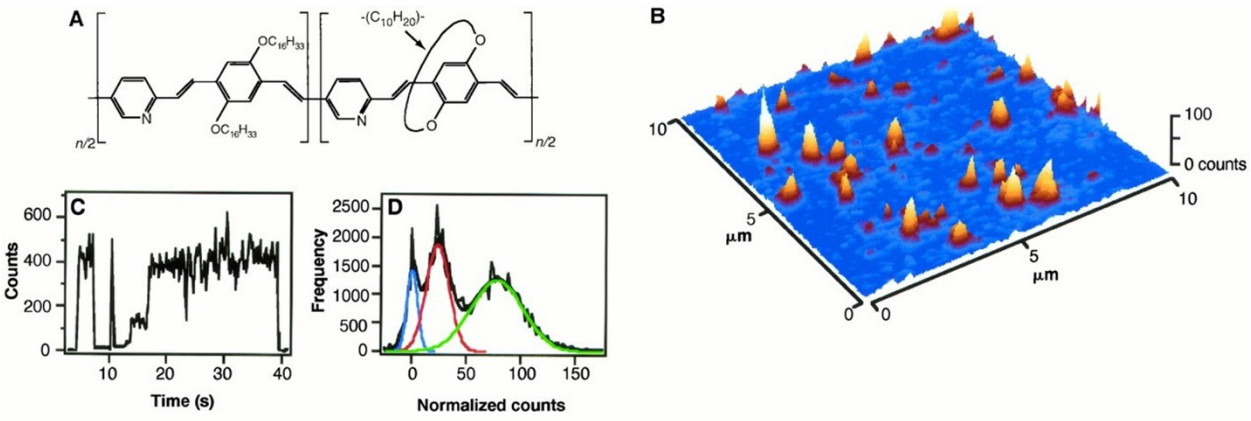

Figure 1.15. Detection of single CP molecules using confocal microscopy. (A) Chemical structure of the conjugated polymer under study. The polymer is formed by the copolymerization of poly(*p*-phenylene vinylene) and poly(*p*-pyridylene vinylene) derivatives. (B) Fluorescence scanning confocal image of the single polymer molecules. The fluorescence intensity is shown on a height and colour scale. (C) Representative fluorescence intensity versus time trajectory for a single polymer molecule demonstrating discrete, reversible transitions and single step photobleaching. (D) Histogram of the different intensity states observed in the intensity versus time trajectories of 40 different polymer chains. Three different intensity states, dark, intermediate, and bright are fit to the Gaussian distributions plotted in blue, red, and green, respectively. Adapted with permission from reference [116] (Copyright, 1997, The American Association for the Advancement of Science).

Following the demonstration of single step photobleaching in individual conjugated polymer chains by Vanden Bout *et al*., the number of SMS studies on CPs flourished. The presence of discrete intensity jumps in single polymer intensity versus time trajectories became well-known as a signature of efficient energy migration. The observation of different photophysical signatures also provided evidence for different conformations coexisting within samples of spin-coated MEH-PPV, emphasizing the inherent heterogeneity present in polymer thin films.[159] Experiments using polarized excitation light were also used to show the degree of structural order based on the

extent of emission anisotropy from individual MEH-PPV polymer chains.[66, 160] The emission anisotropy data was then correlated to the results of Monte Carlo simulations to determine probable chain conformations (see Figure 1.16A).[66] In this study and others,[59, 161] tetrahedral defects (*e.g.*, saturated carbons) along the polymer chain were determined to play a critical role in dictating the polymer conformation.

It is well-known from the polymer science literature that the conformation of polymers in solutions is intimately related to polymer-solvent ineractions.[162] In 2000, Huser and coworkers studied chains of MEH-PPV spin cast from a poor solvent, toluene, and chains spin cast from a good solvent, chloroform, using SM confocal microscopy.[57] The photophysical behaviour of the chains cast from different solvents varied dramatically. The chains cast from toluene had discrete intensity jumps, the signature of efficient energy migration, whereas the chains cast from chloroform behaved as an ensemble of uncommunicating chromophores and showed exponential photobleaching (see Figure 1.16B). The result from the chains cast from toluene was later reproduced by Ebihara *et al*, who additionally performed molecular dynamics simulations to show that the chain conformation was consistent with a defect coil.[61] Similar behaviour has also been reported recently for SMS studies of regioregular and regiorandom P3HT spun cast from both poor and good solvents.[62] These studies are significant because they show how solution processing conditions (e.g., choice of solvent) can affect the photophysical properties of CP films starting at the level of a single polymer chain.

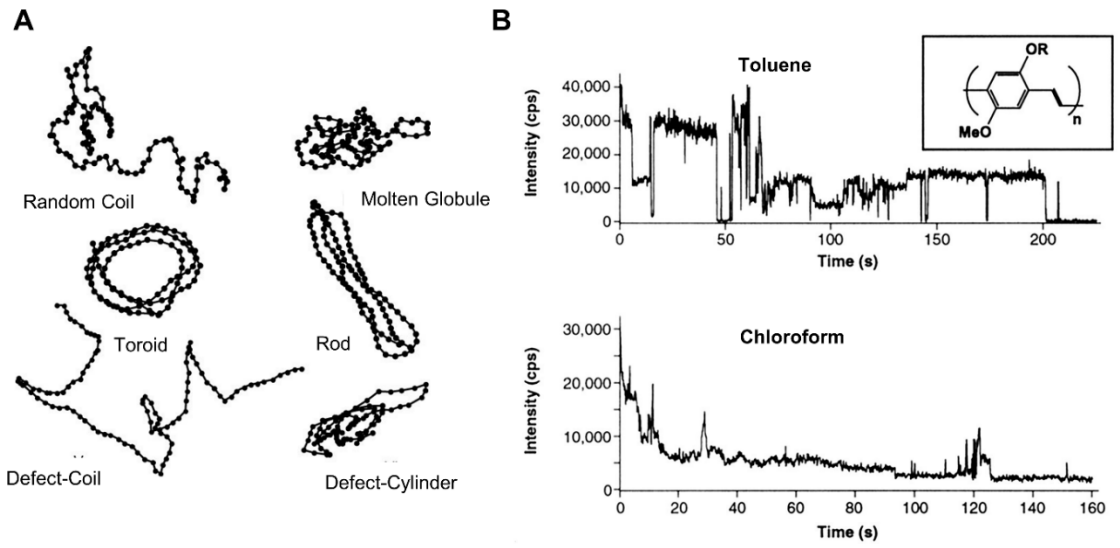

Figure 1.16. Spectroscopic signatures of single CPs adopting different conformations. (A) Results of Monte-Carlo simulations of a 100-repeat unit homopolymer showing different possible conformations. Adapted with permission from reference [66] (Copyright, 2000, Nature Publishing Group). (B) Emission intensity versus time trajectories extracted from confocal microscopy of single MEH-PPV polymers cast from toluene or chloroform. Adapted with permission from reference [57] (Copyright, 2000, National Academy of Sciences).

Through the mid to late 2000s, SMS studies continued to help refine our understanding of CP photophysics. Low temperature experiments were conducted to probe the nature of the individual chromophores along an MEH-PPV chain, showing that multiple emissive species are responsible for the inhomogeneous broadening of the ensemble absorption and emission spectra.[163-165] Thiessen *et al*. collected low temperature, single molecule emission spectra of the polymer P3HT and showed that the chromophores exhibited a wide range of S_0-S_1 energy gaps, which they attributed to structural and conformational disorder at the single chromophore level (see Figure 1.17A).[71]

Although the presence of disorder at the single chromophore level was acknowledged, the consensus was still that structure-property correlations in CPs stemmed mainly from differences in morphology, not differences between individual chromophores.[166] Toward this end, a number of studies examined the effect of side chains on energy migration in CPs. Sugimoto *et al*. studied a polythiophene grafted with side chains of polystyrene and concluded based on photobleaching dynamics, emission anisotropy, and single molecule emission spectra that the bulky side chains prevented the polymer from adopting a collapsed conformation and lowered the efficiency of

energy migration compared to a polythiophene without bulky side chains (see Figure 1.17B and 1.17C).[167] Hu *et al*. also concluded that the distribution of side chains strongly affects polymer conformation at the single molecule level from the results of their study of regiorandom P3HT and poly(3-hexyl-2,5-thienylene vinylene).[168]

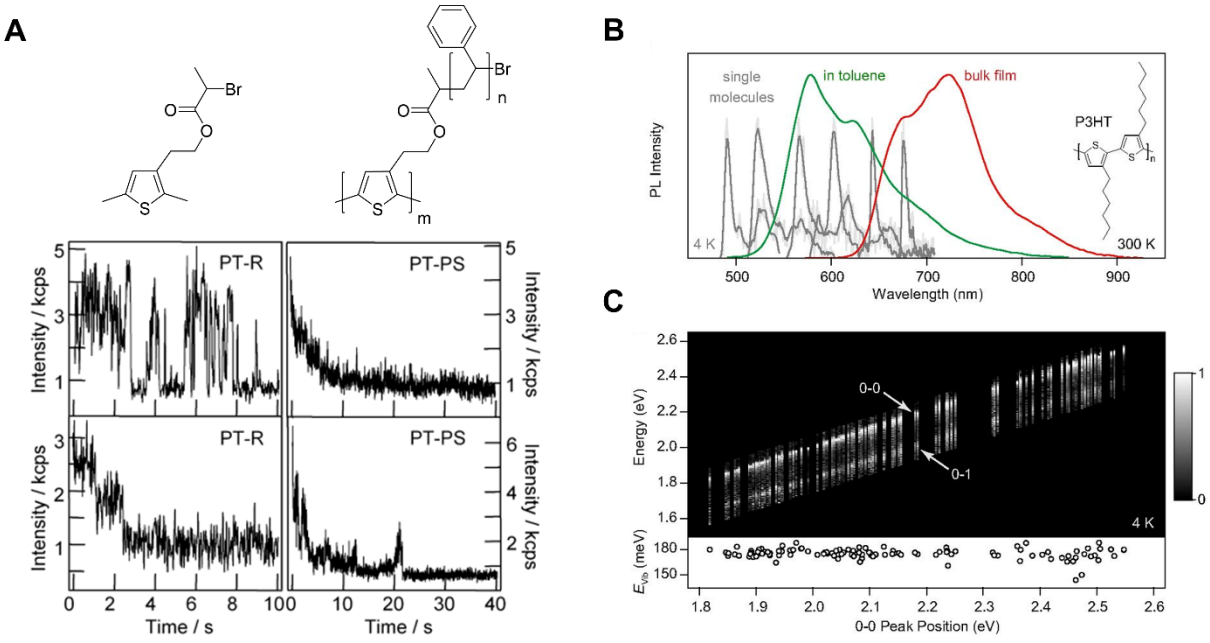

Figure 1.17. Effect of side chains on energy migration in single CP molecules. (A) Fluorescence intensity versus time trajectories obtained from confocal microscopy of individual polythiophene polymers. Polymers without bulky sidechains (left column) show discrete intensity fluctuations and stepwise photobleaching indicative of efficient energy migration whereas polymers grafted with polystyrene side chains (right column) show exponential photobleaching indicative of poor energy migration. Adapted with permission from reference [71]. (B) Emission spectra of P3HT in toluene solution (green), drop cast from toluene into a thin film (red), and of single molecules at 4K (grey). (C) Normalized emission spectrum of 115 single molecules sorted by peak energy for the 0-0 transition. The 0-1 vibronic transition is shifted 180 meV from the main peaks. Adapted with permission from reference [167] (Copyright, 2007, John Wiley and Sons).

As more and more scientists were harnessing the power of SMS to study the photophysics of CPs, several developments were taking place in parallel within the broader single molecule community. Of these, the invention of sub-diffraction limit microscopy, for which Eric Betzig, Stefan W. Hell and W.E. Moerner shared the Nobel Prize in Chemistry in 2014, is arguably one of the most significant. These superresolution techniques allow features to be resolved with an order of magnitude greater resolution, by either performing a 2D Gaussian fitting of the fluorescence spot to localize its centre, or by altering the point spread function of the excitation

beam. In 2009, Habuchi *et al*. performed centroid fitting on the emission blinking of single MEH-PPV polymers to localize the emitting sites with nanometer resolution.[169] More than half of the intensity fluctuations were accompanied by a spatial displacement, which the authors interpreted as evidence for energy transfer to different emitting sites (see Figure 1.18A to 1.18E). In 2012, Yu *et al* also used superresolution techniques to quantify the quenching radius of hole polarons in PFBT nanoparticles.[170] Quenching of a portion of the chromophores by the hole polaron led to a dark spot which in turn led to small displacements in the fluorescence spot that could be localized using centroid fitting. In a similar study, Bolinger *et al*. injected hole polarons into single chains or nanoparticles of MEH-PPV electrochemically, and then determined the quenching radius by centroid fitting of the observed displacement in the fluorescence spot (see Figure 1.18F to 1.18H).[171] Interestingly, long-range energy migration (up to 60 nm) was observed for the single polymer chains but not the nanoparticles.[171] The authors speculated that the increased order in the single chain over the NP, which was modeled to have a defect coil conformation, was an important parameter in determining the efficiency of energy migration.[171] It is also possible that the presence of defects in NPs or films may lead to an underestimation in the exciton diffusion length by competing with the injected hole polaron as alternative quenchers.

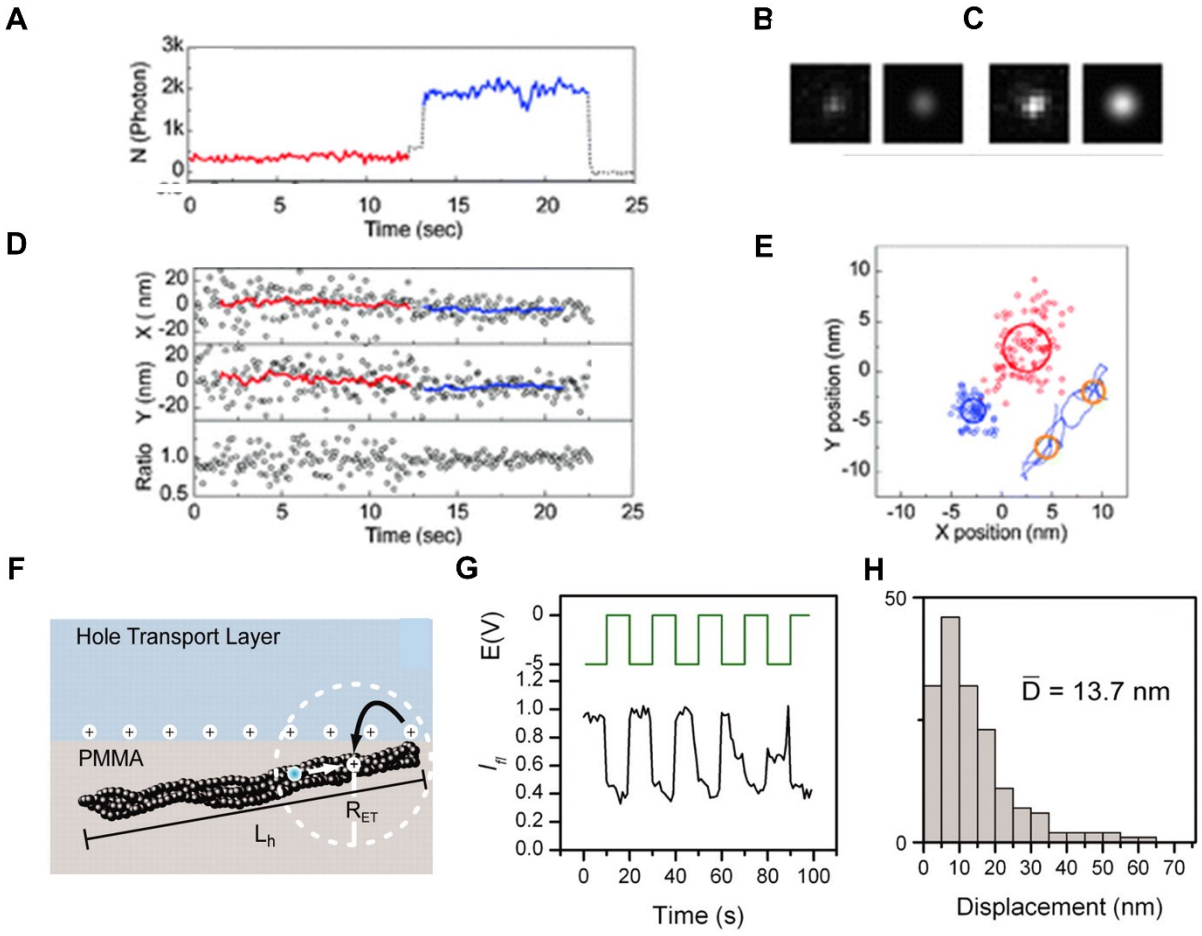

Figure 1.18. Detection of exciton migration in CPs using superresolution techniques. (A) Fluorescence intensity versus time trajectory for a single MEH-PPV molecule showing high and low intensity states. (B) and (C) Fluorescence microscopy image of a single MEH-PPV molecule (left) and 2D Gaussian fitting (right) for the low and high intensity states, respectively. (D) Centroid positions of the emissive site along the x (top) and y (centre) directions. (E) Plot showing the centroid position calculated at each time point along the y and x axis. The large circles show the location of the emitting sites and the width of the circle represents the standard deviation. Adapted with permission from reference [169] (Copyright, 2009, Royal Society of Chemistry). (F) Drawing of an MEH-PPV chain with length L_h cast on a PMMA matrix next to a hole transporting layer. The quenching radius of the hole polaron is illustrated by a white, dashed circle. (G) Fluorescence intensity versus time trajectory of a single MEH-PPV molecule (black, bottom) under an applied bias (green, top). (H) Histogram of the total centroid displacement ($D = \sqrt{x^2 + y^2}$) determined from 167 MEH-PPV molecules. The mean displacement is 13.7 nm, but displacements up to 60 nm are observed in some cases. Adapted with permission from reference [171] (Copyright, 2011, American Association for the Advancement of Science).

Several SMS studies published within the last few years have further explored the idea that efficient energy migration is facilitated by long-range order in the polymer packing.[115, 172-174] In

2014, Hu *et al*. used a technique called solvent vapor annealing (SVA) to create P3HT aggregates for SMS imaging, effectively adopting a procedure first reported by Vogelsang *et al.* in 2011[115, 175] Single polymer chains embedded in PMMA were exposed to N_2 saturated with solvent. The solvent caused swelling of the PMMA matrix, allowing the previously immobilized polymers to diffuse within the matrix and form aggregates. The authors compared the efficiency of energy migration in aggregates of regioregular P3HT, which exhibits highly ordered packing, to aggregates of regiorandom P3HT, which has relatively disordered packing, and concluded that disordered packing, even in small aggregates, strongly impedes interchain energy transfer. This conclusion was also reached by Camacho *et al*., who compared the energy funneling efficiency of a polyfluorene bis-vinylphenylene derivative to the light harvesting antenna of purple bacteria (LH2) using two dimensional polarization imaging.[172] As expected for a naturally occurring light harvesting complex, the funneling efficiency of LH2 was close to unity, whereas the value for the CP was much lower. Insulation of the polymer backbone by cyclodextrin, however, recovered funneling efficiencies close to unity, demonstrating the importance of order in the efficiency of energy migration and the role that structural scaffolding can play in helping to achieve that order. The use of lipid membranes as a scaffold for controlling the packing and relative orientation of conjugated polyelectrolytes in the context of light harvesting is explored in Chapter 3 of this thesis.

In all the SMS studies on CPs highlighted so far, the polymers had been immobilized in the solid state. For certain applications, particularly those involving water-soluble conjugated polyelectrolytes, the ability to study the photophysics of single polymers in their native environment may reveal more insights, particularly in regards to conformational dynamics. One of the challenges in meeting this objective is to find an appropriate immobilization strategy for imaging over extended time periods.

In the single molecule biophysics community, biomolecules are frequently modified with a biotin moiety and attached *via* the binding of the biotin to an imaging surface bearing streptavidin or neutravidin, where the dissociation constant of the biotin/protein complex is extremely low, at *ca.* 10^{-15} M^{-1}[176] In 2013, Delgarno *et al*. used this strategy to immobilize a polythiophene for SM imaging in buffer (see Figure 1.19A).[177] Fluctuations in the fluorescence intensity representing transitions to dark states (*e.g.*, radicals) and photobleaching were observed and addition of an

enzymatic oxygen scavenger was found to improve the stability and lifetime of the fluorescent signal.

The complexation of polymers with nanostructures such as liposomes[70, 90] or silica nanoparticles[94, 98] has been pursued by our laboratory at McGill University as an alternative immobilization strategy for SM imaging. In 2010, Karam *et al*. reported the encapsulation of single molecules of MPS-PPV inside of liposomes 200 nm in diameter, thus localizing the polymer within a diffraction limited spot (see Figure 1.19B).[70] The authors ensured that each liposome contained at most 1 MPS-PPV molecule by relying on encapsulation statistics for a very dilute solution (*i.e.*, most liposomes contain zero polymers, *ca.* 20% contain 1 polymer, and accordingly very few are expected to contain 2 polymers). One of the key advantages to the liposome encapsulation strategy is that the polymers are freely diffusing, thus allowing their photophysical properties to be interrogated in the native state.[70] The authors found that freely floating MPS-PPV within liposomes showed signature behavior of coiled conjugated polymers in terms of exhibiting few emissive sites, implying efficient energy migration. By changing the nature of the membrane from anionic to zwitterionic, thus favoring polymer embedding within the amphiphilic lipids, the authors next showed that the polymer behaved as a collection of independent emissive chromophores, a manifestation of poor energy transfer arising from the deaggregation of the polymer within the membrane.

The adsorption of MPS-PPV onto surface-functionalized 100 nm diameter silica nanoparticles has also been established as a platform for SMS studies (see Figure 1.19C).[94, 98] Like the liposomes, the NP scaffold localizes the polymers within a diffraction limited spot. Although this strategy is not easily amenable to the study of single polymer chains, the photophysical behaviour of the NPs under SM imaging conditions is an important subject in the context of creating new markers for biological imaging or the development of new biosensing platforms. For example, Chapter 2 of this thesis presents an assay to detect membrane dynamics of individual liposomes by monitoring their effect on the emissive properties of MPS-PPV coated NPs using TIRFM.

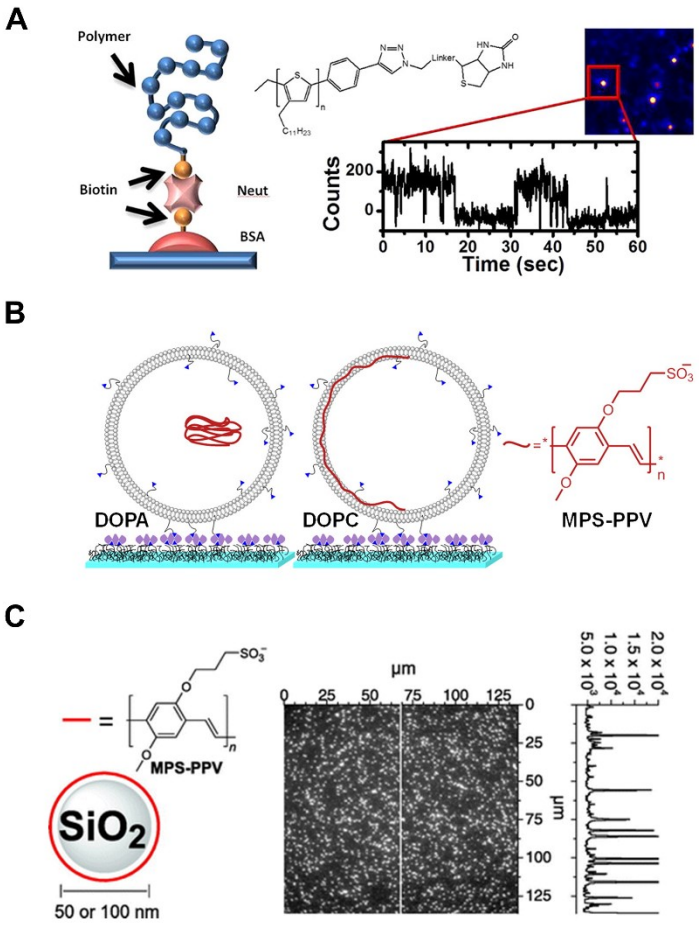

Figure 1.19. Immobilization strategies for SMS imaging of CPs in solution. (A) Binding of a CP modified with a biotin moiety to a coverslip using biotin/streptavidin interactions. Adapted with permission from reference [177] (Copyright, 2013, The American Chemical Society). (B) Encapsulation of a CPE within the 200 nm diameter liposomes. The partitioning of the polymer between the membrane phase and the aqueous compartment is controlled by modifying the charge on the lipid head groups. Adapted with permission from reference [70]. (C) Absorption of a CPE onto silica nanoparticles. The adsorption is mediated by electrostatic attraction between the pendant sulfonate groups of the polyanion and charged amine groups on the surface-functionalized NP. Adapted with permission from reference [98] (Copyright, 2011, NRC Research Press).

1.5 Controlling conjugated polymer photophysics by manipulating the environment

In the previous sections, our current understanding of the intimate relationship between conformation and energy transfer in CPs was discussed. Although this relationship makes a complete understanding of the photophysics of CPs a complex problem, it also offers a unique opportunity to control their properties by coaxing them into a desired conformation or aggregation

state. In this sense, scientists have a much larger parameter space to work in beyond synthetic modification of the polymer's chemical structure. In the case of conjugated polyelectrolytes, the parameter space is even larger, since additional factors such as pH, ionic strength/nature of counter ions, surfactants, and even biological/biomimetic structures such as lipid membranes can be used to tune the photophysical properties. In this section, the effect of environmental properties on the photophysics of CPs will be discussed, with an emphasis on the conjugated polyanions used in this thesis: MPS-PPV and PPE-CO_2.

1.5.1 Solvent and counter ions

In solution, polymer chains may exist either as molecularly dissolved species or as aggregates, depending on the solvent-polymer interactions. Several techniques, including steady-state and time-resolved fluorescence spectroscopy, UV-Vis absorption spectroscopy, and light scattering measurements are used to infer the nature of the species present. Experimentally, aggregates may be detected by changes in size *via* dynamic light scattering (DLS),[178] or spectroscopically by fluorescence correlation spectroscopy (FCS).[179] Spectroscopic signatures of aggregates include red-shifted absorption and emission spectra, spectral broadening, and reduced fluorescence quantum yields.[180-184] These red shifts may be due to aggregation facilitating energy transfer to low-energy sites[89, 185] or to the formation of excimer-like species, where the electronic mixing of the neighbouring chains occurs.[180] The formation of aggregates may also help induce greater planarity in the polymer chains, increasing the effective conjugation length and reducing the band gap.[181, 184, 186]

One of the interesting features of CPs spin cast from solution is that the polymer chains have memory of their solution conformation in the solid state. A fascinating study published by Vogelsang *et al*. in 2011 showed the effect of solvent on the conformational dynamics of single MEH-PPV chains in real time.[175] The chains were initially spin cast onto a PMMA matrix, where their conformation was shown to be heterogeneous spectroscopically. Some chains were relatively disordered and kinetically trapped in a high energy state whereas others were relatively ordered and represented a lower energy state. Upon exposing the film to N_2 saturated with solvent vapor (*i.e.*, solvent vapor annealing), the PMMA matrix swelled and the polymer chains were free to adjust their conformation and diffuse through the matrix (Figure 1.20A). During this process, the emission of the MEH-PPV chains was collected using TIRFM (Figure 1.20B). The intensity

versus time trajectory for a chain showed fluctuations in intensity related to the dynamics of the chain adopting collapsed (low intensity) *versus* extended (high intensity) conformations during solvent vapor annealing. Translational diffusion of the chain through the matrix was also observed during this time interval. After SVA was completed, emission polarization experiments confirmed that all of the chains were present in the ordered, low energy conformation.[175]

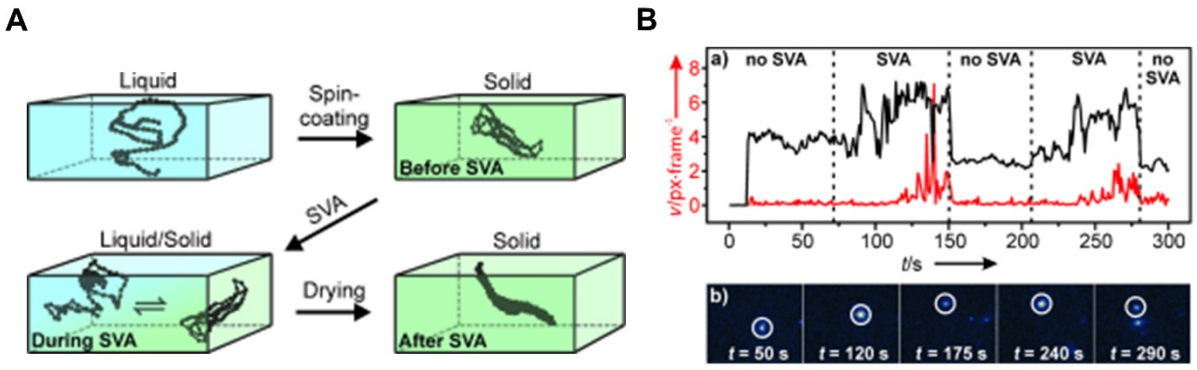

Figure 1.20. Observation of real time conformational changes in single CP molecules. (A) Scheme showing the solvent vapor annealing process. MEH-PPV chains in solution are spin cast onto a PMMA matrix. The chains embedded in the poly(methacrylic acid) matrix have memory of their conformation in solution. During solvent vapor annealing, the matrix swells and the polymer chains explore different conformations. Upon drying of the film, the polymers are left in a more thermodynamically favorable conformation. (B) Fluorescence intensity versus time trajectory for a single MEH-PPV molecule before, during, and after solvent vapor annealing (black). Intensity fluctuations related to the dynamic equilibrium between different chain conformations are observed during SVA. The velocity of the fluorescent spot (*i.e.*, the diffusion of the polymer) is plotted in red. The polymer is mobile during SVA but is stationary otherwise. Adapted with permission from reference [175] (Copyright, 2011, John Wiley and Sons).

The first study demonstrating the spectroscopic signatures of aggregate and excimer formation in PPE polymers was reported by Halkyard *et al*. in 1998, who compared the spectra obtained in mixtures of solvent (chloroform) and non-solvent (methanol).[187] The presence of aggregates was confirmed by filtration through a membrane with a 1.5 µm pore size and they were spectroscopically distinguished by the appearance of a sharp absorption peak at 440 nm and a broad emission peak at 504 nm. Tan *et al*. and Zhao *et al*. also observed similar spectroscopic features for water soluble PPEs with sidechains bearing SO_3^- and CO_2^- groups, respectively.[180, 186] These polymers are molecularly dissolved in methanol and present as aggregates in aqueous solution (see Figure 1.21). Despite the presence of the charged side chains, pi-pi stacking

interactions between the hydrophobic backbones is proposed as one of the major forces driving the aggregation of CPEs in water. Increasing the number of charged groups was recently reported as a successful strategy for avoiding aggregation of PPE oligomers in water.[188] The presence of counterions has been demonstrated by multiple groups to drive the aggregation of CPEs.[92, 179, 181, 189-192] This effect may be explained by the counterions shielding electrostatic repulsion between chains, or, in the case of multivalent ions, by facilitating aggregation *via* polymer-polymer bridging. In addition, CPEs are susceptible to pH-induced aggregation in a manner that depends on the pK_a of their ionisable side chains.[193-195]

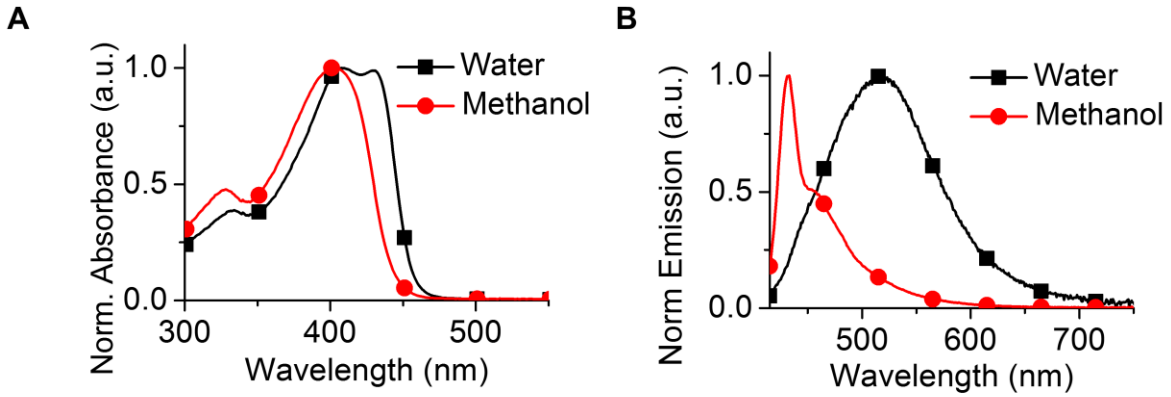

Figure 1.21. Spectroscopy of aggregated and molecularly dissolved PPE-CO_2. (A) and (B) Absorption and emission spectrum of PPE-CO_2 (n = 7) in water (black squares) and methanol (red circles), respectively. Adapted with permission from reference [183] (Copyright, 2014, The American Chemical Society).

1.5.2 Complexation with surfactants

Complexation of CPEs with surfactants is another widely used strategy to control their photophysical properties in aqueous solution[89, 196-203] and in thin films.[204-205] The effect of surfactant complexation on the energy migration and amplified quenching efficiency of CPEs is of particular interest in the context of developing highly sensitive biosensors.[53] Addition of surfactants to aqueous solutions of CPEs tends to result in a number of changes to their conformation/aggregation that lead to concomitant changes in their photophysical properties. In a typical example, Chen *et al*. reported in 2000 that the addition of the cationic surfactant dodecyltrimethylammonium bromide (DTAB) to MPS-PPV in aqueous solution resulted in a 20-fold enhancement in the emission intensity and the appearance of a well-defined vibronic shoulder

at *ca.* 625 nm at a DTAB:PRU ratio of 10:1 (Figure 1.22A).[185] These observations were consistent with the surfactant inducing a conformational change from a disordered structure to a more ordered structure. Extension of the polymer chain would decrease the occurrence of interchain interactions that promote charge transfer reactions or excimer formation, thus restoring the fluorescence quantum yield and providing for a structured emission spectrum. In addition, the emission was no longer dependent on the excitation wavelength after complexation with DTAB, consistent with reduced disorder.

Several groups have elucidated the structure of CPE-surfactant complexes using techniques such as DLS, small angle neutron scattering (SANS), small angle X-ray scattering (SAXS) and liquid phase atomic force microscopy (AFM).[206-208] For example, Knaapila *et al*. studied the interaction of a cationic polythiophene with the anionic surfactant sodium dodecyl phosphate (SDS) and found that addition of surfactant eliminated interparticle order within the polymer aggregates in water, leading to the formation of rod-like or sheet-like polymer/SDS aggregates.[206] In this sense, the polymer may still be part of an aggregate but behave spectroscopically like a molecularly dissolved chain. Additionally, the authors noted that precipitation may occur when the overall charge of the polymer/surfactant aggregate becomes neutral, an important caveat to be aware of when working with these complexes in solution.

In another study, Heeley *et al*. studied the aggregation properties of two different CPEs with oppositely charged surfactants as a function of surfactant concentration.[208] They found that the emission quantum yield of the CPEs first increased at low surfactant concentrations, decreased at intermediate concentrations, and then increased again at concentrations approaching the CMC upon addition of the oppositely charged surfactant. The changes in the quantum yield were correlated to changes in the aggregate size using light scattering measurements. The decrease in the quantum yield was associated with the formation of large polymer/surfactant aggregations and the recovery at the CMC was concomitant with the formation of spherical/cylindrical surfactant micelles that templated the extension of the CPE chains (see Figure 1.22B). The authors concluded that the effect was driven by a combination of hydrophobic and electrostatic interactions along with the propensity of the surfactant to form micelles, where some amount of each factor is required. Overall, the significance of these investigations is that the photophysical and aggregation properties of CPEs can be tuned by the appropriate application of common surfactant agents,

providing another dimension to achieve the desired properties outside of chemical modification of the polymer chain. The ability of the surfactant to template the self-assembly of CPEs into structures with long-range order provides interesting opportunities in the context of improving biosensors and controlling energy migration within these materials.

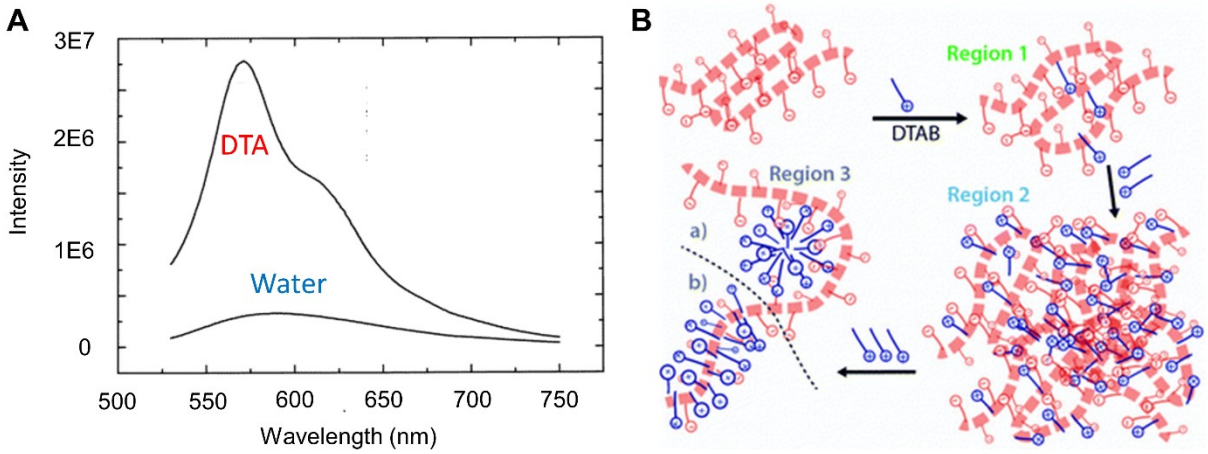

Figure 1.22. Interaction of CPEs with surfactants. (A) Emission spectrum of MPS-PPV in water or mixed with the cationic surfactant DTA in a 10:1 surfactant:PRU ratio. Emission enhancement and the appearance of vibronic structure are evidence for DTAB inducing increased order in the MPS-PPV chain. Adapted with permission from reference [185] (Copyright, 2000, The American Chemical Society). (B) Scheme showing different stages of complex formation between a polyanion and the cationic surfactant DTAB. At low concentrations, DTAB breaks interchain interactions between the folded polyanion. At intermediate concentrations, DTAB induces cross linking of the CPE chains and large aggregates form. At high concentrations, DTAB templates the CPE by forming spherical (a, top) or cylindrical (b, bottom) micelles. Adapted with permission from reference [208] (Copyright, 2013, Royal Society of Chemistry).

1.5.3 Complexation with lipid membranes

Given the readiness with which CPEs interact with surfactants in aqueous solution, researchers have also explored their interaction with lipids, biomolecules with amphiphilic properties. The spontaneous insertion of CPEs into lipid bilayer membranes has led to several interesting applications, most notably the development of biosensing platforms,[45, 53, 209-212] biocidal agents based on the disruption of bacterial membranes by CPE insertion,[158, 213-217] as well as the use of CPEs to enhance electrical conductivity in microbial fuel cells.[218-224] In this section, however, the main focus will be on highlighting studies that show the fundamental relationship between CPE/membrane morphology and its effect on CPE photophysics. In general, the

association of CPEs with lipid membranes has been shown to lead to increased emission quantum yields and blue shifted emission spectra,[90, 183, 192, 225-229] similar to the changes induced by complexation with surfactants. Emission enhancement and blue-shifted emission are both signatures of polymer deaggregation that is facilitated *via* interaction with the membrane. The association of CPEs with the membrane has also been confirmed by the observation of FRET from the CPE donor to a membrane-bound acceptor.[70, 90, 225, 227-228]

Polymers with various backbone structures including PPVs,[70, 90, 192, 230] PPEs,[183, 226, 228] polythiophenes,[225, 229, 231-233] and polyfluorenes[227, 234-235] have all been shown to interact with lipid membranes. The effect of factors including lipid charge,[70, 183, 226, 235] polymer chain length,[183, 226] as well as the nature of the lipid headgroup[158, 226] and the polymer sidechains[225, 228, 234] on the interaction have also been explored. In 2008, Ngo *et al*. reported the encapsulation of MPS-PPV inside of 100 nm diameter liposomes formed from the monounsaturated, zwitterionic lipid DOPC, a popular model for mammalian cell membranes.[90] The presence of an unquenchable fraction of polymer emission upon addition of the electron acceptor methyl viologen provided evidence for the encapsulation of the polymer within the liposomes. An increase in the fluorescence quantum yield as well as a blue shift in the emission spectrum was noted, suggesting that the encapsulated polymer was associated with the membrane, thus leading to an extension of the polymer backbone and the observed photophysical properties. The conclusion that the polymer was embedded within the membrane was further corroborated by FRET studies that showed efficient energy transfer between MPS-PPV and the lipophilic energy acceptor 1,1′-dioctadecyl-3,3,3′,3′-tetramethylindodicarbocyanine perchlorate (DiD). A follow-up study published in 2010 showed that the addition of the anionic lipid DOPA to the DOPC liposomes in a 1:3 ratio prevented the association of MPS-PPV with the membrane, presumably because of electrostatic repulsion between the negatively charged membrane and the negatively charged sulfonate side chains of the polymer.[70] In chapter two of this thesis, the interaction between MPS-PPV and liposomes formed from the cationic lipid DOTAP is reported, where DOTAP is shown to be more effective at deaggregating the polymer chains than DOPC, as evidenced by a greater enhancement to the fluorescence quantum yield and the appearance of vibrational structure in the emission spectrum.

The influence of the charge on the lipid headgroup was also investigated by Karam *et al.* in the interaction of lipid membranes with PPE polymers with side chains bearing charged

carboxylate groups (PPE-CO_2).[183] The distinct spectroscopic signatures of PPE-CO_2 aggregates versus single chains were used to determine the extent of interaction with 200 nm diameter liposomes prepared from 1,2-dioleoyl-sn-glycero-3-phosphate (DOPA), 1,2-dioleoyl-sn-glycero-3-phosphocholine (DOPC), and 1,2-dioleoyl-sn-glycero-3-phosphocholine (DOTAP) (anionic, zwitterionic, and cationic lipids, respectively). Titrating liposome solutions with increasing amounts of PPE-CO_2 revealed that while no interaction occurred with anionic DOPA, membrane embedding was observed for zwitterionic DOPC and cationic DOTAP, with DOTAP accommodating a larger amount of polymer than DOPC (Figure 1.23). In addition, shorter polymers (n = 7 PRUs) were found to incorporate more easily than longer polymers (n = 49 PRUs). These results were similar to those reported by Wang *et al*. for the interaction of a cationic PPE with model membranes composed of DOPC or negatively charged *E. coli* total lipid extract.[226] Overall, it was concluded that CPEs bind readily to zwitterionic or oppositely charged membranes, driven by a combination of electrostatic and hydrophobic interactions.

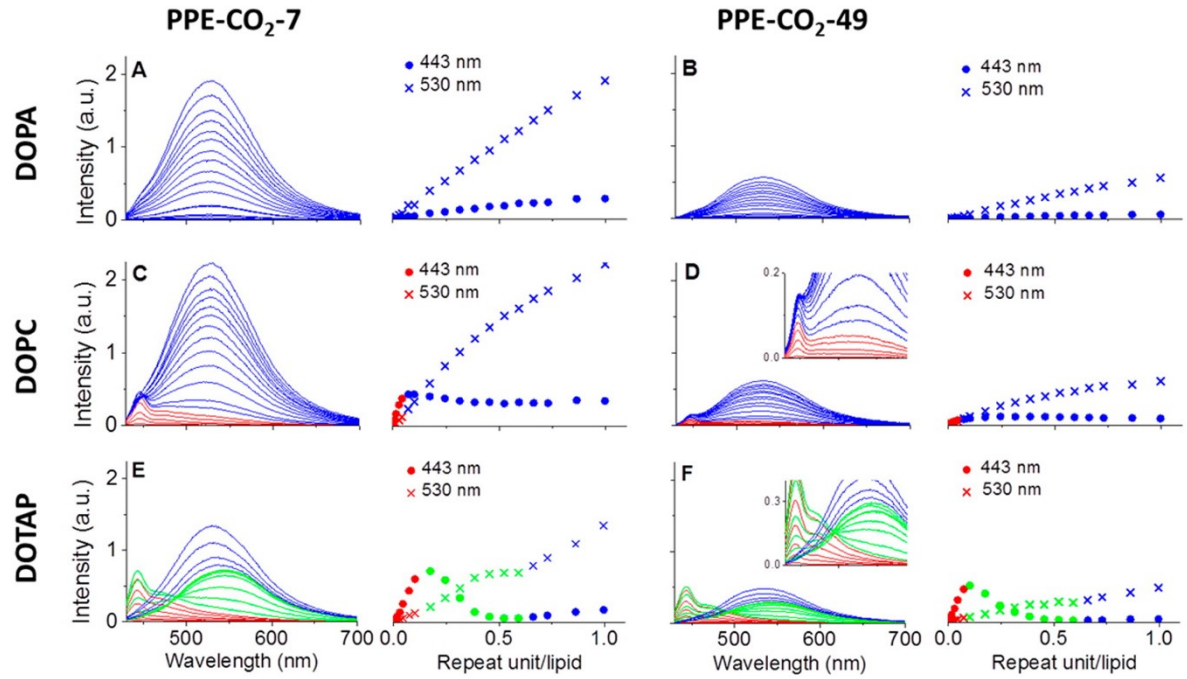

Figure 1.23. Incorporation of PPE-CO_2 into lipid membranes. (A-F) Titration of 1.0×10^{-5} M lipids with increasing amounts of PPE-CO_2-7 and PPE-CO_2-49. The lipid concentration was kept constant, and the polymer repeat unit to lipid ratio was varied from 0.001 to 1. The emission intensity of the polymer after each addition is shown. Also shown is the emission intensity at 443 nm (deaggregated) and 530 nm (aggregated) versus PRU:lipid ratio for all experiments. Left

column: plots obtained with PPE-CO_2-7, Right column: plots obtained with PPE-CO_2-49. The first, second, and third rows show results acquired with DOPA, DOPC, and DOTAP, respectively. Experiments were conducted in 150 mM NaCl and 10 mM HEPES, pH 7.3. The spectra are corrected for liposome scattering. Adapted with permission from reference [183] (Copyright, 2014, The American Chemical Society).

The organization of the lipid/CPE complexes has been shown to depend strongly on the nature of the lipid headgroup. This is largely because the self-assembly of lipid molecules is governed by their shape, or intrinsic curvature, which depends on whether the width of the polar headgroup is smaller, equal to, or larger than the width of the hydrophobic tails. Lipids with zero intrinsic curvature (*i.e.*, cylindrically shaped) tend to form bilayers whereas lipids with positive or negative intrinsic curvature (*i.e.,* wedge shaped) tend to form micelles or inverted phases, respectively (see Figure 1.24A).[236] For example, cationic PPEs have been shown to selectively perturb bacterial membranes over mammalian membrane mimics. Bacterial membranes are enriched with phosphatidylethanolamines (PE) lipids, which have a negative intrinsic curvature. The increased propensity of these lipids to form inverted hexagonal structures leads to the formation of transmembrane pores around the CPE, leading to severe membrane perturbation, leakage of cell contents, and death.[214] In contrast, PPE associated with bilayers of phosphatidylcholine (PC) lipids, which have zero intrinsic curvature, is believed to adsorb as a carpet on the bilayer (Figure 1.24B).[214] Due to their smaller size, oligomers have also been shown by fluorescence polarization experiments to span the bilayer, with the hydrophobic backbone between the hydrophobic interior of the bilayer and the terminal charged side chains associated with the polar head group region (Figure 1.24C).[230]

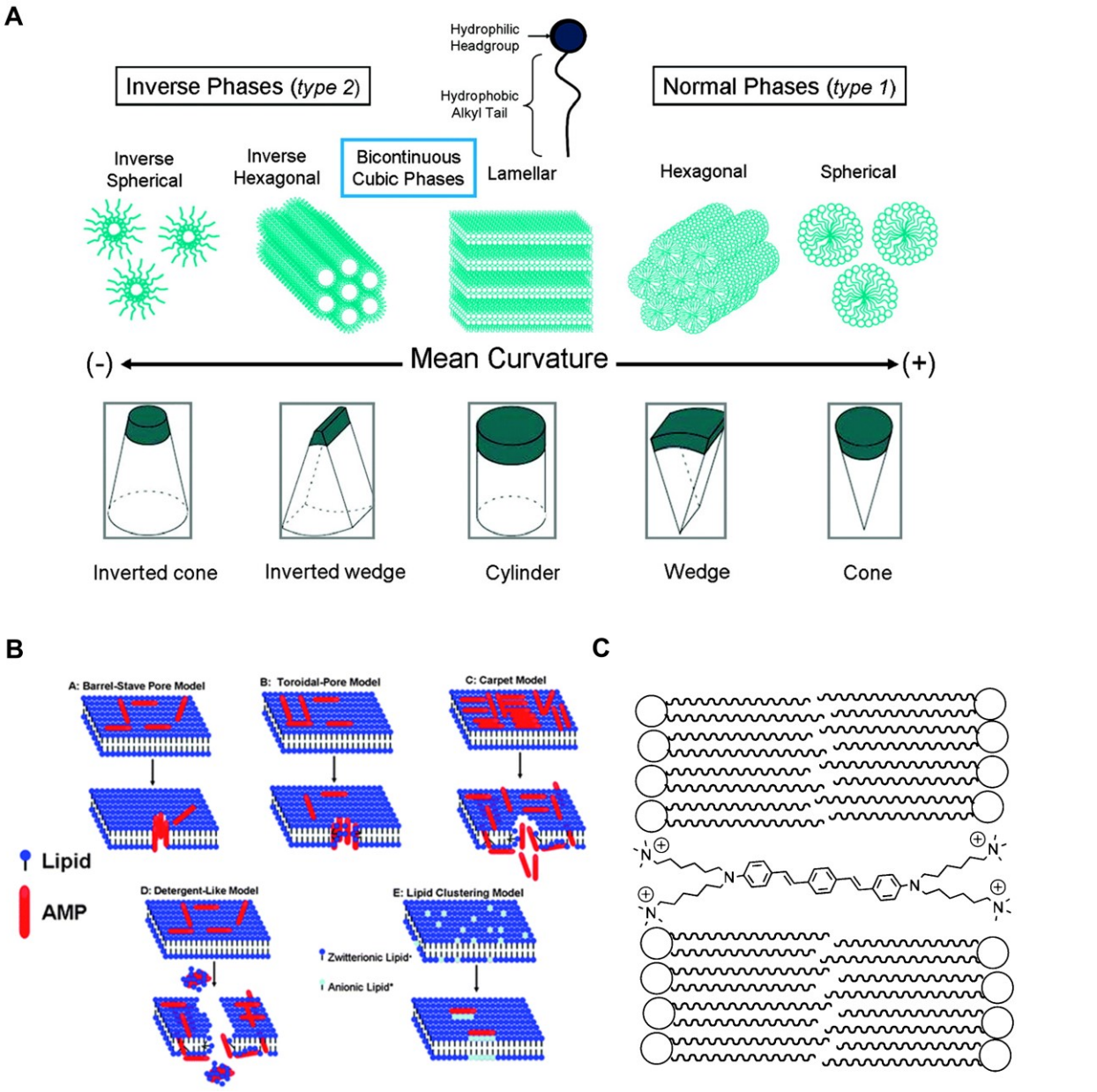

Figure 1.24. Structural understanding of CPE and lipid membrane interactions. (A) Diagram showing the most favourable self-assembly structures for lipid molecules depending on their intrinsic curvature. Adapted with permission from reference [237] (Copyright, 2011, The American Chemical Society). (B) Model showing possible mechanisms by which antimicrobial peptides (AMPs, red) may perturb lipid membranes. CPEs are thought to disrupt membranes *via* similar mechanisms depending on the chemical structure of the polymer and its chain length. Adapted with permission from reference [214] (Copyright, 2012, Royal Society of Chemistry). (C) Diagram illustrating the proposed placement of a poly(phenylene vinylene) oligoelectrolyte within a lipid bilayer. The hydrophobic polymer backbone resides within the hydrophobic region of the membrane while the terminal charged side chains interact with the lipid polar head groups.

Adapted with permission from reference [230] (Copyright, 2010, The American Chemical Society).

Although the fact that CPEs will readily associate with lipid membranes is now well-established, the exact position of the polymer is often not known. Houston *et al*. have recently published a study focused on determining how the localization of polythiophene-based CPEs within bilayers of the zwitterionic lipid DPPC is controlled by the nature of the charged polymer sidechains.[225] CPEs possessing anionic, zwitterionic, and cationic side chains were studied. Although all three polymers demonstrated affinity for the vesicles, they showed varying levels of incorporation and were localized in different regions of the lipid bilayer. FRET experiments to a membrane polarity probe as well as epifluorescence and atomic force microscopy revealed that the cationic CPE formed amorphous aggregates on the vesicle surface, the zwitterionic CPE was embedded inside of the hydrophobic core, and the anionic CPE formed a shell of protruding chains around the surface. DLS experiments showed a significant increase in the hydrodynamic diameter of the vesicles in the presence of the anionic CPE, suggesting that the protruding chains promote vesicle fusion, a phenomenon also noted by Karam *et al*. in the interaction of PPE-CO_2 (n = 49) with DOTAP.[183] The difference in the interaction between the cationic and the anionic CPEs was attributed to the fact that the outmost charge on the zwitterionic head group is a cationic trimethylammonium group, and that this charge is what the polyelectrolyte will first interact with when it encounters the membrane. The preferential localization of an anionic polythiophene within the lipid headgroups has recently been exploited as a probe for membrane phase transitions, since the organization of the headgroups is highly sensitive to the membrane phase, which in turn affects the photophysical properties of the CPE.[229]

1.6 Research goals and scope of thesis

Research on CP materials has now spanned several decades and encompasses quests to invent new structures and understand their fundamental photophysical properties, as well as their implementation in commercially successful devices. As discussed in the previous sections of this chapter, a substantial amount of effort has been made toward untangling the complex photophysics of CPs. Using a combination of ensemble and SMS techniques, researchers have determined the relationship between single chain conformation and energy transfer efficiency, which ultimately dictates the emissive properties of the polymer. Studies on CP films have likewise shown that the

film morphology is intimately related to energy transfer efficiency. Many of the lessons learned from studies on CP photophysics are also applicable to CPEs, where additional factors such as the nature of charged groups and counter ions, ionic strength, and complexation with surfactants or lipid membranes can also impact their conformation, and thus their photophysical properties. This thesis is focused specifically on the interaction between CPEs and oppositely charged lipid membranes. Fundamental knowledge of how CPE/membrane constructs behave at both the structural and the photophysical level is exploited to develop applications in diverse areas, including membrane biophysics and solar light harvesting systems.

In chapter 2, the interaction between the conjugated polyanion MPS-PPV and liposomes prepared from the cationic lipid DOTAP is exploited to observe membrane dynamics at the single particle level. MPS-PPV adsorbed onto 100 nm diameter SiO_2 NPs is observed to spontaneously embed within the DOTAP membrane, leading to a dramatic emission enhancement of *ca.* 25-fold due to the membrane-induced deaggregation of the polymer backbone. A combination of cryo transmission electron microscopy (cryo TEM) and ensemble fluorescence quenching studies reveal that the incoming liposomes adsorb and then deform to match the curvature of the CPE coated SiO_2 nanoparticle surface. By monitoring the photophysical changes occurring in MPS-PPV, the dynamics of liposome deformation and polymer deaggregation are followed using ensemble and SMS fluorescence techniques. Two-color TIRF microscopy is used to monitor the emission intensity of the MPS-PPV coated NPs adsorbed on the surface of a glass coverslip in one channel and the arrival of dye-labeled liposomes flowing in solution in the other channel. The colocalization of liposomes with MPS-PPV coated NPs and the dynamics of the ensuing deaggregation of the polymer backbone is thus recorded for hundreds of individual liposomes interacting with NPs. The effect of variables including the liposome concentration and size on the magnitude and timescale of the MPS-PPV emission enhancement is reported.

Chapter 3 explores the interaction of CPEs with lipid membranes toward an entirely different application: the development of artificial light harvesting systems. Several previous studies suggested that increasing the order of conjugated polymer materials improves the efficiency of energy transfer, which motivated this study on the use of lipid membranes as a template to control the arrangement of light harvesting polymers to facilitate the efficient funneling of absorbed light energy to a reaction centre, or trap. The addition of PPE-CO_2 polyanions with

an average of 7 PRUs to aqueous solutions of 200 nm diameter DOTAP liposomes resuls in their spontaneous incorporation within the lipid membrane, where fluorescence spectroscopy reveals that the embedded polymers exists as deaggregated, or molecularly dissolved chains. Importantly, it is determined that the membrane can accommodate a large number of polymers before self-quenching of the polymer emission occurred and that the embedded polymers does not perturb the lipid bilayer even when present at a high density. The energy transferred from the light absorbing polymers to FRET and electron acceptors is determined to evaluate the efficiency of the antenna and the role of polymer-polymer homotransfer in energy funneling to the trap.

One of the limiting factors to performing SMS studies on CPEs such as the one reported in chapter 2 of this thesis is the photostability of the polymer itself. In response to this challenge, chapters 4 and 5 present fundamental studies of the photostability PPE-CO_2 polymers under SMS imaging conditions and evaluates several solution additives on their photostabilizing ability. PPE-CO_2-49 is adsorbed onto surface-modified SiO_2 NPs *via* electrostatic interactions or embedded in the membrane of DOTAP liposomes and the polymer coated NPs/liposomes are then deposited onto a glass coverslip for TIRF imaging. The initial intensity as well as the total number of photons emitted by the individual NPs under different buffer conditions and two different laser excitation powers is determined. The effect of adding small molecule triplet quenchers/antioxidants to the buffer as well as removing oxygen using an enzymatic oxygen scavenging is assessed. From these studies, anti fading cocktails for improving the photon output of PPE-CO_2-49 in both aqueous and membrane environments are identified.

1.7 References

1. McDonald, R. N.; Campbell, T. W. The Wittig Reaction as a Polymerization Method1a. *J. Am. Chem. Soc.* **1960,** *82*, 4669-4671.

2. McNeill, R.; Siudak, R.; Wardlaw, J.; Weiss, D. Electronic Conduction in Polymers. I. The Chemical Structure of Polypyrrole. *Aust. J. Chem.* **1963,** *16*, 1056-1075.

3. Bolto, B.; Weiss, D. Electronic Conduction in Polymers. II. The Electrochemical Reduction of Polypyrrole at Controlled Potential. *Aust. J. Chem.* **1963,** *16*, 1076-1089.

4. Bolto, B.; McNeill, R.; Weiss, D. Electronic Conduction in Polymers. III. Electronic Properties of Polypyrrole. *Aust. J. Chem.* **1963,** *16*, 1090-1103.

5. De Surville, R.; Jozefowicz, M.; Yu, L. T.; Pepichon, J.; Buvet, R. Electrochemical Chains Using Protolytic Organic Semiconductors. *Electrochim. Acta* **1968,** *13*, 1451-1458.

6. Letheby, H. Xxix.-on the Production of a Blue Substance by the Electrolysis of Sulphate of Aniline. *J. Chem. Soc.* **1862,** *15*, 161-163.

7. MacDiarmid, A. G. "Synthetic Metals": A Novel Role for Organic Polymers (Nobel Lecture). *Angew. Chem. Int. Edit.* **2001,** *40*, 2581-2590.

8. Chiang, C. K.; Fincher, C. R.; Park, Y. W.; Heeger, A. J.; Shirakawa, H.; Louis, E. J.; Gau, S. C.; MacDiarmid, A. G. Electrical Conductivity in Doped Polyacetylene. *Phys. Rev. Lett.* **1977,** *39*, 1098-1101.

9. Yu, G.; Gao, J.; Hummelen, J. C.; Wudl, F.; Heeger, A. J. Polymer Photovoltaic Cells: Enhanced Efficiencies Via a Network of Internal Donor-Acceptor Heterojunctions. *Science* **1995,** *270*, 1789-1791.

10. Halls, J. J. M.; Pichler, K.; Friend, R. H.; Moratti, S. C.; Holmes, A. B. Exciton Diffusion and Dissociation in a Poly(P-Phenylenevinylene)/C_{60} Heterojunction Photovoltaic Cell. *Appl. Phys. Lett.* **1996,** *68*, 3120-3122.

11. Choi, H.; Mai, C.-K.; Kim, H.-B.; Jeong, J.; Song, S.; Bazan, G. C.; Kim, J. Y.; Heeger, A. J. Conjugated Polyelectrolyte Hole Transport Layer for Inverted-Type Perovskite Solar Cells. *Nat. Commun.* **2015,** *6*, 7348.

12. Günes, S.; Neugebauer, H.; Sariciftci, N. S. Conjugated Polymer-Based Organic Solar Cells. *Chem. Rev.* **2007,** *107*, 1324-1338.

13. He, Z.; Zhong, C.; Huang, X.; Wong, W.-Y.; Wu, H.; Chen, L.; Su, S.; Cao, Y. Simultaneous Enhancement of Open-Circuit Voltage, Short-Circuit Current Density, and Fill Factor in Polymer Solar Cells. *Adv. Mater.* **2011,** *23*, 4636-4643.

14. He, Z.; Zhong, C.; Su, S.; Xu, M.; Wu, H.; Cao, Y. Enhanced Power-Conversion Efficiency in Polymer Solar Cells Using an Inverted Device Structure. *Nat Photon* **2012,** *6*, 591-595.

15. Hu, S.; Zhong, C.; Wu, H.; Cao, Y. Organic Optoelectronic Devices Containing Water/Alcohol-Soluble Conjugated Polymers and Conjugated Polyelectrolytes*. In *Conjugated Polyelectrolytes*; Wiley-VCH Verlag GmbH & Co. KGaA: 2012; pp 345-388.

16. Kesters, J.; Govaerts, S.; Pirotte, G.; Drijkoningen, J.; Chevrier, M.; Van den Brande, N.; Liu, X.; Fahlman, M.; Van Mele, B.; Lutsen, L.; Vanderzande, D.; Manca, J.; Clément, S.; Von Hauff, E.; Maes, W. High-Permittivity Conjugated Polyelectrolyte Interlayers for High-Performance Bulk Heterojunction Organic Solar Cells. *ACS Appl. Mater. Interfaces* **2016,** *8*, 6309-6314.

17. Seo, J. H.; Gutacker, A.; Sun, Y.; Wu, H.; Huang, F.; Cao, Y.; Scherf, U.; Heeger, A. J.; Bazan, G. C. Improved High-Efficiency Organic Solar Cells Via Incorporation of a Conjugated Polyelectrolyte Interlayer. *J. Am. Chem. Soc.* **2011,** *133*, 8416-8419.

18. Mwaura, J. K.; Pinto, M. R.; Witker, D.; Ananthakrishnan, N.; Schanze, K. S.; Reynolds, J. R. Photovoltaic Cells Based on Sequentially Adsorbed Multilayers of Conjugated Poly(P-Phenylene Ethynylene)S and a Water-Soluble Fullerene Derivative. *Langmuir* **2005,** *21*, 10119-10126.

19. Mayer, A. C.; Scully, S. R.; Hardin, B. E.; Rowell, M. W.; McGehee, M. D. Polymer-Based Solar Cells. *Mater. Today* **2007,** *10*, 28-33.

20. Li, G.; Shrotriya, V.; Huang, J.; Yao, Y.; Moriarty, T.; Emery, K.; Yang, Y. High-Efficiency Solution Processable Polymer Photovoltaic Cells by Self-Organization of Polymer Blends. *Nat. Mater.* **2005,** *4*, 864-868.

21. Polymer Photovoltaics - Materials, Physics, and Device Engineering. Huang, F.,Yip, H.-L.,Cao, Y., Eds. Royal Society of Chemistry: Cambridge, 2015.

22. Cai, W.; Gong, X.; Cao, Y. Polymer Solar Cells: Recent Development and Possible Routes for Improvement in the Performance. *Sol. Energy Mater. Sol. Cells* **2010,** *94*, 114-127.

23. Krebs, F. C. Fabrication and Processing of Polymer Solar Cells: A Review of Printing and Coating Techniques. *Sol. Energy Mater. Sol. Cells* **2009,** *93*, 394-412.

24. Li, G.; Zhu, R.; Yang, Y. Polymer Solar Cells. *Nat Photon* **2012,** *6*, 153-161.

25. Zhao, W.; Qian, D.; Zhang, S.; Li, S.; Inganäs, O.; Gao, F.; Hou, J. Fullerene-Free Polymer Solar Cells with over 11% Efficiency and Excellent Thermal Stability. *Adv. Mater.* **2016,** *28*, 4734-4739.

26. Zheng, Z.; Zhang, S.; Zhang, J.; Qin, Y.; Li, W.; Yu, R.; Wei, Z.; Hou, J. Over 11% Efficiency in Tandem Polymer Solar Cells Featured by a Low-Band-Gap Polymer with Fine-Tuned Properties. *Adv. Mater.* **2016,** *28*, 5133-5138.

27. Lu, L.; Zheng, T.; Wu, Q.; Schneider, A. M.; Zhao, D.; Yu, L. Recent Advances in Bulk Heterojunction Polymer Solar Cells. *Chem. Rev.* **2015,** *115*, 12666-12731.

28. Yan, J.; Saunders, B. R. Third-Generation Solar Cells: A Review and Comparison of Polymer:Fullerene, Hybrid Polymer and Perovskite Solar Cells. *RSC Advances* **2014,** *4*, 43286-43314.

29. Park, S. H.; Roy, A.; Beaupre, S.; Cho, S.; Coates, N.; Moon, J. S.; Moses, D.; Leclerc, M.; Lee, K.; Heeger, A. J. Bulk Heterojunction Solar Cells with Internal Quantum Efficiency Approaching 100%. *Nat Photon* **2009,** *3*, 297-302.

30. Kim, J. Y.; Lee, K.; Coates, N. E.; Moses, D.; Nguyen, T.-Q.; Dante, M.; Heeger, A. J. Efficient Tandem Polymer Solar Cells Fabricated by All-Solution Processing. *Science* **2007,** *317*, 222.

31. Burroughes, J. H.; Bradley, D. D. C.; Brown, A. R.; Marks, R. N.; Mackay, K.; Friend, R. H.; Burns, P. L.; Holmes, A. B. Light-Emitting Diodes Based on Conjugated Polymers. *Nature* **1990,** *347*, 539-541.

32. Friend, R. H.; Gymer, R. W.; Holmes, A. B.; Burroughes, J. H.; Marks, R. N.; Taliani, C.; Bradley, D. D. C.; Santos, D. A. D.; Bredas, J. L.; Logdlund, M.; Salaneck, W. R. Electroluminescence in Conjugated Polymers. *Nature* **1999,** *397*, 121-128.

33. Zheng, H.; Zheng, Y.; Liu, N.; Ai, N.; Wang, Q.; Wu, S.; Zhou, J.; Hu, D.; Yu, S.; Han, S.; Xu, W.; Luo, C.; Meng, Y.; Jiang, Z.; Chen, Y.; Li, D.; Huang, F.; Wang, J.; Peng, J.; Cao, Y. All-Solution Processed Polymer Light-Emitting Diode Displays. *Nat. Commun.* **2013,** *4*, 1971.

34. Gustafsson, G.; Cao, Y.; Treacy, G. M.; Klavetter, F.; Colaneri, N.; Heeger, A. J. Flexible Light-Emitting Diodes Made from Soluble Conducting Polymers. *Nature* **1992,** *357*, 477-479.

35. Gross, M.; Muller, D. C.; Nothofer, H.-G.; Scherf, U.; Neher, D.; Brauchle, C.; Meerholz, K. Improving the Performance of Doped [Pi]-Conjugated Polymers for Use in Organic Light-Emitting Diodes. *Nature* **2000,** *405*, 661-665.

36. Yokota, T.; Zalar, P.; Kaltenbrunner, M.; Jinno, H.; Matsuhisa, N.; Kitanosako, H.; Tachibana, Y.; Yukita, W.; Koizumi, M.; Someya, T. Ultraflexible Organic Photonic Skin. *Science Advances* **2016,** *2*.

37. Zhou, Q.; Swager, T. M. Method for Enhancing the Sensitivity of Fluorescent Chemosensors: Energy Migration in Conjugated Polymers. *J. Am. Chem. Soc.* **1995,** *117*, 7017-7018.

38. Heeger, P. S.; Heeger, A. J. Making Sense of Polymer-Based Biosensors. *Proc. Natl. Acad. Sci. U. S. A.* **1999,** *96*, 12219-12221.

39. Jiang, H.; Taranekar, P.; Reynolds, J. R.; Schanze, K. S. Conjugated Polyelectrolytes: Synthesis, Photophysics, and Applications. *Angew. Chem. Int. Edit.* **2009,** *48*, 4300-4316.

40. Lahiff, E.; Lynam, C.; Gilmartin, N.; O'Kennedy, R.; Diamond, D. The Increasing Importance of Carbon Nanotubes and Nanostructured Conducting Polymers in Biosensors. *Anal. Bioanal. Chem.* **2010,** *398*, 1575-1589.

41. Liang, J.; Li, K.; Liu, B. Visual Sensing with Conjugated Polyelectrolytes. *Chem. Sci.* **2013,** *4*, 1377-1394.

42. Liu, Y.; Ogawa, K.; Schanze, K. S. Conjugated Polyelectrolytes as Fluorescent Sensors. *J. Photochem. Photobiol., C* **2009,** *10*, 173-190.

43. Wang, D.; Gong, X.; Heeger, P. S.; Rininsland, F.; Bazan, G. C.; Heeger, A. J. Biosensors from Conjugated Polyelectrolyte Complexes. *Proc. Natl. Acad. Sci. U. S. A.* **2002,** *99*, 49-53.

44. Zeineldin, R.; Piyasena, M. E.; Bergstedt, T. S.; Sklar, L. A.; Whitten, D.; Lopez, G. P. Superquenching as a Detector for Microsphere-Based Flow Cytometric Assays. *Cytometry A* **2006,** *69A*, 335-341.

45. Bajaj, A.; Miranda, O. R.; Kim, I.-B.; Phillips, R. L.; Jerry, D. J.; Bunz, U. H. F.; Rotello, V. M. Detection and Differentiation of Normal, Cancerous, and Metastatic Cells Using Nanoparticle-Polymer Sensor Arrays. *Proc. Natl. Acad. Sci. U. S. A.* **2009,** *106*, 10912-10916.

46. Gaylord, B. S.; Massie, M. R.; Feinstein, S. C.; Bazan, G. C. Snp Detection Using Peptide Nucleic Acid Probes and Conjugated Polymers: Applications in Neurodegenerative Disease Identification. *Proc. Natl. Acad. Sci. U. S. A.* **2005,** *102*, 34-39.

47. Wosnick, J. H.; Liao, J. H.; Swager, T. M. Layer-by-Layer Poly(Phenylene Ethynylene) Films on Silica Microspheres for Enhanced Sensory Amplification. *Macromolecules* **2005,** *38*, 9287-9290.

48. Chen, L.; McBranch, D. W.; Wang, H.-L.; Helgeson, R.; Wudl, F.; Whitten, D. G. Highly Sensitive Biological and Chemical Sensors Based on Reversible Fluorescence Quenching in a Conjugated Polymer. *Proc. Natl. Acad. Sci. U. S. A.* **1999,** *96*, 12287-12292.

49. McQuade, D. T.; Hegedus, A. H.; Swager, T. M. Signal Amplification of a "Turn-on" Sensor: Harvesting the Light Captured by a Conjugated Polymer. *J. Am. Chem. Soc.* **2000,** *122*, 12389-12390.

50. Brouard, D.; Viger, M. L.; Bracamonte, A. G.; Boudreau, D. Label-Free Biosensing Based on Multilayer Fluorescent Nanocomposites and a Cationic Polymeric Transducer. *ACS Nano* **2011,** *5*, 1888-1896.

51. Wu, D.; Yang, J.; Feng, F.; Schanze, K. S. Sensing Via Quenching of Conjugated Polyelectrolyte Fluorescence. In *Conjugated Polyelectrolytes*; Wiley-VCH Verlag GmbH & Co. KGaA: 2012; pp 169-200.

52. Lemieux, É. J.; Leclerc, M. Sensing Via Conformational Changes of Conjugated Polythiophenes. In *Conjugated Polyelectrolytes*; Wiley-VCH Verlag GmbH & Co. KGaA: 2012; pp 231-261.

53. Ngo, A. T.; Karam, P.; Cosa, G. Conjugated Polyelectrolyte-Lipid Interactions: Opportunities in Biosensing. *Pure Appl. Chem.* **2011,** *83*, 43-55.

54. Toal, S. J.; Trogler, W. C. Polymer Sensors for Nitroaromatic Explosives Detection. *J. Mater. Chem.* **2006,** *16*, 2871-2883.

55. Lange, U.; Roznyatovskaya, N. V.; Mirsky, V. M. Conducting Polymers in Chemical Sensors and Arrays. *Anal. Chim. Acta* **2008,** *614*, 1-26.

56. Alvarez, A.; Costa-Fernández, J. M.; Pereiro, R.; Sanz-Medel, A.; Salinas-Castillo, A. Fluorescent Conjugated Polymers for Chemical and Biochemical Sensing. *TrAC Trends in Analytical Chemistry* **2011,** *30*, 1513-1525.

57. Huser, T.; Yan, M.; Rothberg, L. J. Single Chain Spectroscopy of Conformational Dependence of Conjugated Polymer Photophysics. *Proc. Natl. Acad. Sci. U. S. A.* **2000,** *97*, 11187-11191.

58. Huser, T.; Yan, M. Solvent-Related Conformational Changes and Aggregation of Conjugated Polymers Studied by Single Molecule Fluorescence Spectroscopy. *J. Photochem. Photobiol., A* **2001,** *144*, 43-51.

59. White, J. D.; Hsu, J. H.; Fann, W. S.; Yang, S.-C.; Pern, G. Y.; Chen, S. A. Deduction of the Conformation of Short Chain Luminescent Conjugated Polymers from Single Molecule Photophysics. *Chem. Phys. Lett.* **2001,** *338*, 263-268.

60. Schwartz, B. J. Conjugated Polymers as Molecular Materials: How Chain Conformation and Film Morphology Influence Energy Transfer and Interchain Interactions. *Annu. Rev. Phys. Chem.* **2003,** *54*, 141-172.

61. Ebihara, Y.; Vacha, M. Relating Conformation and Photophysics in Single Meh-Ppv Chains. *J. Phys. Chem. B* **2008,** *112*, 12575-12578.

62. Chen, P.-Y.; Rassamesard, A.; Chen, H.-L.; Chen, S.-A. Conformation and Fluorescence Property of Poly(3-Hexylthiophene) Isolated Chains Studied by Single Molecule Spectroscopy: Effects of Solvent Quality and Regioregularity. *Macromolecules* **2013,** *46*, 5657-5663.

63. Kobayashi, H.; Onda, S.; Furumaki, S.; Habuchi, S.; Vacha, M. A Single-Molecule Approach to Conformation and Photophysics of Conjugated Polymers. *Chem. Phys. Lett.* **2012,** *528*, 1-6.

64. Bolinger, J. C.; Traub, M. C.; Brazard, J.; Adachi, T.; Barbara, P. F.; Vanden Bout, D. A. Conformation and Energy Transfer in Single Conjugated Polymers. *Acc. Chem. Res.* **2012,** *45*, 1992-2001.

65. Pace, G.; Friend, R. Optical Processes in Conjugated Polyelectrolytes Dependence on Chain Conformation and Film Morphology. In *Conjugated Polyelectrolytes*; Wiley-VCH Verlag GmbH & Co. KGaA: 2012; pp 389-410.

66. Hu, D.; Yu, J.; Wong, K.; Bagchi, B.; Rossky, P. J.; Barbara, P. F. Collapse of Stiff Conjugated Polymers with Chemical Defects into Ordered, Cylindrical Conformations. *Nature* **2000,** *405*, 1030-1033.

67. Pope, M.; Swenberg, C. E.; Pope, M., Electronic Processes in Organic Crystals and Polymers. Oxford University Press: New York, 1999.

68. Bässler, H.; Schweitzer, B. Site-Selective Fluorescence Spectroscopy of Conjugated Polymers and Oligomers. *Acc. Chem. Res.* **1999,** *32*, 173-182.

69. Dykstra, T. E.; Hennebicq, E.; Beljonne, D.; Gierschner, J.; Claudio, G.; Bittner, E. R.; Knoester, J.; Scholes, G. D. Conformational Disorder and Ultrafast Exciton Relaxation in Ppv-Family Conjugated Polymers. *J. Phys. Chem. B* **2008,** *113*, 656-667.

70. Karam, P.; Ngo, A. T.; Rouiller, I.; Cosa, G. Unraveling Electronic Energy Transfer in Single Conjugated Polyelectrolytes Encapsulated in Lipid Vesicles. *Proc. Natl. Acad. Sci. U. S. A.* **2010,** *107*, 17480-17485.

71. Thiessen, A.; Vogelsang, J.; Adachi, T.; Steiner, F.; Vanden Bout, D.; Lupton, J. M. Unraveling the Chromophoric Disorder of Poly(3-Hexylthiophene). *Proc. Natl. Acad. Sci. U.S.A.* **2013,** *110*, E3550-E3556.

72. Barbara, P. F.; Gesquiere, A. J.; Park, S.-J.; Lee, Y. J. Single-Molecule Spectroscopy of Conjugated Polymers. *Acc. Chem. Res.* **2005,** *38*, 602-610.

73. Lakowicz, J. R., Principles of Fluorescence Spectroscopy. Springer: New York, 2006.

74. Turro, N. J.; Ramamurthy, V.; Scaiano, J. C., Principles of Molecular Photochemistry : An Introduction. University Science Books: Sausalito, Calif., 2009.

75. Sariciftci, N. S., *Primary Photoexcitations in Conjugated Polymers Molecular Exciton Versus Semiconductor Band Model*. 1 ed.; World Scientific Publishing Co.: Singapore, 1997.

76. Heeger, A. J.; Kivelson, S.; Schrieffer, J. R.; Su, W. P. Solitons in Conducting Polymers. *Reviews of Modern Physics* **1988,** *60*, 781-850.

77. Lauchlan, L.; Etemad, S.; Chung, T. C.; Heeger, A. J.; MacDiarmid, A. G. Photoexcitations in Polyacetylene. *Phys. Rev. B* **1981,** *24*, 3701-3711.

78. Shacklette, L. W.; Chance, R. R.; Ivory, D. M.; Miller, G. G.; Baughman, R. H. Electrical and Optical Properties of Highly Conducting Charge-Transfer Complexes of Poly(p-Phenylene). *Synth. Met.* **1980,** *1*, 307-320.

79. Brédas, J. L.; Chance, R. R.; Silbey, R. Comparative Theoretical Study of the Doping of Conjugated Polymers: Polarons in Polyacetylene and Polyparaphenylene. *Phys. Rev. B* **1982,** *26*, 5843-5854.

80. Keiji Kanazawa, K.; Diaz, A. F.; Gill, W. D.; Grant, P. M.; Street, G. B.; Piero Gardini, G.; Kwak, J. F. Polypyrrole: An Electrochemically Synthesized Conducting Organic Polymer. *Synth. Met.* **1980,** *1*, 329-336.

81. Bradley, D. D. C.; Evans, G. P.; Friend, R. H. Characterisation of Poly (Phenylenevinylene) by Infrared and Optical Absorption. *Synth. Met.* **1987,** *17*, 651-656.

82. Rauscher, U.; Schutz, L.; Greiner, A.; Bassler, H. Site-Selective Spectroscopy of Matrix-Isolated Conjugated Polymers. *J. Phys.: Condens. Matter* **1989,** *1*, 9751.

83. Rauscher, U.; Bässler, H.; Bradley, D. D. C.; Hennecke, M. Exciton Versus Band Description of the Absorption and Luminescence Spectra in Poly(\Textit{P} -Phenylenevinylene). *Phys. Rev. B* **1990,** *42*, 9830-9836.

84. Bässler, H.; Gailberger, M.; Mahrt, R. F.; Oberski, J. M.; Weiser, G. Exciton Versus Band Description of the Absorption, Luminescence and Electro-Absorption of Poly(Phenylphenylenevinylene) and Poly(Dodecylthiophene). *Synth. Met.* **1992,** *49*, 341-352.

85. Harris, D. C.; Bertolucci, M. D., Symmetry and Spectroscopy : An Introduction to Vibrational and Electronic Spectroscopy. Dover Publications: New York, 1989.

86. Breuer, G. M.; Lee, E. K. C. Fluorescence Quenching by Singlet Energy Transfer. Role of Dipole-Dipole and Exchange Mechanisms. *Chem. Phys. Lett.* **1972,** *14*, 407-410.

87. Shimizu, Y.; Azumi, T. Mechanism of External Heavy Atom Effect on Intersystem Crossing in Fluid Solutions. Analysis Based on Fluorescence Decay Data. *J. Phys. Chem.* **1982,** *86*, 22-26.

88. Rehm, D.; Weller, A. Kinetics of Fluorescence Quenching by Electron and H-Atom Transfer. *Isr. J. Chem.* **1970,** *8*, 259-271.

89. Chen, L.; McBranch, D.; Wang, R.; Whitten, D. Surfactant-Induced Modification of Quenching of Conjugated Polymer Fluorescence by Electron Acceptors: Applications for Chemical Sensing. *Chem. Phys. Lett.* **2000,** *330*, 27-33.

90. Ngo, A. T.; Karam, P.; Fuller, E.; Burger, M.; Cosa, G. Liposome Encapsulation of Conjugated Polyelectrolytes: Toward a Liposome Beacon. *J. Am. Chem. Soc.* **2008,** *130*, 457-459.

91. Lee, L. Y. C.; Hurst, J. K.; Politi, M.; Kurihara, K.; Fendler, J. H. Photoinduced Diffusion of Methyl Viologen across Anionic Surfactant Vesicle Bilayers. *J. Am. Chem. Soc.* **1983,** *105*, 370-373.

92. Tan, C.; Atas, E.; Müller, J. G.; Pinto, M. R.; Kleiman, V. D.; Schanze, K. S. Amplified Quenching of a Conjugated Polyelectrolyte by Cyanine Dyes. *J. Am. Chem. Soc.* **2004,** *126*, 13685-13694.

93. Jørgensen, M.; Norrman, K.; Krebs, F. C. Stability/Degradation of Polymer Solar Cells. *Sol. Energy Mater. Sol. Cells* **2008,** *92*, 686-714.

94. Liu, H.-W.; Ngo, A. T.; Cosa, G. Enhancing the Emissive Properties of Poly(P-Phenylenevinylene)-Conjugated Polyelectrolyte-Coated SiO_2 Nanoparticles. *J. Am. Chem. Soc.* **2011,** *134*, 1648-1652.

95. Dave, R.; Terry, D. S.; Munro, J. B.; Blanchard, S. C. Mitigating Unwanted Photophysical Processes for Improved Single-Molecule Fluorescence Imaging. *Biophys. J.* **2009,** *96*, 2371-2381.

96. Zheng, Q.; Juette, M. F.; Jockusch, S.; Wasserman, M. R.; Zhou, Z.; Altman, R. B.; Blanchard, S. C. Ultra-Stable Organic Fluorophores for Single-Molecule Research. *Chem. Soc. Rev.* **2014,** *43*, 1044-1056.

97. Aitken, C. E.; Marshall, R. A.; Puglisi, J. D. An Oxygen Scavenging System for Improvement of Dye Stability in Single-Molecule Fluorescence Experiments. *Biophys. J.* **2008,** *94*, 1826-1835.

98. Ngo, A. T.; Lau, K. L.; Quesnel, J. S.; Aboukhalil, R.; Cosa, G. Deposition of Anionic Conjugated Poly(Phenylenevinylene) onto Silica Nanoparticles Via Electrostatic Interactions — Assembly and Single-Particle Spectroscopy. *Can. J. Chem.* **2011,** *89*, 385-394.

99. Muller-Meskamp, L.; Fahlteich, J.; Krebs, F. C. Barrier Technology and Applications. In *Stability and Degradation of Organic and Polymer Solar Cells*; John Wiley & Sons, Ltd: 2012; pp 269-329.

100. Vogelsang, J.; Kasper, R.; Steinhauer, C.; Person, B.; Heilemann, M.; Sauer, M.; Tinnefeld, P. A Reducing and Oxidizing System Minimizes Photobleaching and Blinking of Fluorescent Dyes. *Angew. Chem. Int. Edit.* **2008,** *47*, 5465-5469.

101. Glembockyte, V.; Lincoln, R.; Cosa, G. Cy3 Photoprotection Mediated by Ni^{2+} for Extended Single-Molecule Imaging: Old Tricks for New Techniques. *J. Am. Chem. Soc.* **2015,** *137*, 1116-1122.

102. Glembockyte, V.; Lin, J.; Cosa, G. Improving the Photostability of Red- and Green-Emissive Single-Molecule Fluorophores Via Ni^{2+} Mediated Excited Triplet-State Quenching. *J. Phys. Chem. B* **2016,** *120*, 11923-11929.

103. Moerner, W. E.; Kador, L. Optical Detection and Spectroscopy of Single Molecules in a Solid. *Phys. Rev. Lett.* **1989,** *62*, 2535-2538.

104. Orrit, M.; Ha, T.; Sandoghdar, V. Single-Molecule Optical Spectroscopy. *Chem. Soc. Rev.* **2014,** *43*, 973-976.

105. Methods of Single-Molecule Fluorescence Spectroscopy and Microscopy. *Rev. Sci. Instrum.* **2003,** *74*, 3597-3619.

106. Chen, P.; Zhou, X.; Andoy, N. M.; Han, K.-S.; Choudhary, E.; Zou, N.; Chen, G.; Shen, H. Spatiotemporal Catalytic Dynamics within Single Nanocatalysts Revealed by Single-Molecule Microscopy. *Chem. Soc. Rev.* **2014,** *43*, 1107-1117.

107. Stratmann, S. A.; van Oijen, A. M. DNA Replication at the Single-Molecule Level. *Chem. Soc. Rev.* **2014,** *43*, 1201-1220.

108. Janssen, K. P. F.; De Cremer, G.; Neely, R. K.; Kubarev, A. V.; Van Loon, J.; Martens, J. A.; De Vos, D. E.; Roeffaers, M. B. J.; Hofkens, J. Single Molecule Methods for the Study of Catalysis: From Enzymes to Heterogeneous Catalysts. *Chem. Soc. Rev.* **2014,** *43*, 990-1006.

109. Lu, H. P.; Xun, L.; Xie, X. S. Single-Molecule Enzymatic Dynamics. *Science* **1998,** *282*, 1877.

110. Min, W.; English, B. P.; Luo, G.; Cherayil, B. J.; Kou, S. C.; Xie, X. S. Fluctuating Enzymes: Lessons from Single-Molecule Studies. *Acc. Chem. Res.* **2005,** *38*, 923-931.

111. Juette, M. F.; Terry, D. S.; Wasserman, M. R.; Altman, R. B.; Zhou, Z.; Zhao, H.; Blanchard, S. C. Single-Molecule Imaging of Non-Equilibrium Molecular Ensembles on the Millisecond Timescale. *Nat Meth* **2016,** *13*, 341-344.

112. Roy, R.; Hohng, S.; Ha, T. A Practical Guide to Single-Molecule Fret. *Nat. Methods* **2008,** *5*, 507-516.

113. Super-Resolution Fluorescence Microscopy. *Annu. Rev. Biochem.* **2009,** *78*, 993-1016.

114. Gahlmann, A.; Moerner, W. E. Exploring Bacterial Cell Biology with Single-Molecule Tracking and Super-Resolution Imaging. *Nat Rev Micro* **2014,** *12*, 9-22.

115. Hu, Z.; Adachi, T.; Haws, R.; Shuang, B.; Ono, R. J.; Bielawski, C. W.; Landes, C. F.; Rossky, P. J.; Vanden Bout, D. A. Excitonic Energy Migration in Conjugated Polymers: The Critical Role of Interchain Morphology. *J. Am. Chem. Soc.* **2014,** *136*, 16023-16031.

116. Bout, D. A. V.; Yip, W.-T.; Hu, D.; Fu, D.-K.; Swager, T. M.; Barbara, P. F. Discrete Intensity Jumps and Intramolecular Electronic Energy Transfer in the Spectroscopy of Single Conjugated Polymer Molecules. *Science* **1997,** *277*, 1074-1077.

117. Nguyen, T.-Q.; Martini, I. B.; Liu, J.; Schwartz, B. J. Controlling Interchain Interactions in Conjugated Polymers: The Effects of Chain Morphology on Exciton−Exciton Annihilation and Aggregation in Meh−Ppv Films. *J. Phys. Chem. B* **1999,** *104*, 237-255.

118. Beljonne, D.; Pourtois, G.; Silva, C.; Hennebicq, E.; Herz, L. M.; Friend, R. H.; Scholes, G. D.; Setayesh, S.; Müllen, K.; Brédas, J. L. Interchain Vs. Intrachain Energy Transfer in Acceptor-Capped Conjugated Polymers. *Proc. Natl. Acad. Sci. U.S.A.* **2002,** *99*, 10982-10987.

119. Forster, T. Experimentelle Und Theoretische Untersuchung Des Zwischenmolekuken Ubergangs Von Elektronenanregungsenergie. *Z. Naturforschg* **1949,** *4a*, 321-327.

120. Förster, T. Zwischenmolekulare Energiewanderung Und Fluoreszenz. *Annalen der Physik* **1948,** *437*, 55-75.

121. Gidi, Y.; Götte, M.; Cosa, G. Conformational Changes Spanning Angstroms to Nanometers Via a Combined Protein-Induced Fluorescence Enhancement–Förster Resonance Energy Transfer Method. *J. Phys. Chem. B.* **2017,** *121*, 2039-2048.

122. Hariri, A. A.; Hamblin, G. D.; Gidi, Y.; Sleiman, H. F.; Cosa, G. Stepwise Growth of Surface-Grafted DNA Nanotubes Visualized at the Single-Molecule Level. *Nat Chem* **2015,** *7*, 295-300.

123. Srinivas, G.; Yethiraj, A.; Bagchi, B. Fret by Fet and Dynamics of Polymer Folding. *J. Phys. Chem. B.* **2001,** *105*, 2475-2478.

124. Saccà, B.; Meyer, R.; Feldkamp, U.; Schroeder, H.; Niemeyer, C. M. High-Throughput, Real-Time Monitoring of the Self-Assembly of DNA Nanostructures by Fret Spectroscopy. *Angew. Chem. Int. Edit.* **2008,** *47*, 2135-2137.

125. Loura, L. M. S.; Prieto, M. Fret in Membrane Biophysics: An Overview. *Front. Physiol.* **2011,** *2*, 82.

126. Prevo, B.; Peterman, E. J. G. Forster Resonance Energy Transfer and Kinesin Motor Proteins. *Chem. Soc. Rev.* **2014,** *43*, 1144-1155.

127. Michalet, X.; Weiss, S.; Jäger, M. Single-Molecule Fluorescence Studies of Protein Folding and Conformational Dynamics. *Chem. Rev.* **2006,** *106*, 1785-1813.

128. Beljonne, D.; Curutchet, C.; Scholes, G. D.; Silbey, R. J. Beyond Förster Resonance Energy Transfer in Biological and Nanoscale Systems. *J. Phys. Chem. B.* **2009,** *113*, 6583-6599.

129. Tweet, A. G.; Bellamy, W. D.; Gaines, C. L. J. Fluorescence Quenching and Energy Transfer in Monomolecular Films Containing Chlorophyll. *J. Chem. Phys.* **1964,** *41*, 2068-2077.

130. Fung, B. K.-K.; Stryer, L. Surface Density Determination in Membranes by Fluorescence Energy Transfer. *Biochemistry* **1978,** *17*, 5241-5248.

131. Estep, T. N.; Thompson, T. E. Energy Transfer in Lipid Bilayers. *Biophys. J.* **1979,** *26*, 195-207.

132. Wolber, P. K.; Hudson, B. S. An Analytic Solution to the Förster Energy Transfer Problem in Two Dimensions. *Biophys. J.* **1979,** *28*, 197-210.

133. Dewey, T. G.; Hammes, G. G. Calculation on Fluorescence Resonance Energy Transfer on Surfaces. *Biophys. J.* **1980,** *32*, 1023-1035.

134. Snyder, B.; Freire, E. Fluorescence Energy Transfer in Two Dimensions. A Numeric Solution for Random and Nonrandom Distributions. *Biophys. J.* **1982,** *40*, 137-148.

135. Lakowicz, J., Principles of Fluorescence Spectroscopy. Kluwer Academic/Plenum Publishers: New York, Boston, Dordrecht, London, Moscow, 1999.

136. Loura, L. M.; Fedorov, A.; Prieto, M. Resonance Energy Transfer in a Model System of Membranes: Application to Gel and Liquid Crystalline Phases. *Biophys. J.* **1996,** *71*, 1823-1836.

137. Braslavsky, S. E.; Fron, E.; Rodriguez, H. B.; Roman, E. S.; Scholes, G. D.; Schweitzer, G.; Valeur, B.; Wirz, J. Pitfalls and Limitations in the Practical Use of Forster's Theory of Resonance Energy Transfer. *Photochem. Photobiol. Sci.* **2008,** *7*, 1444-1448.

138. Muñoz-Losa, A.; Curutchet, C.; Krueger, B. P.; Hartsell, L. R.; Mennucci, B. Fretting About Fret: Failure of the Ideal Dipole Approximation. *Biophys. J.* **2009,** *96*, 4779-4788.

139. Wong, K. F.; Bagchi, B.; Rossky, P. J. Distance and Orientation Dependence of Excitation Transfer Rates in Conjugated Systems: Beyond the Förster Theory. *J. Phys. Chem. A* **2004,** *108*, 5752-5763.

140. Wiesenhofer, H.; Beljonne, D.; Scholes, G. D.; Hennebicq, E.; Brédas, J. L.; Zojer, E. Limitations of the Förster Description of Singlet Exciton Migration: The Illustrative Example of Energy Transfer to Ketonic Defects in Ladder-Type Poly(Para-Phenylenes). *Adv. Funct. Mater.* **2005,** *15*, 155-160.

141. Lemmer, U.; Mahrt, R. F.; Wada, Y.; Greiner, A.; Bässler, H.; Göbel, E. O. Picosecond Hopping Relaxation in Conjugated Polymers. *Chem. Phys. Lett.* **1993,** *209*, 243-246.

142. Kersting, R.; Lemmer, U.; Mahrt, R. F.; Leo, K.; Kurz, H.; Bässler, H.; Göbel, E. O. Femtosecond Energy Relaxation in Pi-Conjugated Polymers. *Phys. Rev. Lett.* **1993,** *70*, 3820-3823.

143. Hayes, G. R.; Samuel, I. D. W.; Phillips, R. T. Exciton Dynamics in Electroluminescent Polymers Studied by Femtosecond Time-Resolved Photoluminescence Spectroscopy. *Phys. Rev. B* **1995,** *52*, R11569-R11572.

144. Warmuth, C.; Tortschanoff, A.; Brunner, K.; Mollay, B.; Kauffmann, H. F. Excitonic Fs-Luminescence Rise in Poly(Phenylenevinylene), Ppv. *J. Lumin.* **1998,** *76*, 498-501.

145. Harrison, N. T.; Baigent, D. R.; Samuel, I. D. W.; Friend, R. H.; Grimsdale, A. C.; Moratti, S. C.; Holmes, A. B. Site-Selective Fluorescence Studies of Poly(P-Phenylene Vinylene) and Its Derivatives. *Phys. Rev. B* **1996,** *53*, 15815-15822.

146. Woo, H. S.; Lhost, O.; Graham, S. C.; Bradley, D. D. C.; Friend, R. H.; Quattrocchi, C.; Brédas, J. L.; Schenk, R.; Müllen, K. Optical Spectra and Excitations in Phenylene Vinylene Oligomers. *Synth. Met.* **1993,** *59*, 13-28.

147. Collini, E.; Scholes, G. D. Coherent Intrachain Energy Migration in a Conjugated Polymer at Room Temperature. *Science* **2009,** *323*, 369-373.

148. Nguyen, T.-Q.; Wu, J.; Doan, V.; Schwartz, B. J.; Tolbert, S. H. Control of Energy Transfer in Oriented Conjugated Polymer-Mesoporous Silica Composites. *Science* **2000,** *288*, 652-656.

149. Nguyen, T. Q.; Wu, J.; Tolbert, S. H.; Schwartz, B. J. Control of Energy Transport in Conjugated Polymers Using an Ordered Mesoporous Silica Matrix. *Adv. Mater.* **2001,** *13*, 609-611.

150. Beljonne, D.; Pourtois, G.; Shuai, Z.; Hennebicq, E.; Scholes, G. D.; Brédas, J. L. Energy Transfer in π-Conjugated Polymers: Interchain Vs. Intrachain Processes in Polyindenofluorene. *Synth. Met.* **2003,** *137*, 1369-1371.

151. Heun, S.; Mahrt, R. F.; Greiner, A.; Lemmer, U.; Bassler, H.; Halliday, D. A.; Bradley, D. D. C.; Burn, P. L.; Holmes, A. B. Conformational Effects in Poly(P-Phenylene Vinylene)s Revealed by Low-Temperature Site-Selective Fluorescence. *J. Phys.: Condens. Matter* **1993,** *5*, 247.

152. Rossi, G.; Chance, R. R.; Silbey, R. Conformational Disorder in Conjugated Polymers. *J. Chem. Phys.* **1989,** *90*, 7594-7601.

153. Yan, M.; Rothberg, L. J.; Papadimitrakopoulos, F.; Galvin, M. E.; Miller, T. M. Defect Quenching of Conjugated Polymer Luminescence. *Phys. Rev. Lett.* **1994,** *73*, 744-747.

154. Rothberg, L. J.; Yan, M.; Papadimitrakopoulos, F.; Galvin, M. E.; Kwock, E. W.; Miller, T. M. Photophysics of Phenylenevinylene Polymers. *Synth. Met.* **1996,** *80*, 41-58.

155. Schaller, R. D.; Lee, L. F.; Johnson, J. C.; Haber, L. H.; Saykally, R. J.; Vieceli, J.; Benjamin, I.; Nguyen, T.-Q.; Schwartz, B. J. The Nature of Interchain Excitations in Conjugated Polymers: Spatially-Varying Interfacial Solvatochromism of Annealed Meh-Ppv Films Studied by near-Field Scanning Optical Microscopy (NSOM). *J. Phys. Chem. B.* **2002,** *106*, 9496-9506.

156. Lupton, J. M. Single-Molecule Spectroscopy for Plastic Electronics: Materials Analysis from the Bottom-Up. *Adv. Mater.* **2010,** *22*, 1689-1721.

157. Thomas, S. W.; Joly, G. D.; Swager, T. M. Chemical Sensors Based on Amplifying Fluorescent Conjugated Polymers. *Chem. Rev.* **2007,** *107*, 1339-1386.

158. Wang, Y.; Schanze, K. S.; Chi, E. Y.; Whitten, D. G. When Worlds Collide: Interactions at the Interface between Biological Systems and Synthetic Cationic Conjugated Polyelectrolytes and Oligomers. *Langmuir* **2013,** *29*, 10635-10647.

159. Yu, J.; Hu, D.; Barbara, P. F. Unmasking Electronic Energy Transfer of Conjugated Polymers by Suppression of O_2 Quenching. *Science* **2000,** *289*, 1327-1330.

160. Hu, D.; Yu, J.; Barbara, P. F. Single-Molecule Spectroscopy of the Conjugated Polymer MEH-PPV. *J. Am. Chem. Soc.* **1999,** *121*, 6936-6937.

161. Hu, D.; Yu, J.; Padmanaban, G.; Ramakrishnan, S.; Barbara, P. F. Spatial Confinement of Exciton Transfer and the Role of Conformational Order in Organic Nanoparticles. *Nano Lett.* **2002,** *2*, 1121-1124.

162. de Gennes, P. G., Scaling Concepts in Polymer Physics. Cornell University Press: 1979.

163. Schindler, F.; Lupton, J. M. Single Chromophore Spectroscopy of MEH-PPV: Homing-in on the Elementary Emissive Species in Conjugated Polymers. *ChemPhysChem* **2005,** *6*, 926-934.

164. Feist, F. A.; Basché, T. Fluorescence Excitation and Emission Spectroscopy on Single MEH-PPV Chains at Low Temperature. *J. Phys. Chem. B.* **2008,** *112*, 9700-9708.

165. Feist, F. A.; Zickler, M. F.; Basché, T. Origin of the Red Sites and Energy Transfer Rates in Single Meh-Ppv Chains at Low Temperature. *ChemPhysChem* **2011,** *12*, 1499-1508.

166. Schindler, F.; Lupton, J. M.; Feldmann, J.; Scherf, U. A Universal Picture of Chromophores in Π-Conjugated Polymers Derived from Single-Molecule Spectroscopy. *Proc. Natl. Acad. Sci. U. S. A.* **2004,** *101*, 14695-14700.

167. Sugimoto, T.; Ebihara, Y.; Ogino, K.; Vacha, M. Structure-Dependent Photophysics Studied in Single Molecules of Polythiophene Derivatives. *ChemPhysChem* **2007,** *8*, 1623-1628.

168. Hu, Z.; Adachi, T.; Lee, Y.-G.; Haws, R. T.; Hanson, B.; Ono, R. J.; Bielawski, C. W.; Ganesan, V.; Rossky, P. J.; Vanden Bout, D. A. Effect of the Side-Chain-Distribution Density on the Single-Conjugated-Polymer-Chain Conformation. *ChemPhysChem* **2013,** *14*, 4143-4148.

169. Habuchi, S.; Onda, S.; Vacha, M. Mapping the Emitting Sites within a Single Conjugated Polymer Molecule. *Chem. Commun.* **2009**, 4868-4870.

170. Yu, J.; Wu, C.; Tian, Z.; McNeill, J. Tracking of Single Charge Carriers in a Conjugated Polymer Nanoparticle. *Nano Lett.* **2012,** *12*, 1300-1306.

171. Bolinger, J. C.; Traub, M. C.; Adachi, T.; Barbara, P. F. Ultralong-Range Polaron-Induced Quenching of Excitons in Isolated Conjugated Polymers. *Science* **2011,** *331*, 565-567.

172. Camacho, R.; Tubasum, S.; Southall, J.; Cogdell, R. J.; Sforazzini, G.; Anderson, H. L.; Pullerits, T.; Scheblykin, I. G. Fluorescence Polarization Measures Energy Funneling in Single Light-Harvesting Antennas—Lh2 Vs Conjugated Polymers. *Sci. Rep.* **2015,** *5*, 15080.

173. Hu, Z.; Liu, J.; Simón-Bower, L.; Zhai, L.; Gesquiere, A. J. Influence of Backbone Rigidness on Single Chain Conformation of Thiophene-Based Conjugated Polymers. *J. Phys. Chem. B* **2012,** *117*, 4461-4467.

174. Vogelsang, J.; Adachi, T.; Brazard, J.; Vanden Bout, D. A.; Barbara, P. F. Self-Assembly of Highly Ordered Conjugated Polymer Aggregates with Long-Range Energy Transfer. *Nat. Mater.* **2011,** *10*, 942-946.

175. Vogelsang, J.; Brazard, J.; Adachi, T.; Bolinger, J. C.; Barbara, P. F. Watching the Annealing Process One Polymer Chain at a Time. *Angew. Chem. Int. Edit.* **2011,** *50*, 2257-2261.

176. Michael Green, N. [5] Avidin and Streptavidin. In *Methods Enzymol.*; Meir, W.,Edward, A. B., Eds.; Academic Press: 1990; Vol. Volume 184, pp 51-67.

177. Dalgarno, P. A.; Traina, C. A.; Penedo, J. C.; Bazan, G. C.; Samuel, I. D. W. Solution-Based Single Molecule Imaging of Surface-Immobilized Conjugated Polymers. *J. Am. Chem. Soc.* **2013,** *135*, 7187-7193.

178. Nguyen, T.-Q.; Doan, V.; Schwartz, B. J. Conjugated Polymer Aggregates in Solution: Control of Interchain Interactions. *J. Chem. Phys.* **1999,** *110*, 4068-4078.

179. Yang, J.; Wu, D.; Xie, D.; Feng, F.; Schanze, K. S. Ion-Induced Aggregation of Conjugated Polyelectrolytes Studied by Fluorescence Correlation Spectroscopy. *J. Phys. Chem. B* **2013,** *117*, 16314-16324.

180. Tan, C.; Pinto, M. R.; Schanze, K. S. Photophysics, Aggregation and Amplified Quenching of a Water-Soluble Poly(Phenylene Ethynylene). *Chem. Commun.* **2002**, 446-447.

181. Jiang, H.; Zhao, X.; Schanze, K. S. Amplified Fluorescence Quenching of a Conjugated Polyelectrolyte Mediated by Ca^{2+}. *Langmuir* **2006,** *22*, 5541-5543.

182. Swager, T. M.; Gil, C. J.; Wrighton, M. S. Fluorescence Studies of Poly(P-Phenyleneethynylene)S: The Effect of Anthracene Substitution. *J. Phys. Chem.* **1995,** *99*, 4886-4893.

183. Karam, P.; Hariri, A. A.; Calver, C. F.; Zhao, X.; Schanze, K. S.; Cosa, G. Interaction of Anionic Phenylene Ethynylene Polymers with Lipids: From Membrane Embedding to Liposome Fusion. *Langmuir* **2014,** *30*, 10704-10711.

184. Kim, J.; Swager, T. M. Control of Conformational and Interpolymer Effects in Conjugated Polymers. *Nature* **2001,** *411*, 1030-1034.

185. Chen, L.; Xu, S.; McBranch, D.; Whitten, D. Tuning the Properties of Conjugated Polyelectrolytes through Surfactant Complexation. *J. Am. Chem. Soc.* **2000,** *122*, 9302-9303.

186. Zhao, X.; Jiang, H.; Schanze, K. S. Polymer Chain Length Dependence of Amplified Fluorescence Quenching in Conjugated Polyelectrolytes. *Macromolecules* **2008,** *41*, 3422-3428.

187. Halkyard, C. E.; Rampey, M. E.; Kloppenburg, L.; Studer-Martinez, S. L.; Bunz, U. H. F. Evidence of Aggregate Formation for 2,5-Dialkylpoly(P-Phenyleneethynylenes) in Solution and Thin Films. *Macromolecules* **1998,** *31*, 8655-8659.

188. Feng, F.; Yang, J.; Xie, D.; McCarley, T. D.; Schanze, K. S. Remarkable Photophysics and Amplified Quenching of Conjugated Polyelectrolyte Oligomers. *J. Phys. Chem. Lett.* **2013,** *4*, 1410-1414.

189. Kaur, P.; Yue, H.; Wu, M.; Liu, M.; Treece, J.; Waldeck, D. H.; Xue, C.; Liu, H. Solvation and Aggregation of Polyphenylethynylene Based Anionic Polyelectrolytes in Dilute Solutions†. *J. Phys. Chem. B* **2007,** *111*, 8589-8596.

190. Smith, A.; Shen, C.; Roberts, S.; Helgeson, R.; Schwartz, B. Ionic Strength and Solvent Control over the Physical Structure, Electronic Properties and Superquenching of Conjugated Polyelectrolytes. *Res. Chem. Intermed.* **2007,** *33*, 125-142.

191. Kim, I.-B.; Dunkhorst, A.; Gilbert, J.; Bunz, U. H. F. Sensing of Lead Ions by a Carboxylate-Substituted Ppe: Multivalency Effects. *Macromolecules* **2005,** *38*, 4560-4562.

192. Ngo, A. T.; Cosa, G. Assembly of Zwitterionic Phospholipid/Conjugated Polyelectrolyte Complexes: Structure and Photophysical Properties. *Langmuir* **2009,** *26*, 6746-6754.

193. Pinto, M. R.; Kristal, B. M.; Schanze, K. S. A Water-Soluble Poly(Phenylene Ethynylene) with Pendant Phosphonate Groups. Synthesis, Photophysics, and Layer-by-Layer Self-Assembled Films. *Langmuir* **2003,** *19*, 6523-6533.

194. Fan, Q.-L.; Zhou, Y.; Lu, X.-M.; Hou, X.-Y.; Huang, W. Water-Soluble Cationic Poly(P-Phenyleneethynylene)S (Ppes): Effects of Acidity and Ionic Strength on Optical Behavior. *Macromolecules* **2005,** *38*, 2927-2936.

195. Ji, E.; Whitten, D. G.; Schanze, K. S. Ph-Dependent Optical Properties of a Poly(Phenylene Ethynylene) Conjugated Polyampholyte. *Langmuir* **2010,** *27*, 1565-1568.

196. Lavigne, J. J.; Broughton, D. L.; Wilson, J. N.; Erdogan, B.; Bunz, U. H. F. "Surfactochromic" Conjugated Polymers: Surfactant Effects on Sugar-Substituted Ppes. *Macromolecules* **2003,** *36*, 7409-7412.

197. Hill, E. H.; Sanchez, D.; Evans, D. G.; Whitten, D. G. Structural Basis for Aggregation Mode of Oligo-P-Phenylene Ethynylenes with Ionic Surfactants. *Langmuir* **2013,** *29*, 15732-15737.

198. Stork, M.; Gaylord, B. S.; Heeger, A. J.; Bazan, G. C. Energy Transfer in Mixtures of Water- Soluble Oligomers: Effect of Charge, Aggregation, and Surfactant Complexation. *Adv. Mater.* **2002,** *14*, 361-366.

199. Dalvi-Malhotra, J.; Chen, L. Enhanced Conjugated Polymer Fluorescence Quenching by Dipyridinium-Based Quenchers in the Presence of Surfactant. *J. Phys. Chem. B.* **2005,** *109*, 3873-3878.

200. Dou, W.; Wang, C.; Wang, G.; Ma, Q.; Su, X. Enhance Effect of Surfactants on the Photoluminescence and Photostability of Water-Soluble Poly(Phenylene Ethynylene). *J. Phys. Chem. B* **2008,** *112*, 12681-12685.

201. Burrows, H. D.; Tapia, M. J.; Silva, C. L.; Pais, A. A. C. C.; Fonseca, S. M.; Pina, J.; Seixas de Melo, J.; Wang, Y.; Marques, E. F.; Knaapila, M.; Monkman, A. P.; Garamus, V. M.; Pradhan, S.; Scherf, U. Interplay of Electrostatic and Hydrophobic Effects with Binding of Cationic Gemini Surfactants and a Conjugated Polyanion: Experimental and Molecular Modeling Studies. *J. Phys. Chem. B.* **2007,** *111*, 4401-4410.

202. Evans, R. C.; Knaapila, M.; Willis-Fox, N.; Kraft, M.; Terry, A.; Burrows, H. D.; Scherf, U. Cationic Polythiophene–Surfactant Self-Assembly Complexes: Phase Transitions, Optical Response, and Sensing. *Langmuir* **2012,** *28*, 12348-12356.

203. Costa, T.; de Azevedo, D.; Stewart, B.; Knaapila, M.; Valente, A. J. M.; Kraft, M.; Scherf, U.; Burrows, H. D. Interactions of a Zwitterionic Thiophene-Based Conjugated Polymer with Surfactants. *Polymer Chemistry* **2015,** *6*, 8036-8046.

204. Thünemann, A. F. Nanostructured Dihexadecyldimethylammonium–Poly(1,4-Phenylene-Ethinylene-Carboxylate): An Ionic Complex with Blue Electroluminescence. *Adv. Mater.* **1999,** *11*, 127-130.

205. Thünemann, A. F.; Ruppelt, D. Electroluminescent Polyelectrolyte−Surfactant Complexes. *Langmuir* **2001,** *17*, 5098-5102.

206. Knaapila, M.; Evans, R. C.; Garamus, V. M.; Almásy, L. s.; Székely, N. m. K.; Gutacker, A.; Scherf, U.; Burrows, H. D. Structure and "Surfactochromic" Properties of Conjugated Polyelectrolyte (Cpe): Surfactant Complexes between a Cationic Polythiophene and Sds in Water. *Langmuir* **2010,** *26*, 15634-15643.

207. Costa, T.; Garner, L. E.; Knaapila, M.; Thomas, A. W.; Rogers, S. E.; Bazan, G. C.; Burrows, H. D. Aggregation Properties of P-Phenylene Vinylene Based Conjugated Oligoelectrolytes with Surfactants. *Langmuir* **2013,** *29*, 10047-10058.

208. Heeley, M. E. H.; Gallaher, J. K.; Nguyen, T. L.; Woo, H. Y.; Hodgkiss, J. M. Surfactant Controlled Aggregation of Conjugated Polyelectrolytes. *Chem. Commun.* **2013,** *49*, 4235-4237.

209. Liu, Y.; Ogawa, K.; Schanze, K. S. Conjugated Polyelectrolyte Based Real-Time Fluorescence Assay for Phospholipase C. *Anal. Chem.* **2007,** *80*, 150-158.

210. Bajaj, A.; Miranda, O. R.; Phillips, R.; Kim, I.-B.; Jerry, D. J.; Bunz, U. H. F.; Rotello, V. M. Array-Based Sensing of Normal, Cancerous, and Metastatic Cells Using Conjugated Fluorescent Polymers. *J. Am. Chem. Soc.* **2010,** *132*, 1018-1022.

211. Zhu, C.; Liu, L.; Yang, Q.; Lv, F.; Wang, S. Water-Soluble Conjugated Polymers for Imaging, Diagnosis, and Therapy. *Chem. Rev.* **2012,** *112*, 4687-4735.

212. Zhu, C.; Yang, Q.; Liu, L.; Wang, S. Visual Optical Discrimination and Detection of Microbial Pathogens Based on Diverse Interactions of Conjugated Polyelectrolytes with Cells. *J. Mater. Chem.* **2011,** *21*, 7905-7912.

213. Corbitt, T. S.; Ji, E.; Wang, Y.; Parthasarathy, A.; Wilde, K. N.; Hill, E. H.; Dascier, D.; Canavan, H. E.; Chi, E. Y.; Schanze, K. S.; Whitten, D. G. Conjugated Polyelectrolyte-Based Biocide Applications. In *Conjugated Polyelectrolytes*; Wiley-VCH Verlag GmbH & Co. KGaA: 2012; pp 263-294.

214. Wang, Y.; Chi, E. Y.; Schanze, K. S.; Whitten, D. G. Membrane Activity of Antimicrobial Phenylene Ethynylene Based Polymers and Oligomers. *Soft Matter* **2012,** *8*, 8547-8558.

215. Wang, Y.; Jett, S. D.; Crum, J.; Schanze, K. S.; Chi, E. Y.; Whitten, D. G. Understanding the Dark and Light-Enhanced Bactericidal Action of Cationic Conjugated Polyelectrolytes and Oligomers. *Langmuir* **2012,** *29*, 781-792.

216. Wang, Y.; Corbitt, T. S.; Jett, S. D.; Tang, Y.; Schanze, K. S.; Chi, E. Y.; Whitten, D. G. Direct Visualization of Bactericidal Action of Cationic Conjugated Polyelectrolytes and Oligomers. *Langmuir* **2012,** *28*, 65-70.

217. Yan, H.; Rengert, Z. D.; Thomas, A. W.; Rehermann, C.; Hinks, J.; Bazan, G. C. Influence of Molecular Structure on the Antimicrobial Function of Phenylenevinylene Conjugated Oligoelectrolytes. *Chem. Sci.* **2016,** *7*, 5714-5722.

218. Zhao, C.-e.; Chen, J.; Ding, Y.; Wang, V. B.; Bao, B.; Kjelleberg, S.; Cao, B.; Loo, S. C. J.; Wang, L.; Huang, W.; Zhang, Q. Chemically Functionalized Conjugated Oligoelectrolyte Nanoparticles for Enhancement of Current Generation in Microbial Fuel Cells. *ACS Appl. Mater. Interfaces* **2015,** *7*, 14501-14505.

219. Yan, H.; Catania, C.; Bazan, G. C. Membrane-Intercalating Conjugated Oligoelectrolytes: Impact on Bioelectrochemical Systems. *Adv. Mater.* **2015,** *27*, 2958-2973.

220. Wang, V. B.; Kirchhofer, N. D.; Chen, X.; Tan, M. Y. L.; Sivakumar, K.; Cao, B.; Zhang, Q.; Kjelleberg, S.; Bazan, G. C.; Loo, S. C. J.; Marsili, E. Comparison of Flavins and a Conjugated Oligoelectrolyte in Stimulating Extracellular Electron Transport from Shewanella Oneidensis Mr-1. *Electrochem. Commun.* **2014,** *41*, 55-58.

221. Hinks, J.; Wang, Y.; Poh, W. H.; Donose, B. C.; Thomas, A. W.; Wuertz, S.; Loo, S. C. J.; Bazan, G. C.; Kjelleberg, S.; Mu, Y.; Seviour, T. Modeling Cell Membrane Perturbation by Molecules Designed for Transmembrane Electron Transfer. *Langmuir* **2014,** *30*, 2429-2440.

222. Sivakumar, K.; Wang, V. B.; Chen, X.; Bazan, G. C.; Kjelleberg, S.; Loo, S. C. J.; Cao, B. Membrane Permeabilization Underlies the Enhancement of Extracellular Bioactivity in

Shewanella Oneidensis by a Membrane-Spanning Conjugated Oligoelectrolyte. *Appl. Microbiol. Biotechnol.* **2014,** *98*, 9021-9031.

223. Hou, H.; Chen, X.; Thomas, A. W.; Catania, C.; Kirchhofer, N. D.; Garner, L. E.; Han, A.; Bazan, G. C. Conjugated Oligoelectrolytes Increase Power Generation in E. Coli Microbial Fuel Cells. *Adv. Mater.* **2013,** *25*, 1593-1597.

224. Du, J.; Thomas, A. W.; Chen, X.; Garner, L. E.; Vandenberg, C. A.; Bazan, G. C. Increased Ion Conductance across Mammalian Membranes Modified with Conjugated Oligoelectrolytes. *Chem. Commun.* **2013,** *49*, 9624-9626.

225. Houston, J. E.; Kraft, M.; Mooney, I.; Terry, A. E.; Scherf, U.; Evans, R. C. Charge-Mediated Localization of Conjugated Polythiophenes in Zwitterionic Model Cell Membranes. *Langmuir* **2016,** *32*, 8141-8153.

226. Wang, Y.; Jones, E. M.; Tang, Y.; Ji, E.; Lopez, G. P.; Chi, E. Y.; Schanze, K. S.; Whitten, D. G. Effect of Polymer Chain Length on Membrane Perturbation Activity of Cationic Phenylene Ethynylene Oligomers and Polymers. *Langmuir* **2011,** *27*, 10770-10775.

227. Kahveci, Z.; Martínez-Tomé, M. J.; Mallavia, R.; Mateo, C. R. Use of the Conjugated Polyelectrolyte Poly{[9,9-Bis(6′-N,N,N-Trimethylammonium)Hexyl]Fluorene-Phenylene} Bromide (HTMA-PFP) as a Fluorescent Membrane Marker. *Biomacromolecules* **2013,** *14*, 1990-1998.

228. Ding, L.; Chi, E. Y.; Schanze, K. S.; Lopez, G. P.; Whitten, D. G. Insight into the Mechanism of Antimicrobial Conjugated Polyelectrolytes: Lipid Headgroup Charge and Membrane Fluidity Effects. *Langmuir* **2009,** *26*, 5544-5550.

229. Houston, J. E.; Kraft, M.; Scherf, U.; Evans, R. C. Sequential Detection of Multiple Phase Transitions in Model Biological Membranes Using a Red-Emitting Conjugated Polyelectrolyte. *Phys. Chem. Chem. Phys.* **2016,** *18*, 12423-12427.

230. Garner, L. E.; Park, J.; Dyar, S. M.; Chworos, A.; Sumner, J. J.; Bazan, G. C. Modification of the Optoelectronic Properties of Membranes Via Insertion of Amphiphilic Phenylenevinylene Oligoelectrolytes. *J. Am. Chem. Soc.* **2010,** *132*, 10042-10052.

231. Dal Molin, M.; Verolet, Q.; Colom, A.; Letrun, R.; Derivery, E.; Gonzalez-Gaitan, M.; Vauthey, E.; Roux, A.; Sakai, N.; Matile, S. Fluorescent Flippers for Mechanosensitive Membrane Probes. *J. Am. Chem. Soc.* **2015,** *137*, 568-571.

232. Doval, D. A.; Molin, M. D.; Ward, S.; Fin, A.; Sakai, N.; Matile, S. Planarizable Push-Pull Oligothiophenes: In Search of the Perfect Twist. *Chem. Sci.* **2014,** *5*, 2819-2825.

233. Johansson, P. K.; Jullesson, D.; Elfwing, A.; Liin, S. I.; Musumeci, C.; Zeglio, E.; Elinder, F.; Solin, N.; Inganäs, O. Electronic Polymers in Lipid Membranes. *Sci. Rep.* **2015,** *5*, 11242.

234. Zhang, X.; Yu, J.; Wu, C.; Jin, Y.; Rong, Y.; Ye, F.; Chiu, D. T. Importance of Having Low-Density Functional Groups for Generating High-Performance Semiconducting Polymer Dots. *ACS Nano* **2012,** *6*, 5429-5439.

235. Kahveci, Z.; Martínez-Tomé, M.; Esquembre, R.; Mallavia, R.; Mateo, C. Selective Interaction of a Cationic Polyfluorene with Model Lipid Membranes: Anionic Versus Zwitterionic Lipids. *Materials* **2014,** *7*, 2120-2140.

236. Gruner, S. M. Intrinsic Curvature Hypothesis for Biomembrane Lipid Composition: A Role for Nonbilayer Lipids. *Proc. Natl. Acad. Sci. U. S. A.* **1985,** *82*, 3665-3669.

237. Kulkarni, C. V. Nanostructural Studies on Monoelaidin–Water Systems at Low Temperatures. *Langmuir* **2011,** *27*, 11790-11800.

Chapter 2: Exploiting conjugated polyelectrolyte photophysics toward monitoring real-time lipid membrane-surface interaction dynamics at the single-particle level

Reproduced with permission from: "Exploiting conjugated polyelectrolyte photophysics toward monitoring real-time lipid membrane-surface interaction dynamics at the single-particle level", **Christina F. Calver**, Hsiao-Wei Liu, & Gonzalo Cosa, *Langmuir*, **2015**, *31*, 11842–11850.

Author Contributions: **Christina F. Calver** performed experiments, analyzed data, and co-wrote the paper. **Dr. Hsiao-Wei Liu** collected initial data and provided feedback on the manuscript. **Prof. G. Cosa** designed the project, guided the interpretation of data, co-wrote the paper, and designed the journal cover.

2.0 Preface

In Chapter 1, the concept of tuning the photophysical/energy transporting properties of CPEs by manipulating their environment (*e.g.*, by changing the solvent, pH, or ionic strength, or *via* association with surfactants or lipid membranes) was introduced. For example, while the polyanion MPS-PPV adopts an aggregated conformation in aqueous solution and is only weakly emissive, favourable hydrophobic and electrostatic interactions with the DOTAP membrane trigger deaggregation of the polyanion backbone, resulting in decreased energy migration to non-emissive trap sites and a recovery of the fluorescence quantum yield. In Chapter 2, the emission enhancement of individual surface-immobilized MPS-PPV-coated NPs interacting with individual DOTAP liposomes in solution is recorded using TIRFM. By following the progress of the emission enhancement in real time, the dynamics of the membrane deformation on the charged surface of the CPE-coated NP are revealed, thus demonstrating a new application of CPEs to the study of membrane biophysics.

2.1 Abstract

Herein we report the real-time observation of the interaction dynamics between cationic liposomes flowing in solution and a surface-immobilized charged scaffolding formed by the deposition of conjugated polyanion poly[5-methoxy-2-(3- sulfopropoxy)-1,4-phenylenevinylene (MPS-PPV) onto 100-nm diameter SiO_2 nanoparticles (NPs). Contact of the freely floating liposomes with the polymer-coated surfaces led to the formation of supported lipid bilayers (SLBs). The interaction of the incoming liposomes with MPS-PPV adsorbed on individual SiO_2 nanoparticles promoted the deaggregation of the polymer conformation and led to large emission intensity enhancements. Single-particle total internal reflection fluorescence microscopy studies exploited this phenomenon as a way to monitor the deformation dynamics of liposomes on surface-immobilized NPs. The MPS-PPV emission enhancement (up to 25-fold) reflected on the extent of membrane contact with the surface of the NP and was correlated with the size of the incoming liposome. The time required for the MPS-PPV emission to reach a maximum (ranging from 400 to 1000 ms) revealed the dynamics of membrane deformation and was also correlated with the liposome size. Cryo-TEM experiments complemented these results by yielding a structural view of the process. Immediately following the mixing of liposomes and NPs the majority of NPs had one or more adsorbed liposomes, yet the presence of a fully formed SLB was rare. Prolonged incubation of liposomes and NPs showed completely formed SLBs on all of the NPs, confirming that the liposomes eventually ruptured to form SLBs. We foresee that the single-particle studies we report herein may be readily extended to study membrane dynamics of other lipids including cellular membranes in live cell studies and to monitor the formation of polymer-cushioned SLBs.

2.2 Introduction

In cells, the ability of lipid membranes to dynamically adjust phase and topology is essential for processes such as vesicle trafficking, cell division, and the formation of complex organelle structures.[1-2] These structural changes require the generation of highly strained membranes whose unfavorable curvature is stabilized by the interplay of electrostatic and hydrophobic interactions with charged biopolymers such as proteins.[1-5] The combination of lipid composition and biopolymer scaffolding results in a rich array of possible forms and textures; this structural diversity has profound implications not only for cell biology but also for

biotechnological applications (e.g., gene delivery via lipoplexes[6-7] or the formation of supported lipid bilayers).[8-9] In this regard, although techniques such as cryo-electron microscopy are able to resolve the structural changes that result from lipid–polymer interactions on the nanoscale,[10-13] the dynamics of how these rearrangements occur are difficult to determine experimentally.

Here, we report an approach to determine the dynamics of lipid–polymer interactions at the single-particle level by monitoring the fluorescence enhancement of a conjugated polyelectrolyte adsorbed on a solid scaffold upon encountering single liposomes. The photophysical properties of conjugated polymers and their charged counterparts, conjugated polyelectrolytes, have been shown to be intimately related to chain conformation.[14-18] Collapsed polymer conformations favor efficient energy transfer to nonemissive trap sites, resulting in a low fluorescence quantum yield.[15, 17, 19] Deaggregation of the polymer backbone through interaction with surfactants,[20-23] including lipids,[24-29] reduces the efficiency of energy transfer and leads to highly increased fluorescence quantum yields. We reasoned that morphological changes experienced by conjugated polyelectrolytes upon contact with a lipid bilayer would lead to spectroscopic changes that could be monitored in real time to unmask the dynamics of membrane deformation on a curved, polymer-coated surface.

Conjugated polyanion poly[5-methoxy-2-(3-sulfopropoxy)-1,4-phenylenevinylene (MPS-PPV) was adsorbed onto the surface of amino-functionalized 100-nm-diameter silica nanoparticles (NPs), and the NPs were in turn immobilized onto a coverslip for single-molecule imaging.[30-31] Using total internal reflection fluorescence microscopy (TIRFM) with a two-color detection scheme, we were able to monitor in real time the encounter and subsequent deformation of incoming liposomes prepared from cationic lipid 1,2-dioleoyl-3-trimethylammonium-propane (DOTAP) on the surface of the NPs. Deaggregation of MPS-PPV upon interaction with excess liposomes led to dramatic (average 23-fold) MPS-PPV emission intensity enhancements. When liposomes were flowed at a lower concentration such that the interaction of individual liposomes could be observed one at a time, the magnitude of the enhancements was related to the liposome size, reflecting on the percentage of NP surface area in contact with the adsorbed liposome and thus providing a measure of liposome deformability. Cryo-TEM micrographs obtained from samples vitrified immediately after mixing further showed adsorbed liposomes deforming to accommodate the curvature of the NPs. Prolonged incubation of liposomes and NPs showed in

turn completely formed supported lipid bilayers (SLBs) on all of the NPs after 30 min, confirming that the liposomes eventually ruptured. The liposome size and the enhancement period (ranging from 400 to 1000 ms) were found to be correlated, providing insight into the time required for the liposome to deform on the surface of the NP and for MPS-PPV to deaggegrate within the membrane.

Given the plethora of conjugated polyelectrolytes currently available[32-33] where the backbone and charge may be independently tailored toward enhancing electrostatic and/or hydrophobic interactions with lipids,[25, 34-35] we foresee that the strategy we report herein toward measuring model lipid membrane dynamics in the presence of a charged scaffolding may be readily extended to a diverse range of lipids and lipid mixtures, including cellular membranes, and may be further exploited with respect to the study of the formation of polymer-cushioned SLBs.

2.3 Results and discussion

2.3.1 Ensemble studies on the interaction of DOTAP liposomes with MPS-PPV

We first explored at the ensemble level the interaction of MPS-PPV-coated NPs with 100-nm-diameter DOTAP liposomes by adding a suspension of NPs to a 100-fold excess of 100-nm-diameter liposomes (final concentrations of 0.1 and 13 nM, respectively). To prepare the MPS-PPV-coated NPs, we adapted a previously reported method to functionalize 100 nm SiO_2nanoparticles with an aminosilane group, thus rendering the particles positively charged at neutral to low pH and facilitating the adsorption of the polyanion via electrostatic interactions.[30-31] The full characterization of the functionalization of SiO_2 to $SiO_2NH_3^+$ and of the adsorption of MPS-PPV onto these particles by transmission electron microscopy (TEM), dynamic light scattering (DLS), and UV–vis and fluorescence spectroscopy is described in section 2.7 (Figures 2.6–2.9). A 23-fold emission enhancement and a new shoulder at 585 nm were observed in the emission spectrum of MPS-PPV adsorbed on the NPs immediately after mixing with the DOTAP liposomes (Figure 2.1A, see also normalized emission spectra, Figure 2.10). Our results are consistent with DOTAP liposomes triggering a reorganization and deaggregation of the polymer adsorbed onto the surface of the NPs,[21, 36] where electrostatic and hydrophobic interactions with DOTAP presumably surpass the electrostatic interaction of the polymer with the aminosilanized surface of the NP.

2.3.2 Adsorption versus rupture of liposomes visualized at the single-NP level

To study the interaction dynamics with DOTAP liposomes and to better understand the mechanistic stages (liposome adsorption, deformation, and rupture, if any),[10, 37-38] we monitored individual polymer-coated nanoparticles using a TIRFM setup adapted with an electron-multiplied charge-coupled device (EMCCD) camera. Our setup allows for the simultaneous tracking of hundreds of individual NPs in parallel with 100 ms time resolution; in this way, the interaction dynamics can be determined for each NP and liposome independently and the extent to which all NPs and liposomes behave homogeneously can be assessed.[38] Dilute solutions of MPS-PPV-coated NPs were injected into preassembled chambers where they adsorbed on top of aminosilanized glass coverslips. The polymer-coated NPs were next excited using a 488 or a 514 nm laser, and the fluorescence intensity of hundreds of individual NPs was monitored over time at an acquisition rate of 10 frames/s. Liposome solutions were flowed through the imaging chamber at a rate of 5 μL/min during image acquisition to record the interaction of incoming liposomes with surface-bound nanoparticles.

Upon flowing a 13 nM solution of DOTAP liposomes (100 nm in diameter), all of the polymer-coated NPs simultaneously showed a stark increase in emission intensity with the arrival of the liposomes (Figure 2.1B). The intensity enhancement calculated by dividing the intensity recorded at the peak by the intensity recorded immediately before the enhancement for 200 individual NPs was 24-fold (±11) on average, similar to that in ensemble solution studies (Figure 2.1A). Under our experimental conditions, nonspecific binding of the positively charged DOTAP liposomes onto the positively charged aminosilanized glass surface was not observed (Figure 2.11).

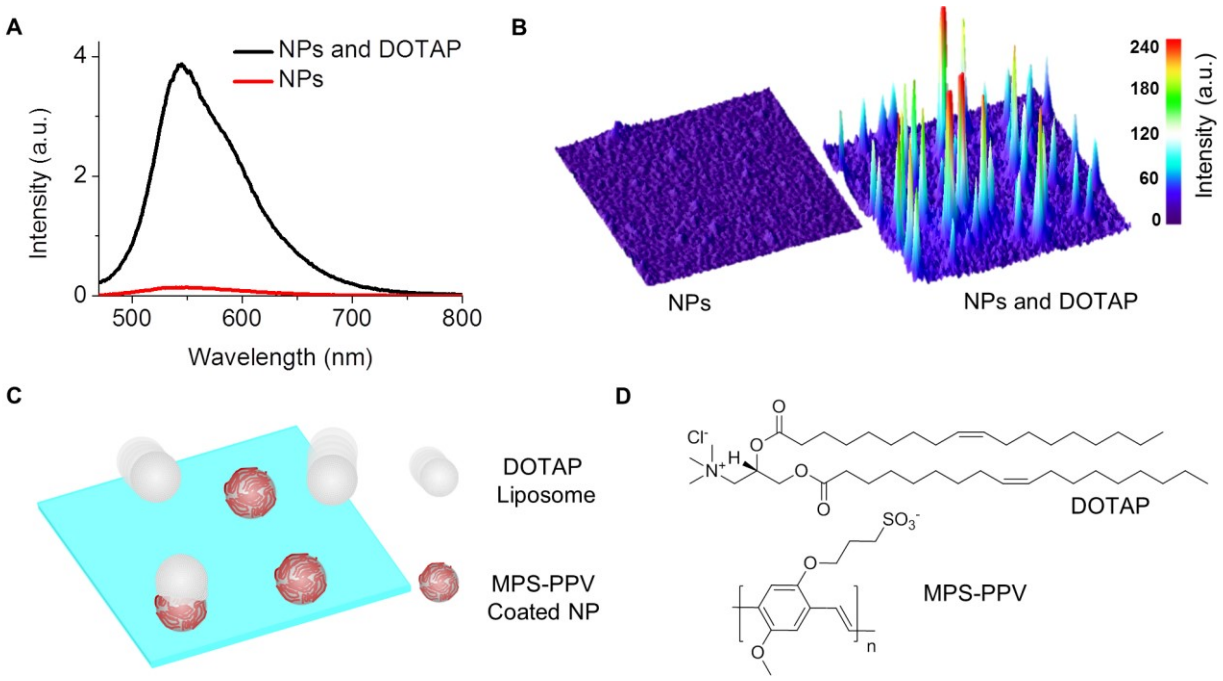

Figure 2.1. Ensemble and single-nanoparticle studies of the emission enhancement of MPS-PPV adsorbed on SiO_2 NPs triggered by interaction with DOTAP liposomes. (A) Emission spectra of 0.1 nM MPS-PPV-coated NPs before (red circles) and after (black squares) addition to 13 nM 100 nm DOTAP liposomes in 3 mM NaCl. (B) Surface plot of MPS-PPV emission intensity obtained by TIRFM before and after 100-nm-diameter DOTAP liposomes 13 nM in concentration were flowed over surface-bound MPS-PPV-coated NPs. (C) Cartoon illustrating the interaction mechanisms between MPS-PPV-coated NPs adsorbed on the surface of a glass coverslip and DOTAP liposomes flowed over the surface. (D) Chemical structures of DOTAP and MPS-PPV.

We were intrigued by the liposome–NP interaction mechanism accounting for the observed MPS-PPV enhancement. Upon considering that the MPS-PPV-coated NPs have a mean diameter of 110 nm, the average 100-nm-diameter liposomes we initially flowed had enough lipid content each to form a complete (or nearly complete) SLB[10, 39-40] on a single NP upon liposome rupture. In this case, the entire surface of the NP would be in contact with the membrane and the emission enhancement is expected to be maximal. In contrast, liposome adsorption and deformation (but no rupture) would render only the fraction of the NP that is in contact with the membrane highly emissive, and the emission enhancement is then expected to be submaximal.

To test whether the liposomes were adsorbing but remaining intact on the surface of the NPs or if they were rupturing to form SLBs, we next measured intensity enhancements under a low concentration of 100-nm-diameter liposomes (0.13 nM, a 100-fold reduction) in order to

record single NP–liposome encounters and determine whether the enhancements were submaximal or maximal, respectively. Under these conditions, only 20% of the single-particle fluorescence intensity versus time trajectories showed an enhancement over the 150 s image acquisition time (Figure 2.2A). The majority of NPs experienced no encounters with liposomes (and thus no emission enhancement), and a subset of particles, ca. 2%, experienced two encounters during the acquisition time, recorded as two distinct intensity jumps of comparable amplitude. The onset of the enhancement was random over time, consistent with the fact that NPs and liposomes have a low encounter probability when liposomes are flowed at this low concentration. The mean enhancement measured for 170 individual NPs was 5.4 ± 2.8-fold for the 100 nm liposomes, ca. 5-fold smaller than the maximum value recorded under excess liposomes for the same NPs. Given this value, we estimated that 20% of the total area of the NP was in contact with a 100 nm liposome on average, in line with a liposome interacting and plausibly deforming on an NP surface rather than with its rupture to form an SLB[10, 39-40] (see also cryo-TEM studies, *vide infra*). The fact that only 20% of the NP surface area was occupied by the adsorbed liposome also opened the possibility of the adsorption of additional liposomes. Indeed, when the liposome concentration was raised 10-fold to 1.3 nM, the fluorescence intensity versus time trajectories of the NPs showed several discrete enhancement "steps" (Figure 2.2B), each of roughly the same magnitude as the single steps recorded at the 0.13 nM liposome concentration (Figure 2.2B). The steps were attributed to the interaction of multiple liposomes on a single NP. As described above, in the presence of the 13 nM liposome solution the onset of the fluorescence enhancement for MPS-PPV-coated NPs was simultaneous; that is, every NP began to be enhanced at approximately the same time (Figure 2.2C), and the mean enhancement was 24-fold. At this concentration, individual liposome–NP encounter events were not well resolved.

We reasoned that larger liposomes may be capable of "engulfing" a larger portion of the NP while still remaining intact, thus leading to larger intensity enhancements. When low concentrations (ca. 0.08 nM) of larger liposomes (up to 400 nm in diameter) were flowed over the NPs, single-step intensity enhancements of up to 23-fold were observed (Figure 2.2D). These enhancements were suggestive of a liposome population possessing a large enough lipid surface area to fully wrap around the NPs upon deformation, leading to complete polymer deaggregation/reorganization and a maximal fluorescence enhancement. Given the large polydispersity of the liposome sample (Figure 2.2E), however, many smaller enhancements were

also observed and the average enhancement calculated for 170 individual NPs was 10.7(±8)-fold. The large distribution in intensity enhancements for the 400 nm sample was correlated with its relatively large polydispersity. By comparison, a narrower enhancement distribution was observed for the 100-nm-diameter liposomes which were also characterized by a smaller polydispersity (Figure 2.2E,F). Upon flowing a 100-fold-larger concentration of 400 nm liposomes, the fluorescence enhancement was simultaneous in time for all particles, and the mean intensity enhancement was 22(±10)-fold (versus 24(±11)-fold for 100 nm liposomes under similar conditions). Under high liposome concentrations the distribution of enhancements is furthermore indistinguishable between the 100 and 400 nm liposome populations (Figure 2.12).

Overall, we observed that the enhanced intensity of the MPS-PPV-coated NPs was positively correlated to the initial intensity of the NPs when the liposomes were flowed in large excess and were not a limiting reagent (Figure 2.2G). The linear correlation is consistent with a relatively uniform deposition of MPS-PPV on a particle-to-particle basis, where the major difference between the NPs is the size of the underlying SiO_2 NP support. The distribution of initial intensities was observed to be correlated with the distribution of sizes observed by dynamic light scattering measurements (Figure 2.13). The presence of more adsorbed polymer on a NP with a larger surface area will in turn lead to a larger initial intensity and a larger enhanced intensity, assuming that every NP has an equal ability to interact with the liposomes and attain a maximal enhancement. In line with the above, when the same liposomes were flowed at a 100-fold-lower concentration (Figure 2.2H) the initial intensity was not correlated to the enhanced intensity. The convergence of the size distribution of NPs (Figure 2.7) and the size distribution of interacting liposomes (Figure 2.2E) at 1:1 stoichiometry resulted in the poor correlation observed.

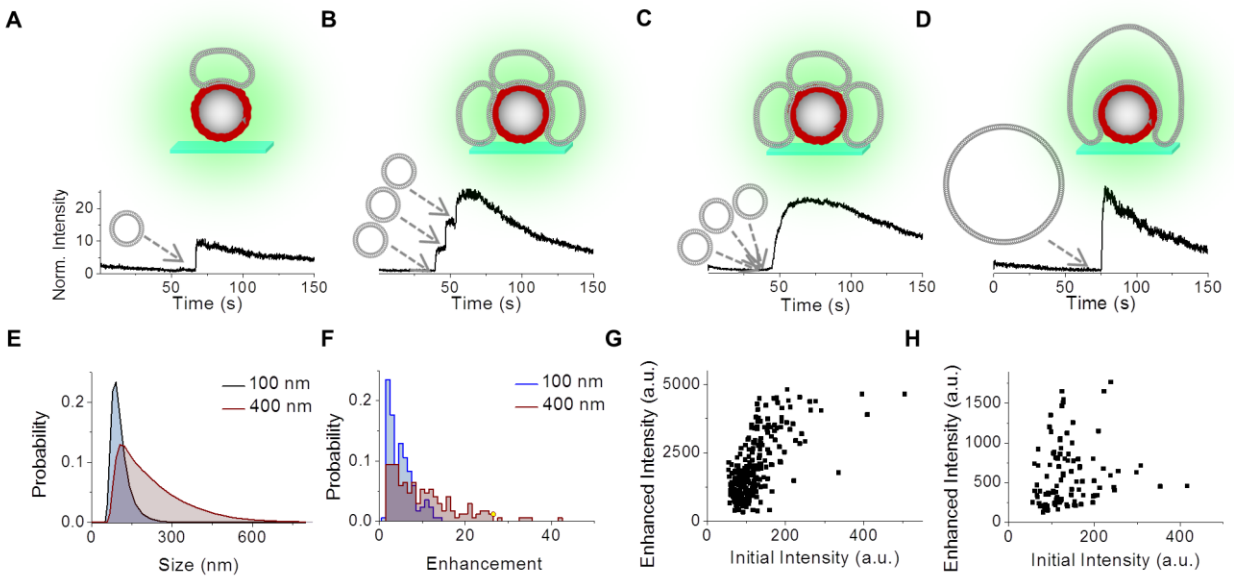

Figure 2.2. Enhancement intensities and dynamics for individual MPS-PPV-coated NPs in response to 100 and 400 nm DOTAP liposomes. Surface-immobilized MPS-PPV-coated NPs were excited with a 488 nm laser (220 μW), and TIRFM images were obtained at a time resolution of 10 frames/s while flowing liposome solutions at a rate of 5 μL per min. (A–D) Representative fluorescence intensity versus time trajectories obtained under the following conditions: (A) 0.13 nM 100 nm liposomes; (B) 1.3 nM 100 nm liposomes; (C) 13 nM 100 nm liposomes; and (D) 0.08 nM 400 nm liposomes. The trajectories were normalized by the intensity of the NP immediately before the enhancement. (E) Size distribution of 100 and 400 nm DOTAP liposomes obtained by dynamic light scattering. (F) Histogram of enhancements recorded while flowing solutions of 0.13 nM 100 nm liposomes and 0.08 nM 400 nm liposomes. Enhancements were determined for 170 MPS-PPV-coated NPs under both conditions. (G, H) Correlation plots between the initial intensity of MPS-PPV-coated NPs and their enhanced intensity after flowing 400 nm liposomes at a high concentration of 8 nM and at a low concentration of 0.08 nM, respectively.

To gain a molecular-level visualization of the interaction of the MPS-PPV-coated NPs and DOTAP liposomes we performed cryo-TEM studies. MPS-PPV-coated NPs were added to excess DOTAP liposomes, and the sample was vitrified within 30 s following mixing. At this stage, many liposomes of varying size were adsorbed onto the MPS-PPV-coated NPs, as revealed by the ring of electron-dense material 4 to 5 nm from the edge of the NPs (Figure 2.3A,B). The adsorbed liposomes were deformed[41] to varying degrees to accommodate the curvature of the NP surface. The engulfment of NPs by larger liposomes was observed as we proposed on the basis of our TIRFM studies (arrow 2 in Figure 2.3A). On some particles, fully formed supported lipid bilayers (SLBs) were observed[10] (arrow 1 in Figure 2.3A), but whereas the majority of NPs had one or more adsorbed liposomes (arrow 3 in Figure 2.3B), the presence of a fully formed SLB was rare.

Importantly, upon prolonged incubation of liposomes and NPs for 30 min and following the removal of the excess liposomes by centrifugation, cryo-TEM images showed completely formed SLBs on all of the NPs (Figure 2.3D,F). Given that some SLBs are already observed within 30 s of mixing we believe that SLB formation is the final fate of the system at long time scales, although it remains an open question as to whether mechanical disruption of the liposomes during the centrifugation step may have accelerated this process. More importantly, however, is the fact that it is unlikely that liposome rupture was responsible for the MPS-PPV emission enhancements observed during the TIRFM microscopy experiments given that these enhancements were found to occur on the tens of milliseconds time scale whereas the near absence of completely formed SLBs in TEM images obtained 30 s following mixing suggested that liposome rupture is a slower process in this system. Dye leakage experiments of red emissive fluorophore Cy5 encapsulated inside liposomes in the presence of external quencher $FeCl_3$ further showed that the majority of liposomes do not rupture within 10 min of mixing with MPS-PPV-coated NPs (Figure 2.14).

A closer inspection of the cryo-TEM micrographs further revealed the close proximity between the membrane and the polymer-coated NP. Considering a 4- to 5-nm-thick bilayer, one may infer that the thickness of the water layer separating the inner lipid leaflet from the NP[42-43] at most 1 nm. Under our resolution it was not possible to distinguish either the inner membrane leaflet or the outer leaflet regardless of whether one observed regions of membrane in contact with NPs or free in vitreous aqueous solution; however, both sections of the membrane (*i.e.*, free in solution or in contact with the NP) were identical, revealing that the interaction with MPS-PPV did not result in membrane thickening. Importantly, the bilayer closely follows the underlying SiO_2 NP topography (Figure 2.3), indicating that the polyelectrolyte does not significantly shield the membrane from the underlying surface roughness.

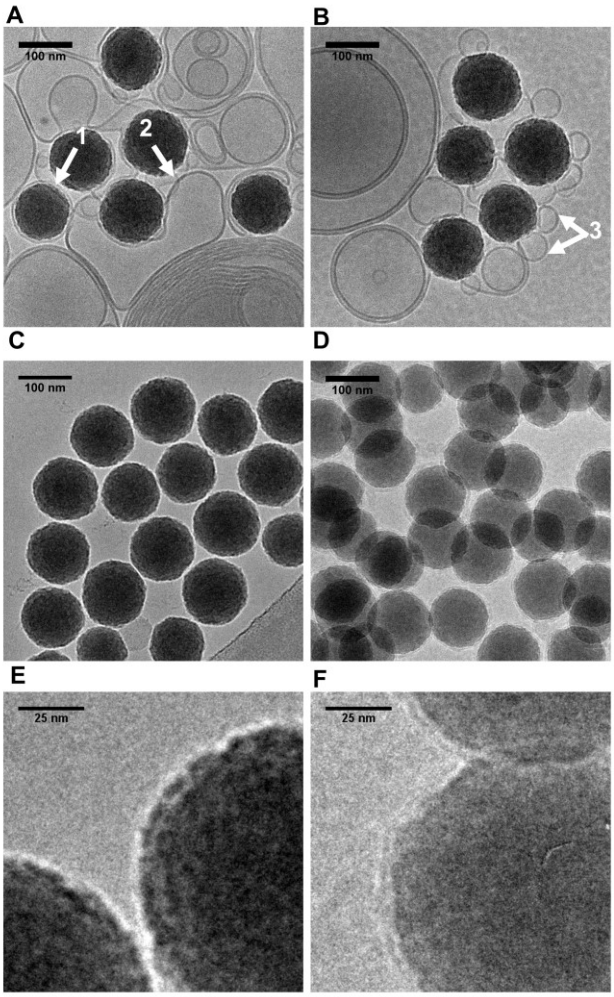

Figure 2.3. Cryo-TEM micrographs of MPS-PPV-coated SiO_2 NPs with 400 nm DOTAP liposomes. (A, B) A solution containing NPs and liposomes was vitrified within 30 s following mixing of the liposomes and the NPs. Arrow 1 points to a fully formed SLB on an NP, arrow 2 points to a large liposome deformed around the surface of an NP, and arrow 3 points to multiple small liposomes adsorbed on the same NP. (C) MPS-PPV-coated NPs. (D) MPS-PPV-coated NPs that were incubated with DOTAP liposomes prior to the removal of the excess liposomes by centrifugation. (E, F) Close-up views of images in panels C and D, respectively. The concentration of NPs was 1 nM, and the concentration of 400-nm-diameter DOTAP liposomes was 8 nM. The samples were suspended in a 3 mM NaCl aqueous solution.

2.3.3 Liposome–NP interaction dynamics and ensuing polymer deaggregation

In subsequent experiments, we sought to simultaneously visualize the liposomes and the surface-bound polymer-coated NPs in parallel channels in order to unequivocally establish their interaction dynamics upon liposome arrival. Experimentally, we labeled the DOTAP liposomes with red, lipophilic dye 1,1′-dioctadecyl-3,3,3′,3′-tetramethylindodicarbocyanine perchlorate

(DiD) in a lipid to DiD molar ratio of 256:1. Both MPS-PPV and DiD were excited with a 514 nm laser. The emission was collected and split into a red (DiD) and a green (MPS-PPV-coated NPs) channel using a 640 nm beamsplitter. NPs were located in the green channel, and the corresponding region was mapped in the red channel to allow us to monitor the appearance of DiD-stained liposomes as the solution flowed in (Figure 2.4).

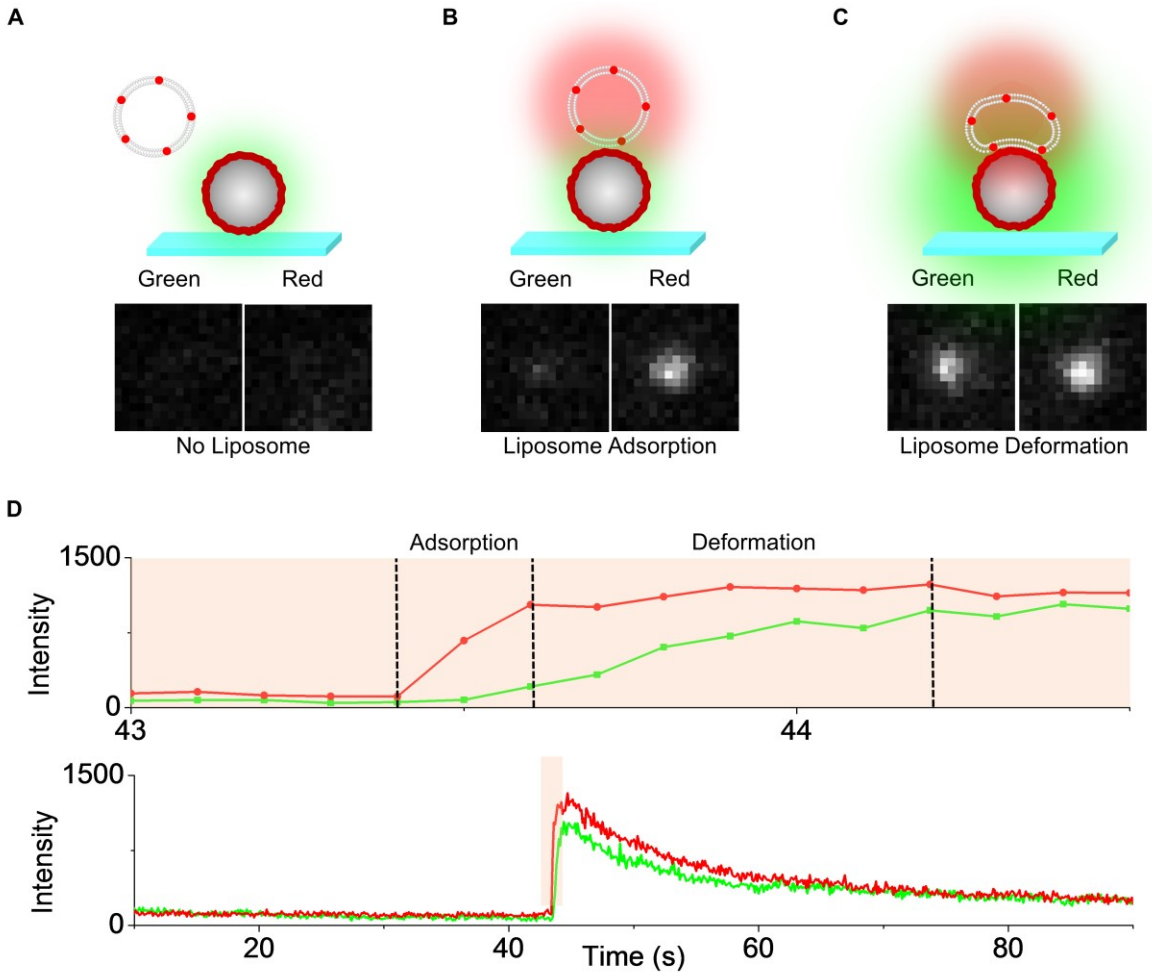

Figure 2.4. Simultaneous visualization of the encounter of a single DOTAP liposome and an MPS-PPV-coated NP. Surface-immobilized MPS-PPV-coated NPs were excited with the 580 μW output of a 514 nm laser, and TIRFM images were obtained at a time resolution of 10 frames/s. DOTAP liposomes (400 nm) labeled with DiD in a 256:1 lipid/dye ratio at a concentration of 0.08 nM in 3 mM NaCl were flowed at a rate of 5 μL/min during imaging. (A) Dimly emissive MPS-PPV-coated NPs are initially visible in the green channel. (B) The colocalization of a DiD-labeled liposome with a NP was signaled by the appearance of a fluorescence signal in the red channel over a period of one or two frames. (C) The colocalization of the liposome triggered the onset of the MPS-PPV fluorescence enhancement. (D) Representative fluorescence intensity versus time trajectory for an NP interacting with a DOTAP liposome in a two-channel experiment. The full

trajectory is shown at the bottom. Highlighted is the portion where the incoming liposome interacts with the NP, shown in greater detail at the top.

The concentration of the 400 nm liposome solution that flowed during imaging was optimized to 0.080 nM liposomes so that the majority of NPs (81%) did not interact with a liposome during the image acquisition time. The intensity–time trajectories for these NPs in the green channel displayed an exponentially decaying intensity arising from the photobleaching of MPS-PPV, and the intensity recorded in the red channel mirrored the green channel due to 25% crosstalk. In the remaining trajectories, the colocalization of a red-emissive liposome with a green-emissive NP was signaled by a rapid increase in the fluorescence intensity monitored in the red channel occurring over a maximum of two 100 ms frames. A total of 17% of the trajectories showed the colocalization of one liposome, and 2% of the trajectories showed the colocalization of a second liposome. Monitoring both channels simultaneously enabled us to unequivocally establish that every encounter between a liposome and an NP was irreversible (i.e., liposomes did not dock and undock) over the time period observed. Furthermore, we recorded no non-productive liposome–NP encounters (i.e., upon docking, DOTAP liposomes triggered the rapid deaggregation of MPS-PPV in all cases).

The two-color TIRFM experiments additionally showed that the MPS-PPV intensity enhancement recorded was directly proportional to the incoming liposome size (Figure 2.5A), a result that was consistent with the larger enhancements observed on average when larger liposomes were flowed over polymer-coated NPs in one-color experiments (Figure 2.2E,F, *vide supra*). Considering a random distribution of DiD molecules in the lipid membrane, the number of dyes present and thus the intensity of any given liposome are directly proportional to the lipid surface area (i.e., larger liposomes are brighter).[44] The intensity of the incoming liposome in the red channel was positively correlated to the intensity enhancement of MPS-PPV in the green channel (Figure 2.5A). For the same data set, the change in MPS-PPV fluorescence intensity showed a poor correlation to the initial intensity of the NP (Figure 2.5B), consistent with the idea that it is primarily the size of the liposome (amount of lipid entering in contact with MPS-PPV, triggering deaggregation) and not the total amount of MPS-PPV present in an NP that determines the size of the enhancement.

The MPS-PPV enhancement period, defined as the number of frames that elapsed from the onset of MPS-PPV emission enhancement until its peak value is reached, was also investigated with results from the one-color TIRFM experiments as convolution between FRET and DiD photobleaching hampers this study with the two-color data. The fluorescence versus time trajectories of MPS-PPV-coated NPs interacting with individual 100 and 400 nm liposomes (Figure 2.2A,D, respectively) were analyzed, and the distribution of enhancement periods is shown in Figure 2.5C. The mean enhancement period was 430(±70) ms for the 100 nm liposome sample and slightly longer, 630(±110) ms, for the 400 nm liposome sample. The fluorescence enhancement for each NP was also determined. The NPs were sorted into groups based on the size of their enhancement, and the probability of having a given enhancement period within each group was determined (Figure 2.5D). Liposomes triggering smaller enhancements (less than 5-fold) were more likely to have shorter enhancement periods whereas liposomes triggering larger enhancements (greater than 10-fold) were more likely to have longer enhancement periods. Given the positive correlation observed between liposome size and enhancement size in the experiments with dye-labeled liposomes, we may conclude that smaller liposomes are more likely to induce rapid deaggregation of MPS-PPV than larger liposomes. The exact nature of the microscopic rearrangements taking place between the polymer and the liposome is unclear. It is plausible that liposome deformation is the rate-limiting step and that larger liposomes, which have a higher possibility to deform, take longer to explore the surface of the NP than smaller liposomes whose interaction area is more limited.

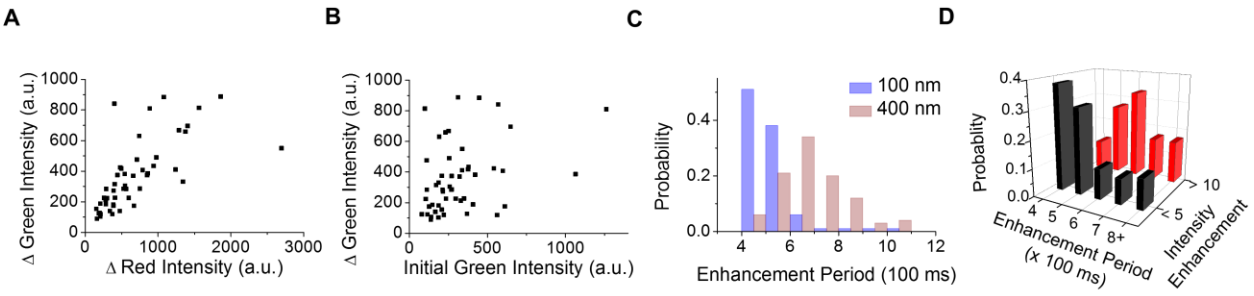

Figure 2.5. Correlation between the emission enhancement magnitude and the enhancement period for an MPS-PPV-coated NP versus liposome size. (A) Correlation plot of the enhanced MPS-PPV intensity in the green emission channel versus the intensity of the dye-labeled liposome in the red emission channel. (B) Correlation plot of the enhanced MPS-PPV emission intensity versus the initial MPS-PPV emission intensity. (C) Distribution of enhancement periods for both 100 and 400 nm liposomes. (D) Distribution of NPs with enhancements of less than 5-fold and enhancements greater than 10-fold sorted by their enhancement periods plotted for NPs interacting with 100- and 400-nm-diameter liposomes. Graphs A and B are plotted using data from two-color TIRFM experiments utilizing 400 nm DOTAP liposomes labeled with DiD in a 256:1 lipid/dye ratio. Surface-bound MPS-PPV-coated NPs were excited with a 514 nm laser (500 μW), and their emission intensity was monitored while flowing liposomes at a concentration of 0.08 nM in 3 mM NaCl. Graphs C and D are plotted using data from one-color TIRFM experiments utilizing 100 and 400 nm DOTAP liposomes in 3 mM NaCl flowed at concentrations of 0.13 and 0.08 nM, respectively. Here, the excitation source was a 488 nm laser (220 μW). All liposome solutions were flowed at a rate of 5 μL/min, and images were acquired with a time resolution of 10 fps.

2.4 Conclusion

We provide a methodology to measure the dynamics of membrane deformation for a membrane in contact with polyelectrolyte scaffolding. Utilizing single-particle fluorescence and exploiting the spectroscopic properties of conjugated polyelectrolytes, which are dimly emissive when aggregated yet highly emissive upon conformational reorganization in the presence of surfactants, including lipids, we can record real-time liposome docking and subsequent deformation on the surface of SiO_2 nanoparticles coated with a conjugated polyelectrolyte. Conformational changes in the conjugated polyelectrolyte as the membrane deforms along the surface curvature of the nanoparticle results in fluorescence intensity enhancements. These enhancements are proportional to the surface coverage by the lipid milieu, providing a means to read to which extent the membrane deforms and how rapidly it is doing so. Larger liposomes, which have a higher possibility to deform, take longer to explore the surface of the NP than smaller liposomes whose interaction area is more limited. Cryo-TEM studies provide a molecular-level

(structural) visualization of the resulting products. Multiple small liposomes are observed interacting with single NPs, and larger liposomes readily engulf a single conjugated polyelectrolyte-coated NP. The adsorbed liposomes underwent varying extents of deformation such that the membrane closely followed the topology of the underlying SiO_2 support. Liposome rupture at longer times ultimately leads to the formation of supported lipid bilayers.

We believe that the development of our approach will enable the interrogation of the dynamics at play as model membranes and cell membranes adjust their phase and topology in the presence of charged scaffoldings. Wisely chosen conjugated polyelectrolyte composites may enable the role of charge and hydrophobic interactions between the membrane and the scaffolding to be reported spectroscopically. Different lipids and lipid mixtures may be monitored, yielding additional information on the role of chemical composition. Physical parameters such as the curvature of the liposomes and the NPs and their role in membrane dynamics could be easily followed.

2.5 References

1. McMahon, H. T.; Gallop, J. L. Membrane Curvature and Mechanisms of Dynamic Cell Membrane Remodelling. *Nature* **2005,** *438*, 590-596.

2. Baumgart, T.; Capraro, B. R.; Zhu, C.; Das, S. L. Thermodynamics and Mechanics of Membrane Curvature Generation and Sensing by Proteins and Lipids. *Annu. Rev. Phys. Chem.* **2011,** *62*, 483-506.

3. Zimmerberg, J.; Kozlov, M. M. How Proteins Produce Cellular Membrane Curvature. *Nat. Rev. Mol. Cell Biol.* **2006,** *7*, 9-19.

4. Brown, M. F. Curvature Forces in Membrane Lipid–Protein Interactions. *Biochemistry* **2012,** *51*, 9782-9795.

5. Stachowiak, J. C.; Brodsky, F. M.; Miller, E. A. A Cost-Benefit Analysis of the Physical Mechanisms of Membrane Curvature. *Nat. Cell Biol.* **2013,** *15*, 1019-1027.

6. Koltover, I.; Salditt, T.; Rädler, J. O.; Safinya, C. R. An Inverted Hexagonal Phase of Cationic Liposome-DNA Complexes Related to DNA Release and Delivery. *Science* **1998,** *281*, 78-81.

7. Caracciolo, G.; Amenitsch, H. Cationic Liposome/DNA Complexes: From Structure to Interactions with Cellular Membranes. *Eur Biophys J* **2012,** *41*, 815-829.

8. Tanaka, M.; Sackmann, E. Polymer-Supported Membranes as Models of the Cell Surface. *Nature* **2005,** *437*, 656-663.

9. Berti, D.; Caminati, G.; Baglioni, P. Functional Liposomes and Supported Lipid Bilayers: Towards the Complexity of Biological Archetypes. *Phys. Chem. Chem. Phys.* **2011,** *13*, 8769-8782.

10. Mornet, S.; Lambert, O.; Duguet, E.; Brisson, A. The Formation of Supported Lipid Bilayers on Silica Nanoparticles Revealed by Cryoelectron Microscopy. *Nano Lett.* **2004,** *5*, 281-285.

11. Golan, S.; Talmon, Y. Nanostructure of Complexes between Cationic Lipids and an Oppositely Charged Polyelectrolyte. *Langmuir* **2012,** *28*, 1668-1672.

12. Bershteyn, A.; Chaparro, J.; Yau, R.; Kim, M.; Reinherz, E.; Ferreira-Moita, L.; Irvine, D. J. Polymer-Supported Lipid Shells, Onions, and Flowers. *Soft Matter* **2008,** *4*, 1787-1791.

13. Frost, A.; Perera, R.; Roux, A.; Spasov, K.; Destaing, O.; Egelman, E. H.; De Camilli, P.; Unger, V. M. Structural Basis of Membrane Invagination by F-Bar Domains. *Cell* **2008,** *132*, 807-817.

14. Bolinger, J. C.; Traub, M. C.; Brazard, J.; Adachi, T.; Barbara, P. F.; Vanden Bout, D. A. Conformation and Energy Transfer in Single Conjugated Polymers. *Acc. Chem. Res.* **2012,** *45*, 1992-2001.

15. Schwartz, B. J. Conjugated Polymers as Molecular Materials: How Chain Conformation and Film Morphology Influence Energy Transfer and Interchain Interactions. *Annu. Rev. Phys. Chem.* **2003,** *54*, 141-172.

16. Kobayashi, H.; Onda, S.; Furumaki, S.; Habuchi, S.; Vacha, M. A Single-Molecule Approach to Conformation and Photophysics of Conjugated Polymers. *Chem. Phys. Lett.* **2012,** *528*, 1-6.

17. Huser, T.; Yan, M.; Rothberg, L. J. Single Chain Spectroscopy of Conformational Dependence of Conjugated Polymer Photophysics. *Proc. Natl. Acad. Sci. U. S. A.* **2000,** *97*, 11187-11191.

18. Ebihara, Y.; Vacha, M. Relating Conformation and Photophysics in Single MEH-PPV Chains. *J. Phys. Chem. B* **2008,** *112*, 12575-12578.

19. Bout, D. A. V.; Yip, W.-T.; Hu, D.; Fu, D.-K.; Swager, T. M.; Barbara, P. F. Discrete Intensity Jumps and Intramolecular Electronic Energy Transfer in the Spectroscopy of Single Conjugated Polymer Molecules. *Science* **1997,** *277*, 1074-1077.

20. Heeley, M. E. H.; Gallaher, J. K.; Nguyen, T. L.; Woo, H. Y.; Hodgkiss, J. M. Surfactant Controlled Aggregation of Conjugated Polyelectrolytes. *Chem. Commun.* **2013,** *49*, 4235-4237.

21. Chen, L.; Xu, S.; McBranch, D.; Whitten, D. Tuning the Properties of Conjugated Polyelectrolytes through Surfactant Complexation. *J. Am. Chem. Soc.* **2000,** *122*, 9302-9303.

22. Costa, T.; Garner, L. E.; Knaapila, M.; Thomas, A. W.; Rogers, S. E.; Bazan, G. C.; Burrows, H. D. Aggregation Properties of P-Phenylene Vinylene Based Conjugated Oligoelectrolytes with Surfactants. *Langmuir* **2013,** *29*, 10047-10058.

23. Dou, W.; Wang, C.; Wang, G.; Ma, Q.; Su, X. Enhance Effect of Surfactants on the Photoluminescence and Photostability of Water-Soluble Poly(Phenylene Ethynylene). *J. Phys. Chem. B* **2008,** *112*, 12681-12685.

24. Ngo, A. T.; Cosa, G. Assembly of Zwitterionic Phospholipid/Conjugated Polyelectrolyte Complexes: Structure and Photophysical Properties. *Langmuir* **2009,** *26*, 6746-6754.

25. Karam, P.; Hariri, A. A.; Calver, C. F.; Zhao, X.; Schanze, K. S.; Cosa, G. Interaction of Anionic Phenylene Ethynylene Polymers with Lipids: From Membrane Embedding to Liposome Fusion. *Langmuir* **2014,** *30*, 10704-10711.

26. Karam, P.; Ngo, A. T.; Rouiller, I.; Cosa, G. Unraveling Electronic Energy Transfer in Single Conjugated Polyelectrolytes Encapsulated in Lipid Vesicles. *Proc. Natl. Acad. Sci. U. S. A.* **2010,** *107*, 17480-17485.

27. Zeineldin, R.; Piyasena, M. E.; Sklar, L. A.; Whitten, D.; Lopez, G. P. Detection of Membrane Biointeractions Based on Fluorescence Superquenching. *Langmuir* **2008,** *24*, 4125-4131.

28. Wang, Y.; Schanze, K. S.; Chi, E. Y.; Whitten, D. G. When Worlds Collide: Interactions at the Interface between Biological Systems and Synthetic Cationic Conjugated Polyelectrolytes and Oligomers. *Langmuir* **2013,** *29*, 10635-10647.

29. Garner, L. E.; Park, J.; Dyar, S. M.; Chworos, A.; Sumner, J. J.; Bazan, G. C. Modification of the Optoelectronic Properties of Membranes Via Insertion of Amphiphilic Phenylenevinylene Oligoelectrolytes. *J. Am. Chem. Soc.* **2010,** *132*, 10042-10052.

30. Ngo, A. T.; Lau, K. L.; Quesnel, J. S.; Aboukhalil, R.; Cosa, G. Deposition of Anionic Conjugated Poly(Phenylenevinylene) onto Silica Nanoparticles Via Electrostatic Interactions — Assembly and Single-Particle Spectroscopy. *Can. J. Chem.* **2011,** *89*, 385-394.

31. Liu, H.-W.; Ngo, A. T.; Cosa, G. Enhancing the Emissive Properties of Poly(P-Phenylenevinylene)-Conjugated Polyelectrolyte-Coated SiO_2 Nanoparticles. *J. Am. Chem. Soc.* **2011,** *134*, 1648-1652.

32. Jiang, H.; Taranekar, P.; Reynolds, J. R.; Schanze, K. S. Conjugated Polyelectrolytes: Synthesis, Photophysics, and Applications. *Angew. Chem. Int. Edit.* **2009,** *48*, 4300-4316.

33. Liu, B.; Bazan, G. C., *Conjugated Polyelectrolytes: Fundamentals and Applications*. Wiley-VCH Verlag GmbH & Co. KGaA: Weinheim, Germany, 2012.

34. Ngo, A. T.; Karam, P.; Cosa, G. Conjugated Polyelectrolyte-Lipid Interactions: Opportunities in Biosensing. *Pure Appl. Chem.* **2011,** *83*, 43-55.

35. Wang, Y.; Jones, E. M.; Tang, Y.; Ji, E.; Lopez, G. P.; Chi, E. Y.; Schanze, K. S.; Whitten, D. G. Effect of Polymer Chain Length on Membrane Perturbation Activity of Cationic Phenylene Ethynylene Oligomers and Polymers. *Langmuir* **2011,** *27*, 10770-10775.

36. Dalvi-Malhotra, J.; Chen, L. Enhanced Conjugated Polymer Fluorescence Quenching by Dipyridinium-Based Quenchers in the Presence of Surfactant. *J. Phys. Chem. B.* **2005,** *109*, 3873-3878.

37. Troutier, A.-L.; Ladavière, C. An Overview of Lipid Membrane Supported by Colloidal Particles. *Adv. Colloid Interface Sci.* **2007,** *133*, 1-21.

38. Johnson, J. M.; Ha, T.; Chu, S.; Boxer, S. G. Early Steps of Supported Bilayer Formation Probed by Single Vesicle Fluorescence Assays. *Biophys. J.* **2002,** *83*, 3371-3379.

39. Hamai, C.; Cremer, P. S.; Musser, S. M. Single Giant Vesicle Rupture Events Reveal Multiple Mechanisms of Glass-Supported Bilayer Formation. *Biophys. J.* **2007,** *92*, 1988-1999.

40. Takáts-Nyeste, A.; Derényi, I. Development of Hat-Shaped Liposomes on Solid Supports. *Langmuir* **2014,** *30*, 15261-15265.

41. Reviakine, I.; Gallego, M.; Johannsmann, D.; Tellechea, E. Adsorbed Liposome Deformation Studied with Quartz Crystal Microbalance. *J. Chem. Phys.* **2012,** *136*, -.

42. Raedler, J.; Strey, H.; Sackmann, E. Phenomenology and Kinetics of Lipid Bilayer Spreading on Hydrophilic Surfaces. *Langmuir* **1995,** *11*, 4539-4548.

43. Bayerl, T. M.; Bloom, M. Physical Properties of Single Phospholipid Bilayers Adsorbed to Micro Glass Beads. A New Vesicular Model System Studied by 2H-Nuclear Magnetic Resonance. *Biophys. J.* **1990,** *58*, 357-362.

44. Larsen, J.; Hatzakis, N. S.; Stamou, D. Observation of Inhomogeneity in the Lipid Composition of Individual Nanoscale Liposomes. *J. Am. Chem. Soc.* **2011,** *133*, 10685-10687.

45. Roy, R.; Hohng, S.; Ha, T. A Practical Guide to Single-Molecule FRET. *Nat. Methods* **2008,** *5*, 507-516.

2.6 Experimental section

2.6.1 Aminosilanization of SiO_2 NPs

The surface charge of the SiO_2 NPs was rendered positive by reaction with an aminosilane to facilitate the deposition of MPS-PPV by electrostatic attraction between the negatively charged sulfonate groups of the polyanion and the positively charged amine groups of the functionalized SiO_2 NPs. A 400 μL aliquot of 5.32% (w/w) SiO_2 NPs in water (Polysciences, Inc.) was transferred to a 1.5 mL Eppendorf tube. (3-Aminopropyl)trimethoxysilane (Sigma-Aldrich) (2.0 μL, 12 μmol) was added with vigorous vortex mixing. The reaction mixture was incubated at room temperature (22–25 °C) for 5 min. Hydrochloric acid (8 μL, 3 M) was added next to protonate the amine groups and quench any unreacted aminosilane. The mixture was immediately centrifuged at 16 060*g* for 5 min. Approximately 90% of the supernatant was removed and replaced with an equal volume of water. The NPs were then resuspended by sonication/vortex mixing. The washing cycle was repeated until the pH of the supernatant was ca. 4. The final concentration of the $SiO_2NH_3^+$ NPs was 65 nM in terms of the number of NPs.

2.6.2 MPS-PPV adsorption on $SiO_2NH_3^+$ NPs

To adsorb MPS-PPV onto the surface of the $SiO_2NH_3^+$ NPs, a suspension of NPs was added to excess MPS-PPV. The presence of excess MPS-PPV prevented the aggregation of NPs by polymer bridging. $SiO_2NH_3^+$ (20 μL, 65 nM) was added to 0.230 mL of water and 0.250 mL of methanol in a 1.5 mL Eppendorf tube. This $SiO_2NH_3^+$ suspension was added, 10 μL at a time, to 1.00 mL of 3 mM MPS-PPV (concentration in terms of polymer repeat units) in 1:1 water/methanol with vigorous vortex mixing. The mixture was agitated gently at room temperature for ca. 30 min and then centrifuged at 16 060*g* for 5 min. The supernatant containing unadsorbed MPS-PPV was removed and replaced with an equal volume of water, and the NPs were resuspended by sonication/vortex mixing. This washing cycle was repeated until traces of MPS-PPV could no longer be detected in the absorbance spectrum of the supernatant. The final concentration of MPS-PPV-coated NPs was 1.3 nM in terms of the number of NPs. The MPS-PPV-coated NPs were stored at 4 °C and protected from light.

2.6.3 Preparation of DOTAP liposomes

To prepare liposomes, 1,2-dioleoyl-3-trimethylammonium-propane chloride salt (DOTAP) powder (Avanti Lipids Corp.) was dissolved in chloroform to a concentration of 0.10 mg/mL. Fifty microliters of this solution were transferred to a small glass vial. The vial was rotated under a stream of argon to evaporate the solvent, forming a thin lipid film along the walls of the vial. The vial was placed under vacuum for an additional 30 min to remove traces of solvent. The dried film was rehydrated in 358 μL of 3 mM NaCl aqueous solution to a final lipid concentration of 20 mM. The suspension was vortex mixed briefly to loosen the film adhering to the walls of the vial. For 100 nm liposomes, the suspension was taken through eight freeze/thaw cycles (5 min on dry ice followed by 5 min in a sonicator bath) to increase the unilamellarity of the liposomes. The suspension was then extruded 11 times through a 100 nm polycarbonate membrane using a miniextruder (Avanti Lipids Corp.). For 400 nm liposomes, the procedure was identical except that the suspension was not subjected to any freeze/thaw cycles and a 400 nm polycarbonate membrane was used instead of a 100 nm membrane. For liposomes containing lipophilic dye 1,1′-dioctadecyl-3,3,3′,3′-tetramethylindodicarbocyanine perchlorate (DiD), the procedure was identical except that an aliquot of DiD dissolved in ethanol was added to the lipids dissolved in chloroform prior to forming the lipid film. The liposomes were stored at 4 °C and protected from light.

2.6.4 Absorption and fluorescence measurements

Absorption and emission spectra were recorded on a Hitachi U2800 spectrophotometer and a Photon Technology International Inc. fluorimeter, respectively. The MPS-PPV-coated NPs were diluted to a concentration of ~0.1 nM in water before acquiring the spectra. The amount of MPS-PPV adsorbed on the NPs was estimated by subtracting the absorbance due to scattering from a blank consisting of uncoated NPs from the absorbance of the NPs with adsorbed MPS-PPV. The sample was excited at 450 nm and the emission spectrum was recorded between 470 and 800 nm, unless otherwise noted.

2.6.5 Formation of DOTAP supported lipid bilayers on MPS-PPV-coated SiO_2 NPs

The formation of DOTAP-supported lipid bilayers on the MPS-PPV-coated SiO_2 NPs was accomplished by incubating a suspension of NPs with excess DOTAP liposomes. In our protocol,

1.5 mL of 0.11 nM MPS-PPV-coated SiO_2 NPs in water was added 10 μL at a time to 1.5 mL of 1 mM (in terms of lipid) DOTAP liposomes (13 nM in 100-nm-diameter liposomes) in Hyclone molecular biology grade water (ThermoScientific) containing 3 mM NaCl with vigorous vortex mixing. The mixture was centrifuged for 5 min at 16 060*g*, and the supernatant containing excess liposomes was removed and replaced with an equal volume of water. The bright-orange pellet was resuspended by sonication and vortex mixing. The final concentration of MPS-PPV-coated NPs with DOTAP was 0.055 nM. For imaging by cryo-TEM, 10× concentrated samples were used. Specifically, 80 nM DOTAP liposomes 400 nm in diameter and 1.1 nM MPS-PPV-coated NPs were mixed and vitrified within 30 s of mixing.

2.6.6 Monitoring the rupture of DOTAP liposomes in contact with MPS-PPV-coated SiO_2 NPs

DOTAP films were rehydrated in a 3 mM NaCl aqueous solution containing 317 μM sulfo-Cy5 carboxylic acid (Lumiprobe) to a final lipid concentration of 20 mM. At this lipid concentration, the volume fraction of the liposomes in solution is 0.07, leading to a theoretical encapsulation efficiency of Cy5 molecules of 7%. The liposomes were then subjected to eight freeze/thaw cycles and extruded though a 100 nm polycarbonate membrane. The liposomes were separated from unencapsulated Cy5 using size exclusion chromatography. DOTAP liposomes (sacrificial liposomes containing no Cy5) (200 μL, 20 mM) were run through a size exclusion column packed with Sephacryl S500HR (Sigma-Aldrich) to prime the column. Next, 200 μL of 20 mM DOTAP containing Cy5 was loaded onto the column. Liposomes containing encapsulated Cy5 molecules eluted in earlier fractions whereas unencapsulated (free) Cy5 had a longer retention time. 0.011 nM DOTAP containing encapsulated Cy5 was added to 0.11 nM MPS-PPV-coated NPs in either 300 μM $FeCl_3$ or a control containing no $FeCl_3$. The Cy5 emission spectrum was monitored immediately and 10 min after mixing. The amount of Cy5 quenching by $FeCl_3$ was proportional to the number of liposomes that formed rupture pores within the 10 min time period. The effectiveness of this method was confirmed by a control experiment where identical samples were subjected to 5 min of freezing on dry ice followed by 5 min of thawing in a water bath. The freeze/thaw cycle mechanically disrupted the lipid membrane, exposing the encapsulated Cy5 molecules to $FeCl_3$, resulting in a nearly complete quenching of their emission.

2.6.7 TIRFM imaging

Glass coverslips were cleaned and functionalized with amine groups in preparation for imaging the MPS-PPV-coated SiO_2 NPs using TIRFM microscopy. Glass jars containing eight coverslips were filled with piranha solution [1 part 30% hydrogen peroxide (Fisher Scientific) and 2 parts concentrated sulfuric acid (ACP Chemicals)] and left to soak for ca. 1 h. The coverslips were then rinsed three times with Hyclone molecular biology grade water (ThermoScientific) and three times with acetone (HPLC grade, Fisher). The coverslips were immersed in 25 mL of acetone and 0.50 mL of Vectabond (Vector Laboratories). The mixture was agitated gently and incubated for 5 min. The acetone/Vectabond mixture was poured out, and the reaction was quenched by rinsing with 2 × 25 mL of water. The coverslips were dried under a stream of nitrogen prior to being fitted with flow chambers. The flow chambers were prepared with a predrilled polycarbonate film (Grace Biolabs) and assembled on top of the coverslips. Silicone ports were glued on top of the chamber with double-sided tape. The volume of the sample chamber was ca. 10 μL.

Electrostatic interactions with the positively charged glass coverslip allowed for the selective adsorption of the negatively charged MPS-PPV-coated SiO_2 NPs on the surface while preventing the nonspecific adsorption of the positively charged DOTAP liposomes. A good surface density of NPs was achieved by injecting 20 μL of 50 pM MPS-PPV-coated NPs in water into the sample chamber and incubating for ca. 1 min. A total of 5 × 20 μL of 3 mM NaCl was then injected to wash away any NPs that were not bound to the surface. Images were acquired while flowing liposome suspensions in 3 mM NaCl aqueous solutions at a rate of 5 μL/min through the chamber using a syringe pump (Harvard Apparatus PHD 2000 Infusion). All experiments were conducted at room temperature (22–25 °C).

The imaging experiments were performed using an Olympus IX71 microscope adapted with an Olympus IX2-RFAEVA-2 turnkey TIRFM module. The excitation source was either the 488 or 514 nm output of a continuous wave argon ion laser (SpectraPhysics). The laser power measured out of the objective was 220 μW for the 488 nm excitation and 580 μW for the 514 nm excitation (ca. 1.0 and 2.6 W cm^{-2}, respectively). The laser beam was introduced by a single-mode fiber optic and was directed by a dichroic beamsplitter (z488rdc or z514rdc, Chroma) to the sample via a high numerical aperture (N.A. = 1.45) oil-immersion objective (Olympus PLAN APO 60×). The fluorescence emission was collected through the same objective and was then transmitted

through an emission filter (HQ500 LP or HQ530 LP, Chroma) and was then separated into two emission channels by a series of dichroic mirrors (640dcxr, Chroma) The images were acquired at an acquisition rate of 50–100 ms using a Cascade 512B EMCCD camera (Roper Scientific, Inc.) controlled by Image Pro software. Intensity versus time trajectories were extracted from background-subtracted images processed using a home-built Matlab routine based on algorithms previously reported by the Ha group.[45]

2.6.8 Cryogenic transmission electron microscopy

To prepare the samples for imaging, 5 μL of sample was added to glow-discharged QUANTIFOIL R 2/2 copper grids. Samples were blotted and frozen hydrated by plunging into a bath of liquid ethane slush. The samples were stored at liquid-nitrogen temperature until transfer to a 626 Single Tilt Cryotransfer System (Gatan Inc.) and observed with an FEI G2 F20 cryo-STEM microscope operated at 200 kV (FEI, Inc.). Images were recorded on a Gatan Ultrascan 4k × 4k Digital (CCD) Camera System camera at a nominal magnification of 50 000× at a defocus level of 4 μm. Samples consisted of MPS-PPV-coated NPs, MPS-PPV-coated NPs incubated for 30 min with 80 nM DOTAP liposomes (excess liposomes were removed by centrifugation), and MPS-PPV-coated NPs mixed with 80 nM DOTAP liposomes immediately before vitrifying. The MPS-PPV-coated NP concentration was 1.1 nM for all samples.

2.6.9 Dynamic light scattering

DLS measurements were acquired using a Malvern Zetasizer Nano ZS equipped with a 633 nm red laser. The samples were equilibrated to a temperature of 25 °C and diluted to a concentration of approximately 0.1 nM in terms of the number of particles. The data was fit using the CONTIN algorithm. The plots shown are the number distributions derived from the raw intensity data.

2.7 Supporting information

2.7.1 Characterization of nanoparticles by transmission electron microscopy and dynamic light scattering

Particle size was determined after each modification step by transmission electron microscopy (TEM) and dynamic light scattering (DLS). The TEM images did not show an appreciable change in the particle core size or appearance after either the aminosilanization or the MPS-PPV adsorption steps (Figure 2.6). DLS measurements showed no change after aminosilanization of the SiO_2 NPs. Upon adsorption of MPS-PPV on SiO2NH3+ the size distribution broadened and shifted toward larger sizes. (Figure 2.7). Although MPS-PPV is a water-soluble polymer, it has a tendency to adopt a self-aggregated conformation in water, likely due to considerable contributions from its hydrophobic backbone. This aggregation, or possibly polymer bridging between several MPS-PPV coated nanoparticles could explain the increased size.

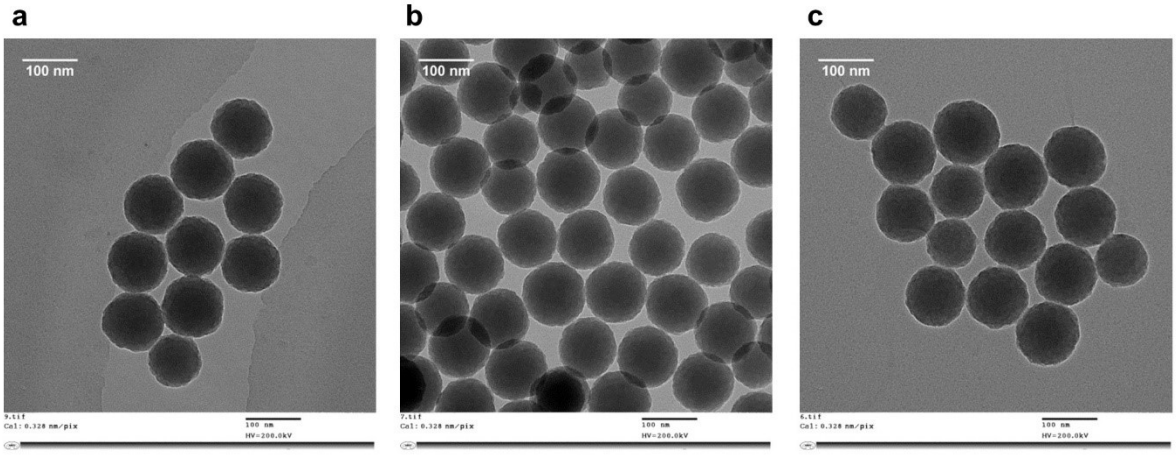

Figure 2.6. Transmission electron micrographs of a) SiO_2 NPs, b) $SiO_2NH_3^+$ NPs, and c) MPS-PPV coated $SiO_2NH_3^+$ NPs. The mean core sizes were 111 (±8) nm, 104 (±12) nm, and 108 (±10) nm, respectively. Scale bar = 100 nm.

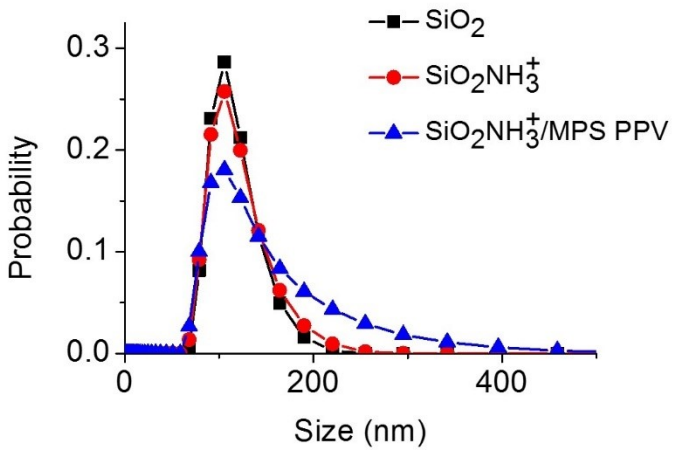

Figure 2.7. Size distributions of SiO_2 NPs, $SiO_2NH_3^+$ NPs, and MPS-PPV coated $SiO_2NH_3^+$ NPs as determined by dynamic light scattering measurements.

2.7.2 Characterization of MPS-PPV coated SiO_2 NPs by UV-vis spectroscopy

In order to determine the amount of MPS-PPV adsorbed on the NPs, the UV-vis absorbance spectra of $SiO_2NH_3^+$ NPs and MPS-PPV coated $SiO_2NH_3^+$ NPs at equal concentrations were acquired (Figure 2.8). The absorbance spectrum of the MPS-PPV coated NPs contained contributions from both the scattering of the SiO_2 NPs and the absorbance of MPS-PPV. In order to deconvolute the spectrum into these two components, the absorbance spectrum of the $SiO_2NH_3^+$ NPs was subtracted from the spectrum of the MPS-PPV coated NPs to remove the contribution due to scattering. The spectrum remaining after subtraction resembled the spectrum of unadsorbed (free) MPS-PPV. Using Beer's Law and an extinction coefficient of 3460 M-1cm-1 per polymer repeat unit, the concentration of MPS-PPV was calculated to be 13 μM. Considering that the NP concentration in the sample was 13 nM, the number of polymer repeat units per NP was determined to be approximately 100,000. The surface area of one MPS-PPV monomer unit was estimated to be 0.36 nm^2 and the total polymer surface area per particle was then 36,000 nm^2. Given that the surface area of a sphere with r = 50 nm is 31,000 nm2, there is enough to MPS-PPV adsorbed onto the particles to cover the surface approximately 1.2 times.

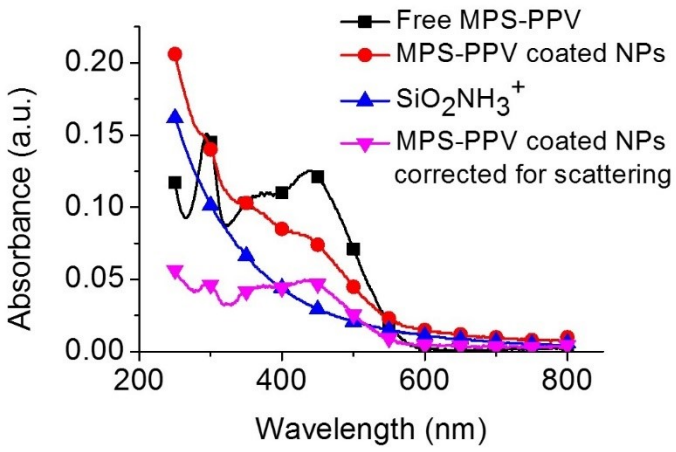

Figure 2.8. Absorbance spectra of 0.13 nM $SiO_2NH_3^+$ NPs and 0.13 nM MPS-PPV coated NPs in water (blue triangles and red circles, respectively). The spectrum of the $SiO_2NH_3^+$ NPs was subtracted from the spectrum of the MPS-PPV coated NPs to correct for the contribution of scattering to the spectrum (inverted purple triangles). The subtracted spectrum is qualitatively similar to the spectrum of free MPS-PPV, as expected (black squares).

2.7.3 Characterization of MPS-PPV coated SiO_2 NPs by ensemble fluorescence spectroscopy

The emission spectrum of the MPS-PPV coated SiO_2 NPs and the emission spectrum of free MPS-PPV were acquired and then compared. There were no spectral differences between the emission spectrum of adsorbed and non-adsorbed MPS-PPV but the emission intensity is quenched 66% upon adsorption onto the nanoparticle (Figure 2.9). The promotion of increased interchain contacts by the NP scaffolding likely increases the amount of polymer self-quenching by increasing the efficiency of exciton hopping to non-emissive trap sites.

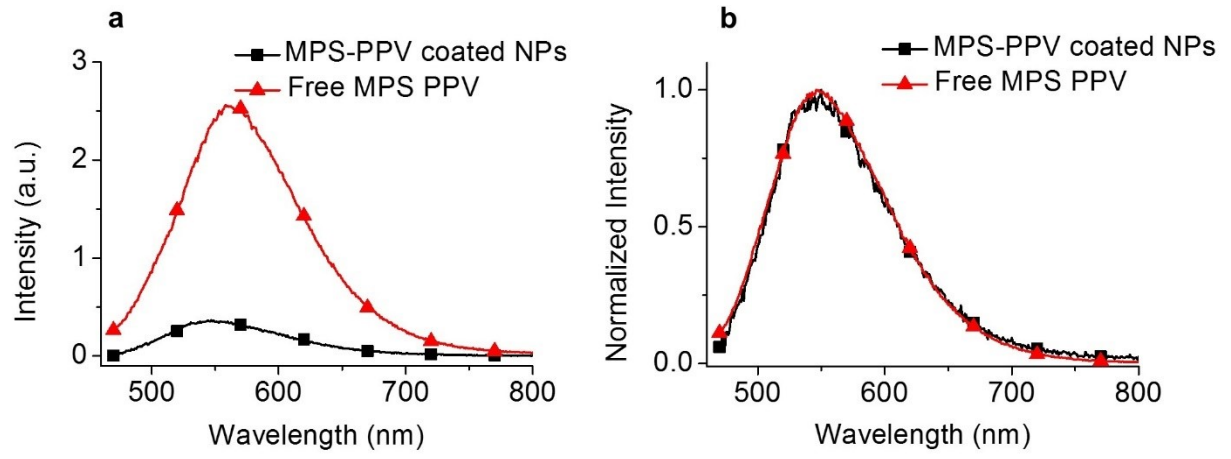

Figure 2.9. Characterization of NPs by fluorescence spectroscopy. a) Emission spectrum of MPS-PPV coated NPs (black squares) and free MPS-PPV (red triangles) in 3 mM NaCl. b) Normalized emission spectra of MPS-PPV coated NPs (black squares) and free MPS-PPV (red triangles) emphasize that the emission profile of MPS-PPV is unchanged upon adsorption on the NP support. The excitation wavelength was 450 nm for all samples.

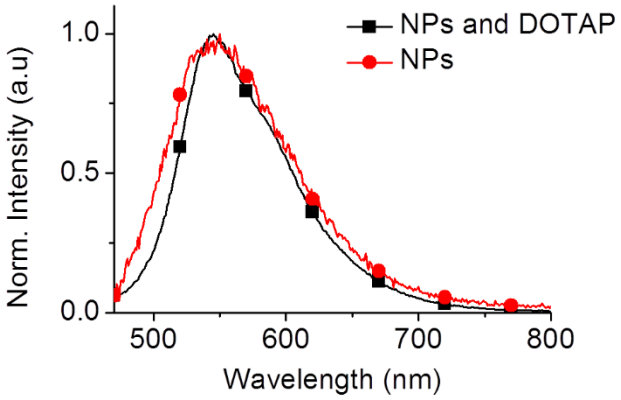

Figure 2.10. Characterization of NPs before and after SLB formation by fluorescence spectroscopy. Normalized emission spectra of 0.1 nM MPS-PPV coated NPs before (red circles) and after (black squares) addition to 13 nM 100 nm DOTAP liposomes in 3 mM NaCl. Spectra are the same as those shown in Figure 2.1A. The excitation wavelength was 450 nm.

2.7.4 Determining the correct solution ionic strength to prevent non-specific adsorption of DOTAP liposomes on aminosilanized glass coverslips for TIRFM studies

To ensure that the interaction between the NPs and the liposomes observed during TIRFM experiments was specific, control experiments with dye-labelled liposomes were performed to assess the extent of non-specific liposome adsorption on the surface. A total of 20 µL of 100 µM

DOTAP (400 nm liposomes) containing the red emitting, lipophilic dye 1,1′-dioctadecyl-3,3,3′,3′-tetramethylindodicarbocyanine perchlorate (DiD) in a lipid to dye ratio of 256:1 were injected into the imaging chamber. The liposomes were incubated for five minutes and then the chamber was rinsed with a solution having the same NaCl concentration. The surface was then imaged to determine the extent of non-specific liposome adsorption (Figure 2.11). The adsorption of liposomes on the surface was first observed at a NaCl concentration of 4 mM (B), with the number of adsorbed liposomes greatly increasing as the NaCl concentration was increased to 50 mM (C). For this reason, experiments were conducted at 3 mM NaCl (A) to minimize the non-specific adsorption of liposomes on the surface.

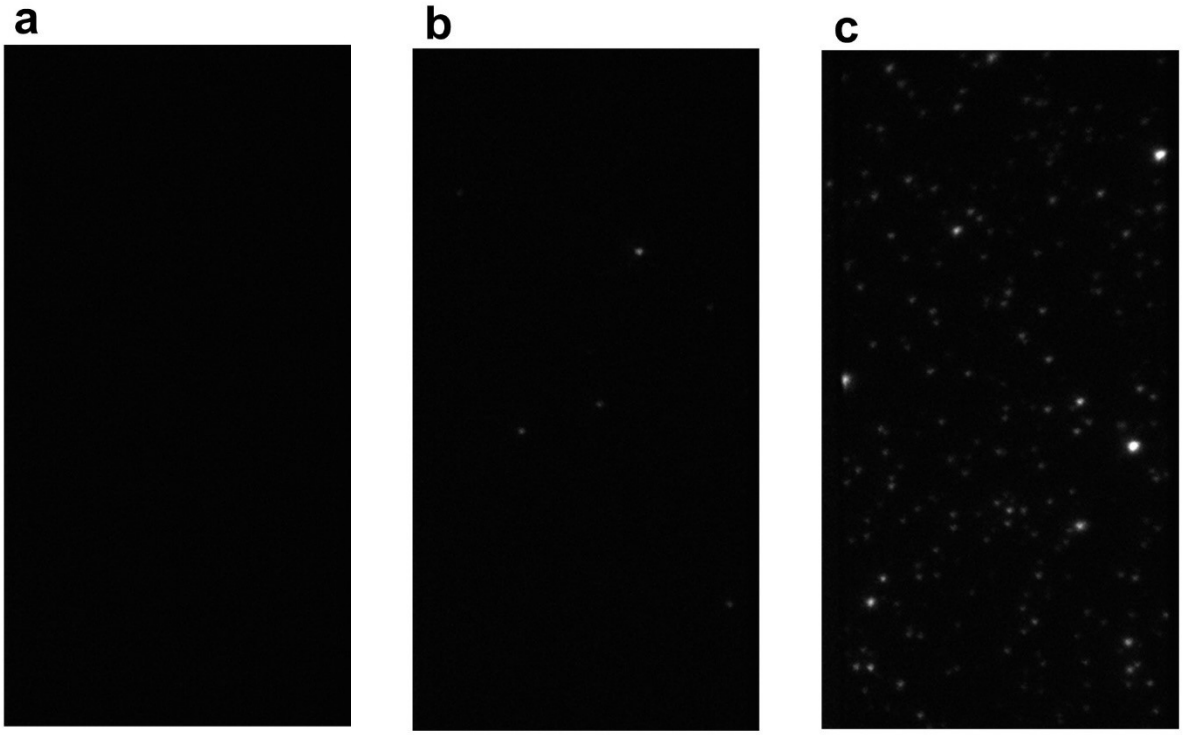

Figure 2.11. Non-specific adsorption of DOTAP liposomes. Images were acquired after five minutes of incubation on a aminosilanized glass coverslips in solution conditions of a) 3 mM NaCl, b) 4 mM NaCl, and c) 50 mM NaCl.

2.7.5 Enhancement of MPS-PPV adsorbed on SiO_2 NPs when DOTAP liposomes are flowed at a high concentration

DOTAP liposomes 100 nm and 400 nm in diameter were flowed over surface-immobilized MPS-PPV coated NPs at high liposome concentrations of 13 and 8 nM, respectively. Both the mean enhancement (23-fold and 22-fold, respectively) and the distribution of enhancements (Figure 2.12) were indistinguishable between the two liposome samples. According to our model, liposomes adsorb on the surface of the MPS-PPV coated NPs causing the deaggregation of MPS-PPV and its concomitant fluorescence enhancement. Under these conditions, liposomes were present in excess such that the surface of the NPs was passivated with adsorbed liposomes and the enhancements observed were maximal. The fact that the 100 nm and 400 nm populations are indistinguishable is consistent with this model in that the size of the liposome does not dictate the extent of the NP emission enhancement so long as MPS-PPV has access to an excess of lipids. The small percentage of outliers (<5%) lying at enhancement values > 50 can be explained by considering that the calculation of the enhancement is particularly sensitive to errors in the determination of the initial intensity. Given the limited dynamic range of the CCD camera, it was necessary to start with a low initial intensity in order to capture the large emission enhancements. An underestimation of the initial intensity could lead to artificially high enhancements as these values were close to the background intensity level. Indeed, the top 5% of enhancements were found to have an average initial intensity of 44±16 which was significantly lower than the average initial intensity of all particles at 81±43. Despite the existence of several outliers, the mean enhancement for both samples agreed well with the enhancement determined in ensemble fluorescence studies.

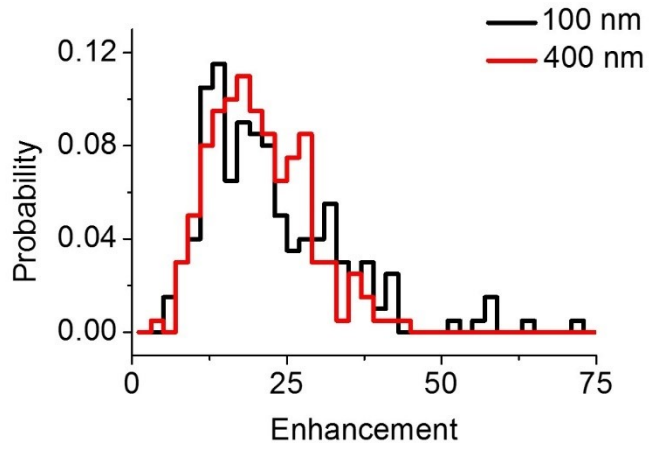

Figure 2.12. Histogram of enhancement values for MPS-PPV coated NPs observed while flowing a high concentration of DOTAP liposomes. 100 nm and 400 nm DOTAP liposomes were flowed

at 13 and 8 nM, respectively. Enhancement values shown in the histogram were determined from the fluorescence intensity versus time trajectories of 200 MPS-PPV coated NPs for both conditions.

2.7.6 Distribution of single MPS-PPV coated NP intensities

The amount of MPS-PPV adsorbed onto the SiO_2 NPs was expected to depend on the surface area of the underlying SiO_2 support. The distribution of MPS-PPV coated NP fluorescence intensities observed during TIRFM experiments was related to the distribution of MPS-PPV coated NP sizes obtained by dynamic light scattering measurements (Figure 2.13).

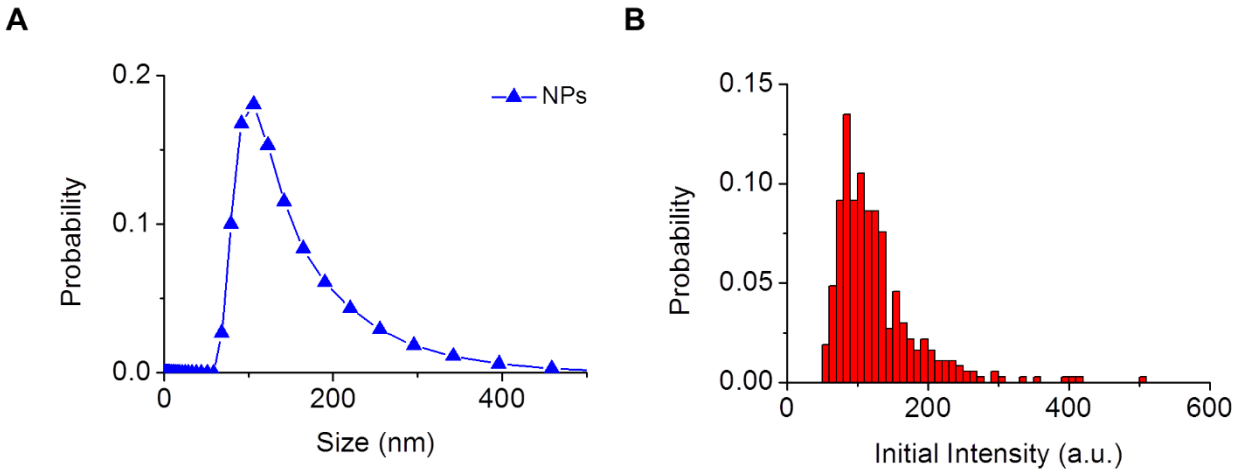

Figure 2.13. Distribution of single MPS-PPV coated NP intensities A) Size distribution of MPS-PPV coated $SiO_2NH_3^+$ NPs determined by dynamic light scattering. B) Histogram of the initial fluorescence intensity values recorded for 371 individual MPS-PPV coated NPs during TIRFM experiments.

2.7.7 Monitoring the rupture of DOTAP liposomes

A dye leakage experiment with the red-emitting fluorophore sulfo-Cy5 carboxylic acid was performed to provide additional evidence that the majority of DOTAP liposomes do not rupture upon adsorption onto the MPS-PPV coated NPs over the timescale observed during the TIRFM experiments. Cy5 was encapsulated within DOTAP liposomes suspended in a solution of the quencher $FeCl_3$. Positively charged Fe^{3+} ions cannot cross the DOTAP membrane but are present in sufficient amount to efficiently quench the emission of the encapsulated fluorophores if the membrane ruptures and releases them into solution. MPS-PPV coated NPs were added to a $FeCl_3$ solution containing DOTAP liposomes with encapsulated Cy5 molecules. The emission spectrum

of Cy5 was measured immediately and ten minutes after mixing (Figure 2.14). Only a slight quenching of the Cy5 emission was observed, which was consistent with relatively slow liposome rupture kinetics under these conditions. In order to prove that the assay was capable of detecting liposome rupture, the liposomes were exposed to conditions that mechanically disrupted the membrane. The mixture of DOTAP, NPs, and $FeCl_3$ was frozen on dry ice (5 min) and then thawed in a water bath (5 min). After this cycle the fluorescence intensity was nearly completely quenched, consistent with liposome rupture rendering the contents vulnerable to quenching by $FeCl_3$

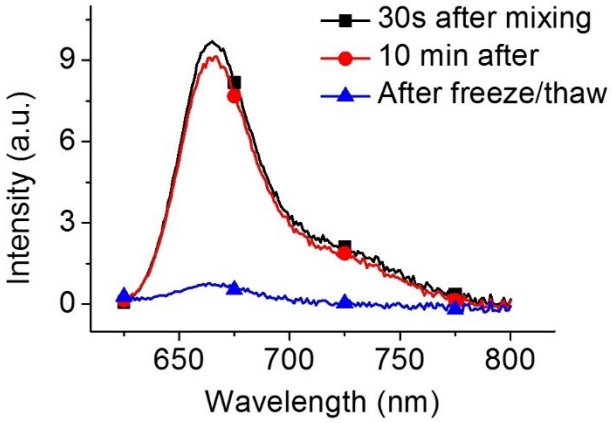

Figure 2.14. Quenching study to quantify the rupture of DOTAP liposomes. Emission intensity of the fluorophore sulfo-Cy5 carboxylic acid initially encapsulated inside of 100 nm DOTAP liposomes at a density of 100 Cy5 per liposome. A 1.1 nM liposome solution in 300 μM $FeCl_3$ was mixed with 0.11 nM MPS-PPV coated NPs. The Cy5 emission spectrum was recorded 30 s (black squares) and 10 min (red circles) after mixing. Also shown is the spectrum of an identical solution that was frozen on dry ice to mechanically disrupt the membrane upon thawing to room temperature (blue triangles). The excitation wavelength was 600 nm for all samples.

Chapter 3: Biomimetic light harvesting antenna based on the self-assembly of conjugated polyelectrolytes embedded within lipid membranes

Reproduced with permission from: "Biomimetic light harvesting antenna based on the self-assembly of conjugated polyelectrolytes embedded within lipid membranes", **Christina F. Calver**, Kirk S. Schanze, & Gonzalo Cosa, *ACS Nano*, **2016**, *10*, 10598-10605.

Author contributions: **Christina F. Calver** performed experiments, analyzed data, and co-wrote the paper. **Prof. Kirk S. Schanze** provided the PPE-CO_2 polymer and provided feedback on the manuscript. **Prof. G. Cosa** designed the project, guided the interpretation of data, and co-wrote the paper.

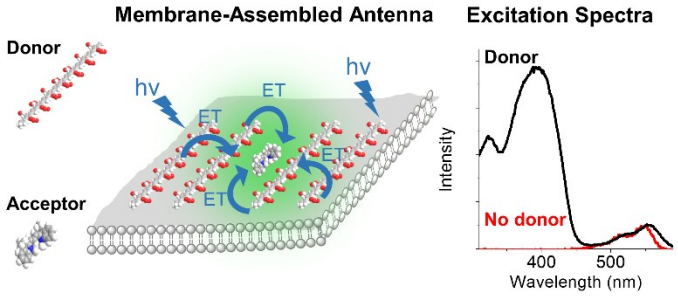

3.0 Preface

Chapter 2 illustrated how liposomes readily interacted with CPE-coated NPs, rapidly deforming to follow their surface curvature and eventually rupturing to form supported lipid bilayers containing embedded CPE. While this study focused on the dynamics of the early stages of the CPE/lipid structure formation, understanding the organization of these structures at the molecular level is another topic of fundamental importance. In Chapter 3, we explore the self-assembly of polyanions containing a poly(phenylene ethynylene) backbone and charged carboxylate side chains (PPE-CO_2) within the membrane of DOTAP liposomes. The PPE-CO_2-containing liposomes were then evaluated toward their performance as a light harvesting antenna, where the organization of the light-absorbing CPEs within the membrane is a critical factor in determining the efficiency of energy migration to a trap/reaction centre.

3.1 Abstract

Here we report a biomimetic light-harvesting antenna based on negatively charged poly(phenylene ethynylene) conjugated polyelectrolytes assembled within a positively charged lipid membrane scaffold constructed by the lipid 1,2-dioleoyl-3-trimethylammonium-propane (DOTAP). Light harvested by the polymers was transferred via through-space mechanisms to a lipophilic energy acceptor (the cyanine dye DiI) whose effective molar absorption was enhanced by up to 18-fold due to the antenna effect. Absorption amplification of DiI was found to be due primarily to direct energy transfer from polymers. The efficiency of homoenergy transfer among polymers was next probed by the membrane embedding fullerene derivative phenyl-C_{61}-butryic acid methyl ester (PCBM) acting as an electron acceptor. PCBM was able to quench the emission of up to five polymers, consistent with a modest amount of homotransfer. The ability of the membrane to accommodate a high density of polymer donors without self-quenching was crucial to the success of electronic energy harvesting achieved. This work highlights the potential of lipid membranes as a platform to organize light-harvesting molecules on the nanoscale toward achieving efficient energy transfer to a target chromophore/trap.

3.2 Introduction

Photosynthesis relies on well-organized arrays of pigment–protein complexes embedded in lipid membranes to capture light energy from the sun. Following excitation of any pigment in the array, the electronic energy is next transferred *via* homoenergy transfer among the supramolecular assembly of chromophores, exploiting an energy gradient, to the reaction center where charge separation occurs.[1-6] Significant efforts are being made to emulate nature's design toward capturing solar energy by assembling artificial light-harvesting antennas coupled to a target chromophore or trap.[7-9] Paramount to a successful outcome is the ability to control the orientation and distance between light-harvesting chromophores as well as between these chromophores and the trap/energy acceptor to maximize energy transfer.[4, 10] One approach is to link donor and acceptor chromophores together *via* covalent bonds. Although this strategy allows for precise control over position to be achieved, synthetic complexity poses limits on the scalability as well as on the number of energy-harvesting donors that can be feasibly incorporated.[10-15] Self-assembly has been proposed as an alternative approach that avoids synthetic complexity while at the same

time increases the flexibility of the design by bringing components together in a modular fashion.[16-30] In self-assembled systems, several challenges must be met: (i) the self-assembly strategy must be able to bring the light-harvesting components within close proximity; (ii) the components should preferably be brought together in such a way that their relative orientations maximize energy transfer; and (iii) energy losses due to self-quenching should be minimized.

Here we report a self-assembled light-harvesting antenna based on a lipid membrane scaffold. The choice of a lipid membrane to compartmentalize and direct the self-assembly of the light-harvesting components was based on a number of advantages that it provides. The lipid molecules themselves self-assemble to form predictable and well-defined structures with long-range order. The innate organization of the lipid bilayer may also be potentially exploited as a means to bring donors and acceptors into close proximity and direct their relative orientation to favor energy transfer. In addition, the presence of a membrane environment opens up the possibility of interfacing synthetic chromophores with naturally occurring reaction center or photostabilizing molecules such as carotenoids to fabricate functionally compatible hybrid light-harvesting complexes.

3.3 Results and discussion

3.3.1 Design of the light harvesting antenna

A conjugated polyelectrolyte with a poly(phenylene ethynylene) backbone and carboxylate side chains with an average chain length of seven polymer repeat units (PRUs) was chosen as the light-harvesting material (PPE-CO_2-7, see Figure 3.1).[31] This choice was inspired by previous observations in our group and by others that conjugated polyelectrolytes, including PPE-CO_2-7, will spontaneously embed within the membrane of zwitterionic (DOPC) or positively charged (DOTAP) liposomes due to a combination of favorable hydrophobic and electrostatic interactions.[32-38] Although PPE-CO_2-7 has a strong tendency to form aggregates in aqueous solution, the emission spectrum of the membrane embedded polymer was characteristic of single PPE chains (λ_{max} absorbance/emission = 400/443 nm), revealing that the polymer–lipid interactions are stronger than the polymer–polymer interactions.[39] We relied upon the solvation environment of the membrane to ensure that the PPE-CO_2-7 polymers were uniformly distributed. The favorable electrostatic and hydrophobic interactions between the polyanion and the positively

charged membrane provided a most suitable "solvent" preventing the polymers from aggregating. The membrane thus allows for the assembly of polymers within close enough proximity for many donors to be packed within the capture area of a single acceptor molecule while avoiding losses due to self-quenching. In addition, the close proximity of the polymer chains was anticipated to facilitate efficient energy migration *via* through space energy transfer among adjacent polymer chains (homo-FRET). Efficient energy migration could in theory enhance the performance of the light-harvesting system by spatially extending the effective capture area of the acceptor.

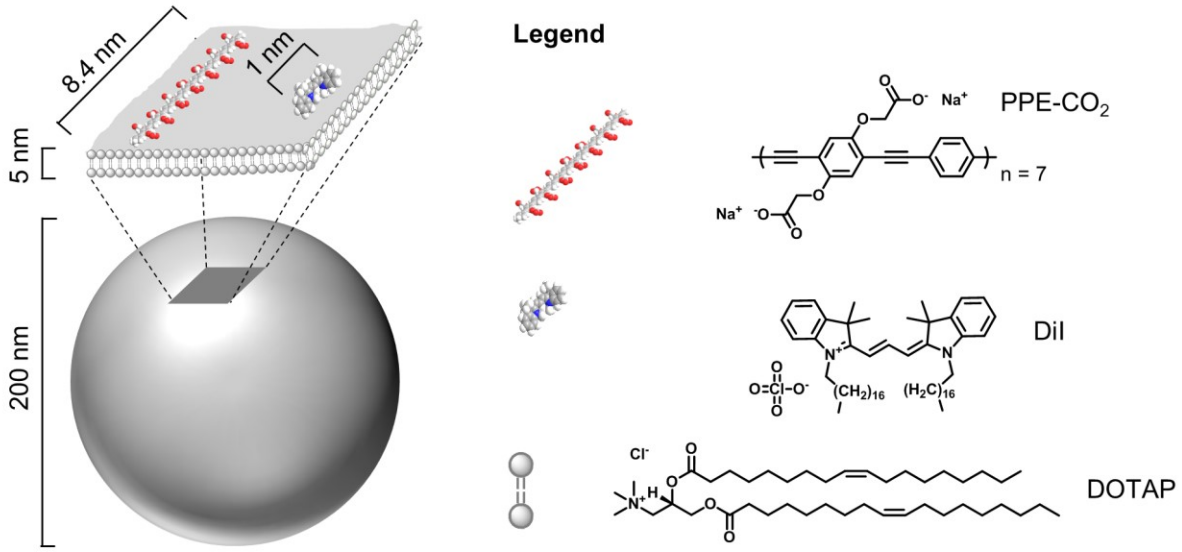

Figure 3.1. Chemical structures of the conjugated polyelectrolyte PPE-CO_2-7, the lipophilic acceptor DiI, and the lipid DOTAP utilized in this study. Shown is a not-to-scale diagram with a lipid slab to illustrate the dimensions of the various elements in the system. We note that the hydrophobic backbone of the polymer is most likely intercalating the lipid bilayer with the charged side-chains facing the water–lipid interface.

To demonstrate that the membrane-embedded polymers functioned as a light-harvesting antenna, the energy transfer between the polymers and a membrane-bound trap/energy acceptor, the lipophilic dye DiI (3H-indolium, 2-[3-(1,3-dihydro-3,3-dimethyl-1-octadecyl-2H-indol-2-ylidene)-1-propenyl]-3,3-dimethyl-1-octadecyl-perchlorate (λ_{max} absorbance/emission = 550/585 nm), was studied (see Figure 3.1). The large superposition of the PPE-CO_2-7 emission spectrum (in its deaggregated form in the membrane) with the absorption spectrum of DiI, together with the large molar extinction coefficients characterizing both chromophores (ε = 196,000 and 148,000 $M^{-1}cm^{-1}$ for PPE-CO_2-7 and DiI, respectively) provided for efficient light capture with a suitable

energy landscape for dipole–dipole coupling and energy transfer from PPE-CO_2-7 to DiI (see Figure 3.7). Favorable electrostatic and hydrophobic interactions between the membrane and the CPE drive the initial membrane-polymer association, but other factors, particularly the intrinsic curvature of the chosen lipids, are critically important in determining the final self-assembled structure. Here, the polymers presumably rest along the bilayer surface according to previous studies,[40] as has been shown with DiI,[41] rather than across the bilayer, an arrangement that may favor efficient coupling of the donor and acceptor transition dipoles. As a consequence of the light harvesting by PPE-CO_2-7, the effective molar absorption coefficient of DiI was increased by *ca*. 18-fold. The PPE-CO_2 antenna not only enhanced the DiI capture radii spatially but also spectrally extends its effective absorption to the blue region of the solar spectrum, where PPE-CO_2-7 absorbs.

3.3.2. Incorporation of PPE-CO_2-7 into DOTAP liposomes

In order to assess the ability of the membrane to accommodate PPE-CO_2-7, we conducted titrations with increasing amounts of polymer added to solutions containing liposomes of the cationic lipid 1,2-dioleoyl-3-trimethylammonium-propane (DOTAP) 200 nm in diameter and prepared in an aqueous solution. Freezing the sample on dry ice and thawing it in a water bath at room temperature was found to increase the amount of deaggregated polymer incorporated in the membrane. The emission intensity attributed to deaggregated polymer chains (λ_{max} = 443 nm) was observed to increase linearly with increasing polymer concentration up to a polymer repeat unit (PRU):lipid ratio of 0.14 (representing 7181 polymers per liposome) (Figure 3.2). PRU:lipid ratios were calculated based on estimations of the lipid concentration after extrusion. The PRU:lipid ratio is nominally 0.10 if losses during liposome extrusion are not accounted for. Based on this polymer loading, a polymer–polymer spacing of *ca*. 1 nm and an effective surface coverage of 43% were calculated, assuming that the polymers form a monolayer (*i.e*., do not stack) within the membrane (see section 3.7.4 for details). Above this ratio, the growth of a new emission band characteristic of the polymer aggregates in water (λ_{max} = 530 nm) was observed, indicating that the membrane was saturated with polymer and that the excess existed as aggregates in solution.

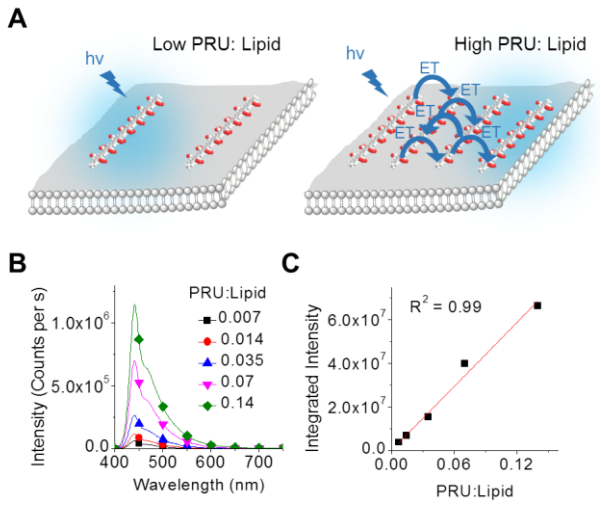

Figure 3.2. Incorporation of PPE-CO_2-7 into DOTAP liposomes. (A) Diagram showing the excitation of PPE-CO_2-7 polymers embedded within a lipid membrane at low and high polymer loadings (left and right, respectively). At high polymer loadings, there is the possibility that excitons may migrate *via* homo-FRET (blue arrows). (B) Emission spectra of PPE-CO_2-7 loaded into 20 pM 200 nm diameter DOTAP liposomes at varying PRU:lipid ratios obtained upon excitation at 390 nm. The concentration of PPE-CO_2-7 was varied, while the lipid concentration was held constant. Spectra plotted are the average of three spectra obtained from experiments carried out in triplicate. (C) Integrated intensity of the emission spectra shown in panel B plotted *versus* the number of polymer repeat units per lipid.

Remarkably, the PPE-CO_2-7 polymers could be loaded into the membrane at a high density (the average center-to-center separation between polymer chains was estimated to be *ca*. 1.9 nm at a PRU:lipid ratio of 0.14, see section 3.7.4) with minimal self-quenching of the emission intensity. In this sense, the polymer-based antenna effectively mimics naturally occurring light-harvesting antennas, where center-to-center chromophore separations of 0.6–2.5 nm are also achieved without self-quenching.[4] Equally remarkably, the linear correlation between the polymer loading and the emission intensity showed that this level of packing may by achieved without additional losses due to self-quenching, a result that makes the PPE-CO_2-7 saturated membrane an excellent candidate for a light-harvesting antenna. The presence of even small amounts of defective, nonemitting sites in conjugated polymer materials can lead to large losses in devices because of rapid energy transfer to these sites.[42-43] The fact that losses are not observed speaks to the apparent absence of defects in the PPE-CO_2-7 polymers utilized here (the emission quantum yield for PPE-CO_2-7 within the membranes was estimated to be similar to that reported in methanol, *ca*. 0.64).[31] The rigidity of the relatively short, rod-like negatively charged polymers

together with the scaffolding provided by the cationic lipid may impart the polymer-membrane self-assembled structures desirable spectroscopic and mechanical properties enabling efficient chain packing, ultimately yielding an efficient light-harvesting antenna.

3.3.3 Cryo-TEM imaging of lipid bilayers containing embedded PPE-CO_2-7

Cryogenic transmission electron microscopy (cryo-TEM) was next performed in order to gain an understanding of the lipid/polymer structures at the molecular level. Equal volumes of aqueous solutions of PPE-CO_2-7 (1.4 mM in terms of PRUs) and freshly prepared liposomes (10 mM lipid, *ca*. 28 nM liposomes) were mixed together to yield a sample with a PRU:lipid ratio of 0.14, representing a membrane saturated with polymer (*vide supra*). Samples were then vitrified immediately following mixing and imaged using cryo-TEM (see also Figure 3.8 for negative stained TEM control images). The structures observed were predominately spherical and unilamellar (Figure 3.3A), with an average diameter of 130 ± 50 nm (N = 162). Images obtained at higher magnification revealed that the membrane retained a bilayer structure with the lipid head groups of the inner and outer membrane leaflets clearly visible after polymer insertion (Figure 3.3B). Figure 3.3C shows a zoomed in portion of Figure 3.3B to more clearly visualize the two layers of the bilayer. The thickness of the lipid bilayer was *ca*. 4 nm, consistent with other reports of lipid membranes imaged by cryo-TEM,[33, 44] showing that even large amounts of embedded polymer does not lead to substantial thickening of the membrane.

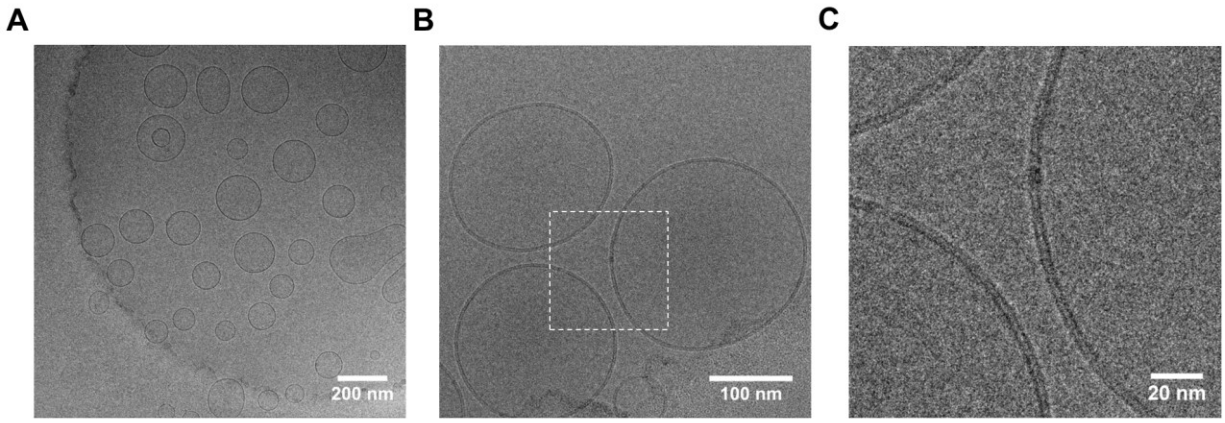

Figure 3.3. Cryo-TEM images of vitrified aqueous solutions of DOTAP liposomes containing PPE-CO_2-7. (A) Low-magnification image showing a selection of representative liposomes. (B) High-magnification image where the head groups of the inner and outer membrane leaflets of the bilayer are visible. (C) Expansion of the area enclosed by the dashed white square superimposed on panel B to aid in visualizing the bilayer. The liposome concentration was 28 pM and the polymer concentration was 0.14 PRU:lipid.

3.3.4 Absorption amplification of DiI

The performance of the PPE-CO_2-7 antenna was subsequently evaluated by determining the amount of energy transferred from the antenna to the lipophilic acceptor/trap chromophore DiI. The experiments were conducted by exciting solutions of DOTAP liposomes 200 nm in diameter and containing on average 614 DiI and 614 PPE-CO_2-7 molecules at 390 nm, near the absorbance maximum of the polymer. The average DiI loading employed, equivalent to a 1.7×10^{-3} DiI:lipid mole ratio, was selected to ensure a large separation (*ca*. 16 nm, see section 3.7.5 for details) between adjacent DiI molecules within the liposome bilayer, precluding homoenergy transfer between DiI molecules from taking place. In turn, the polymer loading was chosen such that the average edge-to-edge separation between DiI and PPE-CO_2-7 was 5 nm, (see section 3.7.5 for details), which is equal to the Forster radius (R_0) estimated for a single PPE-CO_2-7/DiI donor/acceptor pair such that at least some extent of energy transfer from the polymer to DiI is expected. Consistent with energy transfer from the PPE-CO_2-7 antenna to DiI, we observed efficient sensitization of DiI emission (λ_{max} = 580 nm) by photoexcited PPE-CO_2-7 when both were present in the membrane of DOTAP liposomes. This was evidenced by the appearance of a new peak in the excitation spectrum whose shape and position corresponded to the PPE-CO_2-7 absorption spectrum and whose intensity was related to the extent to which sensitation takes place (Figure 3.4A). A 45% quenching of the PPE-CO_2-7 emission intensity in the presence of DiI

compared to a sample containing the same amount of polymer but no DiI was observed, also consistent with FRET (Figure 3.4B). Control experiments with liposomes containing DiI but no polymer showed no DiI emission upon excitation at 390 nm (*i.e.*; direct excitation of DiI was negligible), see Figure 3.4B).

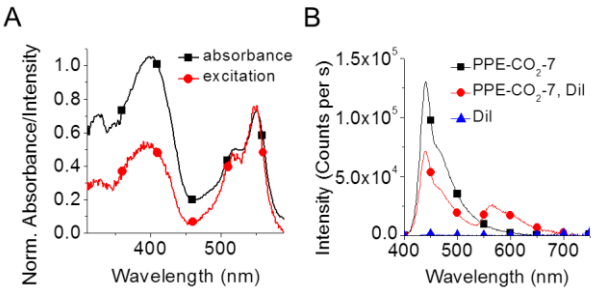

Figure 3.4. Energy transfer from PPE-CO_2-7 to DiI. (A) Absorbance spectrum of a sample of 390 pM 200 nm diameter DOTAP liposomes containing 614 PPE-CO_2-7 polymers per liposome (black squares) and excitation spectrum obtained by monitoring DiI emission at 600 nm of a sample containing 20 pM liposomes and also containing 614 polymers per liposome (red circles). The spectra were first normalized by the DiI absorption/excitation peak at 550 nm and were then normalized by the value of the PPE-CO_2-7 absorbance at 400 nm in order to more clearly show what fraction of the energy absorbed was ultimately transferred to DiI. (B) Emission spectrum of 20 pM 200 nm diameter DOTAP liposomes containing 614 PPE-CO_2-7 polymers per liposome (black squares), both 614 PPE-CO_2-7 and 614 DiI molecules per liposome (red circles), or 614 DiI per liposome (blue triangles). PPE-CO_2-7 was excited at 390 nm. Scattering from the liposomes has been subtracted from all spectra, and the contribution of PPE-CO_2-7 emission has also been subtracted from the excitation spectrum (see sections 3.7.6 and 3.7.7 and Figures 3.9 and 3.10 for details).

The absorption amplification of DiI in the presence of PPE-CO_2-7 (defined as the ratio of the area of the PPE-CO_2-7 excitation peak to the area of the DiI excitation peak) provided an additional quantitative measure of the antenna performance (Figure 3.4).[17, 24] In order to find the absorption amplification of DiI, increasing amounts of polymer were added to liposome samples containing a constant amount of DiI (614 DiI/liposome). The excitation spectra of the samples were next acquired by monitoring the DiI emission at 600 nm. Following spectral deconvolution (see section 3.7.7 and Figure 3.10 for details), the peak-area ratio of the peaks observed at 550 nm (corresponding to the direct excitation of DiI) and at 400 nm (attributed to the sensitization of DiI upon PPE-CO_2-7 excitation) yielded a value for the absorption amplification. This value allowed us to quantify the energy transfer from the antenna to the acceptor/trap at various loadings of PPE-

CO_2-7. The contribution of polymer emission at the monitoring wavelength of 600 nm was subtracted from the excitation spectra such that the polymer excitation peak only represented energy that was transferred to DiI (see section 3.7.7 and Figure 3.10 for details). Importantly, control experiments showed that the fluorescence quantum yield of DiI was unchanged in the presence of PPE-CO_2-7 (Figure 3.11), justifying use of the sensitized DiI emission as a means to quantify the amount of energy transferred from the polymer and collected by DiI.

The absorption amplification of DiI increased as a function of polymer loading (Figure 3.5B), indicating that DiI collected more energy from PPE-CO_2-7 at higher polymer loadings. Specifically, at low PPE-CO_2-7 loadings, when homo-FRET between adjacent polymer chains is expected to be negligible, DiI may only collect energy from its nearest neighbor (Figure 3.5A). Assuming a single donor partner located at an optimal distance, the absorption amplification would be expected to reach a maximum value determined by the area of the PPE-CO_2-7 excitation peak divided by the DiI excitation peak in units of molar absorptivity ($M^{-1}cm^{-1}$). This ratio was found to be equal to 2.4 (this upper bound limit would be encountered for a 100% energy transfer condition, see Figure 3.12). At the highest polymer loading (7181 polymers per liposome, see section 3.7.3 for calculation of this value), the area of the PPE-CO_2-7 excitation peak was 12.5 ± 0.4-fold larger than the area of the DiI excitation peak, well exceeding the value of 2.4-fold expected for one polymer and highlighting the fact that DiI was collecting energy from multiple polymer chains (Figure 3.5B). To show that DiI and PPE-CO_2-7 do not preassociate or form a static complex within the membrane, a sample containing 50 DiI and 50 PPE-CO_2–7 polymers per liposome was prepared. At this low loading, the average distance between the donor and the acceptor would be *ca*. 22 nm, and therefore no energy transfer is expected if the components are well-dispersed within the membrane. Indeed, negligible FRET was observed (see Figure 3.13), leading to the conclusion that the polymer and the acceptor do not have a strong tendency to preassociate.

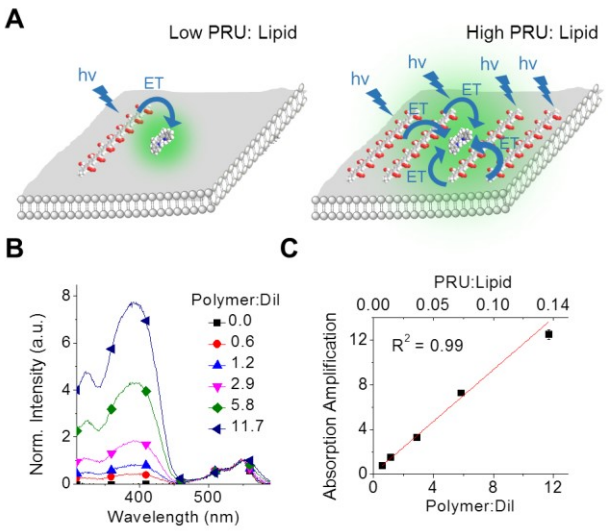

Figure 3.5. Absorption amplification of DiI. (A) Diagram showing energy transfer from PPE-CO_2-7 embedded within a lipid membrane to DiI at low and high polymer loadings (left and right diagrams, respectively). At low polymer loadings, DiI may only collect energy from its nearest neighboring polymer, whereas at high polymer loadings, the high density of donors allows DiI to collect energy harvested from multiple polymers either through direct energy transfer or through homotransfer followed by direct transfer. (B) Excitation spectra of 20 pM 200 nm DOTAP liposomes containing 614 DiI per liposome and varying amounts of PPE-CO_2-7. The spectra are obtained by monitoring DiI emission at 600 nm. The contribution of PPE-CO_2-7 emission at 600 nm has been subtracted from the spectra (see section 3.7.7 and Figure 3.10 for details). The spectra are normalized to a value of 1 at the DiI excitation maximum of 550 nm in order to more clearly show the absorption amplification factor. (C) Absorption amplification of DiI *versus* polymer:DiI ratio. The amount of polymer is varied, while the amount of DiI is held constant at 614 DiI per liposome. Spectra plotted are the average of three spectra obtained from experiments carried out in triplicate.

Assuming that orientation factors are not affected by the density of polymers in the membrane, a linear relationship between the energy transfer efficiency *versus* the number of donors is expected, since the average distance between the donor and the acceptor will remain constant regardless of how many polymers are added to the membrane (assuming that homotransfer between donors does not occur). In the case of homotransfer, however, the effective DiI-polymer separation will decrease because excitations from more distant polymer chains will have a pathway to migrate closer to the DiI trap, leading the plot in Figure 3.5C to be superlinear as opposed to linear. Since a linear and not a superlinear plot were obtained, this suggests that homotransfer does not compete effectively with other decay pathways (*e.g.*; energy transfer to DiI or radiative decay) in this system.

3.3.5. Optimization of the light harvesting antenna

Conditions that would maximize the performance of the light-harvesting antenna were next sought. In real photosynthetic systems, the antenna size per reaction center depends on the available light, and evolution dictates a perfect balance to ensure maximum light harvesting at minimum trap/reaction center cost, given the pressures of the environment.[45-46] Here, to maximize the amount of light harvested, the highest load of antennas possible before saturation of the membrane, obtained at 0.14 PRU:lipid (*vide supra*), was used. The loading of the energy acceptor DiI was next optimized. The optimal DiI loading represents a compromise between loading DiI at the highest possible density and thus ensuring that all of the energy harvested by the antenna reaches the traps *versus* reducing the DiI density to maximize the energy collected by each trap individually (Figure 3.6A). The former extreme favors energy collection with the associated penalty of increasing traps, whereas the latter minimizes the number of traps to the detriment of energy collection.

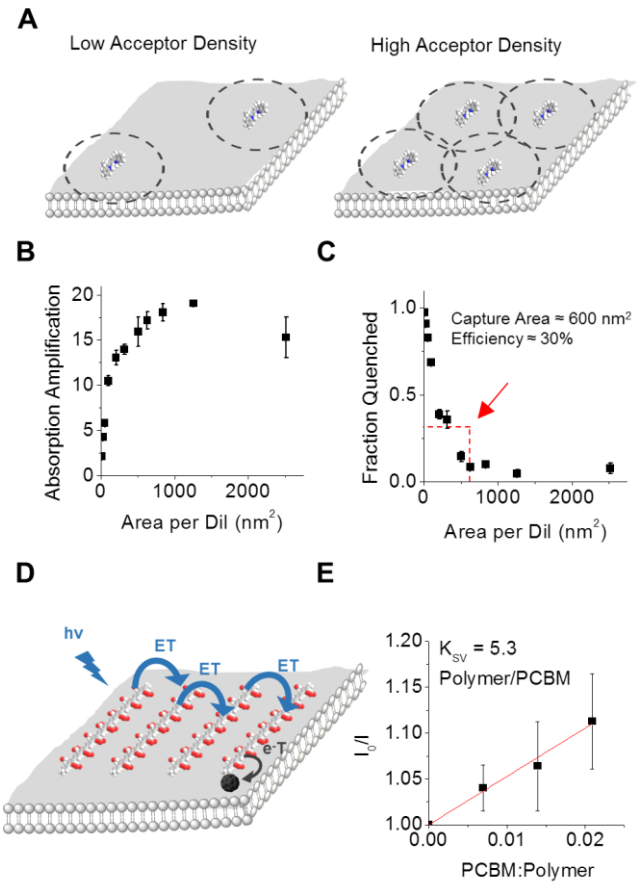

Figure 3.6. Optimization of the light harvesting antenna. (A) Cartoon illustrating the energy collecting area associated with each individual DiI molecule assuming that there exists a large density of PPE-CO_2-7 antennas. At low DiI acceptor surface densities, a fraction of the light harvested by the polymer may not reach the acceptor. In turn at high acceptor surface densities, individual DiI molecules compete with each other for excitons from PPE-CO_2-7 (illustrated by the overlapping of the dashed lines). (B) Absorption amplification of DiI as a function of membrane area per DiI in the membrane of 200 nm diameter DOTAP liposomes containing 0.14 PRU:lipid PPE-CO_2-7. (C) Fraction of PPE-CO_2-7 emission that is quenched by DiI as a function of membrane area per DiI in the membrane of 200 nm DOTAP liposomes containing 0.14 PRU:lipid PPE-CO_2-7. The plots in panels B and C were obtained by averaging the results obtained from experiments performed in triplicate. Error bars are the standard deviation of the mean values. (D) Diagram showing energy migration within the PPE-CO_2-7 antenna toward the electron acceptor PCBM. The left-most polymer is initially excited, and the blue arrows represent the energy transfer *via* FRET between polymers. The black arrow represents the photoinduced electron transfer from the excited polymer to a PCBM molecule within close proximity. (E) Stern–Volmer plot of the quenching of PPE-CO_2-7 emission by PCBM in the membrane of 200 nm DOTAP liposomes containing 0.14 PRU:lipid and 0–0.0004 PCBM:lipid. The data points are the average of 7–10 replicates with the error bars showing the standard deviation.

Experimentally, the absorption amplification of DiI was used to quantify the energy collected per acceptor/trap. DOTAP liposomes were prepared with DiI loadings ranging from 50 to 10,000 chromophores per liposome. The excitation spectrum of each sample was acquired, and the absorption amplification of DiI was determined in each case. Each DiI was associated with an antenna centered on a circle whose capture area is defined by the total surface area of the liposome ($4\pi r^2$) divided by the total number of DiI per liposome. As the area per DiI in the membrane increased, the absorption amplification of DiI initially increased Figure 3.6B. This is consistent with the idea that each individual DiI encounters reduced competition from neighboring DiI molecules for polymer excitons as their density decreases. The upward trend in the absorption amplification eventually plateaued at low DiI surface density values, yielding a maximum absorption amplification value of *ca*. 18. Based on the plateau observed in the plot in Figure 3.6B, the capture area of DiI was estimated to be *ca*. 600 nm^2, which corresponds to a capture radius of *ca*. 14 nm. The number of polymers within the capture area was then estimated from the surface density of polymers within the membrane to obtain a value of *ca*. 34 polymers per DiI (600 nm^2 × 7181 polymers/(4π × 100 nm^2)), corresponding to *ca*. 238 PRUs. The overall energy transfer efficiency within the capture area was then interpolated from Figure 3.6C to be *ca*. 30%. By comparison, naturally occurring light-harvesting antennas typically incorporate *ca*. 200 chromophores and achieve quantum efficiencies of 50–90%.[4, 47]

The fraction of energy absorbed by the antenna that is ultimately transferred to the acceptor is also an important consideration when evaluating the overall performance of a light-harvesting system. To determine the transfer efficiency, we calculated the fraction of PPE-CO_2-7 emission that was quenched by energy transfer at each DiI loading. The emission spectrum of each sample was obtained by exciting PPE-CO_2-7 at 390 nm. The spectra were compared to a control sample containing the same amount of PPE-CO_2-7 but no DiI in order to determine the quenching of the donor emission. As expected, as the number of acceptors in the membrane increased, the polymer emission quenching also increased (Figure 3.6C). At DiI loadings exceeding 2500 DiI per liposome (corresponding to DiI-DiI separations ≤8 nm and areas of ≤50 nm^2 per DiI), more than 85% of the energy harvested by PPE-CO_2-7 was transferred to DiI, although as one may observe from Figure 3.6B, the absorption amplification of each individual DiI at these loadings is relatively small at <5-fold, since the acceptors must share the energy harvested by the polymers between themselves.

3.3.6. The role of homotransfer in the light harvesting antenna

To probe the extent of homotransfer in the antenna, we utilized an electron acceptor, the fullerene derivative phenyl-C_{61}-butryic acid methyl ester (PCBM), closely resembling a fullerene derivative shown to quench the emission of the polymer PPE-SO_3 *via* photoinduced electron transfer.[48] Given the large solubility of C_{60} and related compounds within lipid bilayers[49] and their suitable redox properties, PCBM provides for an ideal electron acceptor to probe energy migration within the membrane embedded antenna. Here, PCBM acts as a reaction center where charge separation occurs effectively transducing the electronic energy harvested by the antenna into chemical energy.

Given the short distance range (few angstroms) characterizing electron transfer, PCBM was anticipated to quench its nearest neighbor, *ca*. 0–2 polymers, unless energy migration through the antenna was effectively taking place thus amplifying the number of PPE-CO_2-7 polymers quenched (Figure 3.6D). To quantify the extent of quenching, liposomes were prepared containing 0.14 PRU:lipid and incorporating PCBM at PCBM:lipid molar ratios of 1:7200, 1:4800, and 1:2400, low enough to prevent PCBM aggregation.[50-51] The emission of the polymer was quenched as a function of increasing PCBM concentration within the membrane (Figure 3.14). The Stern–Volmer plot of the emission quenching was linear, rendering a K_{SV} value of 5.3 polymers quenched per PCBM molecule (Figure 3.6E). While this result indicates that homotransfer between the polymers of the antenna does occur, it also shows that excitons generated more than two polymers away are unlikely to reach the fullerene reaction center.

3.4 Conclusion

We have reported a biomimetic artificial light-harvesting system based on the self-assembly of light-harvesting conjugated polyelectrolytes embedded within lipid membranes. The PPE-CO_2-7 polymers can be loaded into the membrane of DOTAP liposomes at a high density (estimated at less than 2 nm center-to-center average separation distance) with minimal energy losses due to self-quenching. While amplified absorption, a marker of through space energy transfer, was observed for the membrane embedded energy acceptor DiI, our results pointed to a dominant contribution of direct PPE-DiI energy transfer, where homotransfer between polymers acting as relay units could not be clearly discerned. Quenching studies with electron acceptors

ultimately illustrated that homotransfer takes place in the system albeit only though a relatively short distance range. The dominance of direct energy transfer from PPE-CO_2-7 to DiI over homotransfer between polymers in this system provides knowledge that may help in improving the performance of this or similar systems in the future. Our current efforts are focused on characterizing the orientation of the polymers within the membrane and elucidating the factors that control their self-assembly. Understanding the orientation will enable one to engineer the nanoscale assembly toward improving the efficiency of the FRET processes occurring in the membrane. In addition, the incorporation of CPEs within membranes offers great flexibility in design, as the polymer structure may be readily modified to optimize the charge, length, and transition energy of the polymer.[52-53] More broadly, the demonstration of lipid membranes as a platform for assembling an artificial light-harvesting antenna opens the possibility of interfacing synthetic conjugated polyelectrolytes with reaction centers and photostabilizing molecules such as carotenoids, to fabricate functionally compatible hybrid light-harvesting complexes.

3.5 References

1. Scholes, G. D.; Fleming, G. R. Energy Transfer and Photosynthetic Light Harvesting. In *Adventures in Chemical Physics*; John Wiley & Sons, Inc.: 2005; pp 57-129.

2. Light-Harvesting Antennas in Photosynthesis. 1 ed.; Green, B. R. P., W.W., Ed. Springer Netherlands: 2003.

3. Yang, M.; Agarwal, R.; Fleming, G. R. The Mechanism of Energy Transfer in the Antenna of Photosynthetic Purple Bacteria. *J. Photochem. Photobiol., A* **2001,** *142*, 107-119.

4. Scholes, G. D.; Fleming, G. R.; Olaya-Castro, A.; van Grondelle, R. Lessons from Nature About Solar Light Harvesting. *Nat Chem* **2011,** *3*, 763-774.

5. van Grondelle, R.; Novoderezhkin, V. I. Energy Transfer in Photosynthesis: Experimental Insights and Quantitative Models. *Phys. Chem. Chem. Phys.* **2006,** *8*, 793-807.

6. Renger, T. Theory of Excitation Energy Transfer: From Structure to Function. *Photosynth. Res.* **2009,** *102*, 471-485.

7. Benniston, A. C.; Harriman, A. Artificial Photosynthesis. *Mater. Today* **2008,** *11*, 26-34.

8. Balzani, V.; Credi, A.; Venturi, M. Photochemical Conversion of Solar Energy. *ChemSusChem* **2008,** *1*, 26-58.

9. Gust, D.; Moore, T. A.; Moore, A. L. Solar Fuels Via Artificial Photosynthesis. *Acc. Chem. Res.* **2009,** *42*, 1890-1898.

10. Ziessel, R.; Harriman, A. Artificial Light-Harvesting Antennae: Electronic Energy Transfer by Way of Molecular Funnels. *Chem. Commun.* **2011,** *47*, 611-631.

11. Ziessel, R.; Ulrich, G.; Haefele, A.; Harriman, A. An Artificial Light-Harvesting Array Constructed from Multiple Bodipy Dyes. *J. Am. Chem. Soc.* **2013,** *135*, 11330-11344.

12. Garg, V.; Kodis, G.; Liddell, P. A.; Terazono, Y.; Moore, T. A.; Moore, A. L.; Gust, D. Artificial Photosynthetic Reaction Center with a Coumarin-Based Antenna System. *J. Phys. Chem. B.* **2013,** *117*, 11299-11308.

13. Balzani, V.; Bergamini, G.; Ceroni, P.; Marchi, E. Designing Light Harvesting Antennas by Luminescent Dendrimers. *New J. Chem.* **2011,** *35*, 1944-1954.

14. Choi, M.-S.; Yamazaki, T.; Yamazaki, I.; Aida, T. Bioinspired Molecular Design of Light-Harvesting Multiporphyrin Arrays. *Angew. Chem. Int. Edit.* **2004,** *43*, 150-158.

15. Adronov, A.; Frechet, J. M. J. Light-Harvesting Dendrimers. *Chem. Commun.* **2000**, 1701-1710.

16. Wasielewski, M. R. Self-Assembly Strategies for Integrating Light Harvesting and Charge Separation in Artificial Photosynthetic Systems. *Acc. Chem. Res.* **2009,** *42*, 1910-1921.

17. Pu, F.; Wu, L.; Ju, E.; Ran, X.; Ren, J.; Qu, X. Artificial Light-Harvesting Material Based on Self-Assembly of Coordination Polymer Nanoparticles. *Adv. Funct. Mater.* **2014,** *24*, 4549-4555.

18. Peng, H.-Q.; Xu, J.-F.; Chen, Y.-Z.; Wu, L.-Z.; Tung, C.-H.; Yang, Q.-Z. Water-Dispersible Nanospheres of Hydrogen-Bonded Supramolecular Polymers and Their Application for Mimicking Light-Harvesting Systems. *Chem. Commun.* **2014,** *50*, 1334-1337.

19. Peng, H.-Q.; Chen, Y.-Z.; Zhao, Y.; Yang, Q.-Z.; Wu, L.-Z.; Tung, C.-H.; Zhang, L.-P.; Tong, Q.-X. Artificial Light-Harvesting System Based on Multifunctional Surface-Cross-Linked Micelles. *Angew. Chem.* **2012,** *124*, 2130-2134.

20. Rao, K. V.; Datta, K. K. R.; Eswaramoorthy, M.; George, S. J. Light-Harvesting Hybrid Assemblies. *Chem. Eur. J.* **2012,** *18*, 2184-2194.

21. Rao, K. V.; Datta, K. K. R.; Eswaramoorthy, M.; George, S. J. Light-Harvesting Hybrid Hydrogels: Energy-Transfer-Induced Amplified Fluorescence in Noncovalently Assembled Chromophore–Organoclay Composites. *Angew. Chem. Int. Edit.* **2011,** *50*, 1179-1184.

22. Adams, P. G.; Collins, A. M.; Sahin, T.; Subramanian, V.; Urban, V. S.; Vairaprakash, P.; Tian, Y.; Evans, D. G.; Shreve, A. P.; Montaño, G. A. Diblock Copolymer Micelles and Supported Films with Noncovalently Incorporated Chromophores: A Modular Platform for Efficient Energy Transfer. *Nano Lett.* **2015,** *15*, 2422-2428.

23. Sahin, T.; Harris, M. A.; Vairaprakash, P.; Niedzwiedzki, D. M.; Subramanian, V.; Shreve, A. P.; Bocian, D. F.; Holten, D.; Lindsey, J. S. Self-Assembled Light-Harvesting System from Chromophores in Lipid Vesicles. *J. Phys. Chem. B.* **2015,** *119*, 10231-10243.

24. Woller, J. G.; Hannestad, J. K.; Albinsson, B. Self-Assembled Nanoscale DNA–Porphyrin Complex for Artificial Light Harvesting. *J. Am. Chem. Soc.* **2013,** *135*, 2759-2768.

25. Zou, Q.; Zhang, L.; Yan, X.; Wang, A.; Ma, G.; Li, J.; Möhwald, H.; Mann, S. Multifunctional Porous Microspheres Based on Peptide–Porphyrin Hierarchical Co-Assembly. *Angew. Chem. Int. Edit.* **2014,** *53*, 2366-2370.

26. Liu, K.; Xing, R.; Chen, C.; Shen, G.; Yan, L.; Zou, Q.; Ma, G.; Möhwald, H.; Yan, X. Peptide-Induced Hierarchical Long-Range Order and Photocatalytic Activity of Porphyrin Assemblies. *Angew. Chem. Int. Edit.* **2015,** *54*, 500-505.

27. Zou, Q.; Liu, K.; Abbas, M.; Yan, X. Peptide-Modulated Self-Assembly of Chromophores toward Biomimetic Light-Harvesting Nanoarchitectonics. *Adv. Mater.* **2016,** *28*, 1031-1043.

28. Bhattacharyya, S.; Jana, B.; Patra, A. Multichromophoric Organic Molecules Encapsulated in Polymer Nanoparticles for Artificial Light Harvesting. *ChemPhysChem* **2015,** *16*, 796-804.

29. Dutta, P. K.; Levenberg, S.; Loskutov, A.; Jun, D.; Saer, R.; Beatty, J. T.; Lin, S.; Liu, Y.; Woodbury, N. W.; Yan, H. A DNA-Directed Light-Harvesting/Reaction Center System. *J. Am. Chem. Soc.* **2014,** *136*, 16618-16625.

30. Olive, A. G. L.; Del Guerzo, A.; Schäfer, C.; Belin, C.; Raffy, G.; Giansante, C. Fluorescence Amplification in Self-Assembled Organic Nanoparticles by Excitation Energy Migration and Transfer. *J. Phys. Chem. C* **2010,** *114*, 10410-10416.

31. Zhao, X.; Jiang, H.; Schanze, K. S. Polymer Chain Length Dependence of Amplified Fluorescence Quenching in Conjugated Polyelectrolytes. *Macromolecules* **2008,** *41*, 3422-3428.

32. Karam, P.; Hariri, A. A.; Calver, C. F.; Zhao, X.; Schanze, K. S.; Cosa, G. Interaction of Anionic Phenylene Ethynylene Polymers with Lipids: From Membrane Embedding to Liposome Fusion. *Langmuir* **2014,** *30*, 10704-10711.

33. Calver, C. F.; Liu, H.-W.; Cosa, G. Exploiting Conjugated Polyelectrolyte Photophysics toward Monitoring Real-Time Lipid Membrane-Surface Interaction Dynamics at the Single-Particle Level. *Langmuir* **2015,** *31*, 11842-11850.

34. Ngo, A. T.; Cosa, G. Assembly of Zwitterionic Phospholipid/Conjugated Polyelectrolyte Complexes: Structure and Photophysical Properties. *Langmuir* **2009,** *26*, 6746-6754.

35. Karam, P.; Ngo, A. T.; Rouiller, I.; Cosa, G. Unraveling Electronic Energy Transfer in Single Conjugated Polyelectrolytes Encapsulated in Lipid Vesicles. *Proc. Natl. Acad. Sci. U. S. A.* **2010,** *107*, 17480-17485.

36. Wang, Y.; Schanze, K. S.; Chi, E. Y.; Whitten, D. G. When Worlds Collide: Interactions at the Interface between Biological Systems and Synthetic Cationic Conjugated Polyelectrolytes and Oligomers. *Langmuir* **2013,** *29*, 10635-10647.

37. Ding, L.; Chi, E. Y.; Schanze, K. S.; Lopez, G. P.; Whitten, D. G. Insight into the Mechanism of Antimicrobial Conjugated Polyelectrolytes: Lipid Headgroup Charge and Membrane Fluidity Effects. *Langmuir* **2009,** *26*, 5544-5550.

38. Wang, Y.; Jones, E. M.; Tang, Y.; Ji, E.; Lopez, G. P.; Chi, E. Y.; Schanze, K. S.; Whitten, D. G. Effect of Polymer Chain Length on Membrane Perturbation Activity of Cationic Phenylene Ethynylene Oligomers and Polymers. *Langmuir* **2011,** *27*, 10770-10775.

39. Tan, C.; Pinto, M. R.; Schanze, K. S. Photophysics, Aggregation and Amplified Quenching of a Water-Soluble Poly(Phenylene Ethynylene). *Chem. Commun.* **2002**, 446-447.

40. Wang, Y.; Chi, E. Y.; Schanze, K. S.; Whitten, D. G. Membrane Activity of Antimicrobial Phenylene Ethynylene Based Polymers and Oligomers. *Soft Matter* **2012,** *8*, 8547-8558.

41. Axelrod, D. Carbocyanine Dye Orientation in Red Cell Membrane Studied by Microscopic Fluorescence Polarization. *Biophys. J.* **1979,** *26*, 557-573.

42. Bout, D. A. V.; Yip, W.-T.; Hu, D.; Fu, D.-K.; Swager, T. M.; Barbara, P. F. Discrete Intensity Jumps and Intramolecular Electronic Energy Transfer in the Spectroscopy of Single Conjugated Polymer Molecules. *Science* **1997,** *277*, 1074-1077.

43. Huser, T.; Yan, M.; Rothberg, L. J. Single Chain Spectroscopy of Conformational Dependence of Conjugated Polymer Photophysics. *Proc. Natl. Acad. Sci. U. S. A.* **2000,** *97*, 11187-11191.

44. Tahara, Y.; Fujiyoshi, Y. A New Method to Measure Bilayer Thickness: Cryo-Electron Microscopy of Frozen Hydrated Liposomes and Image Simulation. *Micron* **1994,** *25*, 141-149.

45. Overmann, J.; Cypionka, H.; Pfennig, N. An Extremely Low-Light Adapted Phototrophic Sulfur Bacterium from the Black Sea. *Limnol. Oceanogr.* **1992,** *37*, 150-155.

46. Fassioli, F.; Olaya-Castro, A.; Scheuring, S.; Sturgis, J. N.; Johnson, N. F. Energy Transfer in Light-Adapted Photosynthetic Membranes: From Active to Saturated Photosynthesis. *Biophys. J. 97*, 2464-2473.

47. Fassioli, F.; Dinshaw, R.; Arpin, P. C.; Scholes, G. D. Photosynthetic Light Harvesting: Excitons and Coherence. *J. R. Soc. Interface* **2013,** *11*.

48. Mwaura, J. K.; Pinto, M. R.; Witker, D.; Ananthakrishnan, N.; Schanze, K. S.; Reynolds, J. R. Photovoltaic Cells Based on Sequentially Adsorbed Multilayers of Conjugated Poly(P-Phenylene Ethynylene)S and a Water-Soluble Fullerene Derivative. *Langmuir* **2005,** *21*, 10119-10126.

49. Hungerbuehler, H.; Guldi, D. M.; Asmus, K. D. Incorporation of C60 into Artificial Lipid Membranes. *J. Am. Chem. Soc.* **1993,** *115*, 3386-3387.

50. Bortolus, M.; Parisio, G.; Maniero, A. L.; Ferrarini, A. Monomeric Fullerenes in Lipid Membranes: Effects of Molecular Shape and Polarity. *Langmuir* **2011,** *27*, 12560-12568.

51. Bensasson, R. V.; Bienvenue, E.; Dellinger, M.; Leach, S.; Seta, P. C_{60} in Model Biological Systems. A Visible-Uv Absorption Study of Solvent-Dependent Parameters and Solute Aggregation. *J. Phys. Chem.* **1994,** *98*, 3492-3500.

52. Jiang, H.; Taranekar, P.; Reynolds, J. R.; Schanze, K. S. Conjugated Polyelectrolytes: Synthesis, Photophysics, and Applications. *Angew. Chem. Int. Edit.* **2009,** *48*, 4300-4316.

53. Liu, B.; Bazan, G. C., *Conjugated Polyelectrolytes: Fundamentals and Applications*. Wiley-VCH Verlag GmbH & Co. KGaA: Weinheim, Germany, 2012.

3.6 Experimental section

3.61 Materials

Poly(phenylene ethynylene) carboxylate PPE-CO_2-7 (PDI = 1.7) was synthesized as previously described.[31] Concentrated polymer solutions in water were diluted in Hyclone HyPure molecular biology-grade water purchased from Fisher. DiI was purchased from Invitrogen (Burlington, ON, Canada). DOTAP was acquired from Avanti Polar Lipids (Alabaster, AL). HPLC grade chloroform was purchased from EMD chemicals (Gibbstown, NJ). PCBM was purchased from American Dye Source, Inc. (Baie d'Urfé, Quebec, Canada). All materials were used without further purification.

3.62 Liposome preparation

DOTAP lipid powder was dissolved in chloroform. Aliquots of DiI dissolved in methanol or PCBM dissolved in chloroform were added to the lipid solution when specified. The solvent was evaporated by a stream of argon, and the resulting thin lipid film was placed under vacuum for a minimum of 30 min to remove any remaining solvent. Dry lipid films were then hydrated in water. The samples were subjected to 10 freeze–thaw–sonication cycles (5 min in dry ice/5 min sonication in a water bath at 40°–50 °C) to increase the unilamellarity of the sample. Except for samples containing PCBM, the liposomes were then extruded through a 200 nm polycarbonate membrane using a mini-extruder from Avanti Polar Lipids, Inc. The final lipid concentration was 1.4×10^{-2} M after extrusion, determined by measuring the absorbance of DiI.

3.63 Absorption and emission spectroscopy

Steady-state fluorescence spectroscopy was carried out using a Photon Technology International (PTI) Quanta Master fluorimeter. Absorption spectra were recorded using a Hitachi U2800 UV–vis spectrophotometer. For all steady-state absorption and emission experiments, air equilibrated solutions were placed in 1 × 1 cm quartz cuvettes. For samples containing PPE-CO_2, aliquots of polymer aqueous solution were added to Eppendorf tubes containing DOTAP liposomes and mixed. The samples were then placed on dry ice until completely frozen (*ca*. 10 min) and then completely thawed in a water bath at room temperature (*ca*. 10 min) before acquiring the spectrum.

The additional freeze/thaw step was found to increase the amount of deaggregated polymers incorporated within the lipid membrane.

3.64 Transmission Electron Microscopy

Five μL of the sample suspension was deposited onto a 200-mesh Cu TEM grid with carbon support film immediately after negative glow discharge. After approximately 1–3 min, the excess solution was blotted with filter paper. This was followed by application of a 5 μL drop of a 2% solution of uranyl acetate (UA; SPI Supplies, West Chester, PA). After 1 min, the excess UA was removed with filter paper. After air drying at room temperature, the sample was imaged in an FEI Tecnai 12 BioTwin 120 kV TEM (FEI Company, Hillsboro, OR) equipped with an AMT XR80C CCD Camera System (Advanced Microscopy Techniques, Woburn, MA).

3.65 Cryogenic electron microscopy

Three μL of the sample suspension was pipetted onto a C-Flat 2/2 TEM grid (Protochips, Inc., Morrisville, NC) after positive glow discharge. Excess liquid was blotted with filter paper, and the sample was flash frozen in the hydrated state by plunging into a bath of liquid ethane using the FEI Vitrobot Mark IV Grid Plunging System (FEI Company, Hillsboro, OR). The sample grids were stored at liquid nitrogen temperature and then imaged using the FEI Titan Krios 300 kV cryo-STEM (FEI Company, Hillsboro, OR) equipped with a Falcon 2 Direct Detection Device (DDD; FEI Company) at magnifications of 22,500× (pixel size 3.66A), 37,000× (pixel size 2.24A), 59,000× (pixel size 1.41 A), and 75,000× (pixel size 1.09 A) (defocus level ranging from −1.0 to −4.0 μm) under low dose conditions.

3.7 Supporting information

3.7.1 Spectral overlap of PPE-CO_2-7 emission spectrum and DiI absorption spectrum and calculation of the Förster radius

The Förster radius was calculated by applying the Förster equation:

$$R_0^6 = \frac{9ln10}{128\pi^5 N_A}\frac{\kappa^2 Q_D}{n^4}J$$

Where R_0 is the Forster radius, N_A is Avogadro's number, κ^2 is the dipole orientation factor, Q_D is the fluorescence quantum yield of the donor, n is the refractive index of the medium, and J is the overlap integral.

The overlap integral is defined by the following expression:

$$J = \int f_D(\lambda)\varepsilon_A(\lambda)\lambda^4 d\lambda$$

Where $f_D(\lambda)$ is the donor emission spectrum plotted *versus* wavelength and normalized to an area of 1 and $\varepsilon_A(\lambda)$ is the acceptor absorption spectrum plotted *versus* wavelength. The spectra were multiplied by a factor of λ^4 and then numerically integrated using a spreadsheet. A value of n = 1.4 was used for the refractive index of the DOTAP membrane. A value of 0.64, reported by by Zhao *et al.* for the fluorescence quantum yield of PPE-CO_2-7 in methanol,[31] was used for Q_D. This choice was justified by considering that the emission profile of the polymer embedded in the DOTAP membrane is similar to that of the polymer in methanol, indicating that the two solvent environments are similar. A value of 2/3 for the dipole orientation factor is often assumed, which corresponds to molecules that are isotropically orientated within the fluorescence lifetime as a result of free rotation. Free rotation within the membrane environment is unlikely, particularly for the large polymer molecules, but given the lack of information regarding the relative orientations of the donor and acceptor, a value of 2/3 was nevertheless used to estimate R_0 at a value of 5 nm.

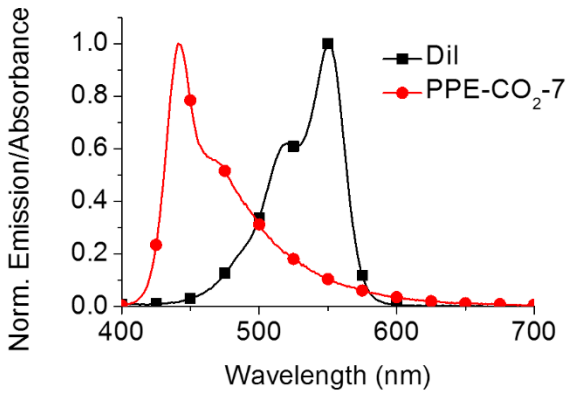

Figure 3.7. Spectral overlap of PPE-CO_2-7 and DiI. Normalized emission spectrum of PPE-CO_2-7 (red circles) and normalized absorption spectrum of DiI (black squares) in DOTAP liposomes showing the spectral overlap. The wavelength of excitation was 390 nm.

3.7.2 Negative stained TEM images of DOTAP liposomes containing PPE-CO_2-7

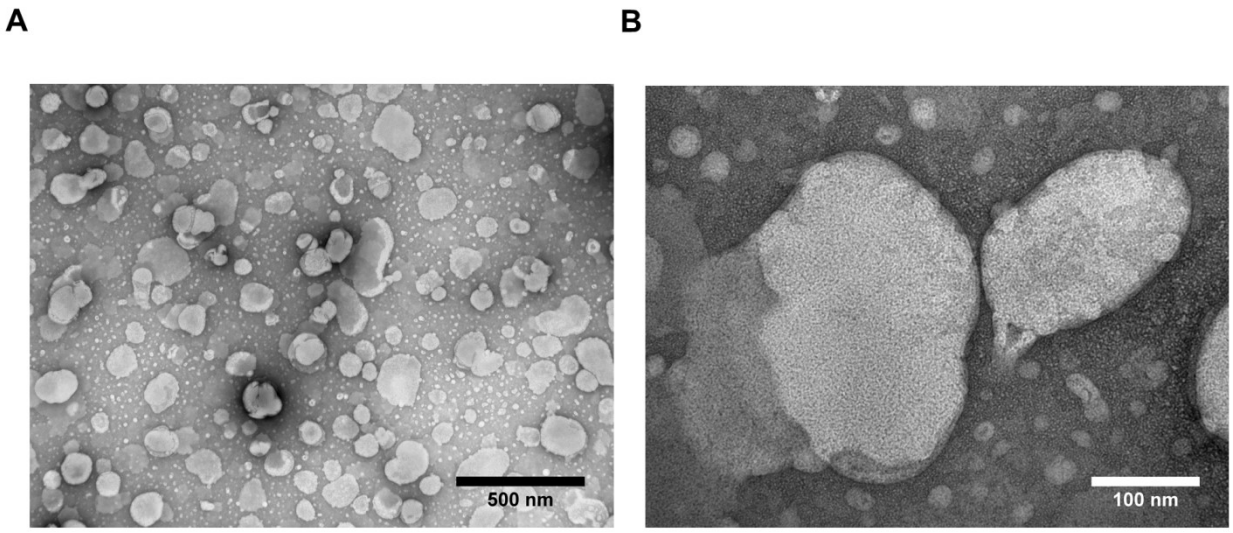

Figure 3.8. Negative stained TEM images of DOTAP liposomes containing PPE-CO_2-7. A) Image obtained at lower magnification. B) Image obtained at higher magnification. Samples contain 28 nM 200 nm diameter DOTAP liposomes and 0.14 PRU:lipid PPE-CO_2-7 prepared in aqueous solution and were negative stained with uranyl acetate. Samples were negative stained with uranyl acetate.

3.7.3 Conversion between polymer concentrations expressed as PRU:lipid and polymers/liposome

Throughout the paper, polymer concentrations were frequently stated as a polymer repeat unit to lipid ratio. Converting these values into a number of polymers per liposome is straight forward. The number of lipids per liposome can be calculated by dividing the surface area of the liposome ($4\pi r^2$) by the surface area of one lipid head group (0.7 nm^2), and then multiplying by 2 to account for the fact that there are two leaflets in the lipid bilayer to give a value of 359,040 lipids per 200 nm diameter DOTAP liposome. The following equation is then used to convert between the two concentration expressions:

$$polymers/liposome = \frac{lipids/liposome * PRU/lipid}{7\ PRU/polymer}$$

3.7.4 Calculation of the average separation distance between donors and acceptors in the membrane

The average distance between PPE-CO_2-7 polymers embedded within the DOTAP membrane was calculated by estimating the area occupied by the polymer chains relative to the area of the membrane. Using the formula for the surface area of a sphere, surface area = $4\pi r^2$, the surface area of one liposome was calculated to be 125,664 nm^2. At the highest polymer loading studied, 0.14 PRU:lipid, the number of polymer chains per liposome was 7181 (see previous section 3.7.3). Assuming that the polymers are assembled in a single layer within the membrane, the membrane area per polymer would be the surface area of the liposome divided by the number of polymers present, 125,664 nm^2/7181 = 17.5 nm^2. The dimensions of one polymer repeat unit (PRU) were estimated to be 1.2 x 0.9 nm using ChemBio3D Ultra version 12.0.2.1076 (CambridgeSoft). The dimensions of one polymer (7 PRUs) are then given by 0.9 nm x (1.2 nm*7) = 0.9 nm x 8.4 nm. To find the distance between polymers, each polymer was placed inside a box with an area equal to 17.5 nm^2. Imagining that the two boxes are touching each other side by side, the distance between polymers will be equal to the distance between the edge of the polymer and the edge of the box multiplied by two. Adding a value of x to each side of the polymer dimensions and setting the product equal to the area of the box results in the following quadratic equation: (0.9 nm+2x)*(8.4 nm+2x) = 17.5 nm^2. Solving for x gives a value of 0.49 nm. Since the polymer

separation is equal to 2*x*, this means that the average edge-edge separation is *ca*. 1 nm and the average center-to-center separation is 1.9 nm under saturation conditions.

The calculation for DiI-DiI spacing is considerably less complex than the calculation for the polymer-polymer spacing, since one can neglect the dimensions of the much smaller DiI molecule when making the calculation. In this case, the DiI spacing is calculated by dividing the surface area of the liposome by the number of DiI to obtain the area per DiI. Taking the square root of the area per DiI and multiplying this value by 2 gives the average center-to-center distance between two DiI molecules in the bilayer (assuming that the bilayer is 2 dimensional).

3.7.5 Determination of the required loading of PPE-CO_2-7 and DiI such that the average edge-to-edge separation within the membrane is equal to the Förster radius

The Förster radius for energy transfer between a single PPE-CO_2-7/DiI donor/acceptor pair was estimated to be 5.0 nm. The dimensions of a box that would enclose one DiI and one PPE-CO_2-7 polymer within an average distance of 5.0 nm were then calculated. The total surface area of the liposome was then divided by the area of the box in order to determine the number of donors and acceptors that needed to be loaded into the liposome to satisfy this condition. The dimensions of one PPE-CO_2-7 PRU were estimated to be 1.2 x 0.9 nm. A 7-mer then has dimensions of 0.9 x 8.4 nm. Adding 5.0 nm on each side of the polymer gives a box of area = (0.9 nm + 5.0 nm + 5.0 nm)*(8.4 nm + 5.0 nm + 5.0 nm) = 200 nm^2. The surface area of a 200 nm liposome was calculated using the formula for the surface area of a sphere: surface area = $4\pi r^2 = 4\pi(100nm)^2$ = 125,664 nm^2. The number of donors and acceptors per liposome is then equal to 125,664 nm^2/200 nm^2 ≈ 614 per liposome.

3.7.6 Subtraction of scattering from emission and excitation spectra

The light scattered by the liposomes was subtracted from the spectra by acquiring an emission of an excitation spectrum containing liposomes only under identical conditions, and then subtracting it from the polymer-containing sample as illustrated in Figure 3.9.

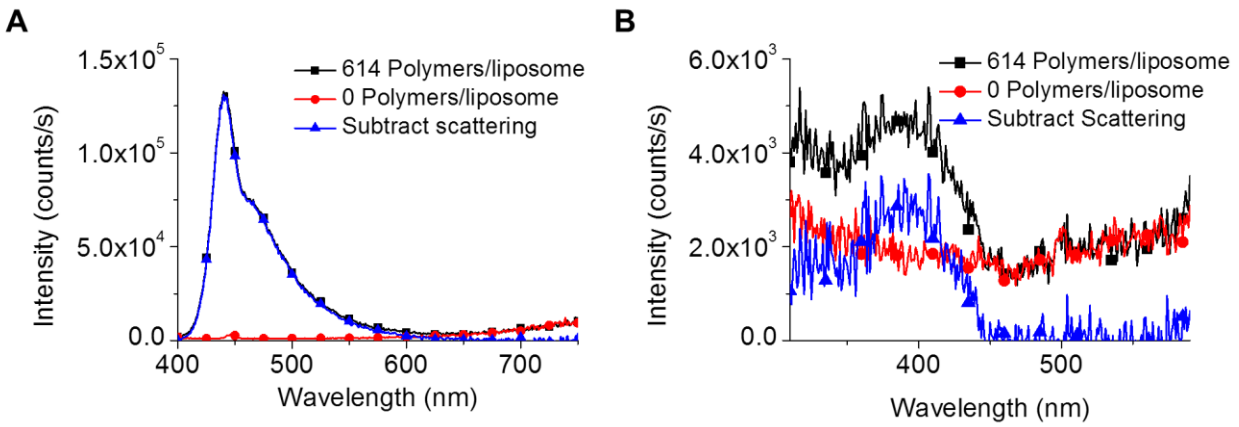

Figure 3.9. Subtraction of scattering from emission and excitation spectra. A) Emission spectrum of 20 pM 200 nm diameter liposomes containing 614 PPE-CO_2-7 polymers per liposome (black squares), 0 PPE-CO_2-7 polymers per liposome (red circles), and the spectrum obtained by subtracting the latter from the former (blue triangles). The excitation wavelength was 390 nm. B) Excitation spectrum of 20 pM 200 nm diameter liposomes containing 614 PPE-CO_2-7 polymers per liposome (black squares), 0 PPE-CO_2-7 polymers per liposome (red circles), and the spectrum obtained by subtracting the latter from the former (blue triangles). The monitoring wavelength was 600 nm.

3.7.7 Correction of the excitation spectra to account for PPE-CO_2-7 emission

Since PPE-CO_2-7 and DiI both emit at 600 nm, the following procedure was used to deconvolute the contribution of the PPE-CO_2-7 emission from the sensitized DiI emission. To do this, the excitation spectrum of a control sample containing an identical amount of polymer but no DiI was acquired to find how large the contribution due to polymer emission. The PPE-CO_2-7 excitation peak in this spectrum is larger than the polymer contribution in the sample containing DiI would be, however, since DiI will partially quench the emission of the polymer. To determine the quenching factor, the emission spectrum of a sample containing polymer only was compared to the emission spectrum of a sample containing polymer and DiI. The polymer was found to be quenched by a factor of 0.55 (Figure 3.10A). The excitation spectrum of the control sample was then multiplied by this factor and subtracted from the sample containing DiI to yield the excitation spectrum containing the contribution of sensitized DiI emission to the polymer excitation peak only (Figure 3.10B).

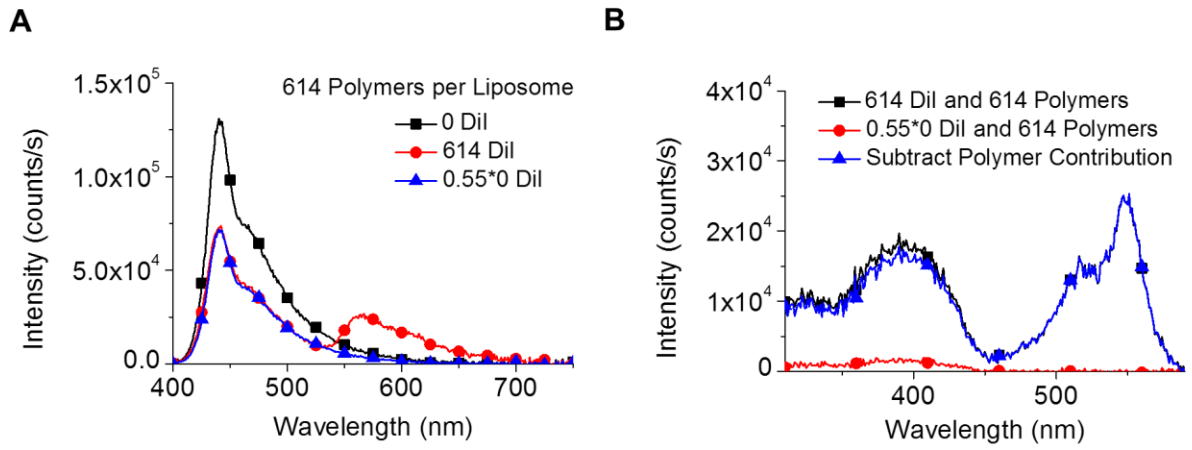

Figure 3.10. Correction of the excitation spectra to account for PPE-CO_2-7 emission. A) Emission spectra of liposomes containing 614 PPE-CO_2-7 polymers per liposome (black squares) or 614 PPE-CO_2-7 polymers and 614 DiI molecules per liposome (red circles). The spectrum of liposomes containing polymer but not DiI was multiplied by a factor of 0.63 (blue triangles) such that the polymer emission matched the polymer emission in the sample containing DiI (red circles). B) Excitation spectra of sample containing 614 PPE-CO_2-7 polymers and 614 DiI per liposome before correction (black squares), a sample containing 614 PPE-CO_2-7 polymers but no DiI multiplied by the quenching factor of 0.55 determined in Figure 3.10A (red circles), and the spectrum obtained after subtraction of the polymer-only sample (blue triangles). All samples contain 20 pM 200 nm diameter DOTAP liposomes. The excitation wavelength for the emission spectra shown in 3.10A was 390 nm. The monitoring wavelength for the excitation spectra shown in Figure 3.10B was 600 nm.

3.7.8 Effect of PPE-CO_2-7 on the emission profile and quantum yield of DiI

The emission spectrum of DiI in liposomes containing PPE-CO_2-7 at a low polymer loading (0.010 PRU:lipid) and a high polymer loading (0.10 PRU:lipid) was acquired and compared to the emission spectrum of DiI in a control sample containing no polymer (Figure 3.11). At the low polymer loading, no shift in the emission profile was observed relative to the emission profile of DiI in liposomes containing no polymer. At a high polymer loading, the ratio between the vibronic peaks changed to favour the more red-shifted peak. The spectra were integrated and the percent difference between the integrated intensities was less than 3%, indicating that although the presence of the polymer may affect the emission profile of DiI, it does not drastically affect its fluorescence quantum yield.

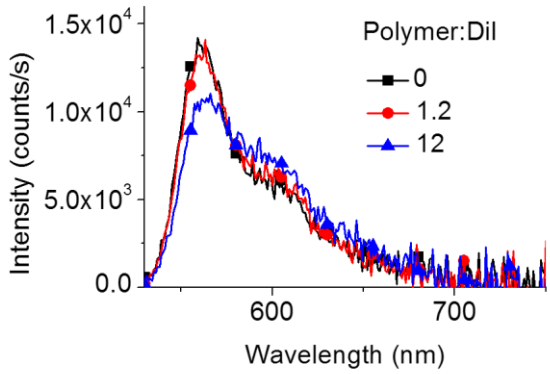

Figure 3.11. Effect of PPE-CO_2-7 on the emission profile and quantum yield of DiI. Emission spectra of 20 pM 200 nm diameter DOTAP liposomes containing 614 DiI per liposome and PPE-CO_2-7 in a ratio of 0, 0.010, or 0.10 PRU:lipid. DiI was excited at 520 nm.

3.7.9 Determination of the maximum absorption amplification of DiI in a 1:1polymer:DiI ratio

The absorption amplification of DiI upon sensitization by a single PPE-CO_2-7 polymer will depend on the light harvesting ability of PPE-CO_2-7 relative to DiI as well as the efficiency that the energy harvested is transferred. Assuming a maximum transfer efficiency of 100%, the absorption amplification will be equal to the ratio of the PPE-CO_2-7 excitation peak to the DiI excitation peak in units of molar absorptivity (Figure 3.12). The ratio of these peaks was determined to be 2.4, representing the expected absorption amplification under the 100% energy transfer condition.

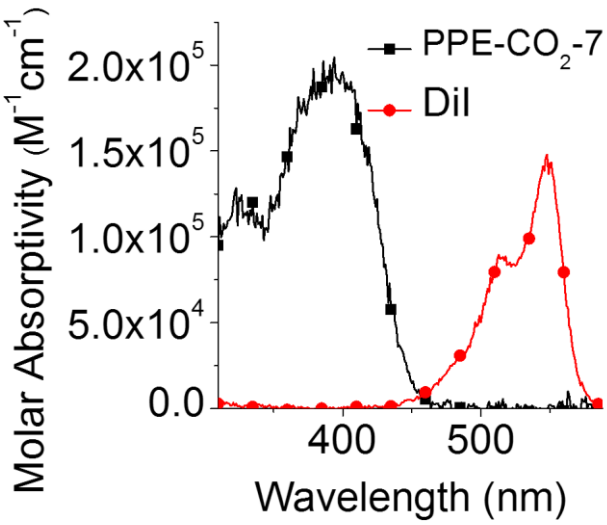

Figure 3.12. Determination of the maximum absorption amplification of DiI. Excitation spectra of PPE-CO_2-7 (black squares) and DiI (red circles) in units of molar absorptivity ($M^{-1}cm^{-1}$). Spectra were acquired by monitoring the emission intensity at 600 nm of aqueous solutions containing 20 pM DOTAP liposome 200 nm in diameter and 0.14 PRU:lipid PPE-CO_2-7 or 5000 DiI per liposome. The spectra were then normalized such that the peak value equaled the molar absorptivity (196,000 $M^{-1}cm^{-1}$ per polymer containing 7 PRUs or 148,000 $M^{-1}cm^{-1}$ per DiI, respectively).

3.7.10 FRET experiments to show that DiI and PPE-CO_2-7 are not pre-associated within the membrane

To show that DiI and PPE-CO_2-7 do not pre-associate or form static complexes within the membrane, a sample containing 50 DiI and 50 PPE-CO_2-7 polymers per liposome was prepared. At this low loading, the average distance between the donor and the acceptor would be *ca.* 22 nm and therefore no energy transfer is expected if the components are well-dispersed within the membrane. The emission spectrum of PPE-CO_2 was acquired and compared to a sample containing the same concentration of PPE-CO_2-7 but no DiI (Figure 3.13A) The presence of energy transfer would be indicated by quenching of the donor emission and/or appearance of the acceptor emission peak, but here the two spectra are identical, consistent with an absence of FRET. In addition, the excitation spectra obtained by monitoring DiI emission at 600 nm showed no PPE-CO_2-7 excitation peak (Figure 3.13B).

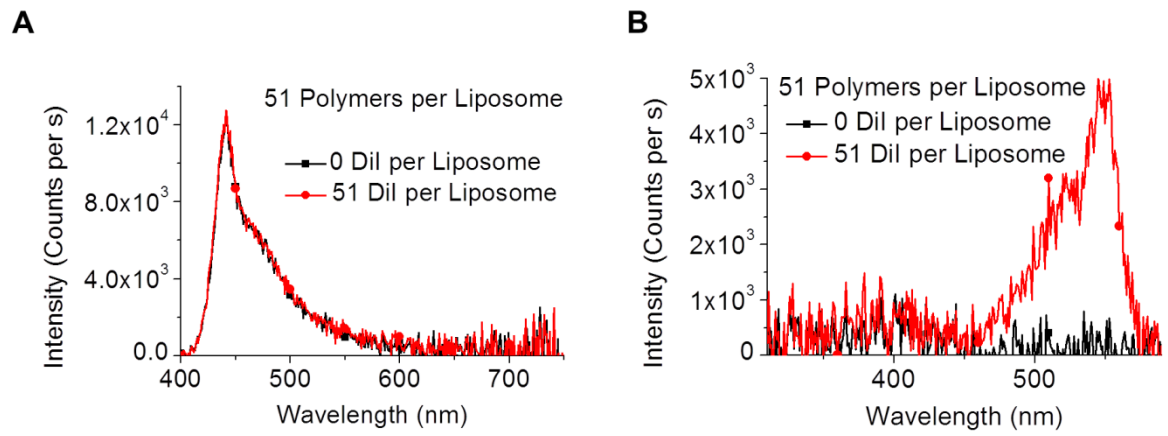

Figure 3.13. Absence of energy transfer between dilute donors and acceptors. A) Emission spectra of PPE-CO_2-7 in 20 pM 200 nm diameter DOTAP liposomes in water upon excitation at 390 nm. B) Excitation spectra obtained from the same samples shown in Figure 3.13A. Samples contain 50 PPE-CO_2-7 polymers per liposome and either 0 or 50 DiI (black squares and red circles, respectively).

3.7.11 Quenching of PPE-CO_2-7 emission intensity by PCBM

The emission spectrum of liposomes containing 0.14 PRU:lipid PPE-CO2-7 and 0.00014, 0.00028, and 0.00042 PCBM:lipid (0, 50, 100, and 150 PCBM:liposome, respectively) was acquired. The intensity of the polymer emission was decreased as the concentration of PCBM in the membrane increased (Figure 3.14).

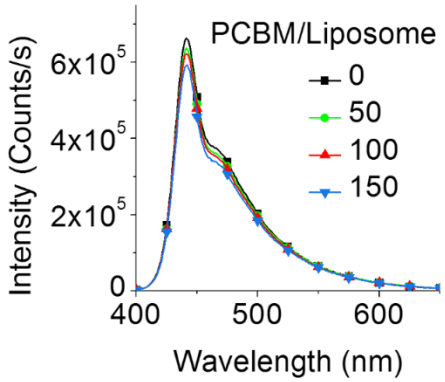

Figure 3.14. Quenching of PPE-CO_2-7 emission intensity by PCBM. Emission spectra of 20 pM 200 nm diameter DOTAP liposomes containing 0.14 PRU:lipid PPE-CO_2-7 and varying amounts of the electron acceptor PCBM The spectra plotted are the average of 7-10 replicated measurements. The excitation wavelength was 390 nm.

Chapter 4: Enhanced photostability of poly(phenylene ethynylene) coated SiO_2 nanoparticles

Author Contributions: **Christina F. Calver** and **Briony A. Lago** performed experiments. **Christina F. Calver** analyzed data and co-wrote the paper. **Prof. Kirk S. Schanze** provided the PPE-CO_2-49 polymer and gave feedback on the manuscript. **Prof. G. Cosa** designed the project, guided the interpretation of data, and co-wrote the paper.

Currently under review at the Journal of Physical Chemistry B.

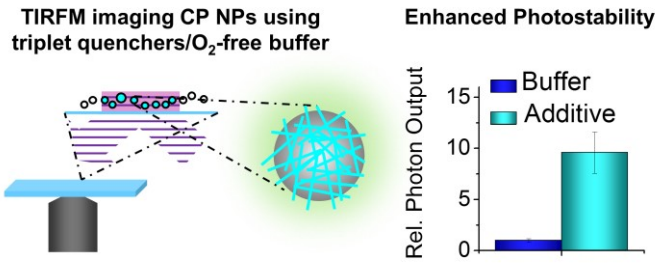

4.0 Preface

Chapter 2 successfully demonstrated a new methodology to study membrane dynamics at the single-particle level by observing their interaction with MPS-PPV coated NPs using TIRFM. One of the future directions identified in this chapter was to explore the interaction of liposomes with surfaces coated with different CPEs (*e.g.*, studying the relatively rigid and needle-like PPE-CO_2 would make an interesting comparison). We found that the rapid photodegradation of the prepared PPE-CO_2 coated NPs under the high excitation powers used in TIRFM experiments posed a significant hurdle, however, since the polymer photobleaches before the arrival of the liposomes and their interaction with the NPs could be recorded. In response to this challenge, Chapter 4 presents results toward improving the photostability of PPE-CO_2 coated NPs under TIRFM imaging conditions. The strategy employed was the addition of small molecule additives (triplet quenchers/antioxidants) to the imaging buffer and the removal of molecular oxygen using an enzymatic oxygen scavenging system. While immediately applicable to the above-mentioned follow up study to Chapter 2, the antifading cocktails developed in Chapter 4 are also useful toward imaging PPE-CO_2 in aqueous solution for other purposes.

4.1 Abstract

Single molecule fluorescence (SMF) studies on conjugated polymers yield enhanced information on exciton dynamics and on the interplay between polymer conformation/morphology and photophysical behavior. SMF studies, however, demand good signal stability, excellent photostability, and high photon yields (a measure of both photostability and brightness) and thus the development of strategies to help CPs meet these requirements is a topic of great interest. Here, we evaluate the effect of several triplet quencher additives on the photostability of a 49-mer long poly(phenylene-ethynylene) conjugated polymer bearing carboxylate side groups (PPE-CO_2-49) that is deposited onto 100 nm diameter SiO_2 nanoparticles (NPs). The additives tested include ascorbic acid (AA), β-mercaptoethanol (BME), Ni^{2+}, trolox (TX), and a trolox/trolox quinone mixture (TX/TQ), used either with or without an enzymatic oxygen scavenging system (glucose oxidase/catalase, GODCAT). Total internal reflection fluorescence microscopy (TIRFM) studies enabled the determination of the effect of the additives on the rates of photobleaching, the initial intensity, and the total photon output for hundreds of conjugated polymer coated SiO_2 nanoparticles monitored in parallel. Addition of the antioxidant/triplet quenchers AA and TX led to a 3-8-fold increase in the number of photons collected as well as an enhancement of the initial emission intensity, consistent with an increase in the duty cycle attributed to the quenching of triplet states. Removal of oxygen led to an impressive 10-15-fold increase in the photostability relative to buffer, implicating ROS as an important agent in the photodegradation of PPE-CO_2-49. Combining AA and TX with GODCAT had a deleterious rather than an additive effect, suggesting that an oxidizing agent is in fact necessary to rescue the polymer from reactive intermediates formed via reaction with AA/TX. β-mercaptoethanol and Ni^{2+} were not found to have useful properties toward the photostabilization of PPE-CO_2-49. The results of this study provide suitable imaging conditions to conduct single molecule imaging experiments on conjugated polyelectrolytes.

4.2 Introduction

The power of single molecule spectroscopy (SMS) studies to unravel the relationship between polymer conformation, energy transfer, and emission at a molecular level both for conjugated polymers (CPs)[1-3]and for their water-soluble counterparts, conjugated polyelectrolytes (CPEs)[4-7] is limited due to extensive photodegradation of these materials. Photodegradation also

limits the practical use of composites of these materials as fluorescent markers in imaging experiments[2, 8-13] and in applications where long-term photostability is paramount, such as solar cells.[14-16] Photodegradation of CPs/CPEs has been linked to singlet oxygen photosensitization and the formation of other reactive oxygen species (ROS) that may then react with the polymer backbone.[17-19] The presence of photooxidized defects on the polymer backbone provides trap sites that quench the fluorescence of neighboring-tightly packed chains by energy[20-22] or electron[3, 23-26] transfer.

A number of strategies have been shown to be effective toward improving the photostability of CPs and CPEs. In the solid state, extended photostabilization has been achieved upon removal of molecular oxygen under high vacuum and sealing of the sample,[3, 16, 27] as well as by incorporating additives–in the form of triplet state quenchers and antioxidants–into polymer thin films.[28] In microheterogeneous solution, coprecipitation of the above additives during the formation of polymer nanoparticles (NPs) has been successfully achieved, resulting in enhanced photostability.[29] For CPEs present in aqueous solution, success has been met by borrowing protocols developed within the SMS biophysics community.[5-7, 30] For example, the photostability of the CPE poly[5-methoxy-2-(3-sulfopropoxy)-1,4-phenylenevinylene] (MPS-PPV) deposited onto SiO_2 NPs was improved by flowing an enzymatic oxygen scavenging system jointly with β-mercaptoethanol (BME).[7] Flowing the antioxidants ascorbic acid (AA) and BME led to the repair of oxidized quenching sites, and BME was additionally shown to quench triplet states in a dynamic fashion resulting in brighter constructs (higher emission duty cycle).

In this work, the effect of several small molecule additives and the removal of oxygen toward enhancing the photostability of a 49-mer long CPE bearing a poly(phenylene ethynylene) backbone and carboxylate side chains (PPE-CO_2-49)[31] was investigated at the single particle level. To facilitate the studies under the high intensity excitation conditions characteristic of single molecule work, the polymer was deposited on the surface of 100 nm diameter SiO_2 NPs. The NPs were previously aminosilanized to favor polymer adsorption via electrostatic interactions,[30] ultimately rendering PPE-CO_2-49 coated SiO_2 NPs. The number of photons emitted by the PPE-CO_2-49-coated NPs under laser excitation in a total internal reflection fluorescence microscope (TIRFM) setup was then determined in buffered solution containing either 1 or 10 mM AA,[32] 143 mM BME,[33-35] 0.1 M Ni^{2+},[36-37] 2 mM Trolox (TX),[33] or Trolox in combination with its oxidized

form, Trolox quinone (TQ) (1.86 mM TX, 0.14 mM TQ—7% TQ).[38] Molecular oxygen was removed by using an enzymatic oxygen scavenging system consisting of glucose oxidase and catalase (GODCAT) in a buffered glucose solution.[39]

The effect of the additives as well as the presence or absence of molecular oxygen on the initial emission intensity and the total number of photons emitted by the PPE-CO_2-49 coated NPs is discussed in the context of both chemical and physical processes. Overall, we found that addition of AA or TX improved the photostability of PPE-CO_2-49 by a factor of 3-8-fold compared to buffer, presumably by quenching triplet states with the effect of reducing the rate of photodegradation through this pathway. Removal of oxygen using the GODCAT scavenging system led to a 15-fold increase in photostability, although using GODCAT in combination with AA or TX was found to have a deleterious, rather than an additive effect. Addition of TQ to the GODCAT/TX mixture led to a recovery of the photostability, suggesting that in the absence of oxygen another oxidizing agent is required to mitigate photobleaching, possibly by quenching radical intermediates formed by reaction of the polymer triplet state with AA or TX. Finally, BME and Ni^{2+} were not found to have any useful properties in the context of the photostablization of PPE-CO_2-49 under the imaging conditions reported here. Altogether our work provides protocols that are useful for SMF studies of conjugated polyelectrolytes bearing a PPE backbone and provides insight into their mechanistic underpinning.

4.3 Results and discussion

4.3.1 Preparation and characterization of PPE-CO_2-49 coated NPs

To immobilize the CPE in a manner convenient for extended single molecule TIRFM imaging studies, the PPE-CO_2-49 polymer was adsorbed onto the surface of 100 nm diameter SiO_2 NPs. The as-purchased SiO_2 NPs was first modified by reaction with an aminosilane to render the surface positively charged, allowing the deposition of PPE-CO_2-49 via electrostatic interactions.[4, 7, 30] Dynamic light scattering (DLS) and zeta potential measurements confirmed that the size distribution of the NPs was unchanged and that the expected surface charge reversal (negative to positive) was observed following modification (Figure 4.1A and 4.1B, respectively). The $SiO_2NH_3^+$ NPs were then added to an excess of aqueous PPE-CO_2-49, incubated, and purified by

repeated centrifugation/washing steps to remove excess polymer. Here, an increase in the particle size by DLS was noted (Figure 4.1 A) and was attributed to polymer bridging between NPs.

Absorbance measurements of the supernatants obtained after each subsequent washing step confirmed that the adsorbed polymer was retained by the particles (Figure 4.7). The amount of polymer adsorbed was next quantified using UV-Vis absorption spectroscopy, where the scattering from a sample containing an equal concentration of uncoated $SiO_2NH_3^+$ NPs was used as a blank. The resulting spectrum resembled that of an aqueous solution of "free" polymer (Figure 4.1C). Absorption spectra further enabled the quantification of the percentage of the NP surface coated by polymer, yielding a value of *ca*. 62% and corresponding to an average of *ca*. 450 polymers per NP (see Supporting Information for details). The emission profile of adsorbed PPE-CO_2-49 was similar to that of free polymer, although a 57% reduction of the fluorescence quantum yield was observed (Figure 4.1D). The emission quenching upon adsorption was attributed to increased homoenergy transfer to trap sites facilitated by the high density of polymers on the NP support.[4, 30]

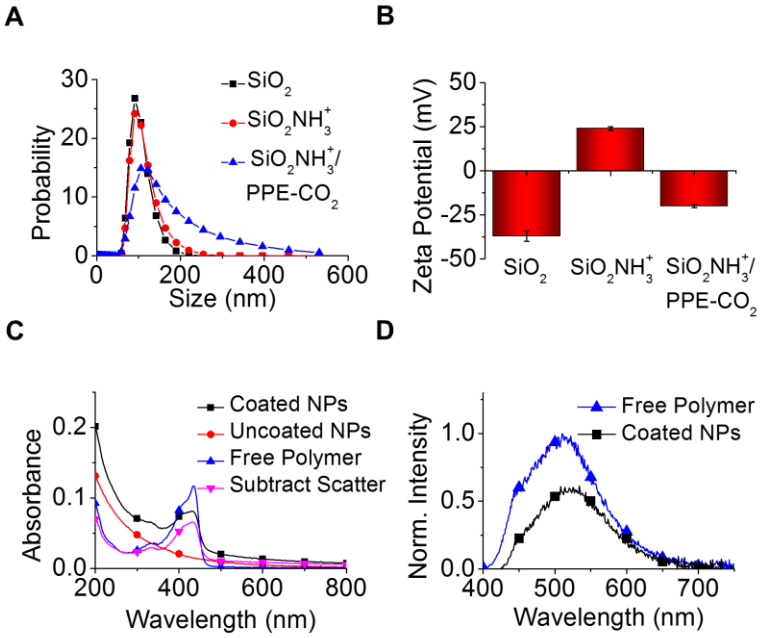

Figure 4.1. Characterization of PPE-CO_2-49 coated NPs. (A) Particle size distributions obtained by DLS measurements on SiO_2 NPs in water brought to pH 10 with sodium hydroxide (NaOH) (black squares), $SiO_2NH_3^+$ NPs in water brought to pH 5 with hydrochloric acid (HCl) (red circles), and PPE-CO_2-49 coated $SiO_2NH_3^+$ NPs in pH 5 water (blue triangles). (B) Zeta potential results for SiO_2 NPs in water brought to pH 10 with NaOH and $SiO_2NH_3^+$ and PPE-CO_2-49 coated

$SiO_2NH_3^+$ NPs in water brought to pH 5 with HCl. The values plotted are the mean result of ten runs collected with three cycles per run. (C) UV-Vis absorption spectra of 0.055 nM PPE-CO_2-49 coated $SiO_2NH_3^+$ NPs (black squares), 0.055 nM $SiO_2NH_3^+$ NPs (red circles), 2 μM PPE-CO_2-49 (blue triangles), and the spectrum obtained by subtracting the spectrum of uncoated NPs from that of the coated NPs, which represents the absorption of adsorbed PPE-CO_2-49 (purple inverted triangles). All samples were in water brought to pH 5 with HCl. (D) Normalized emission spectra of 2 μM PPE-CO_2-49 (blue triangles) and 0.055 nM $SiO_2NH_3^+$ NPs coated with 1.2 uM PPE-CO_2-49 (black squares). All samples were in water brought to pH 5 with HCl. The excitation wavelength was 390 nm.

4.3.2 TIRFM Imaging

To establish the antifading properties of the various cocktails at the single molecule/particle level, TIRFM imaging studies were next conducted with the PPE-CO_2-49 coated NPs adsorbed onto the surface of an aminosilanized glass coverslip (Fig. 4.2A). Hundreds of NPs were simultaneously excited with the evanescent wave produced from the 405 nm output of a continuous wave (CW) laser with the emission collected every 30-200 ms (as stated) using an electron multiplying charged coupled device (EMCCD). Two laser powers, either 0.1 mW or 4.4 mW, were utilized in our work to determine whether either optical saturation, or decreased photon yields due to accelerated photodegradation *via* two photon processes were occurring under higher radiance conditions.

The emission intensity *versus* time trajectories, the initial intensity (defined as the intensity of the first frame normalized by the exposure time, *vide infra***)**, and the total photon count, were subsequently determined for each PPE-CO_2-49 coated NP from the background-subtracted TIRFM movies, see Figure 4.2B, 4.2C and 4.2D, respectively (see also Figure 4.8, 4.9, and 4.10 for additional data under a range of conditions). While the temporal evolution provided insights on the energy transfer processes occurring between polymers, the initial intensity enabled us to determine the duty cycle of the particles. In turn the total number of photons emitted by the particles provided a true measure of the antifading properties of the cocktails. The total number of photons is a parameter that is maximized when the survival time and the intensity are both simultaneously maximized. Care must be taken in evaluating performance based on either survival time or intensity per unit time in isolation, as both parameters are interdependent, *e.g.*, a lower excitation rate will result in a lower rate of photodegradation, but also in dimmer nanoparticles and thus no net gain in photon output overall.

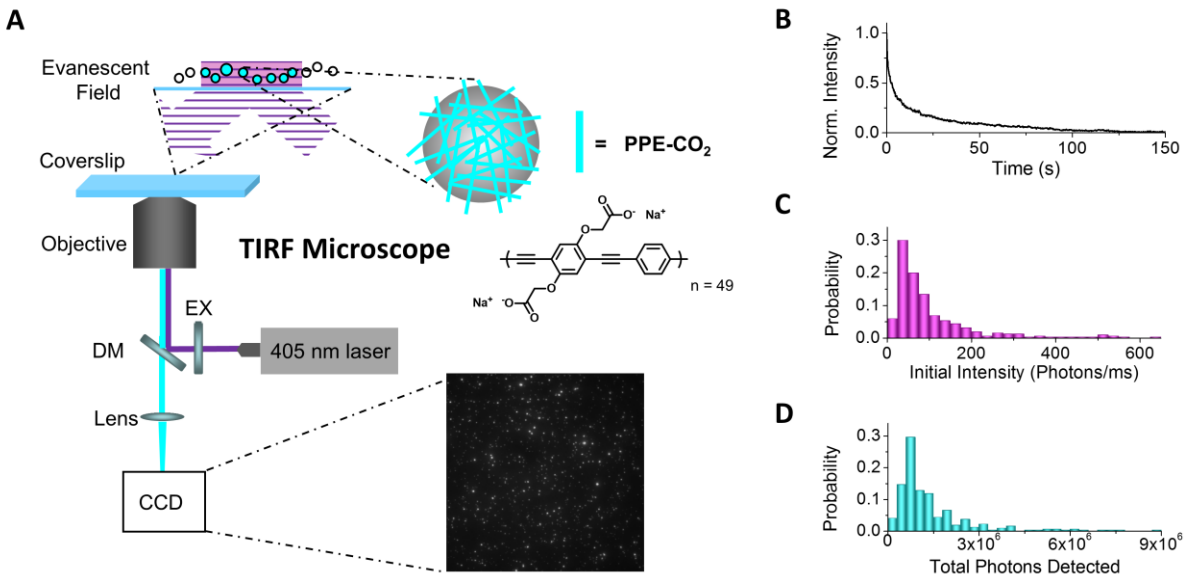

Figure 4.2. Overview of the strategy for determining the effect of additives on the photostability of PPE-CO_2-49. A) Diagram illustrating the experimental setup for evaluating the photostability of the PPE-CO_2-49-coated NPs, including a representative background subtracted TIRFM image. B) Representative (normalized) fluorescence versus time trajectory of a single NP in buffer extracted from analysis of a TIRFM movie. C) and D) Histogram of the initial intensity–in photons/ms–and of the total number of photons, respectively, of NPs in buffer upon excitation at 0.1 mW. For representative trajectories, initial intensity histograms, and total photon histograms for all other conditions please see Figure 4.8, 4.9, and 4.10, respectively.

4.3.3 Single particle intensity versus time trajectories

The intensity versus time trajectories provide a visualization of how long individual PPE-CO_2-49 coated NPs can be monitored in a TIRFM experiment under a set of particular solution conditions and excitation power. Figures 4.3A and 4.3B display representative single particle trajectories acquired at 0.1 and 4.4 mW, respectively. The mean trajectories obtained by averaging the intensity versus time trajectories of the individual NPs normalized by their initial intensity under all conditions are in turn plotted in Figure 4.4A and 4.4B for 4.4 and 0.1 mW excitation powers, respectively. By inspection, the photobleaching trajectories of the NPs under 4.4 mW excitation follow an exponential decay for all conditions, and the timescale of photobleaching is an order of magnitude faster than it is at 0.1 mW, consistent with the 44-fold difference between the two excitation powers. Five of the of the mean normalized trajectories of the NPs under 0.1 mW excitation also show an exponential decay in intensity, but the remaining nine trajectories show a convolution of exponential growth and decay behaviors.

An intensity enhancement similar to what we observed at low excitation powers has been previously reported for PPE[2] and PPV[9] NPs under extended illumination in TIRFM setups. The phenomenon has been rationalized in the context of homoenergy transfer occurring between distant segments of the same chain or between different chains packed together in a film.[40-43] Here, energy migration within the material leads to the funneling of the excitation energy to low energy (red-emissive) or trap (non-emissive) sites.[1, 44] The preferred diffusion of excitons to the trap sites renders these sites prone to degradation by photoinduced processes, effectively eliminating non-emissive sinks and thus accounts for the initial fluorescence enhancement in advance of general photodamage to the polymer backbone (marked by intensity decay). Alternatively, photobleaching of emissive polymer segments may also decrease the efficiency of energy migration to trap sites by effectively removing polymers in the energy transfer pathway, which would also result in an intensity enhancement. Ultimately, both mechanisms would account for an initial increase in the fluorescence quantum yield over time upon illumination.

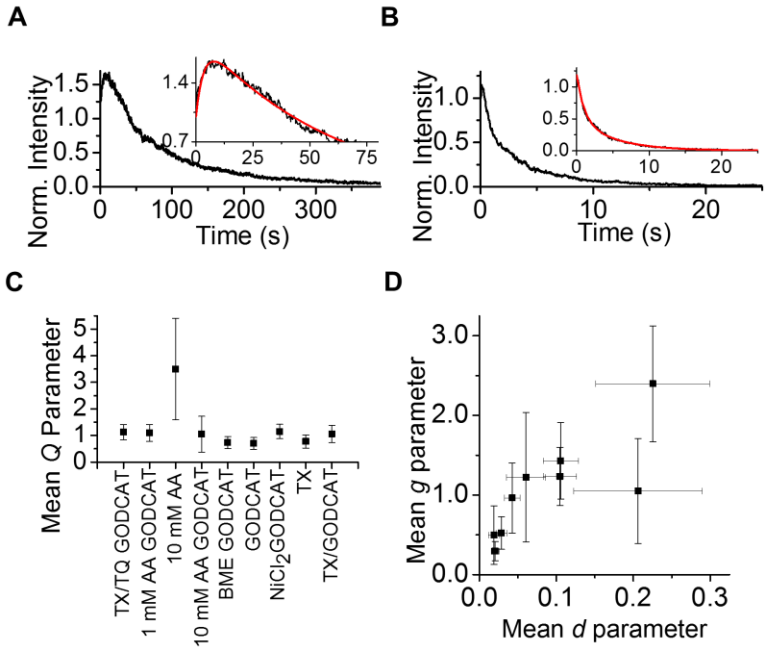

Figure 4.3. Photobleaching kinetic models that describe the behavior of PPE-CO_2-49 coated NPs under illumination in a TIRF setup. (A) and (B) Fluorescence intensity *versus* time trajectories of single representative PPE-CO_2-49 coated NP acquired while flowing a buffered solution of GODCAT at 0.1 (A) and 4.4 mW excitation power (B). Insets show the fitting of the trajectories to Equations 1 and 2, respectively. The traces are normalized to an initial intensity of 1. (C) Mean value of the *Q* parameter obtained by fitting the intensity versus time trajectories obtained under

the solution conditions noted to Equation 1. The excitation power was 0.1 mW. (D) Correlation plot between the *g* and *d* fitting parameters obtained by fitting intensity *versus* time trajectories to Equation 1 under the solution conditions noted. Error bars are the standard deviations of the mean values. The excitation power was 0.1 mW.

To provide a better understanding of the temporal evolution of the intensity, a mathematical model was developed. The model assumes that a heterogeneous sample of polymers exists on each nanoparticle, one being emissive (*i.e.*, "pristine") and the other being initially non-emissive due to the funneling of excitons to non-emissive trap sites. While the former would photobleach, the latter would regenerate pristine emissive chains upon photodegradation of trap sites. The regenerated, pristine chains would then photodegrade with the same rate as the initially emissive polymer chains.

The proposed model is presented mathematically in the form of Equation 1. Here, I_0 is the initial emission intensity of the NP (equal to 1 for a normalized trajectory, and corresponding to pristine chains); and *d* is the rate constant of pristine PPE-CO_2-49 photobleaching, which was found to be adequately approximated by a monoexponential decay function. Also here in the second term *Q* is the relative number of non-emissive chains funneling to trap sites/quenchers, *g* is the rate constant for trap site/quencher disappearance (and also for the regeneration of pristine chains). The individual intensity *versus* time trajectories were fit to Equation 1 and the mean fitting parameters and R^2 values are reported in Table 4.1.

With the exception of 10 mM AA, all of the fits generated values of *Q* that were identical within experimental error (Figure 4.3C). This result was consistent with the relative number of non-emissive trap sites, related to the *Q* parameter, being intrinsic to the NPs and independent of the solution conditions. A positive correlation was also observed between the decay parameters *g* and *d* (Figure 4.3D). Since photobleaching of emissive polymers may reduce the efficiency of energy migration, effectively decreasing *Q*, it follows logically that a faster decay (larger *d*) will also mean a faster recovery (larger *g*) under this model. The positive correlation may also explain why significant emission enhancements were not observed in TIRFM movies acquired at 4.4 mW excitation power (see Figure 4.4A). As the rate of decay increases, the peak of the enhancement is predicted to occur at shorter and shorter times, eventually rendering the enhancement peak unresolvable within the time resolution of the TIRFM experiment.

$$I = I_0 e^{-dt} + \left(\frac{gQ}{d-g}\right)[e^{-gt} - e^{-dt}] \quad (1)$$

In the cases where an emission enhancement was not observed, the individual trajectories could be satisfactory fit under all solution conditions tested to Equation 2, a biexponential decay function where k_1 and k_2 are the rate constants of decay, and A_1 and A_2 represent their relative weights, respectively. See Figure 4.3B for a representative trace and Table 4.2 for a summary of the mean fitting parameters and the R^2 values. The multiexponential nature of the photobleaching was attributed to the fact that many polymers are adsorbed onto each NP where it is plausible that there are multiple microenvironments with different access to O_2, etc. In addition, a distribution of photobleaching rates is expected since the dimensions of the NP scaffold are on the order of the exponential decay of the evanescent field with increasing distance from the surface. For example, at a distance of 100 nm from the surface, the evanescent field produced from a 405 nm laser beam at the glass/water interface will have decayed to *ca*. 75% of its initial intensity, which means that individual polymers are exposed to a continuum of different excitation powers depending on their location on the NP scaffold.

$$I = A_1 e^{-k_1 t} + A_2 e^{-k_2 t} \quad (2)$$

4.3.4 Effect of additives on the initial intensity of PPE-CO_2-49 coated NPs

The effect of additives on the initial intensity of the PPE-CO_2-49 coated NPs was next addressed. Changes in the initial intensity for different solution conditions illustrate how additives may be impacting alternative deactivation pathways from the singlet excited state manifold, effectively changing the emission quantum yield of the polymer, a parameter that will affect the intensity recorded in both bulk and single particle measurements *via* TIRFM. Under the high excitation power conditions characteristic of single molecule studies, the initial intensity also reflects on the duty cycle of the fluorophore in addition to its quantum yield. Transitions to relatively long-lived dark states such as the excited triplet state or radical ions formed upon reaction of the photoexcited fluorophore with either electron donors or acceptors can drastically reduce the rate of photon output by interrupting the rapid cycling between the S_0 ground state and the S_1 excited state and thus the emission of photons. This effect is more noticeable at higher excitation powers, where the cycling between S_0 and S_1 is faster and residence in a non-emissive state provides a relatively larger impact on the emission output. Additives that can shorten the

lifetime of dark states by quenching triplets or radicals are expected to increase the duty cycle resulting in an enhancement of the initial intensity.

Four mechanisms may be considered by which the additives may enhance or quench the initial intensity of PPE-CO_2-49 as recorded in a TIRFM experiment. Firstly, additives employed to quench undesired triplet excited states may also quench the singlet excited state at high concentrations, leading to a reduction of the emission intensity. Secondly, the fluorescence quantum yield of CPEs, including PPE-CO_2-49, is well-known to be linked to the extent of intra and intermolecular aggregation between chains, parameters that are in turn sensitive to the nature of the solvating environment and thus the additives employed.[31, 45] Additives that promote the aggregation (deaggregation) of the polymer chains may thus cause a decrease (increase) in the initial intensity, respectively.[5, 44, 46-49] Thirdly, additives may act to restore emission intensity by "repairing" trap sites, *i.e.* by chemical reaction with oxidative defects effectively removing these quenching sites from the polymer backbone and ultimately reducing the chances of energy dissipation *via* non-emissive pathways from the singlet manifold.[7, 50-51]

The role of mechanisms 1-3 were examined by conducting experiments at the ensemble level, where the additives showed either no effect or only a modest effect (< 50% change) on the intensity of PPE-CO_2-49 (see section 4.7.8. and Figure 4.11). In order to examine the fourth mechanism, additive-induced changes in the duty cycle of the PPE-CO_2-49 coated NPs, we initially sought to compare the change in intensity of the individual NPs before and after flowing the additive following the method previously reported by us.[7] The poor photostability of PPE-CO_2-49 in buffer however placed a severe limitation on this type of experimentation (*i.e* the polymer photobleached before the effect of the new additive could be observed).

The effect of the additives on the duty cycle was ultimately determined by comparing the mean values for the initial intensity obtained under each condition. Panels 4C and 4D illustrate the mean values calculated for NPs excited by both 4.4 and 0.1 mW excitation powers, respectively. In all cases, a large distribution of intensity values was observed, which was attributed to polydispersity in the underlying SiO_2 support and therefore on the amount of polymer adsorbed (*vide infra)*. The degree of polydispersity is similar for all samples, however, implying that trends observed in the mean values likely still reflect the impact of the additives on the duty cycle.

Upon inspection of Figure 4.4C and 4.4D that the positive effect of additives in the initial intensity is more pronounced at higher excitation powers, as a general trend. This observation is consistent with the expectation that changes in the duty cycle are more noticeable at higher excitation rates as the fluorophore approaches optical saturation. Addition of AA (both 1 mM and 10 mM), TX, and TX/TQ enhanced the initial intensity compared to buffer by *ca*. 3-fold upon 4.4 mW excitation, suggesting that these additives can effectively compete with oxygen to quench PPE-CO_2-49 triplet states (Figure 4.4C). Under 0.1 mW excitation, however, no effect on the initial intensity was observed while flowing AA, while the addition of TX and TX/TQ caused a modest enhancement of *ca*. 1.5-fold compared to buffer (Figure 4.4D). Under both excitation powers, BME and Ni^{2+} had no effect on the initial intensity versus buffer, suggesting that these additives are not efficient quenchers of the PPE-CO_2-49 triplet state (Figure 4.4C and Figure 4.4D).

Upon introducing GODCAT and under 4.4 mW excitation power, the initial intensity was increased compared to buffer, Ni^{2+}, and BME (Figure 4.4C). This result was somewhat surprising since removing oxygen, an efficient triplet quencher, would be expected to result in a decrease in the duty cycle (and also, but not relevant to the initial intensity, in a slower photodegradation arising from $^1O_2$ production). An alternative explanation for the increase is that rapid photobleaching under high power in the presence of oxygen within the first acquisition frame leads to a systematic underestimation of the initial intensity. The fact that the addition of GODCAT under 0.1 mW excitation power had a negligible effect on the initial intensity supports this picture, since the rate of photobleaching is slower by approximately an order of magnitude (Figure 4.4D).

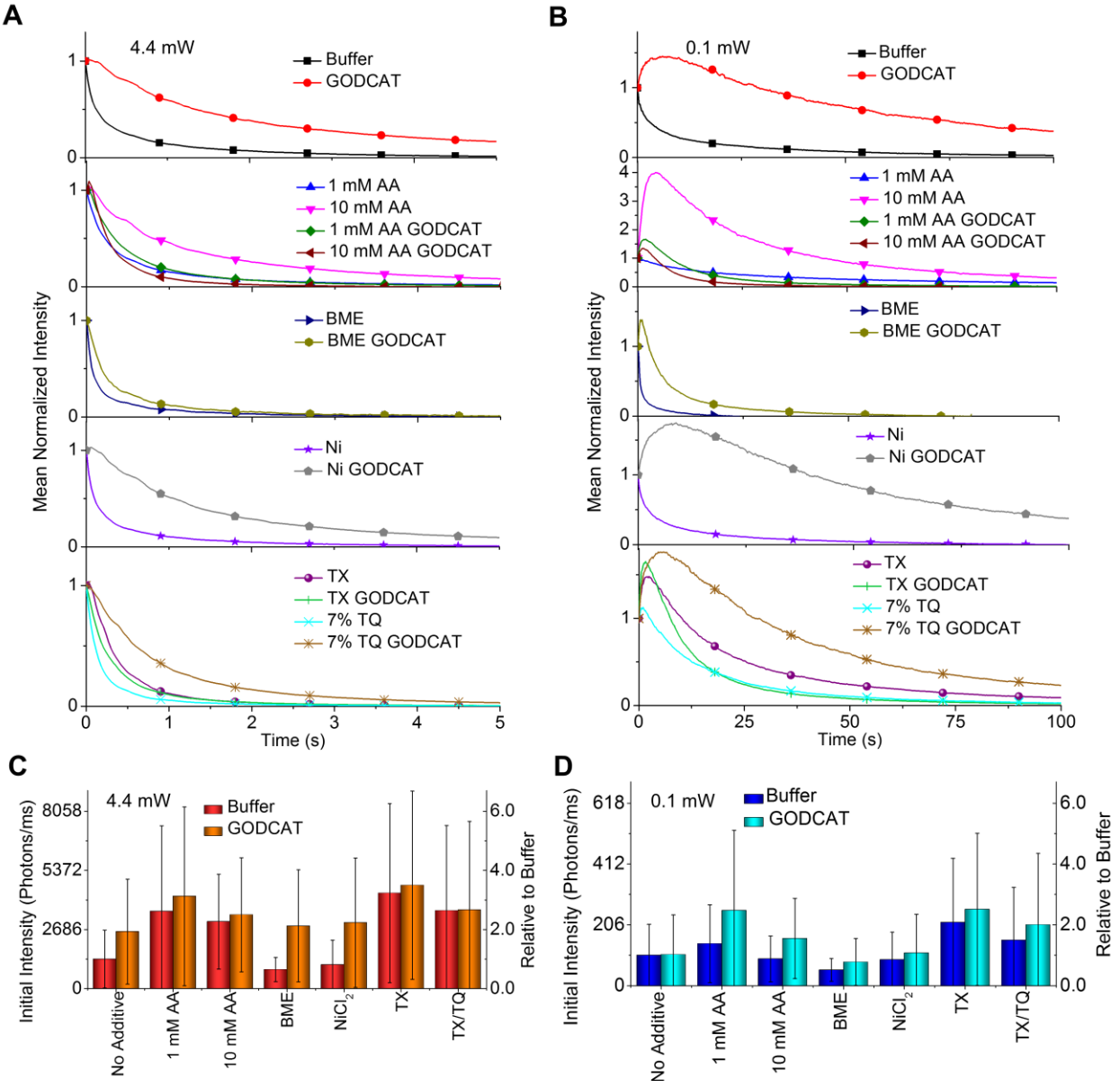

Figure 4.4. Effect of the additives on the mean intensity *versus* time trajectories and the initial intensities of the PPE-CO_2-49 coated NPs. (A) and (B) Mean initial intensity of PPE-CO_2-49 coated NPs obtained under each solution condition with 4.4 mW and 0.1 mW excitation, respectively. The error bars represent the standard deviation in the mean intensity. (C) and (D) Mean traces obtained from the average of fluorescence intensity versus time trajectories of PPE-CO_2-49 coated NPs normalized to an initial intensity of 1. Buffered solutions containing different additives were flowed through the imaging chamber while the NPs were excited with a 405 nm laser at an output power of 4.4 mW and 0.1 mW, respectively.

Notably, throughout the various experimental conditions explored a broad distribution on the values of initial intensity was observed, which was paralleled by an equally broad distribution

of the values of total photons collected per NP before photobleaching. The broad distributions recorded in each case were attributed to the size distribution of the underlying $SiO_2NH_3^+$ NP support. As shown in Figure 1A, the hydrodynamic diameter, (and therefore the radius), of the particles had a relatively large distribution of its own. This large distribution is amplified when the surface area of the particles, proportional to the square of the radius, is considered. It comes thus as no surprise that a large distribution was observed for quantities related to the NP surface area, such as the amount of polymer adsorbed, and in turn the initial emission and total photon count.

The large distribution of initial intensity and total photon count values, combined with the multiexponential photobleaching kinetics recorded for each NP, provided an unusual challenge toward quantifying the photostability of PPE-CO_2-49. To ensure that there were no effects on photostability associated to nanoparticle size/amount of polymer adsorbed, we established that a linear correlation existed between the initial intensity *versus* the total number of photons collected per particle (Figure 4.5). Such an outcome validated that the photobleaching kinetics were not affected by the NP size as otherwise initially brighter (larger) NP would yield proportionally different number of total photons that initially dimer (smaller) NP, where a deviation from linearity would implicate a size effect on kinetics. It follows that the distribution in the photon output can be decoupled from the distribution in the NP initial intensity to reflect the variation in photobleaching kinetics only. To retrieve the distribution in the photobleaching kinetics, each trajectory was thus first normalized by its initial intensity and next integrated. The variation in the integrated areas of the normalized trajectories thus reflected the distribution of photobleaching rates. The relative error (standard deviation/mean) of this distribution was then multiplied by the mean of the total photons collected in order to obtain a distribution of photon output/NP under each condition that is devoid of particle size influence (see error bars in Figure 4.6).

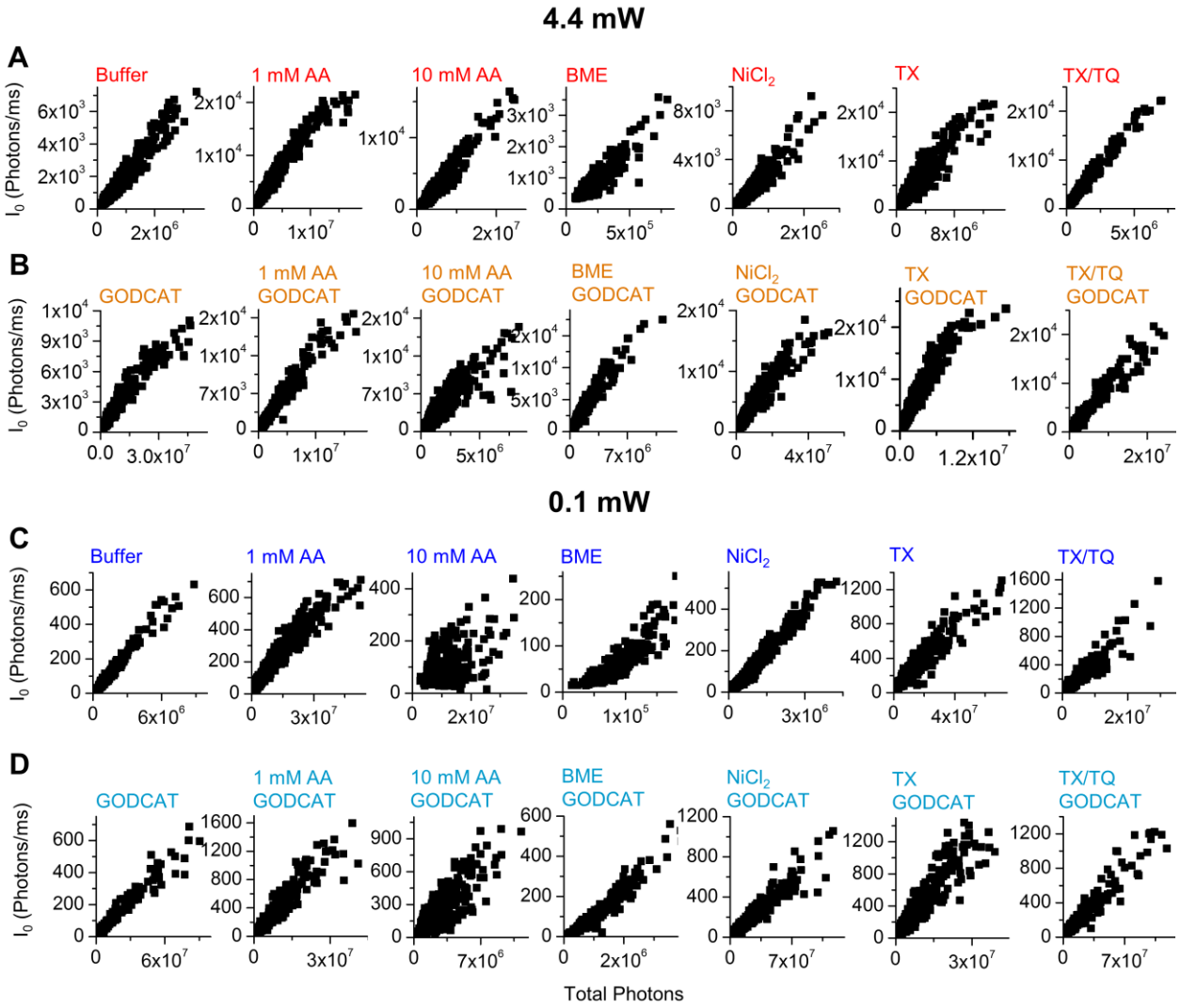

Figure 4.5. Correlation plots of the initial intensity versus the total photon output of the PPE-CO_2-coated NPs. The plotted values were obtained from individual intensity *versus* time trajectories extracted from TIRFM movies acquired while flowing different additives in either buffer or a buffered solution containing GODCAT oxygen scavenger under an excitation power of either 4.4 or 0.1 mW. (A) Buffer, 4.4 mW. (B) GODCAT, 4.4 mW. (C) Buffer, 0.1 mW. (D) GODCAT, 0.1 mW.

4.3.5 Effect of additives on the total photon count (photostablity) of PPE-CO_2-49 coated NPs

The ultimate indicator of photostability is the total number of photons emitted before photobleaching. To facilitate comparison between the different conditions, the mean total photon output –and photon output relative to NPs in buffer only—was plotted for each solution condition under 4.4 and 0.1 mW excitation power in Figure 4.6A and 4.6B, respectively. The effect of each additive on the total photon output is discussed individually below.

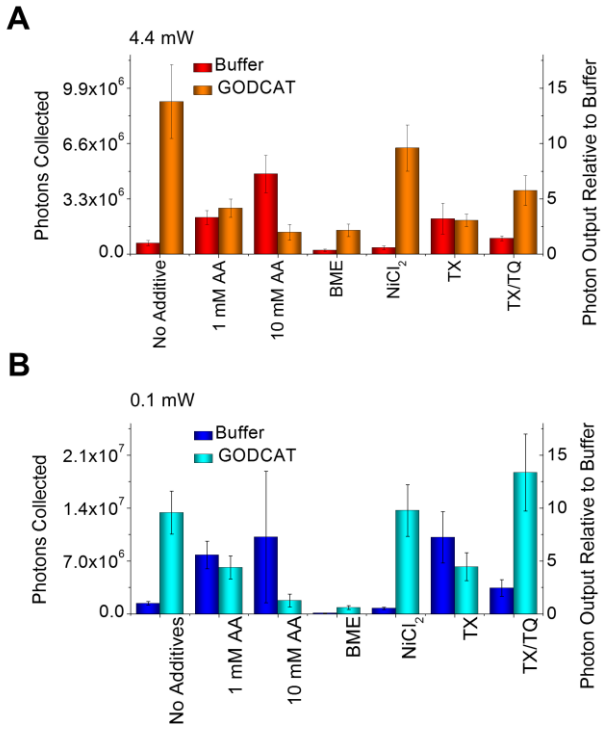

Figure 4.6. (A) and (B) Mean total photons collected from PPE-CO_2-49 coated NPs while flowing buffered solutions containing different additives. The right y-axis shows the number of photons collected relative to the NPs in buffer (*i.e.,* in the absence of any photostabilizing additives). The NPs were excited with a 405 nm laser at an output power of 4.4 and 0.1 mW, respectively. Error bars represent an estimate of the distribution that takes into account the effect of the variation in the number of polymers adsorbed per NP (*vide supra*).

Consistent with oxygen being a key player in the photobleaching pathway of the PPE-CO_2-49 coated NP, removing oxygen using the GODCAT oxygen scavenging system led to an increased photon output of 14-fold and 10-fold compared to buffer under 4.4 and 0.1 mW power, respectively, (Figure 4.6).

The additives BME and Ni^{2+} did not lead to an increase in the photon output compared to either buffer or to GODCAT. In fact, BME led to a decrease of 0.35 and 0.06-fold compared to buffer under 4.4 and 0.1 mW excitation intensity, respectively (Figure 4.5). BME also had a negative effect when mixed with GODCAT, decreasing its effectiveness from 14 to 2.2-fold under 4.4 mW excitation, and from 10-fold to 0.6-fold under 0.1 mW excitation (Figure 4.6). Although the reason for its negative impact is unclear, BME was excluded as a useful additive for TIRFM imaging of PPE-CO_2 based on these results.

Ni^{2+} under the conditions employed was found to be quench the excited singlet state by 70% and by 63% in buffer and in GODCAT, respectively (Figure 4.11). Here, the quenching is likely facilitated by static binding of the Ni^{2+} cation to the CO_2^- groups of the polymer, similar to what has been previously reported for Ni2+ binding to DNA[37, 52] or negatively charged lipid membranes.[37] Given the evidence that Ni^{2+} quenches the singlet excited state, it would also be expected to quench the longer-lived triplet state if the process is energetically favorable. However, no improvement was observed upon removing the competing triplet quencher oxygen. In fact, Ni^{2+} caused a decrease in the photon output of 0.6 and 0.5-fold compared to buffer under 4.4 mW and 0.1 mW excitation power, respectively, and a decrease from 14-fold in GODCAT to 10-fold in $NiCl_2$/GODCAT under 4.4 mW illumination, although no corresponding change was observed under 0.1 mW illumination (Figure 4.6). Ultimately, it was concluded that Ni^{2+} is not a promising additive for TIRFM imaging of PPE-CO_2.

In the case of ascorbic acid, employed at 1 mm concentration, the total photon output was improved by a factor of 3.3 and 5.6-fold upon excitation with 4.4 and 0.1 mW power, respectively (Figure 4.6). At this concentration, AA did not affect the fluorescence quantum yield of PPE-CO_2-49 at the ensemble level (Figure S5E), suggesting that it is unable to intercept the short-lived singlet excited state. 1 mM AA may, however, compete with O_2 to quench the longer-lived triplet states, and it may further intercept any singlet oxygen formed. Both processes ultimately result in a reduction in the amount of singlet oxygen present and a corresponding improvement in the photostability. Increasing the concentration of AA to 10 mM resulted in a further increase in the photon output, to 7.2 and 7.3-fold under 4.4 and 0.1 mW excitation power, respectively (Figure 4.6). In contrast to what was observed with 1 mM AA, the ensemble emission intensity was quenched 75% in 10 mM AA (Figure 4.11E), indicating that it is able to intercept excited singlet states at this concentration. By the same token, however, the efficiency of triplet quenching is also expected to increase, and in this case the improved photostability and increased duty cycle amply compensated for the reduced fluorescence quantum yield under TIRFM imaging conditions.

Interestingly, the effect of adding AA to GODCAT was deleterious rather than additive, with the mean photon output falling from 14-fold in GODCAT to 4-fold in 1 mM AA/GODCAT and to 2-fold in 10 mM AA/GODCAT under 4.4 mW excitation power (Figure 4.6A). Under 0.1 mW excitation power the same trend was observed, with the mean photon output falling from 10-

fold in GODCAT to 4.4-fold in 1 mM AA/GODCAT and to 1.3-fold in 10 mM AA/GODCAT. (Figure 4.6B). This result may be rationalized by considering that AA is a reducing agent that has been previously shown to quench fluorophore triplet states by producing reactive radical anion intermediates,[32] possibly opening up a new pathway for polymer degradation. It is plausible that removal of O_2, an efficient scavenger for radical anions, would increase the population of radical anions and thus the probability of photoinduced degradation of PPE-CO_2-49. From the overall decrease in photon output and the proposed mechanism, one may conclude that the negative impact of photoinduced degradation through radical anion intermediates overpowers the benefit gained by reducing the production of ROS. In order to overcome this problem and also to prevent long off states/instability in the signal intensity, AA is usually used in conjunction with a complementary oxidizing agents, such as methyl viologen (MV^{2+}), that efficiently scavenges radical anions and regenerates the chromophore ground state.[32] Unfortunately, MV^{2+} is also a highly efficient static quencher of PPE-CO_2 fluorescence,[53] thus making it incompatible with fluorescence imaging studies on these materials. Finding a suitable substitute for MV^{2+} may render AA a useful photostabilizing additive in GODCAT as well as in buffer.

Similar results to AA were achieved with TX. The total photon output was improved by a factor of 3.2 and 7.2-fold when 2 mM TX was dissolved in air equilibrated buffer under 4.4 and 0.1 mW excitation power, respectively (Figure 4.6). The ensemble fluorescence spectrum showed no quenching (Figure 4.11E), leading to the conclusion that TX was not intercepting singlet excited states at this concentration. Also similarly to AA, the effect of mixing TX with GODCAT was deleterious, leading to a drop in photon output from 14-fold in GODCAT to 3.1-fold in TX/GODCAT under 4.4 mW excitation power, and from 10-fold in GODCAT to 4.6-fold in TX/GODCAT under 0.1 mW (Figure 4.6). TX, like AA, has been reported to quench triplet states following photoinduced reduction and generation of radical anion intermediates,[38] opening the possibility for photoinduced degradation through this reactive intermediate. Combining TX with its oxidized form, TQ, in a 93:7 mole ratio in a GODCAT containing solution led to a slight improvement in its performance, from 3.1-fold to 5.7-fold under 4.4 mW excitation, and to a remarkable improvement of 4.6-fold to 13.4-fold under 0.1 mW excitation. This result is consistent with TQ reducing radical anions. The fact that a larger improvement was observed under 0.1 mW as opposed to 4.4 mW excitation may suggest that the photoinduced degradation pathway involves light absorption by the radical anion intermediate.

4.4 Conclusion

Several different solution additives have been screened for their ability to improve the photostability of PPE-CO_2-49 in aqueous solution under SM imaging conditions. In the absence of any additives, > 90% of the emission intensity signal from PPE-CO_2-49 adsorbed onto 100 nm diameter SiO_2 NPs was lost after just one second of illumination under 4.4 mW laser power in a TIRFM, highlighting the need to improve its photostability before commencing further SMS studies. In summary, addition of the antioxidant/triplet quenchers AA and TX led to a 3-8-fold increase in the number of photons collected as well as an enhancement of the initial emission intensity, consistent with an increase in the duty cycle attributed to the quenching of triplet states. Removal of oxygen using GODCAT led to an impressive 10-15-fold increase in the photostability relative to buffer, implicating ROS as an important agent in the photodegradation of PPE-CO_2-49. Combining AA and TX with GODCAT had a deleterious rather than an additive effect, suggesting that an oxidizing agent is in fact necessary to rescue the polymer from reactive intermediates formed via reaction with AA/TX. Addition of 15% TQ to the TX/GODCAT mixture restored the photostability, supporting the necessity of an oxidizing agent to complete the reduction/oxidation (ROX) scheme. Although β-mercaptoethanol and Ni^{2+} were also investigated, unfortunately they were not found to have useful properties toward the photostabilization of PPE-CO_2-49.

The highest photon output achieved in this study was 1.9 $x10^7$ per NP, obtained in the presence of TX/TQ and GODCAT under 0.1 mW excitation power (see Figure 4.6B). Considering that there are on average 450 PPE-CO_2-49 polymers adsorbed per NP (see Supporting Information for details), this works out to *ca*. 4.2 $x10^4$ photons per polymer detected before photobleaching. This value places PPE-CO_2-49 within the lower range of commonly used organic single molecule fluorophores, where photon outputs between $1x10^4$-$1x10^6$ are typically reported in TIRF setups.[32, 36, 54-55] We are optimistic that further optimization of the solution conditions (*e.g.*, by examining different concentrations, TX/TQ ratios, and identifying a suitible redox partner to compliment AA) will lead to even larger improvements in PPE-CO_2-49 photostability. Overall, however, we believe that the results reported here provide a solid starting point such that researchers may begin to take full advantage of powerful SMF imaging techniques in the pursuit of understanding complex CPE photophysics or toward the application of these materials in other advanced microscopy assays.

4.5 References

1. Bout, D. A. V.; Yip, W.-T.; Hu, D.; Fu, D.-K.; Swager, T. M.; Barbara, P. F. Discrete Intensity Jumps and Intramolecular Electronic Energy Transfer in the Spectroscopy of Single Conjugated Polymer Molecules. *Science* **1997,** *277*, 1074-1077.

2. Wu, C.; Bull, B.; Szymanski, C.; Christensen, K.; McNeill, J. Multicolor Conjugated Polymer Dots for Biological Fluorescence Imaging. *ACS Nano* **2008,** *2*, 2415-2423.

3. Yu, J.; Hu, D.; Barbara, P. F. Unmasking Electronic Energy Transfer of Conjugated Polymers by Suppression of O_2 Quenching. *Science* **2000,** *289*, 1327-1330.

4. Calver, C. F.; Liu, H.-W.; Cosa, G. Exploiting Conjugated Polyelectrolyte Photophysics toward Monitoring Real-Time Lipid Membrane-Surface Interaction Dynamics at the Single-Particle Level. *Langmuir* **2015,** *31*, 11842-11850.

5. Karam, P.; Ngo, A. T.; Rouiller, I.; Cosa, G. Unraveling Electronic Energy Transfer in Single Conjugated Polyelectrolytes Encapsulated in Lipid Vesicles. *Proc. Natl. Acad. Sci. U. S. A.* **2010,** *107*, 17480-17485.

6. Dalgarno, P. A.; Traina, C. A.; Penedo, J. C.; Bazan, G. C.; Samuel, I. D. W. Solution-Based Single Molecule Imaging of Surface-Immobilized Conjugated Polymers. *J. Am. Chem. Soc.* **2013,** *135*, 7187-7193.

7. Liu, H.-W.; Ngo, A. T.; Cosa, G. Enhancing the Emissive Properties of Poly(P-Phenylenevinylene)-Conjugated Polyelectrolyte-Coated SiO_2 Nanoparticles. *J. Am. Chem. Soc.* **2011,** *134*, 1648-1652.

8. Wu, C.; Szymanski, C.; Cain, Z.; McNeill, J. Conjugated Polymer Dots for Multiphoton Fluorescence Imaging. *J. Am. Chem. Soc.* **2007,** *129*, 12904-12905.

9. Darwish, G. H.; Karam, P. Nanohybrid Conjugated Polyelectrolytes: Highly Photostable and Ultrabright Nanoparticles. *Nanoscale* **2015**.

10. Pu, K.-Y.; Liu, B. Fluorescent Conjugated Polyelectrolytes for Bioimaging. *Adv. Funct. Mater.* **2011,** *21*, 3408-3423.

11. Sun, M.; Sun, B.; Liu, Y.; Shen, Q.-D.; Jiang, S. Dual-Color Fluorescence Imaging of Magnetic Nanoparticles in Live Cancer Cells Using Conjugated Polymer Probes. *Sci. Rep.* **2016,** *6*, 22368.

12. Liu, Y.; Wu, P.; Jiang, J.; Wu, J.; Chen, Y.; Tan, Y.; Tan, C.; Jiang, Y. Conjugated Polyelectrolyte Nanoparticles for Apoptotic Cell Imaging. *ACS Appl. Mater. Interfaces* **2016,** *8*, 21984-21989.

13. Kahveci, Z.; Vázquez-Guilló, R.; Martínez-Tomé, M. J.; Mallavia, R.; Mateo, C. R. New Red-Emitting Conjugated Polyelectrolyte: Stabilization by Interaction with Biomolecules and Potential Use as Drug Carriers and Bioimaging Probes. *ACS Appl. Mater. Interfaces* **2016,** *8*, 1958-1969.

14. Shames, A. I.; Inasaridze, L. N.; Akkuratov, A. V.; Goryachev, A. E.; Katz, E. A.; Troshin, P. A. Assessing the Outdoor Photochemical Stability of Conjugated Polymers by Epr Spectroscopy. *J. Mater. Chem. A* **2016,** *4*, 13166-13170.

15. Neugebauer, H.; Brabec, C.; Hummelen, J. C.; Sariciftci, N. S. Stability and Photodegradation Mechanisms of Conjugated Polymer/Fullerene Plastic Solar Cells. *Sol. Energy Mater. Sol. Cells* **2000,** *61*, 35-42.

16. Jørgensen, M.; Norrman, K.; Krebs, F. C. Stability/Degradation of Polymer Solar Cells. *Sol. Energy Mater. Sol. Cells* **2008,** *92*, 686-714.

17. Burrows, H. D.; Seixas de Melo, J.; Serpa, C.; Arnaut, L. G.; Monkman, A. P.; Hamblett, I.; Navaratnam, S. S1∼>T1 Intersystem Crossing in π-Conjugated Organic Polymers. *J. Chem. Phys.* **2001,** *115*, 9601-9606.

18. Scurlock, R. D.; Wang, B.; Ogilby, P. R.; Sheats, J. R.; Clough, R. L. Singlet Oxygen as a Reactive Intermediate in the Photodegradation of an Electroluminescent Polymer. *J. Am. Chem. Soc.* **1995,** *117*, 10194-10202.

19. Ogilby, P. R. Singlet Oxygen: There Is Indeed Something New under the Sun. *Chem. Soc. Rev.* **2010,** *39*, 3181-3209.

20. List, E. J. W.; Guentner, R.; Scanducci de Freitas, P.; Scherf, U. The Effect of Keto Defect Sites on the Emission Properties of Polyfluorene-Type Materials. *Adv. Mater.* **2002,** *14*, 374-378.

21. Kulkarni, A. P.; Kong, X.; Jenekhe, S. A. Fluorenone-Containing Polyfluorenes and Oligofluorenes: Photophysics, Origin of the Green Emission and Efficient Green Electroluminescence†. *J. Phys. Chem. B* **2004,** *108*, 8689-8701.

22. Romaner, L.; Pogantsch, A.; Scandiucci de Freitas, P.; Scherf, U.; Gaal, M.; Zojer, E.; List, E. J. W. The Origin of Green Emission in Polyfluorene-Based Conjugated Polymers: On-Chain Defect Fluorescence. *Adv. Funct. Mater.* **2003,** *13*, 597-601.

23. Palacios, R. E.; Fan, F.-R. F.; Grey, J. K.; Suk, J.; Bard, A. J.; Barbara, P. F. Charging and Discharging of Single Conjugated-Polymer Nanoparticles. *Nat. Mater.* **2007,** *6*, 680-685.

24. Bolinger, J. C.; Traub, M. C.; Adachi, T.; Barbara, P. F. Ultralong-Range Polaron-Induced Quenching of Excitons in Isolated Conjugated Polymers. *Science* **2011,** *331*, 565-567.

25. Yu, J.; Song, N. W.; McNeill, J. D.; Barbara, P. F. Efficient Exciton Quenching by Hole Polarons in the Conjugated Polymer Meh-Ppv. *Isr. J. Chem.* **2004,** *44*, 127-132.

26. Yu, J.; Wu, C.; Tian, Z.; McNeill, J. Tracking of Single Charge Carriers in a Conjugated Polymer Nanoparticle. *Nano Lett.* **2012,** *12*, 1300-1306.

27. Muller-Meskamp, L.; Fahlteich, J.; Krebs, F. C. Barrier Technology and Applications. In *Stability and Degradation of Organic and Polymer Solar Cells*; John Wiley & Sons, Ltd: 2012; pp 269-329.

28. Andrew, T. L.; Swager, T. M. Reduced Photobleaching of Conjugated Polymer Films through Small Molecule Additives. *Macromolecules* **2008,** *41*, 8306-8308.

29. Tian, Z.; Yu, J.; Wang, X.; Groff, L. C.; Grimland, J. L.; McNeill, J. D. Conjugated Polymer Nanoparticles Incorporating Antifade Additives for Improved Brightness and Photostability. *J. Phys. Chem. B* **2013,** *117*, 4517-4520.

30. Ngo, A. T.; Lau, K. L.; Quesnel, J. S.; Aboukhalil, R.; Cosa, G. Deposition of Anionic Conjugated Poly(Phenylenevinylene) onto Silica Nanoparticles Via Electrostatic Interactions — Assembly and Single-Particle Spectroscopy. *Can. J. Chem.* **2011,** *89*, 385-394.

31. Zhao, X.; Jiang, H.; Schanze, K. S. Polymer Chain Length Dependence of Amplified Fluorescence Quenching in Conjugated Polyelectrolytes. *Macromolecules* **2008,** *41*, 3422-3428.

32. Vogelsang, J.; Kasper, R.; Steinhauer, C.; Person, B.; Heilemann, M.; Sauer, M.; Tinnefeld, P. A Reducing and Oxidizing System Minimizes Photobleaching and Blinking of Fluorescent Dyes. *Angew. Chem. Int. Edit.* **2008,** *47*, 5465-5469.

33. Rasnik, I.; McKinney, S. A.; Ha, T. Nonblinking and Long-Lasting Single-Molecule Fluorescence Imaging. *Nat. Methods* **2006,** *3*, 891-893.

34. Holzmeister, P.; Gietl, A.; Tinnefeld, P. Geminate Recombination as a Photoprotection Mechanism for Fluorescent Dyes. *Angew. Chem. Int. Edit.* **2014,** *53*, 5685-5688.

35. Harada, Y.; Sakurada, K.; Aoki, T.; Thomas, D. D.; Yanagida, T. Mechanochemical Coupling in Actomyosin Energy Transduction Studied by in Vitro Movement Assay. *J. Mol. Biol.* **1990,** *216*, 49-68.

36. Glembockyte, V.; Lin, J.; Cosa, G. Improving the Photostability of Red- and Green-Emissive Single-Molecule Fluorophores Via Ni^{2+} Mediated Excited Triplet-State Quenching. *J. Phys. Chem. B* **2016,** *120*, 11923-11929.

37. Glembockyte, V.; Lincoln, R.; Cosa, G. Cy3 Photoprotection Mediated by Ni^{2+} for Extended Single-Molecule Imaging: Old Tricks for New Techniques. *J. Am. Chem. Soc.* **2015,** *137*, 1116-1122.

38. Cordes, T.; Vogelsang, J.; Tinnefeld, P. On the Mechanism of Trolox as Antiblinking and Antibleaching Reagent. *J. Am. Chem. Soc.* **2009,** *131*, 5018-5019.

39. Joo, C.; Ha, T. Imaging and Identifying Impurities in Single-Molecule Fret Studies. *Cold Spring Harb Protoc.* **2012,** *10*, 1109-1112.

40. Schwartz, B. J. Conjugated Polymers as Molecular Materials: How Chain Conformation and Film Morphology Influence Energy Transfer and Interchain Interactions. *Annu. Rev. Phys. Chem.* **2003,** *54*, 141-172.

41. Scholes, G. D.; Rumbles, G. Excitons in Nanoscale Systems. *Nat. Mater.* **2006,** *5*, 683-696.

42. Bolinger, J. C.; Traub, M. C.; Brazard, J.; Adachi, T.; Barbara, P. F.; Vanden Bout, D. A. Conformation and Energy Transfer in Single Conjugated Polymers. *Acc. Chem. Res.* **2012,** *45*, 1992-2001.

43. Ebihara, Y.; Vacha, M. Relating Conformation and Photophysics in Single Meh-Ppv Chains. *J. Phys. Chem. B* **2008,** *112*, 12575-12578.

44. Huser, T.; Yan, M.; Rothberg, L. J. Single Chain Spectroscopy of Conformational Dependence of Conjugated Polymer Photophysics. *Proc. Natl. Acad. Sci. U. S. A.* **2000,** *97*, 11187-11191.

45. Karam, P.; Hariri, A. A.; Calver, C. F.; Zhao, X.; Schanze, K. S.; Cosa, G. Interaction of Anionic Phenylene Ethynylene Polymers with Lipids: From Membrane Embedding to Liposome Fusion. *Langmuir* **2014,** *30*, 10704-10711.

46. Vogelsang, J.; Brazard, J.; Adachi, T.; Bolinger, J. C.; Barbara, P. F. Watching the Annealing Process One Polymer Chain at a Time. *Angew. Chem. Int. Edit.* **2011,** *50*, 2257-2261.

47. Hu, D.; Yu, J.; Wong, K.; Bagchi, B.; Rossky, P. J.; Barbara, P. F. Collapse of Stiff Conjugated Polymers with Chemical Defects into Ordered, Cylindrical Conformations. *Nature* **2000,** *405*, 1030-1033.

48. Lupton, J. M. Single-Molecule Spectroscopy for Plastic Electronics: Materials Analysis from the Bottom-Up. *Adv. Mater.* **2010,** *22*, 1689-1721.

49. Vogelsang, J.; Lupton, J. M. Solvent Vapor Annealing of Single Conjugated Polymer Chains: Building Organic Optoelectronic Materials from the Bottom Up. *J. Phys. Chem. Lett.* **2012,** *3*, 1503-1513.

50. Park, S.-J.; Gesquiere, A. J.; Yu, J.; Barbara, P. F. Charge Injection and Photooxidation of Single Conjugated Polymer Molecules. *J. Am. Chem. Soc.* **2004,** *126*, 4116-4117.

51. Barbara, P. F.; Gesquiere, A. J.; Park, S.-J.; Lee, Y. J. Single-Molecule Spectroscopy of Conjugated Polymers. *Acc. Chem. Res.* **2005,** *38*, 602-610.

52. Atherton, S. J.; Beaumont, P. C. Quenching of the Fluorescence of DNA-Intercalated Ethidium Bromide by Some Transition-Metal Ions. *J. Phys. Chem.* **1986,** *90*, 2252-2259.

53. Jiang, H.; Zhao, X.; Schanze, K. S. Amplified Fluorescence Quenching of a Conjugated Polyelectrolyte Mediated by Ca^{2+}. *Langmuir* **2006,** *22*, 5541-5543.

54. Zheng, Q.; Juette, M. F.; Jockusch, S.; Wasserman, M. R.; Zhou, Z.; Altman, R. B.; Blanchard, S. C. Ultra-Stable Organic Fluorophores for Single-Molecule Research. *Chem. Soc. Rev.* **2014,** *43*, 1044-1056.

55. Dempsey, G. T.; Vaughan, J. C.; Chen, K. H.; Bates, M.; Zhuang, X. Evaluation of Fluorophores for Optimal Performance in Localization-Based Super-Resolution Imaging. *Nat. Methods* **2011,** *8*, 1027-1036.

56. Roy, R.; Hohng, S.; Ha, T. A Practical Guide to Single-Molecule Fret. *Nat. Methods* **2008,** *5*, 507-516.

4.6 Experimental section

4.6.1 Materials

Poly(phenylene ethynylene) carboxylate PPE-CO_2-49 (PDI = 2.3) was synthesized as previously described.[31] Concentrated polymer solutions in water were diluted in Hyclone HyPure molecular biology-grade water purchased from Fisher. Molecular biology grade solutions of 1 M HEPES (pH 7.3) and 5 M NaCl, hydrogen peroxide (30% solution), HPLC grade acetone, ascorbic acid, and concentrated HCl were purchased from Fisher. Vectabond was purchased from Vector Laboratories. Concentrated sulfuric acid was purchased from ACP Chemicals. 100 nm diameter SiO_2 colloidal solution (5.4% w/v) was purchased from Polysciences, Inc. 3-aminopropyl trimethoxysilane, 2-mercaptoethanol, glucose oxidase, catalase, nickel(II) chloride hexahydrate, glucose, and 6-hydroxy-2,5,7,8-tetramethylchromane-2-carboxylic acid (Trolox) was purchased from Sigma Aldrich. All materials were used without further purification.

4.6.2 Preparation of aminosilanized SiO_2 NPs

The surface of 100 nm diameter SiO_2 NPs was aminosilanized to aid in the deposition of PPE-CO_2-49 *via* electrostatic interactions. A 200 μL aliquot of as-purchased SiO_2 suspension (5.4% w/v) (pH 10) was added to an Eppendorf tube. 3-aminopropyl trimethoxysilane (1 μL) was then added and mixed with vortexing. The reaction mixture was incubated for 5 mins and 3 M HCl (8 μL) was added to protonate the amines and quench the reaction. The SiO_2-NH_3^+ NPs were diluted 5-fold (total volume = 1.2 mL) and precipitated by centrifugation at 16060*g* for 5 mins. 1 mL of the supernatant was removed and replaced by an equal volume of water. The particles were resuspended using vortexing/sonication to break up the pellet and the washing cycle was repeated until the pH of the supernatant was *ca.* 5.5 (typically 3 cycles were required). After the final washing, the NPs were resuspended in 200 μL of water to a final concentration of 65 nM in terms of the number of NPs.

4.6.3 Adsorption of PPE-CO_2-49 onto $SiO_2NH_3^+$ NPs

$SiO_2NH_3^+$ NPs (65 nM, 6 μL) were diluted in water adjusted to pH 5 using HCl (351 μL) in an Eppendorf tube. In a second tube, PPE-CO_2-49 (2.2 mM, 17 μL) was also diluted in water at pH 5 (368 μL). The polymer solution was added to the NP solution all at once and then vortexed briefly. The mixture was incubated for *ca*. 30 mins and then centrifuged at 16060*g* for 5 mins to precipitate the NPs. 0.6 mL of the supernatant was removed, taking care not to disturb the NPs, and replaced with an equal volume of water. The NPs were resuspended using vortexing/sonication. The centrifugation/washing step was repeated until the supernatant showed no trace of polymer by UV-vis absorption measurements (typically 5+ washing cycles were required). Assuming no losses, the final concentration of PPE-CO_2-49-coated NPs was 0.5 nM.

4.6.4 Characterization of NPs

Steady-state fluorescence spectroscopy was carried out using a Photon Technology International (PTI) Quanta Master fluorimeter. Absorption spectra were recorded using a Hitachi U2800 UV–vis spectrophotometer. Dynamic light scattering measurements were performed using a Malvern Zetasizer Nano ZS with equipped with a 633 nm laser. Samples were equilibrated at 25 °C for 5 mins before acquisition. Zeta potential measurements were performed using a ZetaPlus ζ potential analyzer (Brookhaven Instruments Corp.). The reported values are the average obtained from 5 runs consisting of 3 cycles.

4.6.5 Preparation of additive solutions

All solutions were prepared in a buffered solution containing 10 mM HEPEs and 150 mM NaCl, unless otherwise noted. $NiCl_2$*$6H_2O$ was dissolved in deionized water (*ca*. 1 M) and diluted to 0.1 mM in buffer. BME (14.3 M, neat) was diluted to 143 mM in buffer. AA was dissolved in buffer (*ca*. 1 M) and diluted to 10 mM and 1 mM in buffer. TX was dissolved in DMSO (200 mM) and then diluted to 2 mM in buffer. TQ was generated by exposure of a TX solution to UV light (270 nm). The amount of TQ relative to TX was determined to be 7% by UV-Vis spectroscopy following the protocol of Cordes *et al*.[38] GODCAT scavenger was prepared by diluting a 30% (w/v) stock solution of D-glucose to 3% (w/v) in buffer. To this, stock solutions of glucose oxidase and catalase were added to obtain a final concentration of 165 and 1600 units/mL, respectively. All stock solutions were prepared fresh, with the exception of glucose,

glucose oxidase, and catalase, which could be stored for several months at 4 °C. The final volume of all solutions was 0.5 mL.

4.6.6 TIRFM imaging

Glass coverslips were cleaned and functionalized with amine groups in preparation for imaging the PPE-CO_2-49 coated SiO_2 NPs. Coverslips were immersed in piranha solution (1 part 30% hydrogen peroxide and 2 parts concentrated sulfuric acid) and left to soak for *ca.* 1 hour in a glass jar. The piranha solution was poured off and the coverslips were rinsed at least three times with deionized water and then sonicated for 10 mins. The water was poured off and the coverslips were rinsed three times with acetone, taking care to rinse all moisture off the sides of the jar and the lid, followed by another 10 mins of sonication. The coverslips were then immersed in 25 mL of acetone and 0.50 mL of Vectabond was added dropwise. The mixture was agitated gently and incubated for 5 minutes. The acetone/Vectabond mixture was poured out and the reaction was quenched by rinsing with 2x25 mL of water. Prior to imaging, the coverslips were dried under a stream of nitrogen. A predrilled polycarbonate film (Grace Biolabs) with an adhesive side was assembled on top of the coverslips to form a sample chamber (volume = *ca*. 10 µL). Silicone ports were glued on top of the predrilled holes of the chamber with double-sided tape such that solutions containing the additives could be flowed through the chamber.

Electrostatic interactions between the positively charged glass surface and the negatively charged PPE-CO_2-49-coated NPs facilitated their adsorption on the surface of the coverslips for imaging. Approximately 20 µL of a 50 pM solution of NPs in buffer were injected into the imaging chamber and incubated for *ca*. 1 min. The chamber was washed with at least 5x20 µL of buffer to remove unadsorbed NPs. Additional aliquots of NPs were added as needed until a satisfactory surface density was achieved. The NPs were then imaged while flowing buffered solutions containing additives, where noted, using a syringe pump at a rate of 2 µL/min.

Fluorescence imaging was carried out using an inverted Nikon Eclipse Ti microscope equipped with the Perfect Focus System (PFS). The microscope implemented an objective-type TIRF configuration with a Nikon TIRF illuminator and an oil immersion objective (CFI SR Apo TIRF 100× Oil Immersion Objective Lens, numerical aperture (NA) 1.49). The excitation source was the 405 nm output of an Agilent MLC400B Monolithic Laser Combiner. Laser powers of 0.1

mW to4.4 mW were measured out of the objective. The laser beam was passed through a multiband cleanup filter (ZET405/488/561/647x, Chroma Technology) and coupled into the microscope objective using a multiband beam splitter (ZT405/488r/561/640rpc, Chroma Technology). Images were recorded onto a 512x512 pixel region of a back-illuminated electron-multiplying charge-coupled device (EMCCD) camera (iXon X3 DU-897-CS0-#BV, Andor Technology). Data analysis was performed using a home-built analysis routine written in Matlab based on the algorithms developed by the Ha group.[56]

4.7 Supporting information

4.7.1 Purification of PPE-CO_2-49 coated NPs to remove unadsorbed polymer

The PPE-CO_2-49 coated NPs were prepared by adding aminosilanzed NPs ($SiO_2NH_3^+$) to an aqueous solution containing an amount of polymer in excess of what is required to passivate the surface. The PPE-CO_2-49 coated NPs were precipitated by centrifugation and 80% of the supernatant containing the excess, unadsorbed polymer was removed and replaced by an equal volume of water. Only 80% of the total volume was removed at a time to avoid disturbing the NP pellet. The UV-Vis absorption of the supernatants decreased after each centrifugation/washing step (Figure S1A). The expected absorbance of the supernatants was predicted based on a 5-fold dilution of the previous supernatant after each washing step and was compared to the actual absorbance measured (Figure S1B). The experimental values matched the expected values, indicating that the initially adsorbed polymer was not being removed from the NPs in subsequent washing cycles.

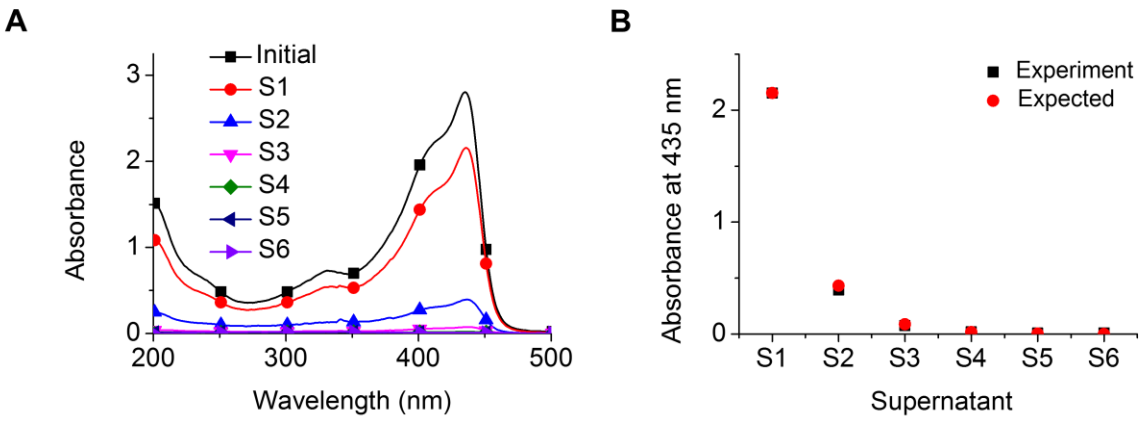

Figure 4.7. Purification of PPE-CO_2-49 coated NPs. (A) UV-Vis absorption spectrum of the initial solution of PPE-CO_2-49 (50 μM) used to coat the NPs (black squares) and of the supernatants removed after centrifugation (S1-S6). The "Initial" and "S1" solutions were diluted to achieve an appropriate concentration for measurement and then these spectra were multiplied by the dilution factor to give the spectra plotted here. (B) The absorbance value of each supernatant at the PPE-CO_2-49 absorption maximum of 435 nm (black squares) is compared to the expected value based strictly on dilution of the remaining unadsorbed polymer after each washing step (red circles).

4.7.2 Calculation of the surface coverage of PPE-CO_2-49 on the NPs

To estimate the surface area of the NPs covered by PPE-CO_2-49, the number of PRUs per NP was determined from UV-Vis absorption measurements. The polymer absorbance of the first supernatant was lower than that of the initial coating solution by a factor of 0.77, indicating that the missing 23% was adsorbed onto the surface of the NPs (Figure S1A). Given that the concentration of the initial coating solution was 5.0×10^{-5} M, this works out to a concentration of 5.0×10^{-5} M*0.23 = 1.15×10^{-5} M PPE-CO_2-49 PRUs adsorbed on the NPs. The surface area of one PRU was estimated to be 1.2 x 0.9 nm = 1.08 nm^2 using ChemBio3D Ultra version 12.0.2.1076 (CambridgeSoft). The total surface area of the polymer was then calculated to be 1.15×10^{-5} M*1.08 nm^2*N_A = 7.74×10^{18} nm^2/L. In turn, the concentration of NPs was 5.26×10^{-10} M and the average surface area of an NP was calculated from the formula for the surface area of a sphere, $4\pi r^2$, where the average value of r was estimated to be 55 nm based on dynamic light scattering data (Figure 1A). The total surface area of the NPs was then calculated to be 5.26×10^{-10} M*3.80×10^4 nm^2*N_A = 1.25×10^{19} nm^2/L. The percentage of the NP surface covered by PPE-CO_2-49 is equal to the surface area of the polymer divided by the surface area of the NPs: (7.74×10^{18} nm^2/L/1.25×10^{19} nm^2/L)*100 = 62%. We also note that this works out to an average of 1.15×10^{-5} M PPE-CO_2-49 PRUs/5.26×10^{-10} M NPs = 21,900 PRUs per NP, or *ca.* 450 polymers where n = 49.

4.7.3 Representative fluorescence intensity versus time trajectories of PPE-CO_2-49 coated NPs

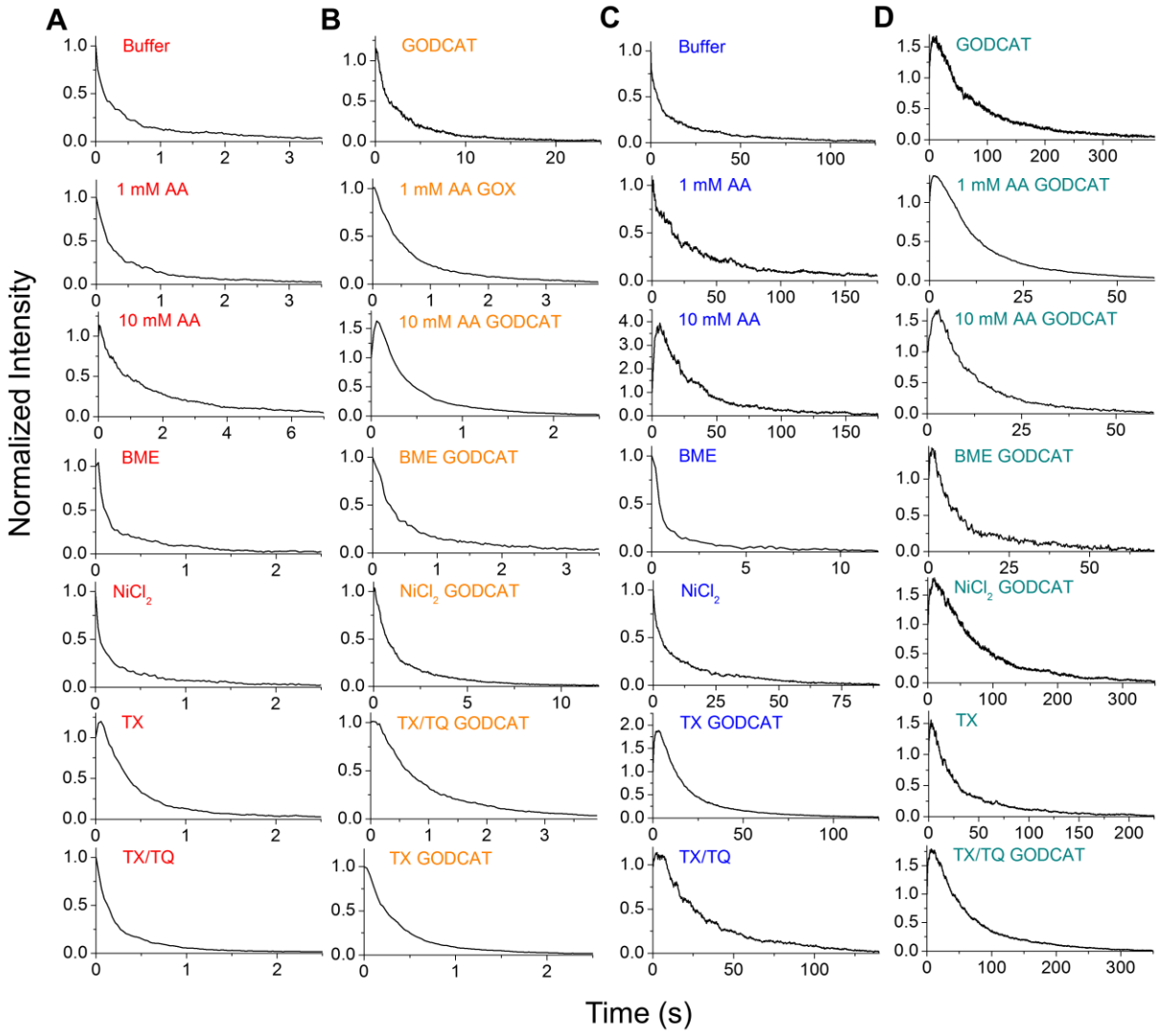

Figure 4.8. Fluorescence intensity versus time trajectories of representative NPs extracted from TIRFM movies acquired while flowing different additives in either buffer or a buffered solution containing GODCAT oxygen scavenger under an excitation power of either 4.4 or 0.1 mW. The trajectories are normalized to an initial intensity of 1. (A) Buffer, 4.4 mW. (B) GODCAT, 4.4 mW. (C) Buffer, 0.1 mW. (D) GODCAT, 4.4 mW.

4.7.4 Histograms of the initial intensity of PPE-CO_2-49 coated NPs

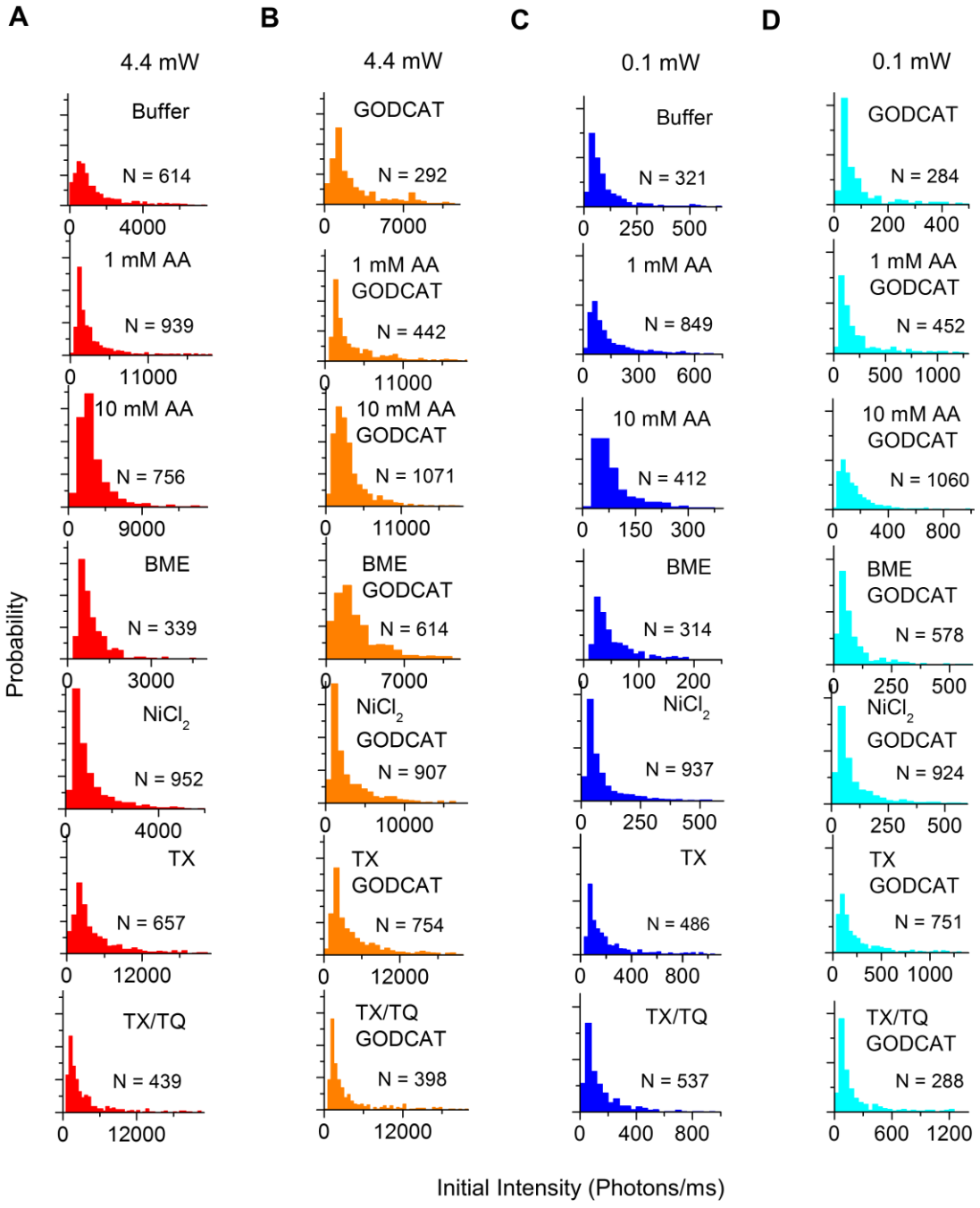

Figure 4.9. Histograms of the initial intensity of NPs in photons/ms extracted from TIRFM movies acquired while flowing different additives in either buffer or a buffered solution containing GODCAT oxygen scavenger under an excitation power of either 4.4 or 0.1 mW. Histograms are normalized to an area of 1. (A) Buffer, 4.4 mW. (B) GODCAT, 4.4 mW. (C) Buffer, 0.1 mW. (D) GODCAT, 4.4 mW.

4.7.5 Histograms of the total photon output of PPE-CO_2-49 coated NPs

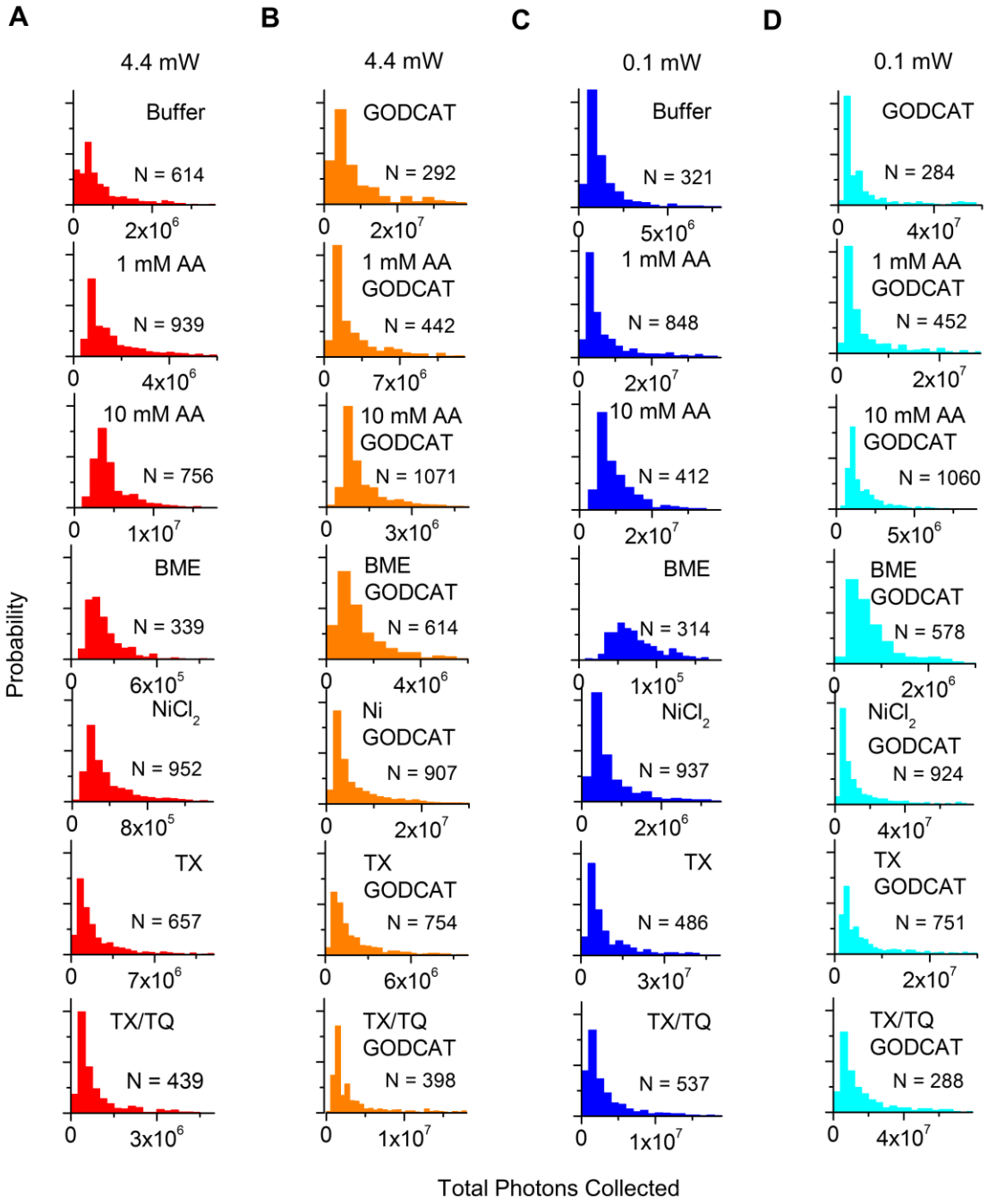

Figure 4.10. Histograms of the total photon output of NPs extracted from TIRFM movies acquired while flowing different additives in either buffer or a buffered solution containing GODCAT oxygen scavenger under an excitation power of either 4.4 or 0.1 mW. Histograms are normalized to an area of 1. (A) Buffer, 4.4 mW. (B) GODCAT, 4.4 mW. (C) Buffer, 0.1 mW. (D) GODCAT, 4.4 mW.

4.7.6. Mean fitting parameters and R^2 values obtained by fitting normalized intensity versus time trajectories to Equation 4.1

Table 4.1. Mean fitting parameters and R^2 value obtained by fitting fluorescence intensity versus time trajectories to Equation 4.1. Entries shaded in blue were acquired while flowing buffered solutions and the indicated additive. Entries shaded in cyan were acquired while flowing buffered solutions containing GODCAT oxygen scavenger and, where indicated, the additive(s). The excitation power was 0.1 mW for all samples.

Sample	*Q*	*d*	*G*	R^2
10 mM AA	3±2	0.04±0.01	1.0±0.4	0.983±0.009
TX	0.8±0.2	0.06±0.03	1.2±0.8	0.95±0.05
1 mM AA GODCAT	1.1±0.3	0.10±0.02	1.2±0.4	0.989±0.008
10 mM AA GODCAT	1.0±0.7	0.21±0.08	1.1±0.7	0.98±0.02
BME GODCAT	0.7±0.2	0.23±0.07	2.4±0.7	0.96±0.03
GODCAT	0.7±0.2	0.019±0.007	0.5±0.4	0.93±0.06
$NiCl_2$ GODCAT	1.1±0.3	0.021±0.005	0.3±0.1	0.97±0.03
TX GODCAT	1.1±0.3	0.11±0.02	1.4±0.5	0.989±0.006
TX/TQ GODCAT	1.1±0.3	0.029±0.007	0.5±0.2	0.98±0.02

4.7.7. Mean fitting parameters and R^2 values obtained by fitting normalized intensity versus time trajectories to Equation 4.2

Table 4.2. Mean fitting parameters and R^2 value obtained by fitting fluorescence intensity versus time trajectories to Equation 4.2. Entries shaded in blue were acquired while flowing buffered solutions and the indicated additive(s) at an excitation power of 0.1 mW. Entries shaded in red were acquired while flowing buffered solutions and, where indicated, the additive(s) at an excitation power of 4.4 mW. Entries shaded in orange were acquired while flowing buffered solutions containing GODCAT oxygen scavenger and, where indicated, the additive(s). The excitation power was 4.4 mW.

Sample	A_1	A_2	k_1	k_2	R^2
0.1 mW					
1 mM AA	0.30±0.08	0.66±0.08	0.01±0.02	0.2±5	0.99±0.03
BME	0.28±0.09	0.76±0.09	0.19±0.09	2.1±0.5	0.98±0.02
Buffer	0.31±0.05	0.55±0.05	0.026±0.006	0.3±0.2	0.99±0.02
$NiCl_2$	0.36±0.06	0.55±0.06	0.046±0.007	0.5±0.2	0.98±0.01
TX/TQ	--	--	--	--	--
4.4 mW					
1 mM AA	0.24±0.06	0.73±0.06	0.6±0.1	4±1	0.995±0.003
10 mM AA	0.5±0.01	0.6±0.1	0.37±0.06	1.9±0.8	0.996±0.002
BME	0.24±0.06	0.75±0.07	1.1±0.3	15±6	0.989±0.007
Buffer	0.33±0.08	9±4	0.8±0.3	0.64±0.08	0.99±0.02
$NiCl_2$	0.27±0.07	0.70±0.07	0.9±0.2	11±4	0.988±0.007
TX	0.1±0.1	1.0±0.2	0.8±0.6	3±2	0.99±0.02
TX/TQ	0.20±0.06	0.79±0.06	1.4±0.3	9±4	0.997±0.002
4.4 mW					
1 mM AA GODCAT	0.24±0.06	0.82±0.08	0.7±0.1	2.9±0.6	0.998±0.002
10 mM AA GODCAT	0.2±0.2	1.0±0.2	1.1±0.4	4±1	0.99±0.01
BME GODCAT	0.2±0.2	0.8±0.1	0.8±0.9	6±6	0.98±0.09
GODCAT	0.25±0.06	0.80±0.07	0.12±0.04	0.8±0.2	0.99±0.03
$NiCl_2$ GODCAT	0.26±0.06	0.83±0.08	0.22±0.04	1.1±0.5	0.996±0.002
TX GODCAT	0.22±0.07	0.79±0.08	1.0±0.3	4±1	0.998±0.007
TX/TQ GODCAT	0.20±0.08	0.86±0.09	0.41±0.09	1.6±0.4	0.998±0.002

4.7.8. Effect of the additives on the ensemble UV-Vis absorption and emission spectra of PPE-CO_2-49

The UV-Vis absorption spectrum of 1.6 μM PPE-CO_2-49 in buffer was acquired and compared to the spectrum in GODCAT (Figure S5A). The spectrum in GODCAT was noticeably different in both shape and absorbance. The absorbance spectrum of GODCAT solution was also acquired (absorbance in the UV region was anticipated due to the presence of amino acids in the enzymes glucose oxidase and catalase) (Figure S5A). The curve obtained by summation of the spectrum of GODCAT and the spectrum of PPE-CO_2-49 in buffer coincided with the spectrum of PPE-CO_2-49 in GODCAT, indicating that this spectrum is a convolution of its components, not that the components of GODCAT scavenger were influencing the absorptive properties of the polymer. Similarly, the other additives were not found to affect the absorptivity of PPE-CO_2-49 in either buffer or in GODCAT (Figure S5B and S5C, respectively).

The effect of the additives on the fluorescence quantum yield of PPE-CO_2-49 was also investigated by comparing its emission profile and intensity in each solution condition. GODCAT alone showed a weak fluorescence signal, but even after considering its contribution, the emission intensity of PPE-CO_2-49 was still enhanced by a factor of 1.2-fold in GODCAT compared to buffer (Figure S5D). As for the other additives, TX and 1 mM AA did not affect the fluorescence quantum yield, BME caused a slight enhancement, and $NiCl_2$ and 10 mM caused fluorescence quenching. These results were consistent in both buffer and in GODCAT (Figure S5E and S5F, respectively).

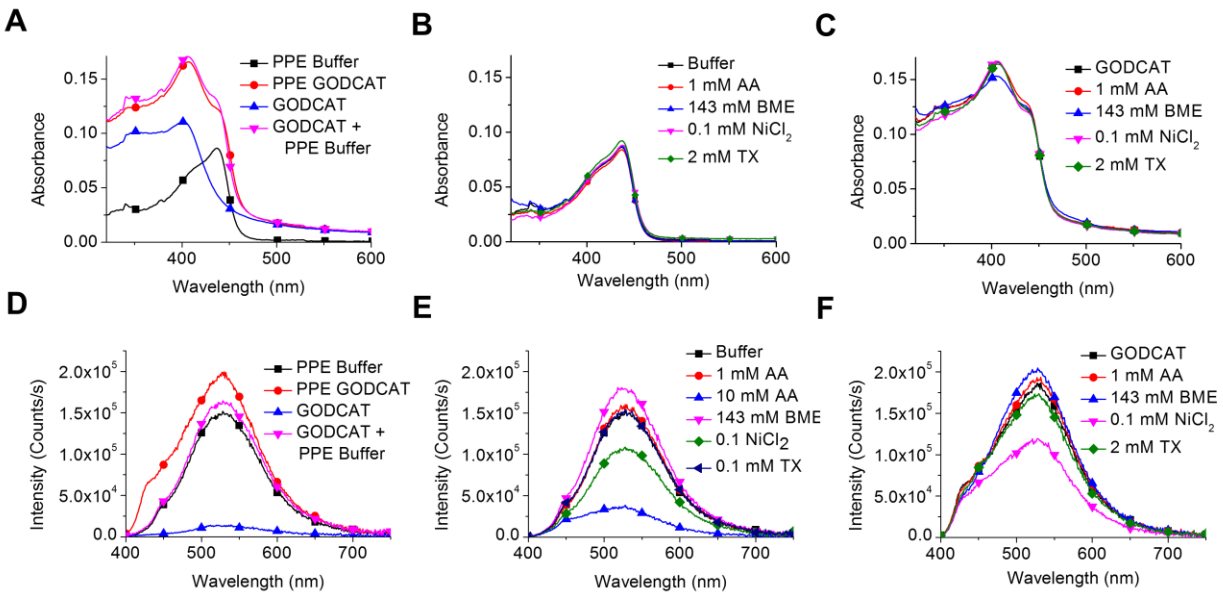

Figure 4.11. Effect of the additives on the ensemble UV-Vis absorption and emission spectra of PPE-CO_2-49. (A) UV-Vis absorption spectra of 1.6 µM PPE-CO_2-49 in buffer or GODCAT (black squares and red circles, respectively), GODCAT (blue triangles), and the spectrum obtained by summation of the spectrum of 1.6 µM PPE-CO_2-49 in buffer and the spectrum of GODCAT (purple inverted triangles). (B) and (C) UV-Vis absorption spectra of 1.6 µM PPE-CO_2-49 in a buffered solution or a buffered solution containing GODCAT oxygen scavenger, respectively (black squares) as well as containing either 1 mM AA (red circles), 143 mM BME (blue triangles), 0.1 mM $NiCl_2$ (purple inverted triangles) or 2 mM TX (green diamonds). (D), (E), and (F) Emission spectrum of the samples whose UV-Vis absorption spectra is shown in (A), (B) and (C), respectively. The excitation wavelength was 390 nm. Spectra are corrected for background and photomultiplier tube sensitivity.

Chapter 5: Additives for enhanced photostability of a poly(phenylene ethynylene)-based conjugated polyelectrolyte in lipid membranes

Author Contributions: **Christina F. Calver** and **Briony A. Lago** performed experiments. **Christina F. Calver** analyzed data and co-wrote the paper. **Prof. Kirk S. Schanze** provided the PPE-CO_2-49 polymer. **Prof. G. Cosa** designed the project, guided the interpretation of data, and co-wrote the paper.

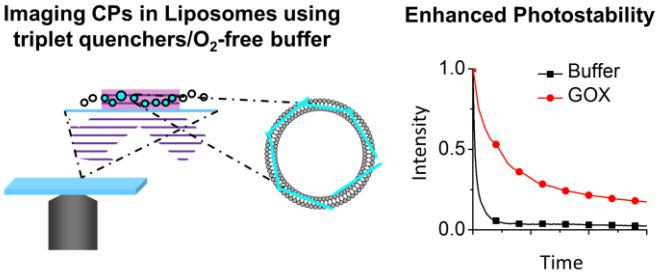

5.0 Preface

The previous chapter reported the use of different additives (triplet quenchers/oxygen scavenging system) toward improving the photostability of the CPE PPE-CO_2-49 in aqueous solution under SMF imaging conditions. From this study, several antifading cocktails for performing SMF experiments on PPE-CO_2-49 were identified. Encouraged by these results, Chapter 5 reports a similar study on the use of different additives toward improving the photostability of PPE-CO_2-49 embedded in liposome membranes. This study was motivated, in part, by our desire to extend our study on the membrane-assembled light harvesting antenna reported in Chapter 3 by imaging supported lipid bilayers containing embedded conjugated polyelectrolyte. Such an experiment, however, required that the brightness/photostability of the membrane-embedded PPE-CO_2 be improved. Although much of the methodology used in Chapter 5 mirrors that used in Chapter 4, subtle distinctions arose when considering the two different systems, particularly in the selection of appropriate additives to match the solubility of the aqueous *versus* membrane environment.

5.1 Abstract

The high excitation powers required to observe single molecules often results in undesirable photophysical behaviour (blinking, photobleaching) that inhibits studies using single molecule fluorescence (SMF) techniques. In response to this challenge, here we report several antifading cocktails designed to improve the photostability, when embedded within lipid membranes, of a 49-mer long poly(phenylene-ethynylene) conjugated polyelectrolyte bearing carboxylate side groups (PPE-CO_2-49). Total internal reflection fluorescence microscopy (TIRFM) studies were conducted to monitor the emission intensity of ten/hundreds of surface-immobilized PPE-CO_2-49-containing liposomes in parallel. The effect of adding the hydrophobic triplet quenchers β-mercaptoethanol (BME), cyclooctatetraene (COT), and α-tocopherol (TOC) to the imaging buffer as well as the effect of oxygen removal on the photostability of the PPE-CO_2-49-containing liposomes was then determined. The best result was achieved with TOC (1:100 lipid) used in combination with the oxygen scavenger glucose oxidase, where an increase in the photon output between 20-40-fold was observed, providing for an increased opportunity to observe the behaviour of membrane-embedded PPE-CO_2 over time at the single chain level.

5.2 Introduction

The last years have seen a surge in the use of conjugated polyelectrolytes (CPEs) to interrogate lipid membrane systems and on the exploitation of CPE-lipid membrane composites. We may cite for the former case the use of CPEs to probe membrane phase transitions[1-2], fusion,[3-4] and deformation in contact with surfaces[5] and for the latter case applications in light harvesting,[6] microbial fuel cells,[7-10] antimicrobial agents,[11-13] and biosensors.[14-16]

While the use of CPEs and conjugated polymers in association with lipid membranes is becoming more prevalent in biological and material fluorescence imaging studies,[5, 14, 17-21] several limitations must be overcome to facilitate their adoption as fluorescent markers and to make them more suitable for study using these techniques. These limitations are related to the photophysical/photochemical behaviour of CPEs (*e.g.,* blinking, photobleaching) under the high excitation rates demanded by single molecule experiments.[22-24]

Here we report on our efforts to enhance the photostability of a 49-mer long poly(phenylene-ethynylene) conjugated polymer bearing carboxylate side groups (PPE-CO_2-49) when embedded within lipid bilayers of 200 nm liposomes prepared from the positively charged lipid 1,2-dioleoyl-3-trimethylammonium-propane (DOTAP). This work builds upon widely used methodologies used to enhance the photostability of fluorescent dyes in single molecule studies. These methods are based on the removal of molecular oxygen and the addition of small molecule triplet quenchers/antioxidant to the imaging buffer. We have previously encountered success with these strategies, having shown that a selection of additives including ascorbic acid (AA), trolox (TX), and an enzymatic oxygen scavenging system consisting of glucose oxidase (GOX) and catalase in a 3% (w/v) glucose solution are effective in improving the photostability of PPE-CO_2-49 adsorbed on SiO_2 nanoparticles in aqueous solution. In this chapter, the choice of additives was adapted to consider the fact that the CPEs are embedded within the lipid membrane, and therefore lipophilic additives, rather than their water-soluble counterparts, were selected to ensure close proximity, when needed, of additive and the CPE.

Given the hydrophobic nature of the DOTAP lipid membrane, the small polar organic molecule β-mercaptoethanol (BME), long-used as a photostabilizing agent for fluorescence imaging,[25-27] was included in this study. As a replacement for the water-soluble antioxidant TX, we selected α-tocopherol (TOC). TOC and TX share the same redox-sensitive moiety, but TOC is more hydrophobic due to its long hydrocarbon tail. Both TX and BME have been previously reported to quench triplet states by a reduction/oxidation (ROX) mechanism,[28-29] where the radical anion intermediate formed *via* reaction with the excited triplet state is either returned to the ground state *via* reaction with an oxidizing agent[28] or *via* geminate recombination with the reducing agent within the solvent cage of the initially formed radical pair, respectively.[29] Similar processes are expected to take place within the membrane if the membrane-embedded CPE and the additives encounter each other. The additive AA, which operates in a similar manner to TX and BME and was shown to be effective in extending the lifetime of PPE-CO_2-49 in aqueous solution (see Chapter 4),[30] was excluded, however, since as a highly charged molecule it is unable to penetrate the lipid membrane to participate in electron transfer reactions with the CPE. For the same reason Ni^{2+}, a triplet quencher that acts *via* energy transfer[31] (a physical rather than a chemical process), was also excluded from the present study. As an alternative, cyclooctatetraene (COT) was selected for study based on reports of its ability to efficiently quench fluorophore triplet states[24, 32-36] via

energy transfer (physical process)[37] coupled with its ability to interact with lipid membranes.[38]. An enzymatic oxygen scavenging system[39] consisting of glucose oxidase (GOX) and D(+) glucose was also used to determine the effect of removing oxygen on the photostability of PPE-CO_2-49, both alone and in combination with the other three additives.

5.3 Results and Discussion

5.3.1 TIRFM imaging of PPE-CO_2-49 embedded in DOTAP liposomes

The PPE-CO_2-49 containing liposomes were prepared by adding aliquots of PPE-CO_2-49 in aqueous solution to DOTAP liposomes containing 1% (mol/mol) biotinylated lipid in buffered solution. The polymer was added to the liposomes instead of *vice versa* to prevent agglomeration and to achieve a more homogeneous sample.[40] Addition of the full aliquot of CPE resulted in samples where the polymer was present at a mole ratio of 0.005 PRU:lipid, which corresponds to *ca*. 36 polymers per 200 nm diameter liposome (see section 5.6.2). In preparation for TIRFM imaging, the polymer-containing liposomes were next immobilized *via* biotin/streptavidin interactions on polyethylene-glycol (PEG) coated surface-modified glass coverslips affixed with an imaging chamber.[19] Tens/hundreds of liposomes containing PPE-CO_2-49 were excited with the totally internally reflected output of a 405 nm continuous wave (CW) laser with the emission recorded every 30-200 ms (as stated) using an electron multiplying charged coupled device (EMCCD). Two laser powers, either 0.1 mW or 4.4 mW, were utilized in this work. The additives BME (143 mM), COT (10 mM), and GOX (165 units/mL in 3% D-glucose w/v) were flowed through the imaging chamber in solution. TOC was added to the lipid solution in a molar ratio of 1:100 prior to formation of the dry lipid film that was later rehydrated to form liposomes. We did not attempt to pre-incorporate BME or COT into the lipid film due to the high volatility of these reagents. As a result, the amount of BME or COT that partitioned into the membrane from solution was not determined. Following data acquisition, the fluorescence intensity *versus* time trajectories of the individual liposomes were extracted from the TIRF images using home-built MATLAB routines based on the algorithms developed by the Ha group.[41] The trajectories were then subjected to further analysis to determine the initial intensity (defined as the number of photons per ms detected per liposome in the first frame) and the total number of photons emitted per liposome.

5.3.2 Colocalization of PPE-CO_2-49 with the membrane marker DiD

To confirm that PPE-CO_2-49 was associated with the DOTAP liposomes under the TIRFM imaging conditions, the liposomes were labeled with the lipophilic membrane marker 1,1′-dioctadecyl-3,3,3′,3′-tetramethylindodicarbocyanine perchlorate (DiD) and images were obtained by exciting DiD at 647 nm. Colocalization studies were then conducted by comparing to the images obtained by exciting PPE-CO_2-49 at 405 nm in the same region (Figures 5.1A and B). Figure 5.1C shows a Pearson correlation plot between emission intensities in the red and green channel illustrating that i) CPE are localized within liposomes and ii) that the DiD emission, proportional to the surface area of the liposome and thus to the square of its radius, is also proportional to the PPE-CO_2-49 emission indicating the CPE distributes homogeneously within the liposomes.

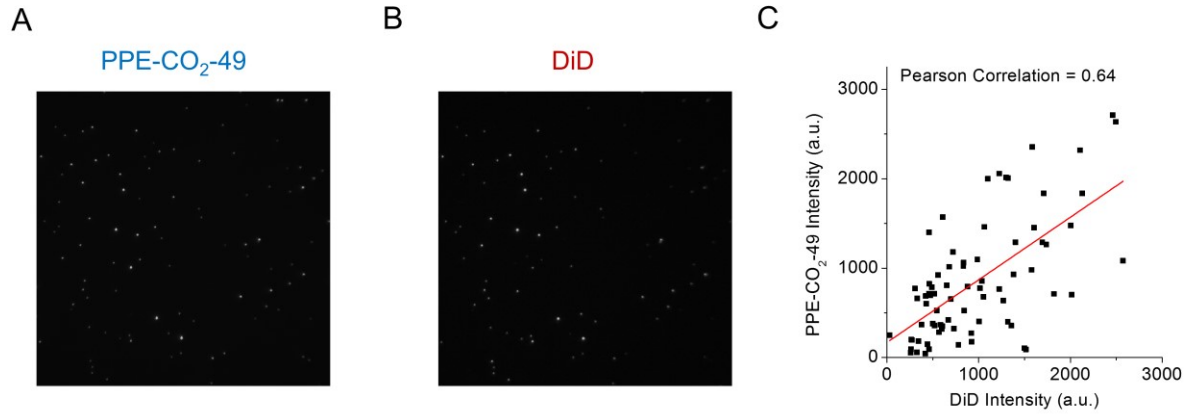

Figure 5.1. Colocalization of PPE-CO_2-49 and the membrane marker DiD in DOTAP liposomes. (A) Image obtained by exciting the region at 405 nm to image PPE-CO_2-49. (B) Image obtained by exciting the region at 647 nm to image DiD. Direct excitation either of PPE-CO_2-49 at 647 nm or of DiD at 405 nm was negligible (data not shown). (C) Pearson correlation plot of the initial intensity of PPE-CO2-49 versus DiD obtained from Figure 5.1A and 5.1B, respectively. Liposomes contained 0.05 PRU:lipid PPE-CO_2-49 and 0.00003 DiD:lipid (*ca.* 10 DID molecules per 200 nm diameter liposome).

5.3.3 Photostability of PPE-CO_2-49 in liposomes compared to PPE-CO_2-49 adsorbed on SiO_2 nanoparticles

Before tackling the effect of the additives on the photostability of PPE-CO_2-49, it is informative to compare the behavior of the polymer in liposomes *versus* the polymer adsorbed on 100 nm SiO_2 NPs in the absence of additives under TIRFM imaging conditions. To compare the

emission intensity of the polymers in the different environments, the initial values of the intensity *versus* time trajectories were extracted from liposomes containing 0.005 PRU:lipid PPE-CO_2-49 and for PPE-CO_2-49 coated NPs prepared as reported in Chapter 4. The initial intensity was defined by first converting the signal of the first frame into the number of photons detected by the EMCCD camera. This value was then normalized by the length of the frame in milliseconds to compare data acquired at different frame rates. Next, the mean number of photons detected per liposome/NP was calculated. Finally, to account for the fact that the liposomes and the NPs contain different numbers of polymers on average (35 and 450, respectively; see sections 5.6.2 and 4.7.2), the mean number of photons detected was divided by the number of polymers to yield the initial intensity per polymer under both 4.4 mW and 0.1 mW excitation powers (Figure 5.2A and 5.2B, respectively). Under both excitation powers, the polymers embedded in liposomes emitted more photons per ms than the same polymers when adsorbed on NPs. This result is consistent with the smaller emission quantum yield of PPE-CO_2-49 that is reported in an aqueous environment (Φ = 0.1) compared to a membrane[3] or polar organic (*e.g.* methanol)[42] environment (Φ = 0.31). Although the absorption maximum of PPE-CO_2-49 is red-shifted from 410 nm in membranes to a maximum of 437 nm in buffered aqueous solution,[3] the higher molar absorptivity of the PPE-CO_2-49 in buffer[42] compensates for the shift such that the excitation efficiency of the polymer at 405 nm is approximately equivalent in both environments (Figure 5.3), so the difference in initial intensities is not due to this factor.

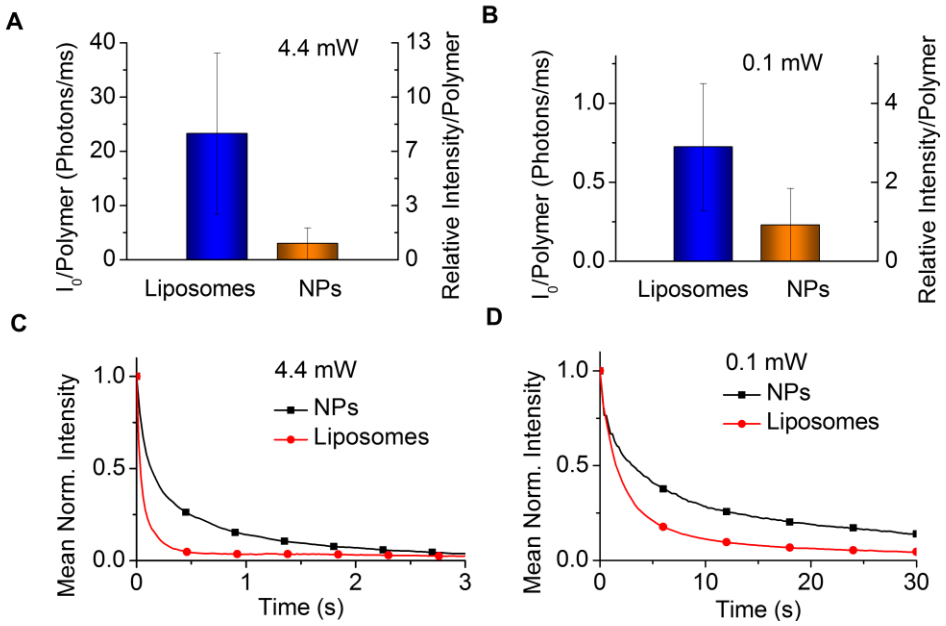

Figure 5.2. Behaviour of PPE-CO_2-49 embedded in liposomes compared to PPE-CO_2-49 adsorbed on NPs under TIRFM imaging. (A) and (B) Mean initial intensity per polymer in liposomes and NPs under 4.4 mW and 0.1 W excitation power, respectively. (C) and (D) Mean of the normalized intensity *versus* time trajectories obtained under 4.4 mW and 0.1 mW excitation power, respectively.

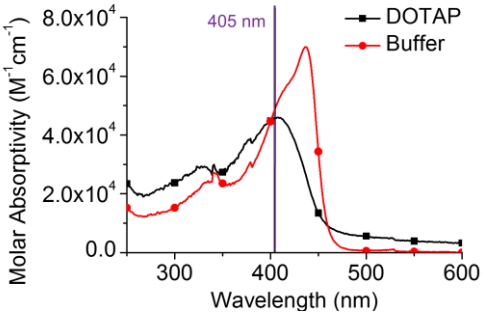

Figure 5.3. Molar absorptivity of PPE-CO_2-49 in DOTAP liposomes and buffer. Absorption spectra of solutions containing PPE-CO_2-49 (1.5 μM in terms of PRU) with and without DOTAP were acquired and then normalized to the reported values of the molar absorptivity at λ_{max} (4.6×10^4 and 7.0×10^4 $M^{-1}cm^{-1}$ per PRU, respectively[42]).

The behaviour of the intensity *versus* time trajectories for the PPE-CO_2-49-containing liposomes and the PPE-CO_2-49 coated NPs was similar, with both displaying exponential photobleaching under 4.4 and 0.1 mW excitation powers (Figure 5.2C and 5.2D, respectively). The intensity decay rate of the NPs was, however, slower than that of the liposomes, where fitting the trajectories to a biexponential decay function (Equation 5.1) resulted in time constants that were *ca*. 5-fold longer for the NPs than the liposomes. Considering that the initial intensity of the

NPs was also quenched by *ca.* 5-fold relative to the liposomes (Figure 5.2A and 5.2B), we may conclude that there is not a substantial difference in the total number of photons emitted by PPE-CO_2-49 before photobleaching in the two environments. Importantly, inspection of the trajectories reveals that photobleaching of the PPE-CO_2-49-containing liposomes occurs within just 0.5 s under 4.4 mW excitation power, illustrating how the poor native photostability of PPE-CO_2-49 places a severe constraint on the timescale that these polymers can be observed under typical SMF imaging conditions, underscoring the need for improved photostability.

$$I = A_1 e^{-\frac{t}{\tau_1}} + A_2 e^{-\frac{t}{\tau_2}} + y_0 \quad (1)$$

5.3.4 Effect of the polymer concentration on the intensity versus time trajectories

Anticipating that the possibility of energy transfer between PPE-CO_2-49 polymers might affect the behaviour of the intensity *versus* time trajectories, liposomes containing different polymer loadings (0.005, 0.010, 0.025, 0.050, and 0.075 PRU:lipid), and thus different expected energy transfer efficiencies, increasing in the above order, were prepared and imaged in the TIRFM setup. In the presence of GOX under 4.4 mW excitation power, the trajectories were characterized by an exponential decay in the emission intensity, where the rate of photobleaching was independent of the polymer loading (Figure 5.4A). Under 0.1mW excitation, however, an initial enhancement in the trajectories was observed in addition to exponential photobleaching. The size of the enhancement decreased as the polymer loading was decreased, with the enhancement being almost non-existent at 0.005 PRU:lipid (Figure 5.4B), suggesting that the phenomenon leading to the intensity enhancement is associated with the presence of energy transfer between polymers in the membrane (and is more critical with larger polymer loadings). In Chapter 4, the intensity *versus* time trajectories of the PPE-CO_2-49 coated NPs in the presence of numerous additives acquired under 0.1 mW excitation power were also characterized by an initial intensity enhancement followed by exponential photobleaching (Figure 4.4). In the case of the NPs, we hypothesized that this signature enhancement behavior reflected the fact that the adsorbed polymers were present at a high density (*ca.* 62% estimated surface coverage, see section 4.7.2), which was expected to provide for efficient homotransfer between polymers. Energy transfer was related to the observed intensity enhancement *via* a mechanism where the excitation energy is selectively funnelled to trap/quench sites. The photo-induced destruction of these sites then results in an increase in the fluorescence quantum yield and a recovery of the emission intensity.

The observed trend where the intensity enhancement decreased with the density of polymers embedded in the membrane is consistent with the hypothesis we proposed to explain the behaviour of the NPs. Here, a decreasing polymer density corresponding to a drop in the efficiency of energy transfer results in a reduction in the rate of trap site destruction/quantum yield recovery. To prevent convolution of the results by the effect of energy transfer, all further experiments were performed at the a low polymer density of 0.005 PRU:lipid, which corresponded to *ca.* 35 polymers per 200 nm diameter liposome (see section 5.6.2).

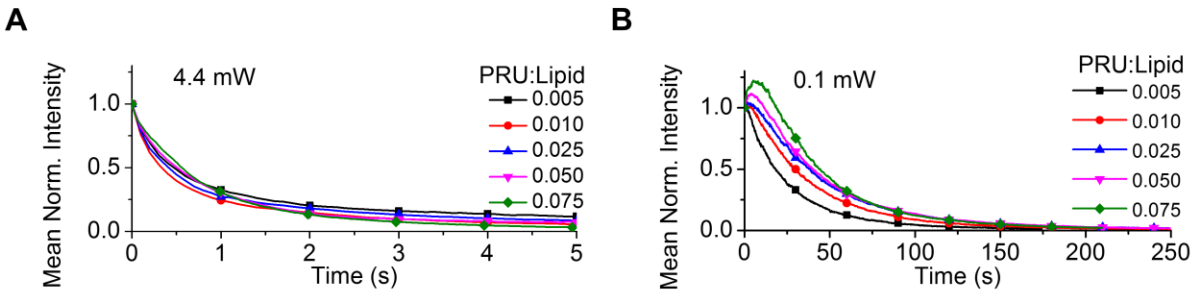

Figure 5.4. Mean, normalized intensity *versus* time trajectories of DOTAP liposomes containing different amounts of PPE-CO_2-49. The samples were excited with either the 4.4 mW (A) or the 0.1 mW (B) output of a 405 nm laser while flowing a buffered solution containing GOX.

5.3.5 Effect of the additives on the initial intensity

The addition of additives to the imaging buffer may affect the intensity of PPE-CO_2-49 by altering its fluorescence quantum yield or its excitation duty cycle. To examine if these effects might be operating in this system, the initial intensity was extracted for each liposome and the mean value was then calculated for each condition (Figure 5.5). The large error bars, representing the standard deviation of the mean initial intensity, were attributed to the size distribution of the liposomes and therefore the number of PPE-CO_2-49 emitters present per liposome. The addition of GOX resulted in a *ca.* 50% quenching of the initial intensity relative to buffer under both 4.4 mW and 0.1 mW excitation power (Figure 5.5A and 5.5B, respectively). One explanation for the decrease is that the removal of oxygen led to a decrease in the duty cycle of PPE-CO_2-49. This is a plausible mechanism given that molecular oxygen is an efficient triplet state quencher[43-44] and therefore its removal is expected to increase the triplet state lifetime, thus decreasing the duty cycle of the fluorophore as it spends more time in the relatively long-lived triplet state. Alternatively, it is possible that the decrease in the initial intensity was caused by GOX invoking a conformational

change in PPE-CO_2-49 that decreased its fluorescence quantum yield. It is plausible that GOX, which is negatively charged at neutral pH,[45] would bind to the positively charged DOTAP membrane, but whether this interaction would influence the photophysical properties of embedded PPE-CO_2-49 has not yet been determined.

The effect of the other additives on the initial intensity of PPE-CO_2-49 embedded in DOTAP liposomes was also examined. The addition of COT was observed to quench the emission intensity of PPE-CO_2-49 by ca. 3-4-fold under both 4.4 mW and 0.1 mW excitation (Figure 5.5A and 5.5B, respectively). It is possible that the intensity drop is caused by quenching of the excited singlet state.[46] If this were the case, then lowering the COT concentration may reduce quenching of the excited singlet state while still allowing for efficient quenching of the much longer-lived triplet state. The addition of TOC, on the other hand, was observed to enhance the initial intensity *ca.* 2-fold compared to buffer under both excitation powers. This result is similar to that observed with PPE-CO_2-49-coated NP in the presence of the water-soluble TOC analogue TX (see Chapter Four). Our results thus indicate that TOC is quenching PPE-CO_2-49 triplet states leading to an increase in the duty cycle and concomitant intensity enhancement. BME, however, was not observed to have a significant effect on the initial intensity of PPE-CO_2-49 embedded in DOTAP liposomes under either excitation power.

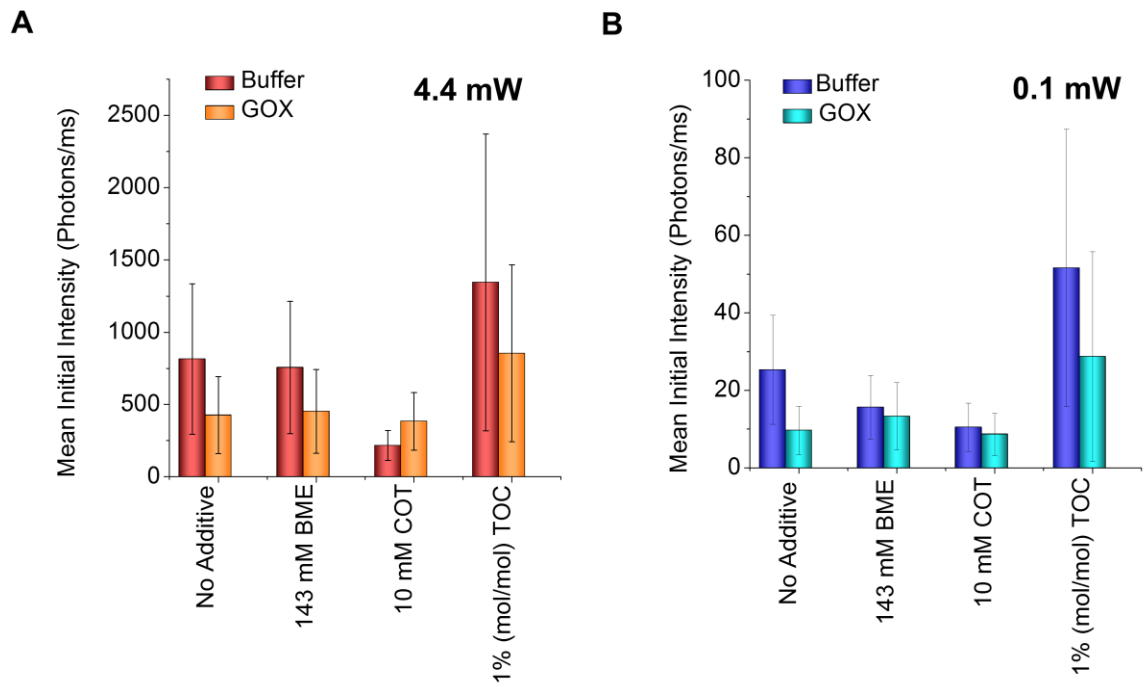

Figure 5.5. Mean initial intensity of PPE-CO_2-49 in DOTAP liposomes in the presence of different additives. (A) Mean initial intensities under 4.4 mW 405 nm illumination. (B) Mean initial intensities under 0.1 mW 405 nm illumination. The liposomes contained PPE-CO_2-49 in a concentration of 0.005 PRU:lipid.

5.3.6 Effect of the additives on the mean intensity *versus* time trajectories

The intensity *versus* time trajectories were next examined to obtain information on the photobleaching kinetics and to assess the time window under which a fluorescence imaging experiment based on monitoring PPE-CO_2-49 emission could be conducted. The individual trajectories were extracted from the TIRFM movies and then normalized by their initial intensity to facilitate comparison across different solution additive conditions. The mean normalized trajectories obtained under both 4.4 mW and 0.1 mW excitation powers are plotted in Figure 5.6A and 5.6B, respectively. In the absence of any additives, the intensity *versus* time trajectories of PPE-CO_2-49 displayed rapid exponential photobleaching behaviour under both excitation powers (Figure 5.6), similar to the results for the PPE-CO_2-49 coated NPs in aqueous solution reported in Chapter 4 (Figure 4.6). We also note here that the trajectories highlight the relatively poor photostability/short observation window of the polymer under these conditions. By inspection of Figure 5.6, it is clear that many additives, both alone and in combination with GOX, led to a

dramatic increase in the lifetime as observed from the intensity versus time trajectories. Lifetime increases were considered in combination with changes in the initial intensity to assess the overall photostability of the PPE-CO_2-49-liposomes in section 5.2.6. below.

Interestingly, we also observed that the trajectories obtained when the imaging buffer contained COT or GOX did not decay to zero, but instead decayed to a residual emission intensity equal to 10-25% of the initial intensity. Even under extended illumination times of up to one hour, the signal from the particles remained constant and complete photobleaching was not observed (data not shown).

To account for the fraction of CPE that remains unbleached several possibilities may be considered. It is possible that PPE-CO_2-49 undergoes transformation to produce a different emissive species (*e.g.* the photobleaching product is also emissive). For example, it has been demonstrated that photooxidation of polyfluorenes leads to the formation of emissive keto defects.[47-51] The presence of the defects is identified by observation of a signature red-shifted blue/green emission band in place of the pristine polymer's blue emission band. In the case of PPE-CO_2-49, however, it is not immediately obvious what the structure of such an emissive defect might be or what role the lipid membrane and GOX and/or COT might have in favoring its formation. Alternatively, it is possible that GOX/COT forms a complex with the membrane-embedded PPE-CO_2-49 polymers and effectively protects a fraction of them from damage by $^1O_2$ or other ROS. Literature precedence supporting this hypothesis include a 2008 study by Dou *et al.*, where they found that the photostability of a PPE polymer substituted with 3-sulfanatopropyloxy groups (PPE-SO_3) was enhanced by up to 12-fold in the presence of various surfactants.[52] They attributed the enhancement to the surfactant's ability to self-assemble around PPE-SO_3 and limit the access of molecular oxygen to the polymer.[52] More recently, Darwish *et al.* reported that the photostability of MPS-PPV was improved under TIRFM imaging conditions when complexed with polyvinylpyrrolidone (PVP)[53] In addition to the protective barrier hypothesis put forward by Dou *et al*., the authors suggested that complexation with PVP might be reducing interchain collisions in solution, where such impact has recently been shown by Tian *et al.* to accelerate the rate of photochemical oxygen-induced chain scission by up to 20-fold.[54] In our system, such a complex would likely involve the DOTAP lipid membrane, since no un-bleachable residual was observed in the intensity *versus* time trajectories of the PPE-CO_2-49-

coated NPs in the presence of GOX in aqueous solution (see Chapter 4), or in other reports of GOX used to improve the photostability of CPs.[55-57] We regard the protective barrier hypothesis as somewhat implausible, however, since it seems unlikely that any such physical barrier against ROS would be so effective that no trace of photobleaching would be observed even after extended (1 hour) exposure to 4.4 mW laser.

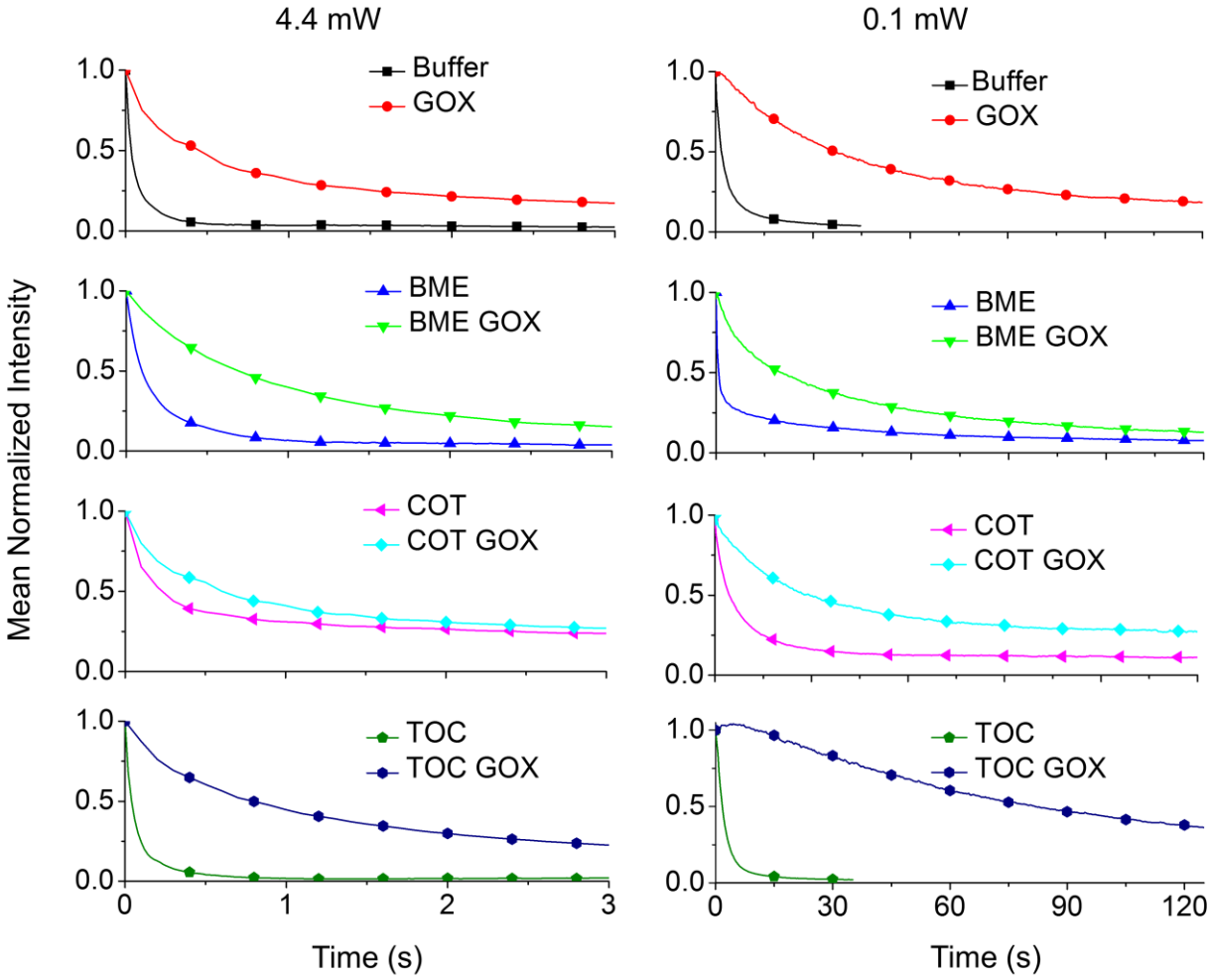

Figure 5.6. Mean, normalized intensity vs time trajectories of PPE-CO_2-49 in DOTAP liposomes in the presence of different additives. (A) Mean trajectories obtained under 4.4 mW 405 nm illumination. (B) Mean trajectories obtained under 0.1 mW 405 nm illumination. Trajectories plotted are the average of several hundred trajectories first normalized by their initial intensity. The liposomes contained PPE-CO_2-49 in a concentration of 0.005 PRU:lipid.

5.3.7 Comparison of the relative number of photons emitted under each condition

To compare the overall effect of the additives on the photostability of the PPE-CO_2-49-containing liposomes the number of photons emitted before photobleaching was ultimately the parameter of choice. In Chapter 4, the number of photons emitted by the PPE-CO_2-49 coated NPs was determined by integrating the area under the individual intensity *versus* time trajectories and converting this value to the total number of photons detected. The mean number of photons detected per NP was then computed and compared across the different solution conditions. For work described in this chapter, since several of the trajectories from the liposomes containing embedded PPE-CO_2-49 do not decay to a residual intensity of zero (see Figure 5.6 and section 5.2.5), it was not possible to perform this type of analysis. Instead, a parameter, *n*, proportional to the number of photons emitted under each condition, was estimated by determining the characteristic decay constant under each condition (τ) and then multiplying τ by the initial number of photons (I_0) under the same condition (Equation 5.2). Normalization by the number obtained in buffer provides a measure of the relative improvement in photostability conferred by each additive in the lower limit (*i.e.*, not accounting for photons emitted by the unbleachable fraction) (Figure 5.6). To determine the decay constants, the mean normalized trajectories plotted in Figure 5.6 were fit to a biexponential decay function (Equation 5.1) to obtain the characteristic short and long decay constants, τ_1 and τ_2. The results of these fits are summarized in Table 5.1.

$$n = I_0\tau \qquad (2)$$

Table 5.1. Fitting parameters and R^2 values obtained upon fitting the mean normalized intensity *versus* time trajectories to Equation 5.1.

Sample	A_1	τ_1 (s)	A_2	τ_2 (s)	y_0	R^2
			0.1 mW			
Buffer	0.66	1.50	0.28	7.60	0.040	0.999
BME	0.67	0.60	0.22	30.0	0.076	0.993
COT	0.40	2.12	0.44	10.3	0.121	0.999
TOC	0.97	2.13	0.10	41.9	-0.028	0.999
GOX	0.62	25.0	0.32	98.7	0.087	0.100
BME GOX	0.312	4.97	0.58	39.3	0.107	0.100
COT GOXr	0.43	14.2	0.28	49.8	0.246	0.999
TOC GOX	0.61	57.2	0.46	190	0.060	0.100
			5.1 mW			
Buffer	0.59	0.023	0.37	0.14	0.035	0.100
BME	0.54	0.073	0.42	0.33	0.047	0.100
COT	0.57	0.125	0.21	1.31	0.214	0.999
TOC	0.72	0.041	0.26	0.22	0.015	0.100
GOX	0.49	0.239	0.37	1.56	0.116	0.997
BME GOX	0.57	0.595	0.36	2.10	0.064	0.100
COT GOXr	0.43	0.265	0.33	1.57	0.223	0.997
TOC GOX	0.40	0.380	0.48	2.21	0.105	0.999

Inspection of Figure 5.7 shows that the estimated number of photons emitted under each condition relative to buffer is similar whether τ_1 or τ_2 is used in the calculation of n. Addition of GOX led to a *ca*. 5-8-fold increase in the number of photons emitted relative to buffer under both illumination powers (Figure 5.7), implicating oxygen in the photodegradation mechanism of PPE-CO_2-49 embedded in liposomes. BME was observed to improve the photostability, albeit modestly (*ca*. 2-fold improvement under both excitation powers). The margin of improvement increased to *ca*. 10-fold when BME was used in combination with GOX. The addition of COT alone did not improve the photon output, but when used in combination with GOX a 2-5-fold increase was observed.

Addition of TOC led to a modest improvement in the photon output when used alone, but when it was combined with GOX the photostability compared to buffer improved by a large margin, estimated to be somewhere between 20-40-fold. This result contrasts the deleterious effect on the PPE-CO_2-49 coated NPs that was reported for the combination of the TOC analogue, Trolox, with oxygen scavenger in Chapter 4. In this case, we proposed that oxygen was responsible for quenching the radical anion formed upon reaction of the CPE excited triplet state with Trolox. Removal of oxygen from the system by GOX left the polymer vulnerable to degradation pathways occurring through its radical anion intermediate, ultimately leading to a decrease in photon output. Although no oxidizing agent was intentionally added to the TOC-containing liposomes, it is possible that conversion of TOC to its oxidized form, alpha-tocopherol quinone, occurred during storage of the compound or preparation of the liposome samples, and that this species was responsible for completing the ROX cycle. Alternatively, it is plausible that geminate recombination between the initial TOC and PPE-CO_2-49 radical pair is responsible for quenching of the radical anion,[29, 58-59] since diffusion from the solvent cage is expected to occur with a diffusion constant that is two orders of magnitude slower in a membrane as opposed to an aqueous environment.[60]

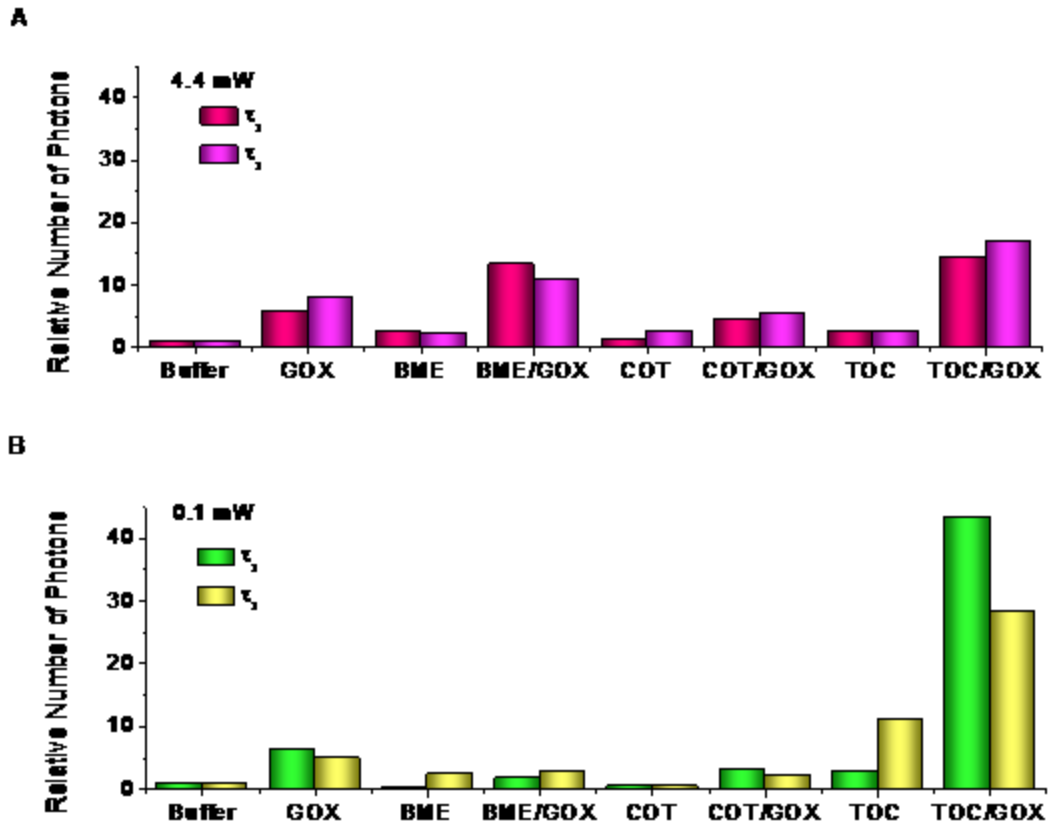

Figure 5.7. Estimated number of photons emitted under each condition relative to buffer. (A) Values obtained under 4.4 mW excitation at 405 nm. (B) Values obtained under 0.1 mW excitation at 405 nm. The values were obtained by multiplying the short and long time constants retrieved by fitting the mean normalized trajectories to a biexponential decay function by the mean initial intensity under the same condition, followed by normalization by the value calculated for buffer. The liposomes contained PPE-CO_2-49 in a concentration of 0.005 PRU:lipid.

5.4 Conclusion

Several different solution additives including BME, COT, TOC, and GOX were screened for their ability to improve the photostability of PPE-CO_2-49 embedded in DOTAP lipid membranes under TIRFM imaging conditions. The best result was achieved with TOC (1:100 lipid) used in combination with GOX, where an increase in the photon output between 20-40 fold was observed relative to buffer conditions, representing a substantial improvement. We are hopeful that by applying the TOC/GOX photostabilization system individual PPE-CO_2 polymers can be detected and observed over time in future TIRFM studies. Remarkably, this study also led to the observation of an un-bleachable fraction accounting for 10-25% of the initial emission intensity in the presence of COT or GOX (alone and in combination with the other three additives).

Although the origin/identity of this fraction has not yet been determined, the discovery of an ultra-photostable emissive conjugated polymer system could have a tremendous impact in the field of fluorescent imaging markers or any other application that requires a bright, stable fluorescent signal.

5.5 References

1. Kahveci, Z.; Martínez-Tomé, M. J.; Mallavia, R.; Mateo, C. R. Use of the Conjugated Polyelectrolyte Poly{[9,9-Bis(6′-N,N,N-Trimethylammonium)Hexyl]Fluorene-Phenylene} Bromide (HTMA-PFP) as a Fluorescent Membrane Marker. *Biomacromolecules* **2013,** *14*, 1990-1998.

2. Houston, J. E.; Kraft, M.; Scherf, U.; Evans, R. C. Sequential Detection of Multiple Phase Transitions in Model Biological Membranes Using a Red-Emitting Conjugated Polyelectrolyte. *Phys. Chem. Chem. Phys.* **2016,** *18*, 12423-12427.

3. Karam, P.; Hariri, A. A.; Calver, C. F.; Zhao, X.; Schanze, K. S.; Cosa, G. Interaction of Anionic Phenylene Ethynylene Polymers with Lipids: From Membrane Embedding to Liposome Fusion. *Langmuir* **2014,** *30*, 10704-10711.

4. Houston, J. E.; Kraft, M.; Mooney, I.; Terry, A. E.; Scherf, U.; Evans, R. C. Charge-Mediated Localization of Conjugated Polythiophenes in Zwitterionic Model Cell Membranes. *Langmuir* **2016,** *32*, 8141-8153.

5. Calver, C. F.; Liu, H.-W.; Cosa, G. Exploiting Conjugated Polyelectrolyte Photophysics toward Monitoring Real-Time Lipid Membrane-Surface Interaction Dynamics at the Single-Particle Level. *Langmuir* **2015,** *31*, 11842-11850.

6. Calver, C. F.; Schanze, K. S.; Cosa, G. Biomimetic Light-Harvesting Antenna Based on the Self-Assembly of Conjugated Polyelectrolytes Embedded within Lipid Membranes. *ACS Nano* **2016,** *10*, 10598-10605.

7. Kirchhofer, N. D.; Chen, X.; Marsili, E.; Sumner, J. J.; Dahlquist, F. W.; Bazan, G. C. The Conjugated Oligoelectrolyte DSSN+ Enables Exceptional Coulombic Efficiency Via Direct Electron Transfer for Anode-Respiring Shewanella Oneidensis Mr-1-a Mechanistic Study. *Phys. Chem. Chem. Phys.* **2014,** *16*, 20436-20443.

8. Garner, L. E.; Thomas, A. W.; Sumner, J. J.; Harvey, S. P.; Bazan, G. C. Conjugated Oligoelectrolytes Increase Current Response and Organic Contaminant Removal in Wastewater Microbial Fuel Cells. *Energy Environ. Sci.* **2012,** *5*, 9449-9452.

9. Hou, H.; Chen, X.; Thomas, A. W.; Catania, C.; Kirchhofer, N. D.; Garner, L. E.; Han, A.; Bazan, G. C. Conjugated Oligoelectrolytes Increase Power Generation in E. Coli Microbial Fuel Cells. *Adv. Mater.* **2013,** *25*, 1593-1597.

10. Yan, H.; Catania, C.; Bazan, G. C. Membrane-Intercalating Conjugated Oligoelectrolytes: Impact on Bioelectrochemical Systems. *Adv. Mater.* **2015,** *27*, 2958-2973.

11. Wang, Y.; Schanze, K. S.; Chi, E. Y.; Whitten, D. G. When Worlds Collide: Interactions at the Interface between Biological Systems and Synthetic Cationic Conjugated Polyelectrolytes and Oligomers. *Langmuir* **2013,** *29*, 10635-10647.

12. Yan, H.; Rengert, Z. D.; Thomas, A. W.; Rehermann, C.; Hinks, J.; Bazan, G. C. Influence of Molecular Structure on the Antimicrobial Function of Phenylenevinylene Conjugated Oligoelectrolytes. *Chem. Sci.* **2016,** *7*, 5714-5722.

13. Zhu, C.; Yang, Q.; Liu, L.; Lv, F.; Li, S.; Yang, G.; Wang, S. Multifunctional Cationic Poly(P-Phenylene Vinylene) Polyelectrolytes for Selective Recognition, Imaging, and Killing of Bacteria over Mammalian Cells. *Adv. Mater.* **2011,** *23*, 4805-4810.

14. Kahveci, Z.; Vazquez-Guillo, R.; Mira, A.; Martinez, L.; Falco, A.; Mallavia, R.; Mateo, C. R. Selective Recognition and Imaging of Bacterial Model Membranes over Mammalian Ones by Using Cationic Conjugated Polyelectrolytes. *Analyst* **2016,** *141*, 6287-6296.

15. Ngo, A. T.; Karam, P.; Cosa, G. Conjugated Polyelectrolyte-Lipid Interactions: Opportunities in Biosensing. *Pure Appl. Chem.* **2011,** *83*, 43-55.

16. Zhu, C.; Liu, L.; Yang, Q.; Lv, F.; Wang, S. Water-Soluble Conjugated Polymers for Imaging, Diagnosis, and Therapy. *Chem. Rev.* **2012,** *112*, 4687-4735.

17. Duarte, A.; Pu, K.-Y.; Liu, B.; Bazan, G. C. Recent Advances in Conjugated Polyelectrolytes for Emerging Optoelectronic Applications†. *Chem. Mater.* **2010,** *23*, 501-515.

18. Cui, Q.; Wang, X.; Yang, Y.; Li, S.; Li, L.; Wang, S. Binding-Directed Energy Transfer of Conjugated Polymer Materials for Dual-Color Imaging of Cell Membrane. *Chem. Mater.* **2016,** *28*, 4661-4669.

19. Karam, P.; Ngo, A. T.; Rouiller, I.; Cosa, G. Unraveling Electronic Energy Transfer in Single Conjugated Polyelectrolytes Encapsulated in Lipid Vesicles. *Proc. Natl. Acad. Sci. U. S. A.* **2010,** *107*, 17480-17485.

20. Wang, B.; Zhu, C.; Liu, L.; Lv, F.; Yang, Q.; Wang, S. Synthesis of a New Conjugated Polymer for Cell Membrane Imaging by Using an Intracellular Targeting Strategy. *Polym. Chem.* **2013,** *4*, 5212-5215.

21. Liu, Y.; Wu, P.; Jiang, J.; Wu, J.; Chen, Y.; Tan, Y.; Tan, C.; Jiang, Y. Conjugated Polyelectrolyte Nanoparticles for Apoptotic Cell Imaging. *ACS Appl. Mater. Interfaces* **2016,** *8*, 21984-21989.

22. Zheng, Q.; Juette, M. F.; Jockusch, S.; Wasserman, M. R.; Zhou, Z.; Altman, R. B.; Blanchard, S. C. Ultra-Stable Organic Fluorophores for Single-Molecule Research. *Chem. Soc. Rev.* **2014,** *43*, 1044-1056.

23. Dave, R.; Terry, D. S.; Munro, J. B.; Blanchard, S. C. Mitigating Unwanted Photophysical Processes for Improved Single-Molecule Fluorescence Imaging. *Biophys. J.* **2009,** *96*, 2371-2381.

24. Widengren, J.; Chmyrov, A.; Eggeling, C.; Löfdahl, P.-Å.; Seidel, C. A. M. Strategies to Improve Photostabilities in Ultrasensitive Fluorescence Spectroscopy. *J. Phys. Chem. A* **2007,** *111*, 429-440.

25. Harada, Y.; Sakurada, K.; Aoki, T.; Thomas, D. D.; Yanagida, T. Mechanochemical Coupling in Actomyosin Energy Transduction Studied by in Vitro Movement Assay. *J. Mol. Biol.* **1990,** *216*, 49-68.

26. Rasnik, I.; McKinney, S. A.; Ha, T. Nonblinking and Long-Lasting Single-Molecule Fluorescence Imaging. *Nat. Methods* **2006,** *3*, 891-893.

27. Yanagida, T.; Nakase, M.; Nishiyama, K.; Oosawa, F. Direct Observation of Motion of Single F-Actin Filaments in the Presence of Myosin. *Nature* **1984,** *307*, 58-60.

28. Cordes, T.; Vogelsang, J.; Tinnefeld, P. On the Mechanism of Trolox as Antiblinking and Antibleaching Reagent. *J. Am. Chem. Soc.* **2009,** *131*, 5018-5019.

29. Holzmeister, P.; Gietl, A.; Tinnefeld, P. Geminate Recombination as a Photoprotection Mechanism for Fluorescent Dyes. *Angew. Chem. Int. Edit.* **2014,** *53*, 5685-5688.

30. Vogelsang, J.; Kasper, R.; Steinhauer, C.; Person, B.; Heilemann, M.; Sauer, M.; Tinnefeld, P. A Reducing and Oxidizing System Minimizes Photobleaching and Blinking of Fluorescent Dyes. *Angew. Chem. Int. Edit.* **2008,** *47*, 5465-5469.

31. Glembockyte, V.; Lincoln, R.; Cosa, G. Cy3 Photoprotection Mediated by Ni^{2+} for Extended Single-Molecule Imaging: Old Tricks for New Techniques. *J. Am. Chem. Soc.* **2015,** *137*, 1116-1122.

32. Zheng, Q.; Jockusch, S.; Zhou, Z.; Altman, R. B.; Zhao, H.; Asher, W.; Holsey, M.; Mathiasen, S.; Geggier, P.; Javitch, J. A.; Blanchard, S. C. Electronic Tuning of Self-Healing Fluorophores for Live-Cell and Single-Molecule Imaging. *Chem. Sci.* **2017,** *8*, 755-762.

33. Altman, R. B.; Terry, D. S.; Zhou, Z.; Zheng, Q.; Geggier, P.; Kolster, R. A.; Zhao, Y.; Javitch, J. A.; Warren, J. D.; Blanchard, S. C. Cyanine Fluorophore Derivatives with Enhanced Photostability. *Nat Meth* **2012,** *9*, 68-71.

34. Zheng, Q.; Jockusch, S.; Zhou, Z.; Altman, R. B.; Warren, J. D.; Turro, N. J.; Blanchard, S. C. On the Mechanisms of Cyanine Fluorophore Photostabilization. *J. Phys. Chem. Lett.* **2012,** *3*, 2200-2203.

35. Weber, J. Study of the Influence of Triplet Quencher on the Photobleaching of Rhodamine-6g. *Opt. Commun.* **1973,** *7*, 420-422.

36. Zietek, B.; Targowski, P.; Baczynski, A.; Bissinger, J. In *Cyclooctatetraene as a Triplet Quencher in Dye Lasers*, 1987; pp 25-29.

37. Turro, N. J., Modern Molecular Photochemistry. Benjamin/Cummings Pub. Co.: Menlo Park, Calif., 1978.

38. Alejo, Jose L.; Blanchard, Scott C.; Andersen, Olaf S. Small-Molecule Photostabilizing Agents Are Modifiers of Lipid Bilayer Properties. *Biophys. J.* **2013,** *104*, 2410-2418.

39. Joo, C.; Ha, T. Imaging and Identifying Impurities in Single-Molecule Fret Studies. *Cold Spring Harb Protoc.* **2012,** *10*, 1109-1112.

40. Ngo, A. T.; Cosa, G. Assembly of Zwitterionic Phospholipid/Conjugated Polyelectrolyte Complexes: Structure and Photophysical Properties. *Langmuir* **2009,** *26*, 6746-6754.

41. Roy, R.; Hohng, S.; Ha, T. A Practical Guide to Single-Molecule Fret. *Nat. Methods* **2008,** *5*, 507-516.

42. Zhao, X.; Jiang, H.; Schanze, K. S. Polymer Chain Length Dependence of Amplified Fluorescence Quenching in Conjugated Polyelectrolytes. *Macromolecules* **2008,** *41*, 3422-3428.

43. Patterson, L. K.; Porter, G.; Topp, M. R. Oxygen Quenching of Singlet and Triplet States. *Chem. Phys. Lett.* **1970,** *7*, 612-614.

44. Hübner, C. G.; Renn, A.; Renge, I.; Urse, P. W. Direct Observation of the Triplet Lifetime Quenching of Single Dye Molecules by Molecular Oxygen. *J. Chem. Phys.* **2001,** *115*, 9619-9622.

45. Wilson, R.; Turner, A. P. F. Glucose Oxidase: An Ideal Enzyme. *Biosens. Bioelectron.* **1992,** *7*, 165-185.

46. Targowski, P.; Ziętek, B.; Bączyński, A. Luminescence Quenching of Rhodamines by Cyclooctatetraene. *Zeitschrift für Naturforschung* **1987,** *42a*, 1009-1013.

47. List, E. J. W.; Guentner, R.; Scanducci de Freitas, P.; Scherf, U. The Effect of Keto Defect Sites on the Emission Properties of Polyfluorene-Type Materials. *Adv. Mater.* **2002,** *14*, 374-378.

48. Lupton, J. M.; Craig, M. R.; Meijer, E. W. On-Chain Defect Emission in Electroluminescent Polyfluorenes. *Appl. Phys. Lett.* **2002,** *80*, 4489-4491.

49. List, E. J. W.; Gaal, M.; Guentner, R.; de Freitas, P. S.; Scherf, U. The Role of Keto Defect Sites for the Emission Properties of Polyfluorene-Type Materials. *Synth. Met.* **2003,** *139*, 759-763.

50. Becker, K.; Lupton, J. M.; Feldmann, J.; Nehls, B. S.; Galbrecht, F.; Gao, D. Q.; Scherf, U. On-Chain Fluorenone Defect Emission from Single Polyfluorene Molecules in the Absence of Intermolecular Interactions. *Adv. Funct. Mater.* **2006,** *16*, 364-370.

51. Romaner, L.; Pogantsch, A.; Scandiucci de Freitas, P.; Scherf, U.; Gaal, M.; Zojer, E.; List, E. J. W. The Origin of Green Emission in Polyfluorene-Based Conjugated Polymers: On-Chain Defect Fluorescence. *Adv. Funct. Mater.* **2003,** *13*, 597-601.

52. Dou, W.; Wang, C.; Wang, G.; Ma, Q.; Su, X. Enhance Effect of Surfactants on the Photoluminescence and Photostability of Water-Soluble Poly(Phenylene Ethynylene). *J. Phys. Chem. B* **2008,** *112*, 12681-12685.

53. Darwish, G. H.; Karam, P. Nanohybrid Conjugated Polyelectrolytes: Highly Photostable and Ultrabright Nanoparticles. *Nanoscale* **2015**.

54. Tian, Y.; Kuzimenkova, M. V.; Xie, M.; Meyer, M.; Larsson, P.-O.; Scheblykin, I. G. Watching Two Conjugated Polymer Chains Breaking Each Other When Colliding in Solution. *NPG Asia Mater* **2014,** *6*, e134.

55. Ngo, A. T.; Lau, K. L.; Quesnel, J. S.; Aboukhalil, R.; Cosa, G. Deposition of Anionic Conjugated Poly(Phenylenevinylene) onto Silica Nanoparticles Via Electrostatic Interactions — Assembly and Single-Particle Spectroscopy. *Can. J. Chem.* **2011,** *89*, 385-394.

56. Liu, H.-W.; Ngo, A. T.; Cosa, G. Enhancing the Emissive Properties of Poly(P-Phenylenevinylene)-Conjugated Polyelectrolyte-Coated Sio_2 Nanoparticles. *J. Am. Chem. Soc.* **2011,** *134*, 1648-1652.

57. Dalgarno, P. A.; Traina, C. A.; Penedo, J. C.; Bazan, G. C.; Samuel, I. D. W. Solution-Based Single Molecule Imaging of Surface-Immobilized Conjugated Polymers. *J. Am. Chem. Soc.* **2013,** *135*, 7187-7193.

58. Glembockyte, V.; Cosa, G. Unpublished Results. **2017**.

59. Tinnefeld, P.; Cordes, T. 'Self-Healing' Dyes: Intramolecular Stabilization of Organic Fluorophores. *Nat Meth* **2012,** *9*, 426-427.

60. Kalyanasundaram, K., Photochemistry in Microheterogeneous Systems. Academic Press: Orlando, 1987; p 388.

5.6 Experimental section

5.6.1 Materials

Poly(phenylene ethynylene) carboxylate PPE-CO_2-49 (PDI = 2.3) was synthesized as previously described.[42] Concentrated polymer solutions in water were diluted in Hyclone HyPure molecular biology-grade water purchased from Fisher. DOTAP and 1,2-dipalmitoyl-*sn*-glycero-3-phosphoethanolamine-N-(biotinyl) (bio-DPPE) were purchased from Avanti Polar Lipids (Alabaster, Alabama, USA). Molecular biology grade solutions of 1 M HEPES (pH 7.3) and 5 M NaCl, hydrogen peroxide (30% solution), HPLC grade acetone, and concentrated HCl were purchased from Fisher. Vectabond was purchased from Vector Laboratories (Burlington, ON, Canada). Concentrated sulfuric acid was purchased from ACP Chemicals. Glucose oxidase, D(+)-glucose, cyclooctatetraene, α-tocopherol, and β-mercaptoethanol were purchased from Sigma Aldrich. DiD was purchased from Invitrogen Canada (Burlington, ON). Poly(ethylene glycol) succinimidyl valerate, MW 5000 (mPEG-SVA) and biotin-PEG-SVA were purchased from Laysan Bio Inc. (Arab, AL). Streptavidin protein was purchased from Life Technologies (Burlington, ON). All materials were used without further purification.

5.6.2 Liposome preparation

DOTAP and bio-DPPE lipid powder were dissolved in chloroform. Aliquots of DiD dissolved in methanol or α-tocopherol (neat) were then added to the lipid solution when noted. The lipid solutions were mixed to a final molar ratio of 99% DOTAP and 1% bio-DPPE. The solvent was evaporated by a stream of argon, and the resulting thin lipid film was placed under vacuum for a minimum of 30 min to remove any remaining solvent. Dry lipid films were then hydrated in a pH 7.3 buffer containing 10 mM 4-(2-hydroxyethyl)-1-piperazineethanesulfonic acid (HEPES) and 150 mM NaCl. The samples were subjected to 10 freeze–thaw–sonication cycles (5 min in dry ice/5 min sonication in a water bath at 40°–50°C) to increase the unilamellarity of the sample. The liposomes were then extruded through a 200 nm polycarbonate membrane using a mini-extruder from Avanti Polar Lipids, Inc. The liposomes were diluted to a lipid concentration of 100 μM and an aliquot of PPE-CO_2-49 dissolved in water was added with vortexing to achieve a final concentration of 0.005 PRU:lipid. Considering that a 200 nm DOTAP liposome is estimated to contain 359,040 lipids (see section 3.7.3), this concentration corresponds to *ca.* 1795 PRUs or 36 PPE-CO_2-49 polymers per liposome.

5.6.3 Coverslip preparation

A glass jar containing 8 glass coverslips was filled with a piranha solution (H_2O_2 (30% vol/vol) and 75% concentrated H_2SO_4) and left to soak for a minimum of one hour. The solution was then poured off and the coverslips were washed multiple times with deionized water followed by 10 minutes of sonication. The rinsing/sonication procedure was then repeated twice with dry acetone (high performance liquid chromatography (HPLC) grade). The coverslips were then incubated in a 1% (v/v) solution of vectabond in acetone to allow the aminosilanization reaction to proceed. After five minutes the reaction mixture was poured off and the coverslips were rinsed twice with water (molecular biology grade) and stored in the jar until further use.

In order to prevent the non-specific adsorption of liposomes or proteins (*e.g.* glucose oxidase), the coverslips were further functionalized with a layer of poly(ethylene glycol). Specifically, the surface of the coverslips was incubated with a solution of poly(ethylene glycol) succinimidyl valerate, molecular weight (MW) 5000 (mPEG-SVA) and biotin-PEG-SVA in a 99:1 ratio (w/w) in 0.1 M sodium bicarbonate. After 3-4 hours, excess PEG solution was rinsed from

the surface with water and the coverslips were dried using a N_2 stream. An imaging chamber (*ca.* 10 µl in volume) was constructed by applying a predrilled polycarbonate film with an adhesive side onto the coverslip. Two silicone ports were then glued on top of the predrilled holes to allow the flow of solutions into and out of the chamber. Prior to imaging, 10 µL of a 0.2 mg/mL streptavidin solution in buffer was injected into the imaging chamber and incubated for 5 mins. Excess streptavidin was washed away with 5x20 µL of buffer.

5.6.4 TIRFM imaging

Fluorescence imaging was carried out using an inverted Nikon Eclipse Ti microscope equipped with the Perfect Focus System (PFS) implementing an objective-type TIRF configuration with a Nikon TIRF illuminator and an oil immersion objective (CFI SR Apo TIRF 100× Oil Immersion Objective Lens, numerical aperture (NA) 1.49). The excitation source was the 405 nm output of an Agilent MLC400B Monolithic Laser Combiner. Laser powers of 0.1 mW-4.4 mW were measured out of the objective. The laser beam was passed through a multiband cleanup filter (ZET405/488/561/647x, Chroma Technology) and coupled into the microscope objective using a multiband beam splitter (ZT405/488r/561/640rpc, Chroma Technology). Images were recorded onto a 512x512 pixel region of a back-illuminated electron-multiplying charge-coupled device (EMCCD) camera (iXon X3 DU-897-CS0-#BV, Andor Technology). Data analysis was performed using a home-built analysis routine written in Matlab based on the algorithms developed by the Ha group.[41] Buffered solutions containing additives were flowed at a rate of 2 µL/min using a syringe pump at the following concentrations, where noted: 143 mM BME (1% v/v), 10 mM COT (prepare by dilution of 1 M COT in DMSO and corresponding to 1% DMSO (v/v) in the final solution), 165 units/mL glucose oxidase in 3% D(+) glucose (v/v). TOC was pre-incorporated into the liposomes at a concentration of 1:100 (TOC:lipid).

Chapter 6: Conclusions and Future Directions

6.1 Contributions to original knowledge and suggestions for future work

This thesis explores how lipid membranes can be used to tune the photophysical/energy transporting properties of conjugated polyelectrolytes (CPEs), with an emphasis on the crucial role that single molecule fluorescence (SMF) microscopy techniques play in the development of new applications based on these materials. Key results include the development of a new methodology to study lipid membrane deformation, the assembly of a light harvesting antenna, and the identification of several antifading cocktails to improve the photostability of CPEs under SMF imaging conditions.

Chapter 2 introduced a new methodology to detect changes in lipid membrane curvature in real-time. Here, the drastic changes in emission quantum yield of the poly(phenylene vinylene) polyanion MPS-PPV that occur upon embedding within lipid membranes were exploited as sensor to record the real-time deformation of liposomes consisting of the cationic lipid DOTAP on the surface of MPS-PPV-coated silicon dioxide nanoparticles (NPs). Using total internal reflection fluorescence microscopy (TIRFM), the docking and subsequent deformation of individual liposomes on hundreds of surface-immobilized NPs was observed in parallel. Conformational changes in the conjugated polyelectrolyte as the membrane deformed along the surface curvature of the nanoparticle resulted in fluorescence intensity enhancements. These enhancements were proportional to the surface coverage by the lipid milieu, providing a means to read to which extent the membrane deformed and how rapidly it was doing so.

By providing a means to determine the dynamics of membrane deformation in response to interaction with a polyelectrolyte scaffold, we anticipate that this study may be of broad interest to the field of cell biology, where it is well-accepted that the ability of the cell membrane to dynamically adjust its phase/topology is essential for numerous cellular processes.[1-2] A parallel can be drawn between the charged biomolecule scaffolds used by nature to coax the cell membrane to adopt strained structures with unfavourable curvature,[3-5] and the curved, charged scaffold provided by the CPE-coated NPs. By playing the role of a scaffold that also doubles as a fluorescent sensor, CPE-coated NPs monitored by TIRFM could provide a unique platform to monitor the dynamics of membrane deformation while systematically varying physical factors

such as NP/membrane curvature and composition, as well as environmental factors like ionic strength.

Another interesting direction would be to study the effect of changing the CPE structure on the dynamics of liposome deformation on the NPs. We may expect the rigid and needle-like PPE-CO_2 polymers to interact differently with the membrane than the more disordered MPS-PPV, for example, perhaps inducing greater strain in the membrane and accelerating rupture upon deformation to form supported lipid bilayers. In Chapter 4, the methodology developed by our group to adsorb MPS-PPV onto surface-modified SiO_2 NPs was easily adapted to produce PPE-CO_2-49 coated NPs; we are therefore confident that our method could also be used to produce monodisperse NPs coated with other CPEs, as desired. Using a combination of cryogenic transmission electron microscopy and TIRFM, the structure and dynamics of the interaction between different CPE-coated NPs with lipid membranes can then be elucidated.

The development of an NP coated with a cationic rather than an anionic CPE would be interesting in the context of studying cellular membranes, which have a net negative charge.[6] In this case, we expect that the polycations would readily adsorb onto the surface of the unmodified SiO_2 NPs owing to the negative charge of the deprotonated silanol groups at neutral pH. The NPs could then be applied as a probe to study uptake by living cells. Although fluorescent NPs have been previously used to study cellular uptake,[7-10] we believe that monitoring the emission enhancement of the CPE-coated NPs may provide an additional dimension of information on the intimate interaction of the membrane with the NP during this process that is not accessible using other probes.

Demonstrating the breadth of applications that may profit from the development of CPE/lipid interactions, Chapter 3 changes focus to explore these materials in the context of light harvesting. Light harvesting systems must absorb large amounts of solar energy and also be able to efficiently funnel this energy to a target where it can be used to do work, *e.g.* drive chemical reactions, *etc*. Here, the self-assembly of a conjugated polyanion with a poly(phenylene ethynylene) backbone (PPE-CO_2-7) into lipid membranes composed of the cationic lipid DOTAP was reported as the basis for a light harvesting antenna. Remarkably, it was found that the membrane scaffold could accommodate the polyanions at a high density (*ca*. 1 nm edge-to-edge separation) without self-quenching, avoiding an important loss mechanism plaguing many other

light harvesting systems. Light harvested by the polymers was then transferred to a model lipophilic energy acceptor (the cyanine dye DiI) whose effective molar absorption was enhanced by up to 18-fold due to the antenna effect. This value is on par with previously reported light harvesting antennas based on self-assembled supramolecular structures.[11] Absorption amplification of DiI was found to be due primarily to direct energy transfer from polymers. The efficiency of homoenergy transfer among polymers was also probed by the membrane embedding fullerene derivative phenyl-C_{61}-butryic acid methyl ester (PCBM) acting as an electron acceptor (quasi reaction center). PCBM quenched the emission of up to five polymers, consistent with a modest amount of homotransfer.

Beyond demonstrating a new light harvesting antenna and reporting its performance, Chapter 3 highlights the advantages of lipid membranes as scaffolds for assembling the components of light harvesting systems in general. Arguably, the most significant discovery of this study was that the lipid membrane can accommodate many polymer donors with minimal losses due to self-quenching. This property was critical to the success of electronic energy harvesting achieved. The physical properties that determine the dispersion of the CPEs within the membrane remain a topic of active research, however, where factors such as the lipid charge, lipid head group type, polymer chain length, and polymer sidechains all have all been recently shown to affect CPE/lipid structures.[12-15] An interesting follow up study would be to assemble a series of different light harvesting antennas based on the methodology developed in Chapter 3, and then screen them for relationships between absorption amplification and factors like those mentioned above, providing a library of information to assist in the design of an improved light harvesting antenna.

Although screening different combinations of CPEs and lipids would help to identify directions for further research, in order to rationally design an improved light harvesting antenna it is also necessary to gain a better understanding of the organization of CPEs within the lipid membrane at the molecular level. Accessing this information is particularly important in the context of light harvesting, since the efficiency of energy transfer is linked to the relative orientation of donor and acceptors. To tackle this problem, we propose fluorescence anisotropy studies on PPE-CO_2 polymers embedded within supported lipid bilayers. By performing these experiments, the orientation of single CPE emission dipoles relative to the surface (*e.g.*, the plane

of the bilayer) could be determined. The effect of the polymer chain length (7 versus 49 PRUs) on the possible orientations could be determined, where the 7-mer is expected to explore more orientations than the 49-mer since its smaller size may allow it to embed both perpendicular and parallel to the membrane plane. SMF experiments in turn could reveal whether the polymers tend to associate within the membrane, forming "rafts" and whether their orientations tend to align with each other or not. Altogether, this line of research would enable us to answer questions about the membrane's ability to organize CPEs toward achieving efficient energy migration and ultimately the design of a high performance light harvesting antenna.

In addition to the physical CPE/lipid interaction, the CPE photophysical properties are critical to the performance of the light harvesting antenna, since these determine the efficiency of homo-energy transfer and the spatial extent of exciton migration within the membrane. For example, all other factors considered equal, we may hypothesize that the selection of a CPE with a longer excited state lifetime will increase the absorption amplification of the trap/reaction centre, since the excitons generated from more distant polymers in the membrane have a greater probability of reaching the trap/reaction centre before decaying *via* a competing process (*e.g.*, emission). Increasing the fluorescence quantum yield may also lead to improved performance by increasing the rate of energy transfer at each step. In addition, increasing the molar absorptivity and/or broadening the absorption spectrum would increase the amount of energy that the antenna can capture. Toward the latter point, the use of several different CPEs that have absorption spectra spanning the visible region could be an interesting strategy to improve the overall light harvesting potential of the antenna.

Sophisticated SMF experiments such as those described in Chapter 2 and in the proposed experiments to extend the work of Chapter 3 demand that the emissive species under study possess excellent signal stability, brightness, and photostability. In Chapters 4 and 5, we report our attempts to improve the photostability of PPE-CO_2-49 under SMF imaging conditions in both aqueous and lipid membrane environments, respectively. Working with PPE-CO_2 adsorbed onto the surface of 100 nm diameter SiO_2 nanoparticles in aqueous solution (Chapter 4) or embedded within the membrane of DOTAP liposomes (Chapter 5), TIRFM was used to monitor the emission intensity of hundreds of surface-immobilized nanoparticles/liposomes in parallel while flowing different solution additives (The water-soluble triplet quenchers/antioxidants ascorbic acid (AA),

β-mercaptoethanol (BME), Ni^{2+}, trolox (TX), and trolox quinone (TQ) in the case of the PPE-CO_2-49-coated NPs and the more hydrophobic additives BME, cyclooctatetraene (COT) and α-tocopherol (TOC) in the case of the PPE-CO_2-49-containing liposomes. The effect of oxygen removal using an enzymatic oxygen scavenging system based on glucose oxidase (GOX) was also determined in both cases.

From these experiments, one of the major contributions was the identification of several antifading cocktails that improve the photostability of PPE-CO_2-49. For the NPs, the best results were obtained using AA and TX in buffer (up to 8-fold improvement) and with the oxygen scavenging system (up to 15-fold improvement). For the liposomes, the most successful cocktail was TOC used in combination with GOX, where a 20-40-fold improvement was observed. By achieving this level of improvement, the number of photons emitted by PPE-CO_2-49 is brought on par with other commonly used fluorophores in SMF experiments, thus expanding the possibilities in terms of the type/timescale of SMF experimentation on CPEs that can feasibly be performed. Armed with this information, we are hopeful that other researchers will be able to readily adapt and optimize our findings toward their own specific imaging requirements.

In addition to providing recipes for anti-fading cocktails, the analysis of the results in Chapters 4 and 5 also contributes toward developing a mechanistic understanding of the photophysics underpinning the action of the additives. Here, the excited triplet state and oxygen were identified as being key players in the photodegradation of PPE-CO_2. The CPE radical anion formed *via* reaction of the excited triplet state with reducing agents such as AA, TX, and TOC was also implicated as an important intermediate in the photobleaching pathway. Although the majority of the results could be rationalized in terms of the photophysics of these species, the identity/origin of the species contributing to the residual intensity (*i.e.*, the "unbleachable fraction") in the intensity *versus* time trajectories of the PPE-CO_2-49-containing liposomes under several solution conditions remains unknown. Uncovering the mechanism behind this phenomenon is an important challenge for future work, since the discovery of a CPE/lipid with unprecedented photostability could have a tremendous impact in the field of fluorescent imaging markers or any other application that requires a bright, stable fluorescent signal.

6.2 References

1. McMahon, H. T.; Gallop, J. L. Membrane Curvature and Mechanisms of Dynamic Cell Membrane Remodelling. *Nature* **2005,** *438*, 590-596.

2. Zimmerberg, J.; Kozlov, M. M. How Proteins Produce Cellular Membrane Curvature. *Nat. Rev. Mol. Cell Biol.* **2006,** *7*, 9-19.

3. Campelo, F.; McMahon, H. T.; Kozlov, M. M. The Hydrophobic Insertion Mechanism of Membrane Curvature Generation by Proteins. *Biophys. J.* **2008,** *95*, 2325-2339.

4. Frost, A.; Perera, R.; Roux, A.; Spasov, K.; Destaing, O.; Egelman, E. H.; De Camilli, P.; Unger, V. M. Structural Basis of Membrane Invagination by F-Bar Domains. *Cell* **2008,** *132*, 807-817.

5. Ren, G.; Vajjhala, P.; Lee, J. S.; Winsor, B.; Munn, A. L. The Bar Domain Proteins: Molding Membranes in Fission, Fusion, and Phagy. *Microbiol. Mol. Biol. Rev.* **2006,** *70*, 37-120.

6. Cooper, G. M.; Hausman, R. E., The Cell : A Molecular Approach. 2016.

7. Fernando, L. P.; Kandel, P. K.; Yu, J.; McNeill, J.; Ackroyd, P. C.; Christensen, K. A. Mechanism of Cellular Uptake of Highly Fluorescent Conjugated Polymer Nanoparticles. *Biomacromolecules* **2010,** *11*, 2675-2682.

8. Zhu, C.; Liu, L.; Yang, Q.; Lv, F.; Wang, S. Water-Soluble Conjugated Polymers for Imaging, Diagnosis, and Therapy. *Chem. Rev.* **2012,** *112*, 4687-4735.

9. Wu, C.; Chiu, D. T. Highly Fluorescent Semiconducting Polymer Dots for Biology and Medicine. *Angew. Chem. Int. Edit.* **2013,** *52*, 3086-3109.

10. Peng, H.-S.; Chiu, D. T. Soft Fluorescent Nanomaterials for Biological and Biomedical Imaging. *Chem. Soc. Rev.* **2015,** *44*, 4699-4722.

11. Woller, J. G.; Hannestad, J. K.; Albinsson, B. Self-Assembled Nanoscale DNA–Porphyrin Complex for Artificial Light Harvesting. *J. Am. Chem. Soc.* **2013,** *135*, 2759-2768.

12. Wang, Y.; Schanze, K. S.; Chi, E. Y.; Whitten, D. G. When Worlds Collide: Interactions at the Interface between Biological Systems and Synthetic Cationic Conjugated Polyelectrolytes and Oligomers. *Langmuir* **2013,** *29*, 10635-10647.

13. Houston, J. E.; Kraft, M.; Mooney, I.; Terry, A. E.; Scherf, U.; Evans, R. C. Charge-Mediated Localization of Conjugated Polythiophenes in Zwitterionic Model Cell Membranes. *Langmuir* **2016,** *32*, 8141-8153.

14. Kahveci, Z.; Martínez-Tomé, M.; Esquembre, R.; Mallavia, R.; Mateo, C. Selective Interaction of a Cationic Polyfluorene with Model Lipid Membranes: Anionic Versus Zwitterionic Lipids. *Materials* **2014,** *7*, 2120-2140.

15. Wang, Y.; Chi, E. Y.; Schanze, K. S.; Whitten, D. G. Membrane Activity of Antimicrobial Phenylene Ethynylene Based Polymers and Oligomers. *Soft Matter* **2012,** *8*, 8547-8558.

List of Publications

1. Karam, P.; Hariri, A. A.; **Calver, C. F.**; Zhao, X.; Schanze, K. S.; Cosa, G. Interaction of anionic phenylene ethynylene polymers with lipids: From membrane embedding to liposome fusion. *Langmuir* **2014,** *30*, 10704-10711.

2. **Calver, C. F.**; Liu, H.-W.; Cosa, G. Exploiting conjugated polyelectrolyte photophysics toward monitoring real-time lipid membrane-surface interaction dynamics at the single-particle level. *Langmuir* **2015,** *31*, 11842-11850.

3. **Calver, C. F.**; Schanze, K. S.; Cosa, G. Biomimetic light-harvesting antenna based on the self-assembly of conjugated polyelectrolytes embedded within lipid membranes. *ACS Nano* **2016,** *10*, 10598-10605.

4. **Calver, C. F.**; Lago, B.A.; Schanze, K. S.; Cosa, G. Enhanced photostability of poly(phenylene ethynylene) coated SiO2 nanoparticles. *J. Phys. Chem. B.*, **2017**, *Under Review*.

5. **Calver, C. F.**; Lago, B.A.; Schanze, K. S.; Cosa, G. Additives for enhanced photostability of a poly(phenylene ethynylene)-based conjugated polyelectrolyte in lipid membranes. *In Preparation*.